MULTI-LAYER MODELS FOR MOVING CONTACT PROBLEMS OF GRADED MATERIALS AND MULTIFERROICS

A THESIS SUBMITTED TO
THE GRADUATE SCHOOL OF NATURAL AND APPLIED SCIENCES
OF
MIDDLE EAST TECHNICAL UNIVERSITY

BY

SELİM ERCİHAN TOKTAŞ

IN PARTIAL FULFILLMENT OF THE REQUIREMENTS
FOR
THE DEGREE OF DOCTOR OF PHILOSOPHY
IN
MECHANICAL ENGINEERING

JANUARY 2024

Approval of the thesis:

MULTI-LAYER MODELS FOR MOVING CONTACT PROBLEMS OF GRADED MATERIALS AND MULTIFERROICS

submitted by **SELİM ERCİHAN TOKTAŞ** in partial fulfillment of the requirements for the degree of **Doctor of Philosophy in Mechanical Engineering Department, Middle East Technical University** by,

Prof. Dr. Halil Kalıpçılar
Dean, **Graduate School of Natural and Applied Sciences**

Prof. Dr. M. A. Sahir Arıkan
Head of the Department, **Mechanical Engineering**

Prof. Dr. Serkan Dağ
Supervisor, **Mechanical Engineering, METU**

Examining Committee Members:

Prof. Dr. Fevzi Suat Kadıoğlu
Mechanical Engineering, METU

Prof. Dr. Serkan Dağ
Mechanical Engineering, METU

Assoc. Prof. Dr. Hüsnü Dal
Mechanical Engineering, METU

Prof. Dr. Recep Güneş
Mechanical Engineering, Erciyes University

Assoc. Prof. Dr. Mehmet Nurullah Balcı
Mechanical Engineering, Hacettepe University

Date: 19.01.2024

I hereby declare that all information in this document has been obtained and presented in accordance with academic rules and ethical conduct. I also declare that, as required by these rules and conduct, I have fully cited and referenced all material and results that are not original to this work.

Name Last name : Selim Ercihan Toktaş

Signature :

ABSTRACT

MULTI-LAYER MODELS FOR MOVING CONTACT PROBLEMS OF GRADED MATERIALS AND MULTIFERROICS

Toktaş, Selim Ercihan
Doctor of Philosophy, Mechanical Engineering
Supervisor: Prof. Dr. Serkan Dağ

January 2024, 202 pages

In the present work, a solution method for the elastodynamic contact problems of rigid punches is developed for several smart systems in two dimensional medium. The considered composite structures always comprise a homogeneneous elastic substrate covered by a coating involving single layer or many sub-layers. The wear resistant coatings encountered in the industry possess heterogeneous structure and their properties are defined by gradation functions. Analytical contact solutions of such coatings generally focus on a single layer coating with exponential gradation through the depth of the coating as it is easier to work with the exponential function in the solution of differential equations. Yet, this assumption lacks in reality due to its limitations since the gradation function can be any function. The mathematical challenges of the random gradation functions are overcome by the discretization of the coating with homogeneous multi-layer modelling (HMLM) method. After homogenization of the structure, the formulation is based on the wave equations of plane elastodynamics and Maxwell's equations depending on the coating type. By examining each layer with its own boundary conditions and applying Galilean and Fourier Transform techniques, the singular integral equation of the contact problem is derived for four different punches. In the next step, this equation is numerically solved by Jacobi expansion-collocation method to obtain the outputs. The main emphasize is the investigation of the influences of the coating type, the speed of the punch, the coating thickness-to-contact length ratio and the coefficient of dynamic friction on contact stresses, electric displacement and magnetic induction.

Keywords: Functionally Graded Materials, Multiferroics, Moving Contact, Singular Integral Equation, Multi-Layer Modelling.

ÖZ

DERECELENDİRİLMİŞ MALZEMELERİN VE MULTİFERROİKLERİN HAREKETLİ TEMAS PROBLEMLERİ İÇİN ÇOK KATMANLI MODELLERİ

Toktaş, Selim Ercihan
Doktora, Makina Mühendisliği
Tez Yöneticisi: Prof. Dr. Serkan Dağ

Ocak 2024, 202 sayfa

Bu çalışmada iki boyutlu ortamdaki çeşitli akıllı sistemlerde rijit zımbaların elastodinamik temas problemleri için bir çözüm yöntemi geliştirilmiştir. Ele alınan kompozit yapılar her zaman homojen bir elastik alt yüzeyden ve bu yüzeyi koruyan tek katman veya çoklu katmanlar içeren bir kaplamadan oluşmaktadır. Endüstride karşılaşılan aşınmaya dirençli kaplamalar heterojen yapıya sahiptirler ve kaplamaların özellikleri derecelendirilme fonksiyonları ile tanımlanır. Bu kaplamaların analitik temas çözümleri genellikle tek katmanlı ve katmanın derinliği yönünde üssel fonksiyonla derecelendirilmiş kaplamalara odaklanmıştır çünkü diferansiyel denklemlerin çözümünde üssel fonksiyon ile çalışmak daha kolaydır. Fakat bu varsayım kısıtlamalarından ötürü gerçekte yeterli değildir çünkü derecelendirilme fonksiyonu herhangi bir fonksiyon olabilir. Rastgele derecelendirilme fonksiyonlarının oluşturduğu matematiksel zorlukların üstesinden kaplamanın homojen çok-katmanlı modelleme (HÇKM) yöntemi ile ayrıklaştırılmasıyla gelinir. Yapının homojenleştirilmesinin ardından formülasyon düzlemsel elastodinamiğin dalga ve kaplama türüne göre Maxwell denklemlerine dayandırılmıştır. Her katmanı kendi içindeki sınır koşulları ile inceleyerek ve Galile ve Fourier Dönüşüm tekniklerini uygulayarak dört farklı zımba için temas problemine ait tekil integral denklemi türetilir. Sonraki aşamada çıktıları elde etmek için bu denklem sayısal olarak Jacobi açılım-sıralama yöntemiyle çözülmüştür. Ana vurgu kaplama türünün, zımba hızının, kaplama kalınlığı-temas uzunluğu oranının ve dinamik sürtünme katsayısının temas gerilmeleri, elektriksel yer değiştirme ve manyetik indüksiyon üzerindeki etkilerinin incelenmesidir.

Anahtar Kelimeler: Fonksiyonel Derecelendirilmiş Malzemeler, Multiferroikler, Hareketli Temas, Tekil İntegral Denklemi, Çok-Katmanlı Modelleme.

To the domestic and national people utterly and solely loyal to Türkiye

ACKNOWLEDGMENTS

Firstly, the author would like to thank to his supervisor Prof. Dr. Serkan Dağ for his help, guidance and mentorship not only in this thesis but also in published articles regarding this research. Without his continuous support and insight, the completion of this dissertation would not have been possible. Hence, working with him was a unique pleasure. Besides his supervisor, the author is also obliged to the thesis examining committee members Assoc. Prof. Dr. Hüsnü Dal and Prof. Dr. Recep Güneş for their encouragement and insightful comments in each meeting.

This work is funded by four programs of Scientific and Technological Research Council of Türkiye (TÜBİTAK). The author gratefully acknowledges the financial support of TÜBİTAK through BİDEB 2211A National PhD Scholarship Program (application number 1649B032100684), 2224A Grant Program for Participation in Scientific Meetings Abroad (application number 1919B022200824), 2250 Performance-Based Scholarships Programme for PhD and Post-Doc Scholars (application number 1229B502305007) and 1002A Short Term Support Module (grant number 122M784). The author would like to express his sincere gratitude and deepest appreciation to the chairman Prof. Dr. Hasan Mandal and senior staff of TÜBİTAK for their presentations and webinars about new TÜBİTAK programs and excellent counseling.

The author worked as teaching assistant in Mechanical Engineering Department at METU during his doctorate education. The author is deeply indebted to his colleagues Instructor Muhtar Ural Uluer and other instructors teaching ME 105 Computer Aided Engineering Graphics course for their understanding and cooperation. Working/collaborating with them was a privilege for him. Lastly, the author wishes to thank to the administrative and secretarial staff Müveyla Kolbaşı and Sevila Şener at METU for their aid in the preparation of necessary documents to participate in national and international events.

TABLE OF CONTENTS

ABSTRACT v

ÖZ vii

ACKNOWLEDGMENTS x

TABLE OF CONTENTS xi

LIST OF TABLES xv

LIST OF FIGURES xix

LIST OF ABBREVIATIONS xxvi

LIST OF SYMBOLS xxvii

CHAPTERS

1 INTRODUCTION 1

1.1 Review of FGMs 1

1.2 Review of Multiferroics 4

1.3 Review of Multi-layer Models 7

1.4 Thesis Aim and Outline 11

2 LITERATURE REVIEW 13

2.1 Literature Review of Multi-Layer and FGMs in Contact Mechanics 13

2.2 Literature Review of Multi-Layer and FGM Multiferroics in Contact Mechanics 16

2.3 Literature Review of Multi-layer Models in Solid Mechanics 20

3 PROBLEM STATEMENT AND FORMULATION 23

3.1 Multi-layer Model 23

3.1.1 Interface Continuity and Boundary Conditions....................................... 29

3.1.1.1 Continuity Conditions along the Interfaces 30
3.1.1.2 Boundary Conditions 33
3.1.2 Derivation of the Singular Integral Equation of Multi-layer Model 34
3.1.3 Derivation of Lateral Contact Stress on the Surface 40
3.2 Multiferroic Structure 41
3.2.1 Interface Continuity and Boundary Conditions 50
3.2.1.1 Continuity Conditions along the Interfaces 50
3.2.1.2 Boundary Conditions 64
3.2.2 Derivation of the Singular Integral Equation of Multiferroic Structure ... 65
3.2.3 Derivation of Lateral Contact Stress, Electric Displacement and Magnetic Induction 69
4 NUMERICAL SOLUTION OF SINGULAR INTEGRAL EQUATION 75
4.1 Flat Punch Problem 75
4.1.1 Multi-layer Model 75
4.1.2 Multiferroic Structure 78
4.2 Triangular Punch Problem 81
4.2.1 Multi-layer Model 81
4.2.2 Multiferroic Structure 84
4.3 Semi-Circular Punch Problem 87
4.3.1 Multi-layer Model 87
4.3.2 Multiferroic Structure 90
4.4 Circular Punch Problem 93
4.4.1 Multi-layer Model 93
4.4.2 Multiferroic Structure 97

5 NUMERICAL RESULTS ... 101
5.1 Numerical Results for Flat and Triangular Punches ... 102
5.1.1 Multi-layer Model ... 102
5.1.1.1 Verification ... 103
5.1.1.2 Parametric Analyses ... 107
5.1.2 Multiferroic Structure ... 114
5.1.2.1 Verification ... 114
5.1.2.2 Parametric Analyses ... 117
5.2 Numerical Results for Semi-Circular Punch ... 126
5.2.1 Multi-layer Model ... 126
5.2.1.1 Verification ... 127
5.2.1.2 Parametric Analyses ... 128
5.2.2 Multiferroic Structure ... 133
5.2.2.1 Parametric Analyses ... 133
5.3 Numerical Results for Circular Punch ... 140
5.3.1 Multi-layer Model ... 140
5.3.1.1 Verification ... 140
5.3.1.2 Parametric Analyses ... 142
5.3.2 Multiferroic Structure ... 151
5.3.2.1 Verification ... 151
5.3.2.2 Parametric Analyses ... 153
5.4 Additional Numerical Results ... 160
6 CONCLUSIONS AND FUTURE WORK ... 165
6.1 Concluding Remarks ... 166

6.2 Future Studies 168

REFERENCES 171

APPENDICES

A. The Details of Asymptotic Analyses 187

B. The Coefficients Found by Asymptotic Analyses 191

C. Properties of Jacobi Polynomials 193

D. The Method of Evaluation of Fredholm Kernels 195

E. Closed Form Solution of Contact Mechanics of Homogenous MEE Half-Plane Indented by Circular Punch 197

CURRICULUM VITAE 201

LIST OF TABLES

TABLES

Table 1.1. A comparison of weaknesses and strengths of multi-layer models. 10
Table 5.1. Number of layers, stresses, and percent approximate errors computed at *s*=0 for a graded coating whose properties are varying with exponential functions in contact with a moving flat punch. 106
Table 5.2. Properties of Ni and ZrO_2 (Abdullaev et al., 2015; Dag, 2007; Opalinska et al., 2015). 109
Table 5.3. Exponents used in parametric analyses for the functionally graded coatings. 109
Table 5.4. Number of layers, stresses, and percent approximate errors computed at *s*=0 for a CR coating in contact with a moving flat punch. 110
Table 5.5. Material properties used in the parametric analyses (set-1) (Annamalai et al., 2018; Elloumi et al., 2013; Giraud and Canel, 2008; Golalikhani et al., 2018; Masys and Jonauskas, 2015; MEMSnet, 2023; Suzuki et al., 2019). 115
Table 5.6. Exponents used in the parametric analyses (set-1). 116
Table 5.7. Number of layers, stresses, electric displacement, magnetic induction and percent approximate errors computed at *s*=0 for an FGM2 coating in contact with a moving flat punch. 119
Table 5.8. Stress intensity factors computed for different MEE coatings in contact with a moving flat punch. 119
Table 5.9. Stress intensity factors computed for an FGM2 coating in contact with a moving flat punch for various values of $\lambda_{(1)}$. 120
Table 5.10. Stress intensity factors computed for an FGM2 coating in contact with a moving flat punch for various values of h_c/b. 122
Table 5.11. Stress intensity factor and contact force computed for different MEE coatings in contact with a moving triangular punch. 124
Table 5.12. Stress intensity factor and contact force computed for an FGM2 coating in contact with a moving triangular punch for various values of $\lambda_{(1)}$. 125

Table 5.13 Stress intensity factor and contact force computed for an FGM2 coating in contact with a moving triangular punch for various values of h_c/b 126
Table 5.14. Number of layers, stresses, and percent approximate errors computed at s=0 for a graded coating whose properties are varying with exponential functions in contact with a moving semi-circular punch...127
Table 5.15. Properties of silicon carbide and aluminum (Eshraghi and Dag, 2018). 128
Table 5.16. Number of layers, stresses, and approximate errors computed at s=0 for a CR coating in contact with a moving semi-circular punch................................129
Table 5.17. Contact force and stress intensity factor computed for FGM coatings in contact with a moving semi-circular punch...130
Table 5.18. Contact force and stress intensity factor computed for a CR coating in contact with a moving semi-circular punch for various values of $\lambda_{(1)}$..................131
Table 5.19. Contact force and stress intensity factor computed for an LN coating in contact with a moving semi-circular punch for various values of b/h. 132
Table 5.20. Contact force and stress intensity factor computed for an MR coating in contact with a moving semi-circular punch for various values of η. 133
Table 5.21. Material properties used in the parametric analyses (set-2) (Ajdour et al., 2016; Annamalai et al., 2018; Elloumi et al., 2013; Giraud and Canel, 2008; Golalikhani et al., 2018; Masys and Jonauskas, 2015; MEMSnet, 2023; Suzuki et al., 2019)...134
Table 5.22. Number of layers, stresses, and approximate errors computed at s=0 for an FGM2 coating in contact with a moving semi-circular punch. 134
Table 5.23. Contact force and stress intensity factor computed for different MEE coatings in contact with a moving semi-circular punch. 136
Table 5.24. Contact force and stress intensity factor computed for an FGM1 coating in contact with a moving semi-circular punch for various values of $\lambda_{(1)}$..............137
Table 5.25. Contact force and stress intensity factor computed for an FGM2 coating in contact with a moving semi-circular punch for various values of h_c/b 138

Table 5.26. Contact force and stress intensity factor computed for an FGM3 coating in contact with a moving semi-circular punch for various values of η................ 140
Table 5.27. Number of layers, stresses, and approximate errors computed at s=0 for a graded coating whose properties are varying with exponential functions in contact with a moving circular punch.. 142
Table 5.28. Material properties and thicknesses used in the solution of the periodic multi-layer coating problem (AZO Materials, 2023; Bhattarai et al., 2018; MEMSnet, 2023; Penkov et al., 2015; Suk et al., 2012)...................................... 143
Table 5.29. Contact force and punch position parameter computed for a periodic multi-layer coating in contact with a moving circular punch for various values of $\lambda_{(1)}$... 144
Table 5.30. Contact force and punch position parameter computed for a periodic multi-layer coating in contact with a moving circular punch for various values of η. 145
Table 5.31. Number of layers, stresses, and approximate errors computed at s=0 for a CR coating in contact with a moving circular punch. 146
Table 5.32. Contact force and punch position parameter computed for FGM coatings in contact with a moving circular punch. 147
Table 5.33. Contact force and punch position parameter computed for a CR coating in contact with a moving circular punch for various values of $\lambda_{(1)}$. 148
Table 5.34. Contact force and punch position parameter computed for an MR coating in contact with a moving circular punch for various values of $\lambda_{(1)}$. 148
Table 5.35. Contact force and punch position parameter computed for a CR coating in contact with a moving circular punch for various values of $(b+a)/h$. 150
Table 5.36. Contact force and punch position parameter computed for a CR coating in contact with a moving circular punch for various values of η. 151
Table 5.37. Comparisons of contact force and punch position parameter for a homogeneous MEE half-plane in contact with a moving circular punch. 153
Table 5.38. Exponents used in the parametric analyses (set-2). 154

Table 5.39. Number of layers, stresses, electric displacement, magnetic induction and percent approximate errors computed at s=0 for an FGM1 in contact with a moving circular punch. 155
Table 5.40. Contact force and punch position parameter for the coating FGM1 in contact with circular punch. 155
Table 5.41. Contact force and punch position parameter computed for different MEE coatings in contact with a moving circular punch. 156
Table 5.42. Contact force and punch position parameter computed for an FGM1 coating in contact with a moving circular punch for various values of $\lambda_{(1)}$. 157
Table 5.43. Contact force and punch position parameter computed for an FGM1 coating in contact with a moving circular punch for various values of $h_c/(b+a)$. 158
Table 5.44. Contact force and punch position parameter computed for an FGM1 coating in contact with a moving circular punch for various values of η. 159
Table 5.45. Material properties and thicknesses of a magnetic storage device (Katta et al., 2009). 162
Table 5.46. Stress intensity factors and contact force computed for a magnetic storage device in contact with a punch. 164

LIST OF FIGURES

FIGURES

Figure 1.1. Schematics of the particulate FGMs with constituent phases. (Popoola et al., 2016; Zhang, C. et al., 2019).. 3
Figure 1.2. Energy coupling mechanism in MEE materials (Palneedi et al., 2016). 5
Figure 1.3. Sample MEE material made of barium titanate and cobalt ferrite (Erdem et al, 2016). 7
Figure 1.4. The schematic illustration of $BaTiO_3/CoFe_2O_4$ composite and the crystal structures of both constituents (Jian and Wong, 2017)... 8
Figure 1.5. Approximate multi-layer models, $\mu(x)/\mu(0)=1-0.8(x/h)^{\gamma}$, N=5. (a) γ=2.0; (b) γ=0.5. 10
Figure 1.6. Comparison of HMLM and Exact Gradation Function: (a) Stiffer coating, from top to bottom, $\mu(x)/\mu(0)=1-0.8(x/h)^{\gamma}$, γ = 5.0,4.0,3.0,2.0,1.0,0.8,0.6,0.4,0.2; (b) Less stiff coating, from top to bottom, $\mu(x)/\mu(0)=0.2+0.8(x/h)^{\gamma}$, γ = 0.2,0.4,0.6, 0.8,1.0,2.0,3.0,4.0,5.0.. 10
Figure 2.1. Schematic illustration of LMLM method (Ke and Wang, 2007). 20
Figure 2.2. Schematic illustration of EMLM method (Guo et al., 2018)................ 21
Figure 2.3. Schematic illustration of HMLM method (Jobin et al., 2017). 21
Figure 3.1. Geometry of general moving contact problem of elastic heterostructure. 24
Figure 3.2. Two-dimensional Galilean Transformation... 25
Figure 3.3. Geometry of general moving contact problem of multiferroic heterostructure.. 42
Figure 4.1. A moving rigid flat punch on FGM coating with arbitrary spatial variations of material properties. 76
Figure 4.2. A moving rigid flat punch on FGM MEE coating with arbitrary spatial variations of material properties. 79
Figure 4.3. A moving rigid triangular punch on FGM coating with arbitrary spatial variations of material properties. 82

Figure 4.4. A moving rigid triangular punch on FGM MEE coating with arbitrary spatial variations of material properties. 85
Figure 4.5. A moving rigid semi-circular punch on FGM coating with arbitrary spatial variations of material properties. 88
Figure 4.6. A moving rigid semi-circular punch on FGM MEE coating with arbitrary spatial variations of material properties. 90
Figure 4.7. A moving rigid circular punch on periodic Co/C coating....................94
Figure 4.8. A moving rigid circular punch on FGM coating with arbitrary spatial variations of material properties..94
Figure 4.9. A moving rigid circular punch on FGM MEE coating with arbitrary spatial variations of material properties. 98
Figure 5.1. Comparison of contact stresses for an isotropic half-plane in contact with a moving flat punch to those given by Eringen and Suhubi (1975) (a) normal stress; (b) normal stress in lateral direction..104
Figure 5.2. Comparison of contact stresses for a graded coating whose properties are varying with power functions in contact with a stationary flat punch to those given by Ke and Wang (2007): (a) normal stress; (b) normal stress in lateral direction.104
Figure 5.3. Comparison of contact stresses for a graded coating whose properties are varying with exponential functions in contact with a moving flat punch to those given by Balci and Dag (2020): (a) normal stress; (b) normal stress in lateral direction. 106
Figure 5.4. Comparison of contact stresses for a graded coating whose properties are varying with exponential functions in contact with a moving triangular punch to those given by Balci and Dag (2020): (a) normal stress; (b) normal stress in lateral direction...107
Figure 5.5. Comparison of the stresses generated by single- and multi-layer models in contact with a moving flat punch. 108
Figure 5.6. Contact stresses computed by considering FGM coatings in contact with a moving flat punch: (a) normal stress; (b) normal stress in lateral direction. 110

Figure 5.7. Stress intensity factors computed by considering FGM coatings in contact with a moving flat punch: (a) $K_I(-1)$ (b) $K_I(1)$. 111

Figure 5.8. Contact stresses computed by considering a CR coating in contact with a moving triangular punch for various values of $\lambda_{(1)}$: (a) normal stress; (b) normal stress in lateral direction. 112

Figure 5.9. Stress intensity factor and normalized punch force computed by considering a CR coating in contact with a moving triangular punch for various values of η. 112

Figure 5.10. Contact stresses computed by considering a CR coating in contact with a moving flat punch for various values of b/h: (a) normal stress; (b) normal stress in lateral direction. 113

Figure 5.11. Stress intensity factors computed by considering a CR coating in contact with a moving flat punch for various values of η. 113

Figure 5.12. Comparisons of contact stresses for an MEE half-plane in contact with a moving flat punch to those given by Zhou and Lee (2012b): (a) normal stress in Z-direction; (b) normal stress in X-direction. 117

Figure 5.13. Mechanic and electro-magnetic results computed for different MEE coatings in contact with a moving flat punch: (a) normal stress in Z-direction; (b) normal stress in X-direction; (c) electric displacement in X-direction; (d) magnetic induction in X-direction. 118

Figure 5.14. Mechanic and electro-magnetic results computed by considering an FGM2 coating in contact with a moving flat punch for various values of $\lambda_{(1)}$: (a) normal stress in Z-direction; (b) normal stress in X-direction; (c) electric displacement in X-direction; (d) magnetic induction in X-direction.................... 120

Figure 5.15. Mechanic and electro-magnetic results computed by considering an FGM2 coating in contact with a moving flat punch for various values of h_c/b: (a) normal stress in Z-direction; (b) normal stress in X-direction; (c) electric displacement in X-direction; (d) magnetic induction in X-direction.................... 121

Figure 5.16. Mechanic and electro-magnetic results computed for different MEE coatings in contact with a moving triangular punch: (a) normal stress in Z-direction; (b) normal stress in X-direction; (c) electric displacement in X-direction; (d) magnetic induction in X-direction. 123
Figure 5.17. Mechanic and electro-magnetic results computed by considering an FGM2 coating in contact with a moving triangular punch for various values of $\lambda_{(1)}$: (a) normal stress in Z-direction; (b) normal stress in X-direction; (c) electric displacement in X-direction; (d) magnetic induction in X-direction. 124
Figure 5.18. Mechanic and electro-magnetic results computed by considering an FGM2 coating in contact with a moving triangular punch for various values of h_c/b: (a) normal stress in Z-direction; (b) normal stress in X-direction; (c) electric displacement in X-direction; (d) magnetic induction in X-direction. 125
Figure 5.19. Comparison of contact stresses for a graded coating whose properties are varying with exponential functions in contact with a moving semi-circular punch to those given by Balci and Dag (2018b): (a) normal stress; (b) normal stress in lateral direction. 128
Figure 5.20. Contact stresses computed by considering FGM coatings in contact with a moving semi-circular punch: (a) normal stress; (b) normal stress in lateral direction. 129
Figure 5.21. Contact stresses computed by considering a CR coating in contact with a moving semi-circular punch for various values of $\lambda_{(1)}$: (a) normal stress; (b) normal stress in lateral direction. 130
Figure 5.22. Contact stresses computed by considering an LN coating in contact with a moving semi-circular punch for various values of b/h: (a) normal stress; (b) normal stress in lateral direction. 131
Figure 5.23. Contact stresses computed by considering an MR coating in contact with a moving semi-circular punch for various values of η: (a) normal stress; (b) normal stress in lateral direction. 132

Figure 5.24. Mechanic and electro-magnetic results computed for different MEE coatings in contact with a moving semi-circular punch: (a) normal stress in *Z*-direction; (b) normal stress in *X*-direction; (c) electric displacement in *X*-direction; (d) magnetic induction in *X*-direction. 136

Figure 5.25. Mechanic and electro-magnetic results computed by considering an FGM1 coating in contact with a moving semi-circular punch for various values of $\lambda_{(1)}$: (a) normal stress in *Z*-direction; (b) normal stress in *X*-direction; (c) electric displacement in *X*-direction; (d) magnetic induction in *X*-direction. 137

Figure 5.26. Mechanic and electro-magnetic results computed by considering an FGM2 coating in contact with a moving semi-circular punch for various values of h_c/b: (a) normal stress in *Z*-direction; (b) normal stress in *X*-direction; (c) electric displacement in *X*-direction; (d) magnetic induction in *X*-direction. 138

Figure 5.27. Mechanic and electro-magnetic results computed by considering an FGM3 coating in contact with a moving semi-circular punch for various values of η: (a) normal stress in *Z*-direction; (b) normal stress in *X*-direction; (c) electric displacement in *X*-direction; (d) magnetic induction in *X*-direction. 139

Figure 5.28. Comparison of contact stresses for a graded coating whose properties are varying with exponential functions in contact with a circular punch to those given by Balci and Dag (2019a): (a) normal stress; (b) normal stress in lateral direction. 141

Figure 5.29. Contact stresses computed by considering a periodic multi-layer coating in contact with a moving circular punch for various values of $\lambda_{(1)}$: (a) normal stress; (b) normal stress in lateral direction. 143

Figure 5.30. Contact stresses computed by considering a periodic multi-layer coating in contact with a moving circular punch for various values of η: (a) normal stress; (b) normal stress in lateral direction. 144

Figure 5.31. Contact stresses computed by considering FGM coatings in contact with a moving circular punch: (a) normal stress; (b) normal stress in lateral direction.146

Figure 5.32. Contact stresses computed by considering a CR coating in contact with a moving circular punch for various values of $\lambda_{(1)}$: (a) normal stress; (b) normal stress in lateral direction. 147
Figure 5.33. Contact stresses computed by considering an MR coating in contact with a moving circular punch for various values of $\lambda_{(1)}$: (a) normal stress; (b) normal stress in lateral direction. 148
Figure 5.34. Contact stresses computed by considering a CR coating in contact with a moving circular punch for various values of $(b+a)/h$: (a) normal stress; (b) normal stress in lateral direction. 149
Figure 5.35. Contact stresses computed by considering a CR coating in contact with a moving circular punch for various values of η: (a) normal stress; (b) normal stress in lateral direction. 150
Figure 5.36. Comparisons of contact stresses for an MEE half-plane in contact with a moving circular punch to closed form solutions for various values of λ: (a) normal stress in Z-direction; (b) normal stress in X-direction; (c) electric displacement in X-direction; (d) magnetic induction in X-direction. 152
Figure 5.37. Mechanic and electro-magnetic results computed for different MEE coatings in contact with a moving circular punch: (a) normal stress in Z-direction; (b) normal stress in X-direction; (c) electric displacement in X-direction; (d) magnetic induction in X-direction. 156
Figure 5.38. Mechanic and electro-magnetic results computed for an FGM1 coating in contact with a moving circular punch for various values of $\lambda_{(1)}$: (a) normal stress in Z-direction; (b) normal stress in X-direction; (c) electric displacement in X-direction; (d) magnetic induction in X-direction. 157
Figure 5.39. Mechanic and electro-magnetic results computed for an FGM1 coating in contact with a moving circular punch for various values of $h_c/(b+a)$: (a) normal stress in Z-direction; (b) normal stress in X-direction; (c) electric displacement in X-direction; (d) magnetic induction in X-direction. 159

Figure 5.40. Mechanic and electro-magnetic results computed for an FGM1 coating in contact with a moving circular punch for various values of η: (a) normal stress in *Z*-direction; (b) normal stress in *X*-direction; (c) electric displacement in *X*-direction; (d) magnetic induction in *X*-direction. 160
Figure 5.41. The moving rigid punches on multi-layer storage device: (a) flat punch; (b) triangular punch. 161
Figure 5.42. Contact stresses computed by considering a magnetic storage device (Katta et al., 2009) in contact with a moving flat punch. (a) Normal stress; (b) normal stress in lateral direction. 162
Figure 5.43. Contact stresses computed by considering a magnetic storage device (Katta et al., 2009) in contact with a moving triangular punch. (a) Normal stress; (b) normal stress in lateral direction. 163

LIST OF ABBREVIATIONS

ABBREVIATIONS

FGM	:	Functionally graded material
CR	:	Ceramic rich
LN	:	Linear
MR	:	Metal rich
H	:	Homogeneous
HMLM	:	Homogeneous multi-layer model
LMLM	:	Linear multi-layer model
EMLM	:	Exponential multi-layer model
MEEM	:	Magneto-electro-elastic material
SIE	:	Singular integral equation

LIST OF SYMBOLS

SYMBOLS

x, y, z	Axes of the stationary coordinate system
X, Y, Z	Axes of the moving coordinate system
V	Punch speed
P	Normal force applied by the punch
Q	Tangential force applied by the punch
η	Coefficient of friction
b	Leading end point of the all punches
$-a$	Trailing end of circular punch
N	Total sublayers of the coating
M	Total number of interlayers
ζ	Fourier Transform variable
$s_{(i)j}$	Roots of the characteristic equation
k_{ij}	Kernels of integral equations
$P_n^{(\alpha_1,\alpha_2)}(s)$	Jacobi polynomial of order n
α_1,α_2	Strengths of normal stress singularities
γ_i	Power constants of material gradation
K_I	Normalized punch stress intensity factor
θ	Inclination angle of the triangular punch
R	Radius of circular and semi-circular punches

CHAPTER 1

INTRODUCTION

This study is conducted to investigate the response of multi-layered heterogeneous structures under frictional and moving contact loading conditions. On top of a substrate, several types of coatings such as FGM, multi-layer, periodic or multiferroic coatings are placed depending on the problem. Transition at the interface between substrate (interlayer for multiferroic case) and coating for FGM coatings is accepted as smooth which means that there are no interfacial defects or jumps. Contact problem of a moving rigid punch which may possess four distinct shapes is examined under plane strain conditions. Punch speed is assumed as constant and implemented as a parameter in the governing partial differential equations. This study embodies all types of contact problems involving elastostatic or elastodynamic cases, single or multi-layer coatings, homogeneous or graded coatings and isotropic or multiferroic coatings. Chapter 1 describes briefly the smart materials and summarizes approximate multi-layer models used in the literature. Finally, the main purpose of the present work is explained in the last section in this chapter.

1.1 Review of FGMs

The modern industry demands everlasting endurance for machinery components which is considerably dependent on surface and wear conditions. Researchers have been working on techniques to reduce these undesirable conditions. Mechanical surface treatments have the top-ranking place amongst surface improvement techniques. Altering the chemical composition of the contacting surfaces, i.e., enhancing the hardness of surfaces may significantly prolong the life-time of the machinery. Cutting tools in manufacturing, sliding bearings in power transmission and braking systems, dental implantations and medical prosthetics, penetration resistant materials for armor plates and bullet-proof vests, MEMS, piezoelectric and thermoelectric devices, protective coatings on hard-disks and thin film coatings necessitate high tribological performance (Bhavar et al., 2017; Li and Han, 2018; Miteva, 2014; Saleh et al., 2020).

In tribological applications, graded coatings are used to create protective layers which prevent the failures stemming from surface cracks caused by fatigue or fretting. Possessing more than one critical characteristic such as resistance against corrosion and wear, thermal endurance, magnetic permeability, dielectric permittivity, flexibility and high strength comes into prominence in the new generation material design. Functionally graded materials (FGMs), classified in an advanced class of engineered composite structures, are recognized by their continuous variation in material composition and mechanical properties in the desired direction due to the change in the volume fractions of constituent phases. Varying composition in microstructure over a geometry is preferred intentionally in order to fabricate materials combining multiple qualifications. Figure 1.1 illustrates an FGM made by particulate dispersion of a constituent in a medium of the other material pair. One can notice the vertical variation of particles which indicates alternating volume fractions of constituent phases across the thickness direction. Properties of such materials can be described by material function $\Lambda(Z)$.

Due to the mixture of two or more constituents (metal/ceramic, ceramic/ceramic, ceramic/glass, piezoelectric-magnetostrictive and etc.), FGMs possess optimized mechanical, thermal and electro-magnetic performances like high fracture toughness, hardness, thermal conductivity or expansion, wear or corrosion resistance and electrical or magnetic energy conversion ability. Mismatching in FGMs also diminishes mechanical or thermal stresses and increase interface bonding strength (El-Wazery and El-Desouky, 2015). Hence, these characteristics enable FGMs to control or limit the damage caused by the contact in tribological applications. Various forms of FGMs can be widely encountered in many areas such as biomedical, manufacturing, aerospace, automotive, textile machinery, computer systems and microelectronics.

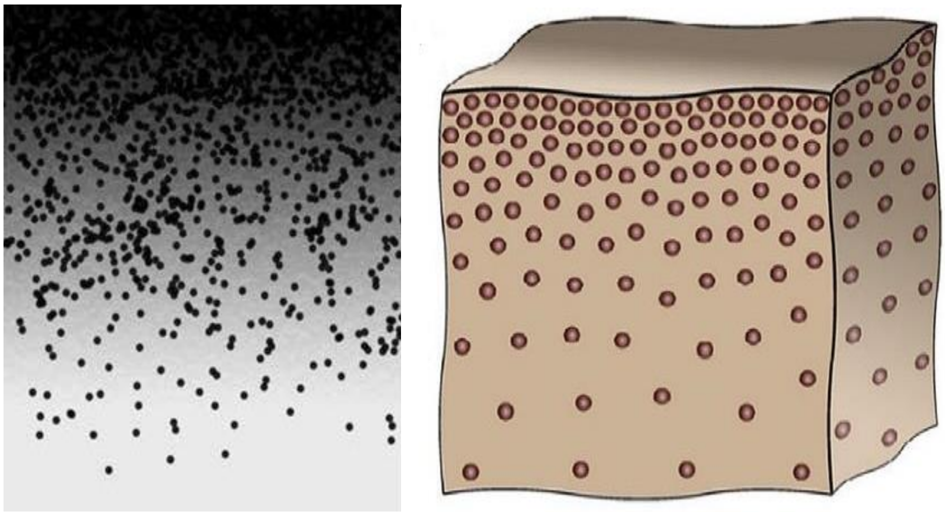

Figure 1.1. Schematics of the particulate FGMs with constituent phases. (Popoola et al., 2016; Zhang, C. et al., 2019)

FGMs are found naturally in living body parts such as the barks of certain trees, bones, teeth, conch and tortoise shells. Dental implants composed of metal inner core and ceramic outer crown are considered as one of the best examples of biomedical FGM and perfect replicas of natural teeth. The core and the crown successfully combine ductility and wear resistance, respectively. Uniting of these properties in a material became critical with the demand of advanced materials in engineering applications. The researchers developed manufacturing processes of FGMs since 1980s. During the past forty years, artificially manufactured FGMs provided special qualifications at any desired spatial location. Amongst the processing techniques of FGMs, one can mention powder technology methods (dry powder processing, tape casting, electrochemical gradation, powder injection molding and self-propagating high temperature synthesis), deposition methods (chemical vapor deposition, physical vapor deposition, electrophoretic deposition, pulsed laser deposition, plasma spraying), in-situ processing methods (laser cladding, spray forming, sedimentation and solidification, centrifugal casting) and rapid prototyping processes (multiphase jet solidification, 3D-printing, laser printing, laser sintering) (Bhavar et al., 2017; Kieback et al., 2003; Saiyathibrahim et al., 2015; Zhang, C. et al., 2019).

1.2 Review of Multiferroics

Multi-functional material design uniting many features generally not found together has attracted the researcher's attention in the contemporary material science. Yet, the contraindication rising due to the need of distinct crystal cell arrangements which contribute different characteristics should be overcome. This phenomenon has become the major and challenging problem in the design of multi-functional multiferroic materials (Spaldin, 2020).

Ferroics are defined as smart materials whose properties can be adjusted by environmental conditions and external stimulus such as moisture, temperature, pressure and external forces (Li et al., 2020; Wadhawan, 2002). In a critical temperature interval, these materials can convert their crystal structures and alter their physical properties exhibiting phase transition (Roy et al., 2012). For instance, Hayward et al. (2005) state that barium titanate in cubic crystal structure transforms into tetragonal, orthorhombic and rhombohedral state near transition temperatures 393 K, 278 K and 183 K, respectively. Compared to non-ferroic phase, the atoms in the crystal structure move slightly and change their neutral position when the temperature reaches to near values of critical temperature. This incident causes the transition to ferroic phase. The main ferroic materials are categorized in three groups depending on their coupling interactions as ferroelectrics, ferromagnetics and ferroelastics (Behera et al., 2021; Bhoi et al., 2021; Ramesh, 2022). Electrical polarization in ferroelectrics, spin polarization in ferromagnetics and strain in ferroelastics may undergo changes when exposed to stress, electric and magnetic fields. The usage of these materials has become popular in novel technological devices.

Multiferroics also known as magneto-electro-elastic materials (MEEMs) are characterized by their ability to transfer energy between elastic, electric, and magnetic fields (Gao et al., 2018). They combine all three ferroic properties in themselves. In other words, exposing MEE materials to mechanical stress creates not only strain but also electric and magnetic potentials or vice versa (Vinyas, 2021).

Hence, full coupling exists between three fields through piezoelectricity, magnetostriction and magnetoelectricity as shown in Figure 1.2.

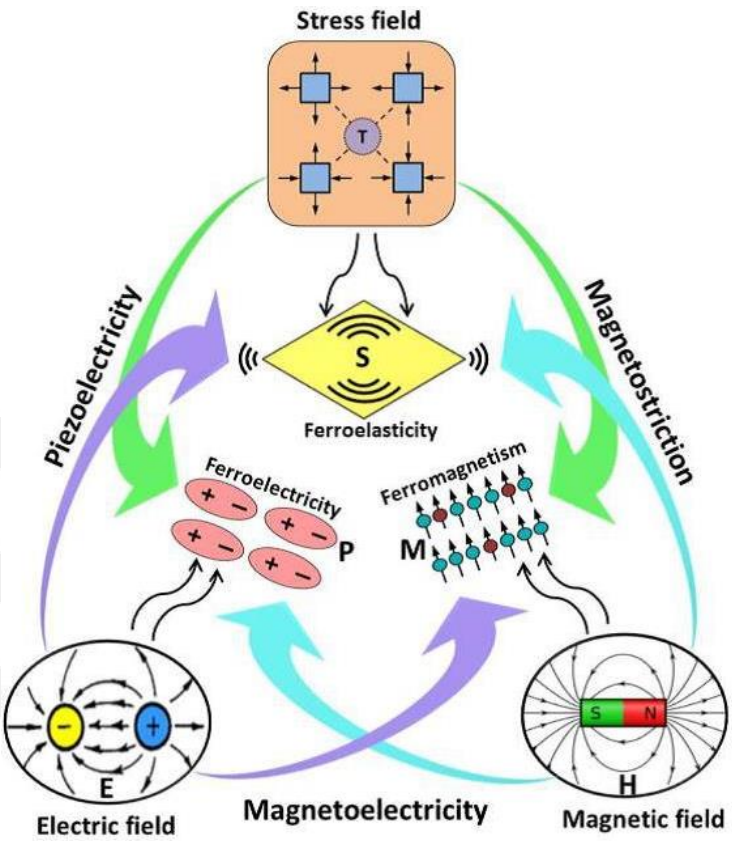

Figure 1.2. Energy coupling mechanism in MEE materials (Palneedi et al., 2016).

Single-phase multiferroics ($BiFeO_3$, $RMnO_3$, Cr_2O_3, Ti_2O_3, $GaFeO_3$, etc.) are common in nature but they do not guarantee strong coupling between electric and magnetic fields (Bishay et al., 2012; Kumar et al., 2020). The reason is that the coupling between ferroelectrics and ferromagnetics in the same phase (crystal structure) leads to the contraindication (Ramesh, 2022). Therefore, their applications are limited compared to multi-phase multiferroics.

Multi-phase multiferroics made of various volume fractions of piezoelectric and piezomagnetic constituents meet the need of MEE materials that possess high magneto-electric coupling. For this reason, this type of MEEMs is generally encountered in industrial designs. Due to their energy coupling capability, multi-phase MEEMs have captured significant attention and provided several opportunities in the recent years especially in micro and nano scaled technological applications such as actuators (Afonin, 2019; Kumar and Sarangi, 2018), energy harvesters (He and Liu, 2022; Liu et al., 2014; Wang et al., 2016), antennas (Hu, 2020), spintronic devices (Chang et al., 2019; Gradauskaite et al., 2021), resonator (Ma et al., 2011), opto-electronic devices (Erum and Iqbal, 2020), transducers (Rupp et al., 2019; Surowiak and Bochenek, 2008), sensors (Daga et al., 2009; Gao et al., 2021; Hosseini et al., 2018; Zhou et al., 2021), memory devices (Ma et al., 2011), biomedical (drug delivery, monitoring, nanorobot and biomaterial) (Apu et al., 2022; Kopyl et al., 2021), composite plates (Xu et al., 2015), shell-core composites (Chaudhuri and Mandal, 2015), polycrystalline structures (Fujii et al., 2022), thin films (Hadouchi et al., 2020; Liang et al., 2021; Matavz et al., 2021) and remotely controlled micromachines (Chen et al., 2016). In the literature, one may find the experimental studies which investigate the performances of multiferroic devices (Du et al., 2013; Malleron et al., 2019; Zhou et al., 2013) and multiferroic materials (Hasanyan et al., 2012; Sayed et al., 2021; Schmitz-Antoniak et al., 2013; Tabakh et al., 2019; Zhao et al., 2014).

The multi-phase multiferroics are mainly manufactured as in the form of particulate, rod and layered composites. (Aguesse et al., 2012; Palneedi et al., 2016; Pradhan et al., 2020; Vopson, 2015). The particulate composites are identified by the presence of the particles of any shape and size suspended in the matrix medium. In the rod composites, the shape of particles is specified as cylindrical rods. Layered composites are made up of the deposition of distinctive layers, having its own properties. When the engineering applications of MEEMs are examined, one can find many examples of multi-layer and functionally graded structures. It is also noted that more efficient coupling performances have been observed in MEE coatings manufactured as multi-layer or functionally graded configurations (Vinyas, 2021). Multi-layer nano structures possessing enhanced magnetic performance (Aguesse et al., 2012), multi-layer thin films produced via chemical deposition (Dai et al., 2014) and tape casting (Hao et al., 2013) methods, multi-layer microelectronic devices

(Scigaj et al., 2016), multi-layer magneto-electric read-head sensors (Ma et al., 2011), MEE micro-beams (Hong et al., 2021), MEE nanoplates (Hosseini et al., 2018) and MEE nanofilms (Liu and Lyu, 2020) optimized by 3D printing (Uetsuji and Wada, 2020) methods can be mentioned as the applications of multi-layer and FGM MEE coatings. The gradation of the properties brings the special customization of the coating and allows the optimization of mechanic and electro-magnetic responses.

A common multi-phase MEEM is the composite made of the combination of $BaTiO_3$ and $CoFe_2O_4$ as shown Figure 1.3. Jian and Wong (2017) worked on the different crystal structures of $BaTiO_3$-$CoFe_2O_4$ pair as shown in Figure 1.4. The diversity of crystal structures in the composite material boosts electro-magnetic coupling effects. Hence, a highly coupled $BaTiO_3$-$CoFe_2O_4$ pair is examined in the present study.

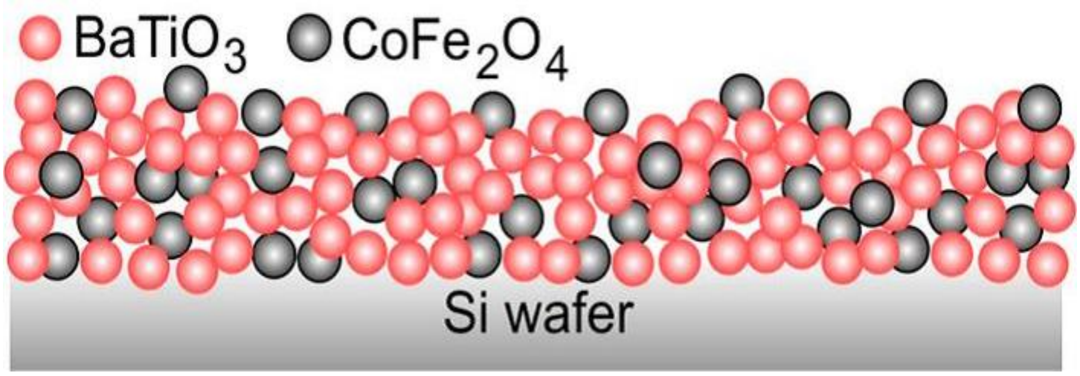

Figure 1.3. Sample MEE material made of barium titanate and cobalt ferrite (Erdem et al., 2016).

1.3 Review of Multi-layer Models

Multi-layer models are the systems of network formed by dispersion of similar types of sublayers possessing different characteristics. A highly heterogeneous structure whose governing equations are impossible to solve for certain analyses can be converted with these models into a simplified multi-layer structure, i.e., these homogenization methods make the examination of highly nonlinear structures possible. The previous studies regarding the multi-layer approximations can be categorized under three groups such as linear multi-layer model (LMLM), exponential multi-layer model (EMLM) and homogeneous multi-layer model (HMLM).

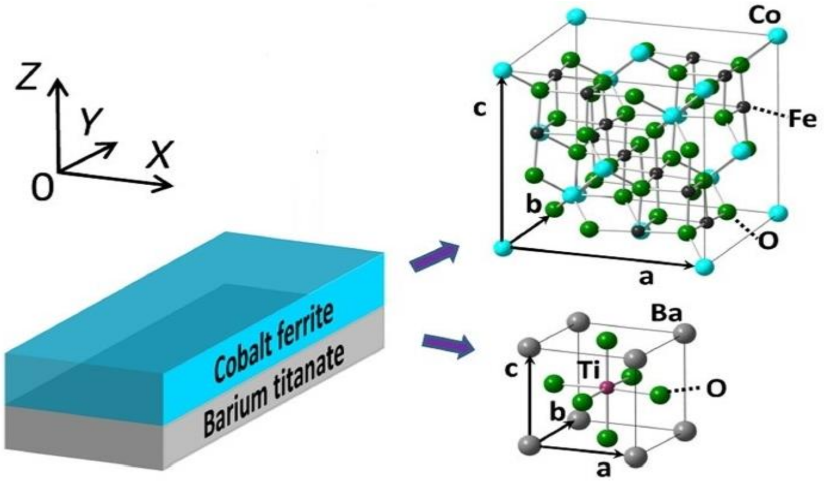

Figure 1.4. The schematic illustration of $BaTiO_3/CoFe_2O_4$ composite and the crystal structures of both constituents (Jian and Wong, 2017).

In LMLM, the scientists receive the help of continuous linear functions to generate an imitative gradation function resembling to the original gradation function of the structure. Keep in mind the fact that any curve can be expressed by a series of linear functions. At the interfaces of multi-layer system, the properties are identical to those of heterogeneous structure while the properties are close enough to the ones of exact gradation function at other locations.

In the second method called as exponential multi-layer model (EMLM), the researchers utilize sub-layer formation in the nonhomogeneous medium by selecting appropriate exponential functions having distinct powers for each layer in order to approximate the original material properties. This imitation is especially advantageous in the solution of differential equations since the derivatives of exponential functions are easy to handle. For this reason, it may be considered as superior compared to LMLM. However, there exists a drawback of this model. All property variations of the material must follow the same proportional pattern in order to make the coefficients of PDEs constant but the proportional material gradation is considered as a major weakness and not a rational restriction in real heterogeneous structures.

The last method is homogeneous multi-layer model (HMLM). In this model, the graded coating is divided into a number of homogeneous layers with constant properties along the thickness direction. This approach also causes mismatches in material properties at the interfaces of the sublayers. On the other hand, it enables to investigate the variation of all material parameters independently. In other words, HMLM overcomes the distinct (nonproportional) variations of all material properties of the coating while the other methods fail to do so. Hence, HMLM is selected in the present study as it eliminates all restrictions in property gradation.

Table 1.1 summarizes the strengths and weaknesses of multi-layer methods explained in the above paragraphs. In Figure 1.5, three multi-layer approximation models with 5 sublayers are illustrated. Two cases of samples namely ceramic-rich ($\gamma > 1$) and metal-rich ($\gamma < 1$) coatings are examined in Figure 1.5a and Figure 1.5b, respectively. The exact gradation functions of the coatings are shown by red colored curves and the functions are given in the label. Approximate HMLM, LMLM, EMLM curves are plotted by black, blue and green colored curves, respectively. As seen, the convergence of HMLM is worse than the other approximations, i.e., the approximate curves for HMLM do not cover the original gradation functions as the curves of LMLM and EMLM do. Yet, an excellent convergence for HMLM can be achieved when an appropriate number of layers is selected. In Figure 1.6a and Figure 1.6b, the convergence of HMLM on material property gradation is shown as the layer number used in the analysis is increased to 100 for stiffer ($\mu(0) > \mu(h)$) and less stiff ($\mu(h) > \mu(0)$) coatings, respectively. As it can be noticed, HMLM fits perfectly on the exact gradation function when N is equated to 100. In the contact analyses, N is generally taken as equal to 100 or even greater than 100. The optimized value for N is obtained by comparative results prepared in convergence tables as mentioned in the next sections. Thus, the accuracy in the results is assured with this way.

Table 1.1. A comparison of weaknesses and strengths of multi-layer models.

	LMLM	EMLM	HMLM
Pro's	-	Fast convergence (Less number of layers)	Simple formulation Nonproportional Gradation
Con's	Variable coefficients in PDEs (Not Applicable)	Proportional Gradation Complex formulation	Slow convergence High number of layers

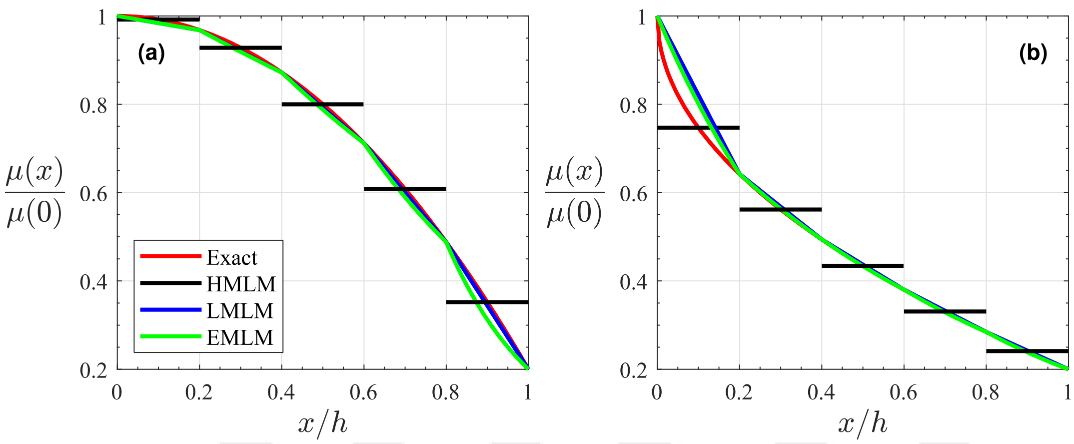

Figure 1.5. Approximate multi-layer models, $\mu(x)/\mu(0)=1-0.8(x/h)^{\gamma}$, N=5. (a) γ=2.0; (b) γ=0.5.

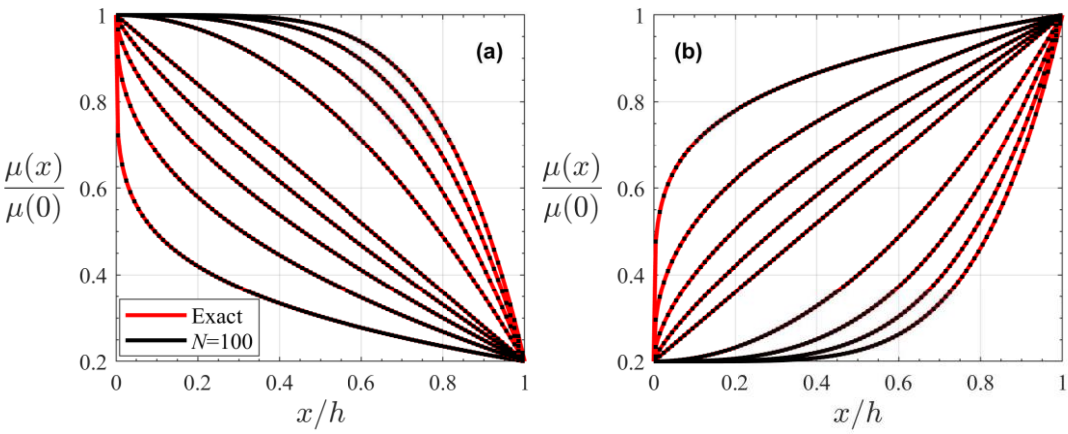

Figure 1.6. Comparison of HMLM and Exact Gradation Function: (a) Stiffer coating, from top to bottom, $\mu(x)/\mu(0)=1-0.8(x/h)^{\gamma}$, γ = 5.0,4.0,3.0,2.0,1.0,0.8,0.6,0.4,0.2; (b) Less stiff coating, from top to bottom, $\mu(x)/\mu(0)=0.2+0.8(x/h)^{\gamma}$, γ = 0.2,0.4,0.6, 0.8,1.0,2.0,3.0,4.0,5.0.

1.4 Thesis Aim and Outline

In this study, the analyses for dynamic frictional contact problems of many multi-layered heterogeneous structures are conducted utilizing integral transform techniques. Flat, triangular, semi-circular and circular shaped punches are considered. Even though there are few studies regarding dynamic contact problems of half-planes and proportional and exponential FGM coatings, the solution of moving contact problems of nonproportional FGM coatings is missing in the literature. Previous studies fail to enlighten the true response of heterogeneous structures since proportional gradation is rare in real life applications. Thus, the present study will be helpful to the researchers in the design and optimization of FGM coatings.

The organization of the dissertation is as follows: Chapter 1 gives general information related to the materials studied in this work. FGMs and multiferroics are described briefly. Approximate multi-layer formations are explained and the scope of the study is defined. In Chapter 2, previous studies done associated with FGMs and multiferroics are summarized. Approximate homogenization models applied in solid mechanics problems are discussed briefly. In Chapter 3, the formulations of the moving contact problems of pure elastic and multiferroic structures are presented in detail. Constitutive relations and governing partial differential equations are written. The continuity, regularity and boundary conditions are stated. Then, the singular integral equation and the equations used in the calculations of other mechanical and electro-magnetic outputs are obtained. Chapter 4 clarifies numerical procedures applied in the solution of singular integral equations. After that, stresses, electric displacement and magnetic induction in X-direction are calculated for heterogeneous systems. In Chapter 5, the explained procedures and obtained results are verified by making comparisons with the ones available in the literature for special and simple cases. The results of the parametric analyses are illustrated in figures and some scalar data are presented in tables. In Chapter 6, the concluding remarks and how the studied models can be improved are summed up.

CHAPTER 2

LITERATURE REVIEW

The analysis of stresses and strains emerging in touching solid bodies is within the interest of contact mechanics. A contact mechanics problem in the plainest case involves two solid bodies interacting with each other while operating. The contacting bodies can be considered as rigid or deformable, elastic or plastic, isotropic or anisotropic, non-ferroic or ferroic, static or dynamic and etc. Hence, the physics and mathematics of the contact problems are built upon the mechanics of materials.

Popov et al. (2019) recall that the pioneers of the field of classical contact mechanics are Hertz and Boussinesq in the 19th century. For the first time, Boussinesq researched the stress distribution in semi-infinite medium contacting with the rigid cylindrical and flat-bottomed punch. Since then, the contact models evolved into an advanced and complicated level. In the upcoming sections in this chapter, the latest published papers regarding the contact mechanics of multi-layer structures, FGMs and multiferroics are discussed.

2.1 Literature Review of Multi-Layer and FGMs in Contact Mechanics

Finite element programs can serve as useful tools by which the stresses in the contact zone are obtained from. McGuiggan et al. (2007) reported both finite element and experimental results of the nanoindentation of layered surfaces. The authors especially looked into the contact mechanics of the surface force apparatus for both including and excluding adhesion. Kot (2012) developed a deformation model for mono and multi-layer coatings based on the results of finite element method and the analyses of nanoindentation tests. Riccardi and Montanari (2004) presented a deep-indentation process with perfectly rigid indenter utilizing finite element (FE) simulations. The finite element analysis of the indentation process used in simulations was verified by experiments with the same geometric models. Jahedi and Adibnazari (2015) prepared 2-D frictional rolling contact simulations of graded coatings under plane strain state. The influences of friction, material properties and coating thickness on stresses in contact zone and at the interface were comprehended. Thermal effects in contact mechanics play critical role in certain applications. Bayat et al. (2019) studied on thermo-elastic contact problem of FGMs for rotating brake disks. Temperature dependent material properties were examined by finite element method. The gradual alteration of the properties of brake disk was assumed to be characterized by power-law functions along the radial direction.

A criterion which might substantially affect the contact condition is surface topography. Several analyses of layered rough surfaces containing data for various surface topographies, elastic and elastic-plastic material properties, normal and tangential loading conditions and dry and wet interfaces were presented by Bhushan and Peng (2002) by applying finite difference, finite element and boundary element methods. In the article by Yastrebov et al. (2011), two approaches representing the surface roughness measured by experiments were examined related to frictionless contact of elasto-plastic medium.

Two of the pioneer studies about elastostatic frictional contact analyses were done by Guler and Erdogan (2004; 2007). The authors formulated an analytical solution method to express normal and lateral contact stresses of an exponentially graded coating through its depth which is perfectly bonded on top of a substrate. The inadequacies of that study are disregarding both punch speed and the variation in the gradation function. In certain applications, the property gradations in the lateral direction are required for the improvement of the mechanical behavior of the structure. A frictional contact model between such a material and a rigid circular stamp was prepared by Dag et al. (2013). In that study, the gradation function was also accepted to be in the exponential form to simplify the model. Alinia and Espo (2020) worked on contact problem of coatings having exponentially varying properties in two dimensions bonded to a half-plane graded only in the lateral direction. Another considered 2-d contact problem in the literature is axisymmetric contact. Liu and Wang (2008) investigated the axisymmetric contact problem of exponential FGM coatings. The authors' concern was to obtain the frictionless contact stresses for flat, spherical and conical indenters.

Several contact models are also proposed in master's thesis and doctoral dissertations. Among them, one can mention the models developed by Guler (2001), Gulver (2009), Arslan, (2016) and Balci (2018). Two papers cited in the above paragraph were published using the data produced in the dissertation of Guler (2001). Gulver (2009) suggested a model for a graded coating in contact with thin film. The structure was loaded in the lateral direction from the tip of the thin film and far-fields. Therefore, only shear stress appears due to the contact without the existence of normal contact stress. Arslan (2016) prepared both a FEM model and an analytical model to examine the contact characteristics of orthotropic coatings. The effects of the ratio of elastic moduli in different directions were illustrated. In addition to the contact stresses, normal and shear interface stresses were also calculated. Finally, Balci (2018) put forward an elastodynamic contact model for the same material model suggested by Guler (2001). The novelty of that dissertation is the implementation of punch speed as an independent parameter into the model. Note that FGM coating considered in all of these thesis and dissertations are proportionally and exponentially varied and except for the dissertation by Balci (2018), the problems were solved by ignoring time dependent effects.

Thin films can be classified as a layer of material attached to the substrates whose dimension in the thickness direction is very small compared to lateral dimensions. There is vast amount of information in the literature directed towards examining contact mechanics of thin films (Merle, 2013; Zhang et al., 2018).

Contact mechanics of moving punch problems interests many scientists since the potential applications of such contact problems in the industry are numerous. De and Patra (1994) and Zhou et al. (2014) solved contact problems of dynamic punches in semi-infinite orthotropic medium. Zhou and Lee (2014) then applied a similar method to examine moving punch problems in any type of anisotropic materials. Comez (2015) and Balci (2020) investigated the influence of punch speed on frictional contact problems of graded layers placed on a rigid structure. Balci and Dag (2018a; 2019a; 2019b; 2020) improved the layer approach by replacing the rigid foundation with homogeneous semi-infinite media.

In the literature, multi-layer coatings and arbitrarily graded coatings are generally classified in the same group. The reason is that the characteristic of gradation functions in arbitrarily graded coatings changes the type of governing PDEs and it is impossible to attain the general solution of such coatings for the contact mechanics problems. For this reason, the researchers developed approximate multi-layer models to overcome this difficulty by converting the arbitrarily graded coating into an adequate number of sub-layers. The studies about diverse types of contact problems involving multi-layer coatings such as the frictionless double contact problem of a two-layer laminate (Yan and Mi, 2017), the elastic rolling problem of wheel-rail contact (Chudzikiewicz and Myśliński, 2011), the axisymmetric problem of multi-layer coatings (Miura et al., 2020), the elastic–plastic penetration problem of a Berkovich pyramid (Kravchuk et al., 2009) and the sliding contact problem of magnetic storage thin-films (Katta et al., 2009) exist in the literature.

The summary in this section indicates that there is no previous work which focuses on a moving frictional contact problem of nonproportionally graded coatings. Applying HMLM approach simplifies the complex material model and allows the solution using integral transform techniques as explained in Section 3.1.

2.2 Literature Review of Multi-Layer and FGM Multiferroics in Contact Mechanics

Investigation of mechanical performances of structures comprising MEE components subjected to external forces applied by another body is one of the major steps in the design process. In the regions where the intensity of contact stress, electric displacement and magnetic induction are quite elevated, surface damage and micro crack formation initiate which then may lead to failure (Ma et al., 2014). Hence, it is crucial that magnetic, electric and mechanical performances of MEE coatings reach to the optimum levels by adjusting layer thicknesses and interface numbers or altering the inhomogeneity exponents. With these design modifications, the resistance against contact deformation, surface damage and electro-magnetic deterioration of MEE coatings may be improved. In short, it is critical to determine the accurate mechanical behavior of MEE coatings under contact loading.

Magneto-electro-elastic materials (MEEMs) comprise of piezoelectric and piezomagnetic constituents and originate the coupling between mechanical deformation and electromagnetic fields. For this reason, MEE materials attract the researchers' attention in many smart device and structure applications. Among these applications, sensors, actuators, transducers, opto-electric devices, storage devices, nano-beams and nano-plates can be mentioned. As a result of the increase in the usage of MEE materials in high technology products, there is a need for estimating the behavior of these products under mechanical loads in order to create more effective designs.

Understanding the influences of wear and friction and determining the connection between stress distribution and electro-magnetic response gained prominence for smart materials in contact with different structural system. For this reason, many studies are conducted concerning ferroics, multiferroics, ferroic FGMs and multiferroic FGMs to outline the contact response. The contact problems involving smart structures and smart coatings in the literature can be mainly divided into two main groups as statically loaded and dynamically loaded problems.

The literature in this section starts with the studies of piezoelectric and piezomagnetic materials since they are the fundamental components of MEEMs. Ke et al. (2008a) investigated the static contact of exponentially graded piezoelectric coating placed on piezoelectric half-plane loaded by frictionless and electrically insulating punch. In addition to equations of motion, Maxwell electric equation is added to the model as one of the governing PDEs. The authors also improved their initial model by adding the separate effects of electrically conducting punch (Ke et al., 2008b) and friction (Ke et al., 2010). Then, Su et al. (2018) worked on a contact model which clarifies the competing influences of electrically conducting punch and friction on contact stresses. Furthermore, a pioneer study about fretting contact of piezoelectric half-planes was carried out by Su et al. (2015). Another advanced study which applies Maugis contact theory was done by Huang and Liu (2019) to enlighten adhesive contact situation between an insulating cylindrical punch and a piezoelectric coating. The studies on the contact problem of piezomagnetic materials are quite limited. A general theory for the axisymmetric indentation of piezomagnetic medium by a flat rigid punch was proposed utilizing the equations of motion and Maxwell magnetic equation by Giannakopoulos and Parmaklis (2007). Now, we switch to the static contact problems in the literature regarding MEEMs. General information about how the contact modelling of MEEMs can be done was firstly presented by Chen et al. (2010). They also convey necessary procedures by supplying certain boundary conditions. For MEEM problems, mechanic-electric-magnetic characteristics are taken into consideration by fully coupled constitutive relations, the wave equations and Maxwell electric and magnetic equations. Elloumi et al. (2013) and Elloumi et al. (2014) carried out the frictional contact analysis of MEE half-plane for conducting flat and cylindrical punches, respectively. Then, Elloumi et al. (2016) outlined an analytical solution methodology for sliding frictional contact of exponentially graded MEE half-plane for conducting flat punch. Comez (2021a) considered thermoelastic contact problem of a MEE layer resting on a rigid body indented by a rigid insulating punch. Zhou and Lee (2013) and Zhou and Kim (2014) worked on the frictional contact situations between MEE half-plane and rigid and insulated punches. Ma et al. (2016) examined the contact between exponentially graded MEE layer on a perfectly insulating rigid half plane and a perfectly conducting rigid punch with frictional heat generation. Ma et al. (2014) and Ma et al. (2015) put forward analytical techniques to analyze frictionless and frictional contact problems involving exponentially graded MEE coatings, respectively. Mechanical analyses of multiferroic thin films and MEE FGM coatings under frictional contact loading were made respectively by Zhang et al. (2017) and Zhang, H. et al. (2019) using a semi-analytical method. In all the studies listed above, the dynamic impacts caused by the speed of the punch are ignored.

When the models of moving contact mechanics of smart materials are focused on, the most recent work on piezoelectric coatings belongs to Comez (2021b). In this study, a model about exponentially graded piezoelectric coatings subjected to loading by frictional dynamic and conducting cylindrical punch was developed. One can mention the study by Zhou and Kim (2013) for moving contact problem of piezomagnetic materials. The authors worked on semi-infinite Terfenol-D and solved the frictional moving contact problem for insulating flat and cylindrical punches. Regarding the studies on moving contact models of MEE materials, it is noticed that the researchers only concentrated on MEE half-plane models. Zhou and Lee (2012a; 2012b) worked on four models for the exact contact analysis of MEE materials indented by a moving rigid punch. Depending on the punch features, all four contact cases (electrically and magnetically conducting, electrically conducting and magnetically insulating, electrically insulating and magnetically conducting, or electrically and magnetically insulating) were investigated. Comez (2021c) improved the indentation model of electrically and magnetically conducting punch developed by Zhou and Lee (2012b) by just implementing the kinetic friction to the model.

To the best of our knowledge, a moving frictional contact problem between a perfectly insulating punch and a multi-layer MEE coating or FGM MEE coating with general variations in physical properties has not been studied in the published literature. Although the engineering applications of MEE materials are generally in the form of multi-layer and functionally graded structures, the researchers were not interested in multi-layer or FGM MEE models because of the difficulties in the formulation. Another missing part in the previous works is that all MEE properties are assumed to vary exponentially across the thickness on contact problems of FGM MEE coatings. Besides, the inhomogeneity exponents of all MEE properties are taken as same in FGM MEE models. In this way, deriving constant coefficient PDEs becomes possible. To fill missing parts about moving contact problems of MEE coatings in the literature, we propose the homogeneous multi-layer modelling method. In short, MEE coatings is examined elaborately in Section 3.2 in this study.

2.3 Literature Review of Multi-layer Models in Solid Mechanics

The first approximation approach of multi-layered models is LMLM as illustrated in Figure 2.1. In this method, the solution relies on stress-based formulation which means that an Airy's stress function is introduced and inserted to PDEs. Then, the solution of Airy's stress function is obtained in the form of Whittaker functions. After lengthy mathematical manipulations, singular integral equation which describes the contact problem is derived (Ke and Wang, 2006; 2007; Liu et al., 2016).

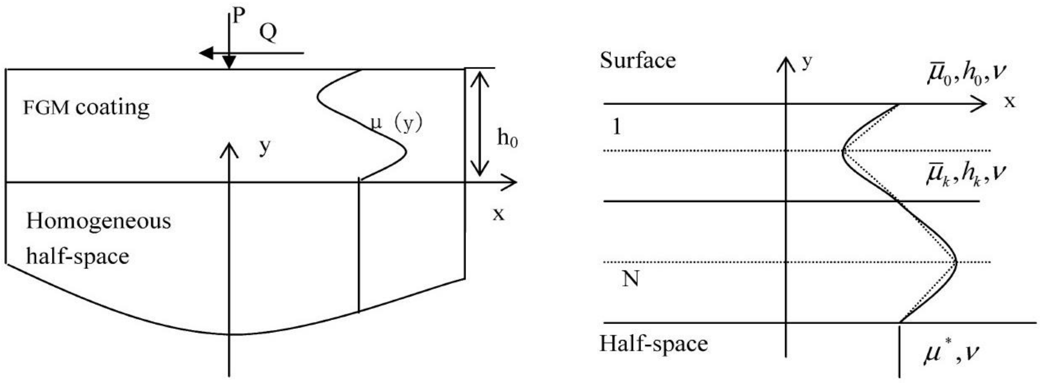

Figure 2.1. Schematic illustration of LMLM method (Ke and Wang, 2007).

Figure 2.2 depicts another multi-layer model called as EMLM. Piece-wise continuous exponential functions are replaced with the exact analytical function. This model is especially preferred in fracture problems. Because the properties of sub-layers in EMLM are absolutely same as the exact gradation functions at the sub-interfaces. One of these sub-interfaces coincides with the tip of the crack so that the mixed mode stress singularities at the crack tip can be found in a more accurate and consistent procedure. With this way, convergence is reached while the number of layers are kept at minimum (Bai et al., 2013; Guo et al., 2018; Guo and Noda, 2007; Wang et al., 2014).

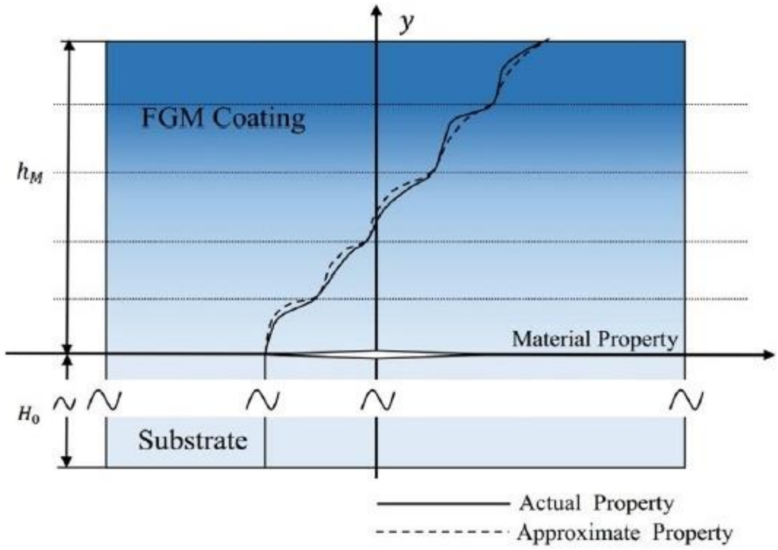

Figure 2.2. Schematic illustration of EMLM method (Guo et al., 2018).

The final and the most favoured method is HMLM applied also by (Liu et al., 2011; 2012; Jobin et al., 2017). As displayed in Figure 2.3, the gradation function is divided into homogeneous parts. The exiguousness in this method is that the continuities in the property functions are broken. However, the continuities in all field quantities such as displacements, stresses and electro-magnetic fields are guaranteed by interface conditions. In short, HMLM is the only agible method if one is interested in the effects of nonproportional gradations.

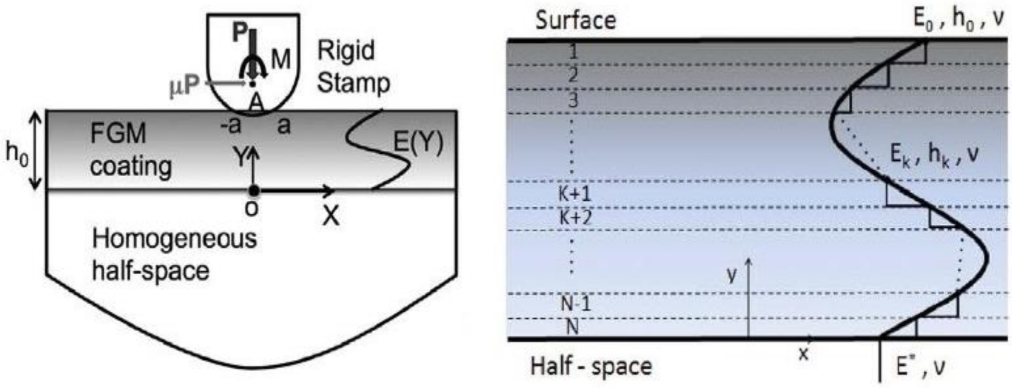

Figure 2.3. Schematic illustration of HMLM method (Jobin et al., 2017).

CHAPTER 3

PROBLEM STATEMENT AND FORMULATION

Integral transform methods are powerful tools in the solutions of solid mechanics problems. Derivation of SIE of the contact problem using integral transform techniques establishes the main framework of this study. The number of indexed papers using this concept regarding contact mechanics has been constantly increasing over the years. The contact modelling of arbitrarily graded coatings gained accelerated trend in the recent years and became a trend topic. Homogeneous multi-layer modelling is an essential and promising tool for precise contact modelling of multi-layer and FGM coatings. HMLM allows us to study on the mechanical behavior of functionally graded coatings with arbitrarily varying material properties. Hence, the novelty of this study is the development of a homogenous multi-layer model which incorporates more variables for contact problems. From this aspect, HMLM has a great potential for new scientific researches.

3.1 Multi-layer Model

The general elastic coating model in contact with a rigid punch is illustrated in Figure 3.1. A randomly graded coating laying on the homogeneous substrate is under the action of rigid moving punch. A perfect bonding between coating and substrate exists in y-direction that means the continuities of field quantities and material properties are preserved. Plane strain conditions are assumed for the composite structures. Total normal and tangential forces exerted by the contact are designated by P and Q. It is assumed that Coulomb's law of friction is valid between these forces ($Q=\eta P$). In the material model, three properties which define the elastic medium namely shear modulus, density and Kolosov's constant are assumed to vary randomly in x-

direction. In order to approximate the exact grading functions, the coating is converted to N number of equally thick homogeneous sub-layers. Homogeneous substrate is chosen as 1^{st} layer and the layer number increases in the negative x-direction, i.e., the coating layers are numbered as i=2,…,N+1. Such a configuration is chosen due to the application order of the interface conditions. In other words, the initial interface conditions that will be applied are the continuity conditions at $x=h$. After that, the conditions between 2^{nd} and 3^{rd} layers are applied and it continues in this way. The subscript in parenthesis '( )' in all variables denotes the layer number.

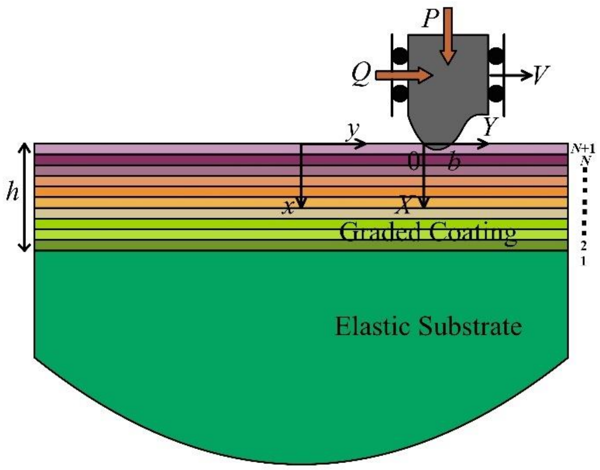

Figure 3.1. Geometry of general moving contact problem of elastic heterostructure.

The punch slides on the coating in y-direction and its speed is designated by V. In this chapter, entire formulation is done as if the punch has an arbitrary shape, however, the contact problems are solved for flat, triangular, semi-circular and circular shaped punch profiles in Chapter 4. Galilean transformation is introduced between the stationary x-y and the moving X-Y coordinate systems as shown in Figure 3.2. By attaching the trailing edge of the punch to the origin of the moving coordinate system, the total length of the contact is defined, i.e., the contact zone is covered by the interval $0 < X < b$.

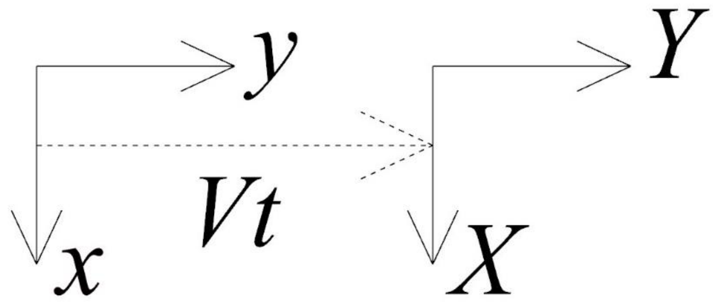

Figure 3.2. Two-dimensional Galilean Transformation

For the plane contact problem, Hooke's law is written in a general form for each layer in the stationary coordinate system as follows:

$$\sigma_{(i)xx}(x,y)=\frac{\mu_{(i)}}{\left(\kappa_{(i)}-1\right)}\left[\left(\kappa_{(i)}+1\right)\frac{\partial u_{(i)}}{\partial x}+\left(3-\kappa_{(i)}\right)\frac{\partial v_{(i)}}{\partial y}\right],\quad \begin{array}{c} i=1,\ d_{(1)}<x, \\ i=2,\dots,N+1,\ d_{(i)}<x<d_{(i-1)}, \end{array} \tag{3.1}$$

$$\sigma_{(i)yy}(x,y)=\frac{\mu_{(i)}}{\left(\kappa_{(i)}-1\right)}\left[\left(3-\kappa_{(i)}\right)\frac{\partial u_{(i)}}{\partial x}+\left(\kappa_{(i)}+1\right)\frac{\partial v_{(i)}}{\partial y}\right],\quad \begin{array}{c} i=1,\ d_{(1)}<x, \\ i=2,\dots,N+1,\ d_{(i)}<x<d_{(i-1)}, \end{array} \tag{3.2}$$

$$\sigma_{(i)xy}(x,y)=\mu_{(i)}\left[\frac{\partial u_{(i)}}{\partial y}+\frac{\partial v_{(i)}}{\partial x}\right],\quad \begin{array}{c} i=1,\ d_{(1)}<x, \\ i=2,\dots,N+1,\ d_{(i)}<x<d_{(i-1)}, \end{array} \tag{3.3}$$

$$d_{(i)}=h\left(1-\frac{(i-1)}{N}\right),\ i=1,\dots,N+1. \tag{3.4}$$

where $u_{(i)}$ and $v_{(i)}$ are displacement components in *x*- and *y*-directions, respectively. The interface locations of each layer in *x* coordinate can be defined by the parameter $d_{(i)}$. Note that first subscript in parenthesis is the layer number while the other subscripts indicate the directions. Kolosov's constant and Poisson's ratio are linked to each other in the plane strain and plane stress states in the following form.

$$\kappa_{(i)} = \begin{cases} 3-4\nu_{(i)}, & \text{for plane strain,} \\ \dfrac{3-\nu_{(i)}}{1+\nu_{(i)}}, & \text{for plane stress.} \end{cases} \tag{3.5}$$

In plane elastodynamics, time dependent equations of motion for each layer in the absence of body forces are defined as below:

$$\frac{\partial \sigma_{(i)xx}}{\partial x} + \frac{\partial \sigma_{(i)xy}}{\partial y} = \rho_{(i)} \frac{\partial^2 u_{(i)}}{\partial t^2},\ i = 1, ..., N+1, \tag{3.6}$$

$$\frac{\partial \sigma_{(i)xy}}{\partial x} + \frac{\partial \sigma_{(i)yy}}{\partial y} = \rho_{(i)} \frac{\partial^2 v_{(i)}}{\partial t^2},\ i = 1, ..., N+1. \tag{3.7}$$

where t and ρ respectively represent time and density. Then, the equations of motion are written in terms of displacement components substituting Eqs. (3.1)-(3.3) into Eqs. (3.6) and (3.7).

$$\frac{\left(\kappa_{(i)}+1\right)}{\left(\kappa_{(i)}-1\right)} \frac{\partial^2 u_{(i)}}{\partial x^2} + \frac{\partial^2 u_{(i)}}{\partial y^2} + \frac{2}{\left(\kappa_{(i)}-1\right)} \frac{\partial^2 v_{(i)}}{\partial x \partial y} = \frac{\rho_{(i)}}{\mu_{(i)}} \frac{\partial^2 u_{(i)}}{\partial t^2},\ i = 1, ..., N+1, \tag{3.8}$$

$$\frac{\left(\kappa_{(i)}+1\right)}{\left(\kappa_{(i)}-1\right)} \frac{\partial^2 v_{(i)}}{\partial y^2} + \frac{\partial^2 v_{(i)}}{\partial x^2} + \frac{2}{\left(\kappa_{(i)}-1\right)} \frac{\partial^2 u_{(i)}}{\partial x \partial y} = \frac{\rho_{(i)}}{\mu_{(i)}} \frac{\partial^2 v_{(i)}}{\partial t^2},\ i = 1, ..., N+1. \tag{3.9}$$

Now, our aim is to eliminate time dependent terms in the equations of motion and make the time dependent contact problem tractable. To do that, two-dimensional Galilean Transformation is introduced as illustrated in Figure 3.2.

$$x = X,\ y = Y + Vt, \tag{3.10}$$

Galilean Transformation connects stationary (x-y) and moving (X-Y) coordinates to each other. The purpose of this transformation is to make displacement and stress components time independent. Note that Galilean Transformation vanishes the time dependent terms under steady state conditions for the constant punch speed V.

In the next steps, the formulation continues with the components in the moving coordinate system. Note that the components written by capital letters indicate that they are identified in the moving coordinate system.

$$u_{(i)}\left(x,y,t\right)=U_{(i)}\left(X,Y\right),\ i=1,...,N+1,\ 0<X<\infty,\ -\infty<Y<\infty, \tag{3.11}$$

$$v_{(i)}\left(x,y,t\right)=V_{(i)}\left(X,Y\right),\ i=1,...,N+1,\ 0<X<\infty,\ -\infty<Y<\infty, \tag{3.12}$$

$$\sigma_{(i)xx}\left(x,y,t\right)=\sigma_{(i)XX}\left(X,Y\right),\ i=1,...,N+1,\ 0<X<\infty,\ -\infty<Y<\infty, \tag{3.13}$$

$$\sigma_{(i)yy}\left(x,y,t\right)=\sigma_{(i)YY}\left(X,Y\right),\ i=1,...,N+1,\ 0<X<\infty,\ -\infty<Y<\infty, \tag{3.14}$$

$$\sigma_{(i)xy}\left(x,y,t\right)=\sigma_{(i)XY}\left(X,Y\right),\ i=1,...,N+1,\ 0<X<\infty,\ -\infty<Y<\infty. \tag{3.15}$$

Then, a system of partial differential equations for each layer is obtained in the moving coordinates as follows:

$$\frac{\left(\kappa_{(i)}+1\right)}{\left(\kappa_{(i)}-1\right)}\frac{\partial^2 U_{(i)}}{\partial X^2}+\left(1-\lambda_{(i)}^2\right)\frac{\partial^2 U_{(i)}}{\partial Y^2}+\frac{2}{\left(\kappa_{(i)}-1\right)}\frac{\partial^2 V_{(i)}}{\partial X\,\partial Y}=0,\ i=1,...,N+1, \tag{3.16}$$

$$\left[\frac{\left(\kappa_{(i)}+1\right)}{\left(\kappa_{(i)}-1\right)}-\lambda_{(i)}^2\right]\frac{\partial^2 V_{(i)}}{\partial Y^2}+\frac{\partial^2 V_{(i)}}{\partial X^2}+\frac{2}{\left(\kappa_{(i)}-1\right)}\frac{\partial^2 U_{(i)}}{\partial X\,\partial Y}=0,\ i=1,...,N+1. \tag{3.17}$$

where $\lambda_{(i)}$ designates nondimensional punch speed of layer i. Note that $\sqrt{\mu_{(i)}/\rho_{(i)}}$ is called as shear wave propagation speed and used in the denominator of $\lambda_{(i)}$.

$$\lambda_{(i)}=\frac{V}{\sqrt{\mu_{(i)}/\rho_{(i)}}},\quad i=1,...,N+1. \tag{3.18}$$

At this step, Fourier Transformation is performed to Y coordinate in Eqs. (3.16) and (3.17) and the solutions for displacement components are searched in the form of exponential functions as follows:

$$U_{(i)}\left(X,Y\right)=\frac{1}{2\pi}\int_{-\infty}^{\infty}\sum_{j=1}^{k}G_{(i)j}e^{\left(s_{(i)j}X+I\zeta Y\right)}d\zeta,\ -\infty<Y<\infty,\quad \begin{array}{c} i=1,\,k=2,\,d_{(1)}<X, \\ i>1,\,k=4,\,d_{(i)}<X<d_{(i-1)}, \end{array} \tag{3.19}$$

$$V_{(i)}\left(X,Y\right)=\frac{1}{2\pi}\int_{-\infty}^{\infty}\sum_{j=1}^{k}G_{(i)j}F_{(i)j}e^{\left(s_{(i)j}X+I\zeta Y\right)}d\zeta,\ -\infty<Y<\infty,\quad \begin{array}{c} i=1,\,k=2,\,d_{(1)}<X, \\ i>1,\,k=4,\,d_{(i)}<X<d_{(i-1)}. \end{array} \tag{3.20}$$

The equation system given in Eqs. (3.16) and (3.17) can be easily expressed in the following matrix form.

$$\begin{vmatrix} \dfrac{\left(\kappa_{(i)}+1\right)}{\left(\kappa_{(i)}-1\right)}s_{(i)j}^{2}-\left(1-\lambda_{(i)}^{2}\right)\zeta^{2} & \dfrac{2I\zeta s_{(i)j}}{\left(\kappa_{(i)}-1\right)} \\ \dfrac{2I\zeta s_{(i)j}}{\left(\kappa_{(i)}-1\right)} & s_{(i)j}^{2}-\zeta^{2}\left(\dfrac{\left(\kappa_{(i)}+1\right)}{\left(\kappa_{(i)}-1\right)}-\lambda_{(i)}^{2}\right) \end{vmatrix}\begin{Bmatrix} G_{(i)j} \\ G_{(i)j}F_{(i)j} \end{Bmatrix}=0. \tag{3.21}$$

By calculating the determinant of the matrix in Eq. (3.21), a fourth order characteristic equation given below is found.

$$\left(s_{(i)j}^{2}-\left(\sqrt{1-\lambda_{(i)}^{2}}\left|\zeta\right|\right)^{2}\right)\left(s_{(i)j}^{2}-\left(\sqrt{1-\frac{\left(\kappa_{(i)}-1\right)}{\left(\kappa_{(i)}+1\right)}\lambda_{(i)}^{2}}\left|\zeta\right|\right)^{2}\right)=0. \tag{3.22}$$

The roots of the characteristic equation $\left(s_{(i)j}\right)$ and the functions $\left(F_{(i)j}\right)$ are found as follows:

$$s_{(1)1}=-\sqrt{1-\lambda_{(1)}^{2}}\left|\zeta\right|,\ s_{(1)2}=-\sqrt{1-\frac{\left(\kappa_{(1)}-1\right)}{\left(\kappa_{(1)}+1\right)}\lambda_{(1)}^{2}}\left|\zeta\right|,\ F_{(1)1}=\frac{Is_{(1)1}}{\zeta},\ F_{(1)2}=\frac{I\zeta}{s_{(1)2}}, \tag{3.23}$$

$$s_{(i)1}=\sqrt{1-\lambda_{(i)}^{2}}\,|\zeta|,\ s_{(i)2}=-s_{(i)1},\ s_{(i)3}=\sqrt{1-\frac{\left(\kappa_{(i)}-1\right)}{\left(\kappa_{(i)}+1\right)}\lambda_{(i)}^{2}}\,|\zeta|,\ s_{(i)4}=-s_{(i)3},\ i=2,\dots,N+1, \tag{3.24}$$

$$\Re\left(s_{(1)1},s_{(1)2}\right)<0,\ \Re\left(s_{(i)1},s_{(i)3}\right)>0,\ \Re\left(s_{(i)2},s_{(i)4}\right)<0,\ i=2,\dots,N+1, \tag{3.25}$$

$$F_{(i)1}=\frac{Is_{(i)1}}{\zeta},\ F_{(i)2}=\frac{Is_{(i)2}}{\zeta},\ F_{(i)3}=\frac{I\zeta}{s_{(i)3}},\ F_{(i)4}=\frac{I\zeta}{s_{(i)4}},\ i=2,\dots,N+1. \tag{3.26}$$

In the formulation, there are a total of 4*N*+2 remaining unknown functions, $G_{(i)j}$ which will be determined from the interface and the boundary conditions.

3.1.1 Interface Continuity and Boundary Conditions

In this section, the unknown functions $G_{(i)j}$ are determined by applying interface continuity and boundary conditions. The required number of conditions is 4*N*+2. As well known, displacement and stress components are continuous functions. Hence, the contact problem has four continuity conditions (4*N*) at each interface. The last two boundary conditions are stress free surface conditions at $X = 0$. In short, a large linear system is formed in multi-layer contact problems.

The method for the solution of $G_{(i)j}$ functions must be as fast as possible. However, calculating the inverse of a quite large matrix is a time-consuming process since *N* is a large number and the terms in this matrix are dependent on Fourier Transform variable ζ. Thus, an algorithm is developed based on applying the interface conditions separately and eliminating some $G_{(i)j}$ functions at each interface. The solution method is explicitly described in the section below.

3.1.1.1 Continuity Conditions along the Interfaces

To begin with, the interface matching conditions state that displacement and stress components are continuous as shown below in Eqs. (3.27)-(3.30).

$$U_{(i)}\left(d_{(i)},Y\right)=U_{(i+1)}\left(d_{(i)},Y\right),\ i=1,...,N,\ -\infty<Y<\infty, \tag{3.27}$$

$$V_{(i)}\left(d_{(i)},Y\right)=V_{(i+1)}\left(d_{(i)},Y\right),\ i=1,...,N,\ -\infty<Y<\infty, \tag{3.28}$$

$$\sigma_{(i)XX}\left(d_{(i)},Y\right)=\sigma_{(i+1)XX}\left(d_{(i)},Y\right),\ i=1,...,N,\ -\infty<Y<\infty, \tag{3.29}$$

$$\sigma_{(i)XY}\left(d_{(i)},Y\right)=\sigma_{(i+1)XY}\left(d_{(i)},Y\right),\ i=1,...,N,\ -\infty<Y<\infty. \tag{3.30}$$

Next, the functions possessing '*' superscripts are defined.

$$G^*_{(1)1}=G_{(1)1}e^{s_{(1)1}d_{(1)}},\ G^*_{(1)2}=G_{(1)2}e^{s_{(1)2}d_{(1)}}, \tag{3.31}$$

$$G^*_{(i+1)j}=G_{(i+1)j}e^{s_{(i+1)j}d_{(i)}},\quad i=1,...,N,\quad j=1,...,4, \tag{3.32}$$

$$G^*_{(i)j}=G_{(i)j}e^{s_{(i)j}d_{(i)}},\quad i=2,...,N,\quad j=1,...,4. \tag{3.33}$$

Then, starting from the interface condition between 1st and 2nd layers, the application order of the boundary conditions goes in negative *X*-direction. The displacement components for 1st and 2nd layers are equated to ach other.

$$\begin{Bmatrix} G^*_{(1)1} \\ G^*_{(1)2} \end{Bmatrix}=\begin{bmatrix} 1 & 1 \\ F_{(1)1} & F_{(1)2} \end{bmatrix}^{-1}\begin{bmatrix} 1 & 1 & 1 & 1 \\ F_{(2)1} & F_{(2)2} & F_{(2)3} & F_{(2)4} \end{bmatrix}\begin{Bmatrix} G^*_{(2)1} \\ G^*_{(2)2} \\ G^*_{(2)3} \\ G^*_{(2)4} \end{Bmatrix}, \tag{3.34}$$

With Eq. (3.34), the displacement continuity is achieved. The representation of stress field continuity is rather complex and assured with

$$\left[r_{(1)}\right]\begin{Bmatrix} G^*_{(1)1} \\ G^*_{(1)2} \end{Bmatrix} = \begin{bmatrix} \Lambda_{(1)} & 0 \\ 0 & \chi_{(1)} \end{bmatrix}\left[r_{(2)}\right]\begin{Bmatrix} G^*_{(2)1} \\ G^*_{(2)2} \\ G^*_{(2)3} \\ G^*_{(2)4} \end{Bmatrix}, \tag{3.35}$$

where the matrices in Eq. (3.35) are explicitly given as

$$\left[r_{(1)}\right] = \begin{bmatrix} (\kappa_{(1)}+1)s_{(1)1} + I\zeta(3-\kappa_{(1)})F_{(1)1} & (\kappa_{(1)}+1)s_{(1)2} + I\zeta(3-\kappa_{(1)})F_{(1)2} \\ I\zeta + F_{(1)1}s_{(1)1} & I\zeta + F_{(1)2}s_{(1)2} \end{bmatrix}, \tag{3.36}$$

$$\chi_{(i)} = \frac{\mu_{(i+1)}}{\mu_{(i)}},\ \Lambda_{(i)} = \chi_{(i)}\frac{\kappa_{(i)}-1}{\kappa_{(i+1)}-1},\quad i=1,\ldots,N, \tag{3.37}$$

$$\left[r_{(i)}\right] = \begin{bmatrix} r_{(i)1} & r_{(i)2} & r_{(i)3} & r_{(i)4} \\ r_{(i)5} & r_{(i)6} & r_{(i)7} & r_{(i)8} \end{bmatrix},\quad i=2,\ldots,N+1, \tag{3.38}$$

$$r_{(i)1} = (\kappa_{(i)}+1)s_{(i)1} + I\zeta(3-\kappa_{(i)})F_{(i)1},\ r_{(i)2} = (\kappa_{(i)}+1)s_{(i)2} + I\zeta(3-\kappa_{(i)})F_{(i)2}, \tag{3.39}$$

$$r_{(i)3} = (\kappa_{(i)}+1)s_{(i)3} + I\zeta(3-\kappa_{(i)})F_{(i)3},\ r_{(i)4} = (\kappa_{(i)}+1)s_{(i)4} + I\zeta(3-\kappa_{(i)})F_{(i)4}, \tag{3.40}$$

$$r_{(i)5} = I\zeta + F_{(i)1}s_{(i)1},\ r_{(i)6} = I\zeta + F_{(i)2}s_{(i)2},\ r_{(i)7} = I\zeta + F_{(i)3}s_{(i)3},\ r_{(i)8} = I\zeta + F_{(i)4}s_{(i)4}. \tag{3.41}$$

Utilizing Eqs. (3.34) and (3.35), the relation between $\{G^*_{(2)1}\quad G^*_{(2)3}\}^T$ and $\{G^*_{(2)2}\quad G^*_{(2)4}\}^T$ can be obtained by eliminating $G^*_{(1)1}$ and $G^*_{(1)2}$. Matrix manipulations below express these procedures.

$$\left[q_{(2)}\right] = \left[r_{(1)}\right]\begin{bmatrix} 1 & 1 \\ F_{(1)1} & F_{(1)2} \end{bmatrix}^{-1}\begin{bmatrix} 1 & 1 & 1 & 1 \\ F_{(2)1} & F_{(2)2} & F_{(2)3} & F_{(2)4} \end{bmatrix}, \tag{3.42}$$

$$\left[q_{(2)}\right] = \begin{bmatrix} q_{(2)1} & q_{(2)2} & q_{(2)3} & q_{(2)4} \\ q_{(2)5} & q_{(2)6} & q_{(2)7} & q_{(2)8} \end{bmatrix}, \tag{3.43}$$

$$\begin{bmatrix} w_{(2)1} & w_{(2)2} \\ w_{(2)3} & w_{(2)4} \end{bmatrix} = \begin{bmatrix} \Lambda_{(1)} r_{(2)1} - q_{(2)1} & \Lambda_{(1)} r_{(2)3} - q_{(2)3} \\ \chi_{(1)} r_{(2)5} - q_{(2)5} & \chi_{(1)} r_{(2)7} - q_{(2)7} \end{bmatrix}^{-1} \begin{bmatrix} q_{(2)2} - \Lambda_{(1)} r_{(2)2} & q_{(2)4} - \Lambda_{(1)} r_{(2)4} \\ q_{(2)6} - \chi_{(1)} r_{(2)6} & q_{(2)8} - \chi_{(1)} r_{(2)8} \end{bmatrix}, \tag{3.44}$$

$$\begin{bmatrix} z_{(2)1} & z_{(2)2} \\ z_{(2)3} & z_{(2)4} \end{bmatrix} = \begin{bmatrix} e^{s_{(2)1}\left(d_{(2)} - d_{(1)}\right)} & 0 \\ 0 & e^{s_{(2)3}\left(d_{(2)} - d_{(1)}\right)} \end{bmatrix} \begin{bmatrix} w_{(2)1} & w_{(2)2} \\ w_{(2)3} & w_{(2)4} \end{bmatrix} \begin{bmatrix} e^{s_{(2)2}\left(d_{(1)} - d_{(2)}\right)} & 0 \\ 0 & e^{s_{(2)4}\left(d_{(1)} - d_{(2)}\right)} \end{bmatrix}, \tag{3.45}$$

$$\begin{Bmatrix} G^*_{(2)1} \\ G^*_{(2)3} \end{Bmatrix} = \begin{bmatrix} z_{(2)1} & z_{(2)2} \\ z_{(2)3} & z_{(2)4} \end{bmatrix} \begin{Bmatrix} G^*_{(2)2} \\ G^*_{(2)4} \end{Bmatrix}, \tag{3.46}$$

At this point, we continue with the algorithm below for the interface conditions generated due to the homogenization of FGM coating.

$$\begin{bmatrix} m_{(i)1} & m_{(i)2} & m_{(i)3} & m_{(i)4} \\ m_{(i)5} & m_{(i)6} & m_{(i)7} & m_{(i)8} \end{bmatrix} = \begin{bmatrix} 1 + z_{(i)1} + z_{(i)3} & 1 + z_{(i)2} + z_{(i)4} \\ F_{(i)1} z_{(i)1} + F_{(i)3} z_{(i)3} + F_{(i)2} & F_{(i)1} z_{(i)2} + F_{(i)3} z_{(i)4} + F_{(i)4} \end{bmatrix}^{-1} \begin{bmatrix} 1 & 1 & 1 & 1 \\ F_{(i+1)1} & F_{(i+1)2} & F_{(i+1)3} & F_{(i+1)4} \end{bmatrix}, \tag{3.47}$$

$$\begin{bmatrix} q_{(i)1} & q_{(i)2} & q_{(i)3} & q_{(i)4} \\ q_{(i)5} & q_{(i)6} & q_{(i)7} & q_{(i)8} \end{bmatrix} = \left[\begin{bmatrix} r_{(i)2} & r_{(i)4} \\ r_{(i)6} & r_{(i)8} \end{bmatrix} + \begin{bmatrix} r_{(i)1} & r_{(i)3} \\ r_{(i)5} & r_{(i)7} \end{bmatrix} \begin{bmatrix} z_{(i)1} & z_{(i)2} \\ z_{(i)3} & z_{(i)4} \end{bmatrix} \right] \begin{bmatrix} m_{(i)1} & m_{(i)2} & m_{(i)3} & m_{(i)4} \\ m_{(i)5} & m_{(i)6} & m_{(i)7} & m_{(i)8} \end{bmatrix}, \tag{3.48}$$

$$\begin{bmatrix} w_{(i)1} & w_{(i)2} \\ w_{(i)3} & w_{(i)4} \end{bmatrix} = \begin{bmatrix} \Lambda_{(i)} r_{(i+1)1} - q_{(i)1} & \Lambda_{(i)} r_{(i+1)3} - q_{(i)3} \\ \chi_{(i)} r_{(i+1)5} - q_{(i)5} & \chi_{(i)} r_{(i+1)7} - q_{(i)7} \end{bmatrix}^{-1} \begin{bmatrix} q_{(i)2} - \Lambda_{(i)} r_{(i+1)2} & q_{(i)4} - \Lambda_{(i)} r_{(i+1)4} \\ q_{(i)6} - \chi_{(i)} r_{(i+1)6} & q_{(i)8} - \chi_{(i)} r_{(i+1)8} \end{bmatrix}, \tag{3.49}$$

$$\begin{bmatrix} z_{(i+1)1} & z_{(i+1)2} \\ z_{(i+1)3} & z_{(i+1)4} \end{bmatrix} = \begin{bmatrix} e^{s_{(i+1)1}\left(d_{(i+1)} - d_{(i)}\right)} & 0 \\ 0 & e^{s_{(i+1)3}\left(d_{(i+1)} - d_{(i)}\right)} \end{bmatrix} \begin{bmatrix} w_{(i)1} & w_{(i)2} \\ w_{(i)3} & w_{(i)4} \end{bmatrix} \begin{bmatrix} e^{s_{(i+1)2}\left(d_{(i)} - d_{(i+1)}\right)} & 0 \\ 0 & e^{s_{(i+1)4}\left(d_{(i)} - d_{(i+1)}\right)} \end{bmatrix}, \tag{3.50}$$

$$\begin{Bmatrix} G^*_{(i+1)1} \\ G^*_{(i+1)3} \end{Bmatrix} = \begin{bmatrix} z_{(i+1)1} & z_{(i+1)2} \\ z_{(i+1)3} & z_{(i+1)4} \end{bmatrix} \begin{Bmatrix} G^*_{(i+1)2} \\ G^*_{(i+1)4} \end{Bmatrix}, \quad i = 2,...,N. \tag{3.51}$$

The algorithm above is developed uniquely for the present study. It is the main work of this dissertation since the value of N is a large number. In the parametric analyses, this algorithm reveals the effects and fulfills the requirements of any property gradation. At the end of the algorithm, we end up with a highly complex relation between $\{G^*_{(N+1)1} \quad G^*_{(N+1)3}\}^T$ and $\{G^*_{(N+1)2} \quad G^*_{(N+1)4}\}^T$.

3.1.1.2 Boundary Conditions

This section actually describes the last step of the procedure for obtaining the unknown functions $\{G^*_{(N+1)2} \quad G^*_{(N+1)4}\}^T$. The boundary conditions below for the uppermost layer in contact with the rigid punch (i=N+1) are applied and all $G_{(i)j}$ functions are written in terms of $P(\zeta)$ and $Q(\zeta)$.

$$\sigma_{(N+1)XX}(0,Y) = \begin{cases} S(Y), \; 0 < Y < b, \\ 0, \; Y < 0, \; b < Y, \end{cases} \tag{3.52}$$

$$\sigma_{(N+1)XY}(0,Y) = \begin{cases} \eta S(Y), \; 0 < Y < b, \\ 0, \; Y < 0, \; b < Y. \end{cases} \tag{3.53}$$

After that, Inverse Fourier Transforms of Eqs. (3.52) and (3.53) are written.

$$\int_0^b S(t)\exp(-I\zeta t)\,dt = P(\zeta), \quad \int_0^b \eta S(t)\exp(-I\zeta t)\,dt = Q(\zeta). \tag{3.54}$$

Once the vector $\{G_{(N+1)2} \quad G_{(N+1)4}\}^T$ is written in terms of $P(\zeta)$ and $Q(\zeta)$, the singular integral equation can be derived.

$$\begin{Bmatrix} G_{(N+1)2} \\ G_{(N+1)4} \end{Bmatrix} = [\Theta]\frac{1}{\mu_{(N+1)}} \begin{Bmatrix} \left(\kappa_{(N+1)} - 1\right)P(\zeta) \\ Q(\zeta) \end{Bmatrix}, \tag{3.55}$$

where the matrix [Θ] is defined as

$$\left[\Theta\right]=\left[\begin{bmatrix} r_{(N+1)2} & r_{(N+1)4} \\ r_{(N+1)6} & r_{(N+1)8} \end{bmatrix}+\begin{bmatrix} r_{(N+1)1} & r_{(N+1)3} \\ r_{(N+1)5} & r_{(N+1)7} \end{bmatrix}\begin{bmatrix} z_{(N+1)1} & z_{(N+1)2} \\ z_{(N+1)3} & z_{(N+1)4} \end{bmatrix}\right]^{-1}. \qquad (3.56)$$

Hence, all $G_{(i)j}$ functions are known in terms of $P(\zeta)$ and $Q(\zeta)$. In the end, the uppermost layer changes its shape because of the indentation of the punch so the punch profile determines the displacement derivative relation which provides the singular integral equation.

3.1.2 Derivation of the Singular Integral Equation of Multi-layer Model

Until now, all functions are found in displacement and stress components. Therefore, it is time to construct the singular integral equation using the displacement derivatives with respect to Y coordinate $\left(\partial U_{(N+1)}/\partial Y \text{ and } \partial V_{(N+1)}/\partial Y\right)$.

$$\lim_{X\to 0}\frac{\partial U_{(N+1)}\left(X,Y\right)}{\partial Y}=\lim_{X\to 0}\frac{1}{2\pi}\int_{-\infty}^{\infty} I\zeta\sum_{j=1}^{4} G_{(N+1)j}\exp\left(s_{(N+1)j}X+I\zeta Y\right)d\zeta, \qquad (3.57)$$

$$\lim_{X\to 0}\frac{\partial V_{(N+1)}\left(X,Y\right)}{\partial Y}=\lim_{X\to 0}\frac{1}{2\pi}\int_{-\infty}^{\infty} I\zeta\sum_{j=1}^{4} G_{(N+1)j}F_{(N+1)j}\exp\left(s_{(N+1)j}X+I\zeta Y\right)d\zeta. \qquad (3.58)$$

Two displacement gradient equations given by Eqs. (3.57) and (3.58) are expressed in the following form.

$$\lim_{X\to 0}2\pi\mu_{(N+1)}\frac{\partial U_{(N+1)}\left(X,Y\right)}{\partial Y}=\int_{-\infty}^{\infty} J_{11}\left(X,Y,t\right)S\left(t\right)dt+\int_{-\infty}^{\infty}\eta J_{12}\left(X,Y,t\right)S\left(t\right)dt, \qquad (3.59)$$

$$\lim_{X\to 0}2\pi\mu_{(N+1)}\frac{\partial V_{(N+1)}\left(X,Y\right)}{\partial Y}=\int_{-\infty}^{\infty}\eta J_{21}\left(X,Y,t\right)S\left(t\right)dt+\int_{-\infty}^{\infty} J_{22}\left(X,Y,t\right)S\left(t\right)dt, \qquad (3.60)$$

where the functions J_{ij}, i=1,2, j=1,2, are defined as

$$J_{11}\left(X,Y,t\right)=\lim_{X\to 0}\int_{-\infty}^{\infty}\omega_{11}\left(X,\zeta\right)\exp\left(-I\zeta\left(t-Y\right)\right)d\zeta, \tag{3.61}$$

$$J_{12}\left(X,Y,t\right)=\lim_{X\to 0}\int_{-\infty}^{\infty}\omega_{12}\left(X,\zeta\right)\exp\left(-I\zeta\left(t-Y\right)\right)d\zeta, \tag{3.62}$$

$$J_{21}\left(X,Y,t\right)=\lim_{X\to 0}\int_{-\infty}^{\infty}\omega_{21}\left(X,\zeta\right)\exp\left(-I\zeta\left(t-Y\right)\right)d\zeta, \tag{3.63}$$

$$J_{22}\left(X,Y,t\right)=\lim_{X\to 0}\int_{-\infty}^{\infty}\omega_{22}\left(X,\zeta\right)\exp\left(-I\zeta\left(t-Y\right)\right)d\zeta. \tag{3.64}$$

where $\omega_{ij}(X,\zeta)$, i=1,2, j=1,2, are provided as

$$\omega_{11}\left(X,\zeta\right)=\text{coeff}\left(I\zeta\sum_{i=1}^{4}G_{(N+1)i}e^{s_{(N+1)i}X},\frac{P}{\mu_{(N+1)}}\right), \tag{3.65}$$

$$\omega_{12}\left(X,\zeta\right)=\text{coeff}\left(I\zeta\sum_{i=1}^{4}G_{(N+1)i}e^{s_{(N+1)i}X},\frac{Q}{\mu_{(N+1)}}\right), \tag{3.66}$$

$$\omega_{21}\left(X,\zeta\right)=\text{coeff}\left(I\zeta\sum_{i=1}^{4}G_{(N+1)i}F_{(N+1)i}e^{s_{(N+1)i}X},\frac{Q}{\mu_{(N+1)}}\right), \tag{3.67}$$

$$\omega_{22}\left(X,\zeta\right)=\text{coeff}\left(I\zeta\sum_{i=1}^{4}G_{(N+1)i}F_{(N+1)i}e^{s_{(N+1)i}X},\frac{P}{\mu_{(N+1)}}\right), \tag{3.68}$$

$\partial U_{(N+1)}(0,Y)/\partial Y$ in Eq. (3.59) varies depending on the punch profile and is an input in the analyses. In the next step, the asymptotic coefficients of the kernels of the integral equation are extracted using asymptotic analyses. These analyses are crucial since the coefficients determine the singular behavior of the integral equation and the strengths of singularities of the stresses. The functions in (3.65)-(3.68) are evaluated as $\zeta\to\infty$. Appendix A explains the details of asymptotic analyses. The results of the asymptotic analyses

$$\omega_{11}^{\infty}(X,\zeta)=I\frac{\zeta}{|\zeta|}p_{11}\exp\left(s_{(N+1)2}X\right)+I\frac{\zeta}{|\zeta|}p_{12}\exp\left(s_{(N+1)4}X\right), \tag{3.69}$$

$$\omega_{12}^{\infty}(X,\zeta)=p_{21}\exp\left(s_{(N+1)2}X\right)+p_{22}\exp\left(s_{(N+1)4}X\right), \tag{3.70}$$

$$\omega_{21}^{\infty}(X,\zeta)=I\frac{\zeta}{|\zeta|}p_{31}\exp\left(s_{(N+1)2}X\right)+I\frac{\zeta}{|\zeta|}p_{32}\exp\left(s_{(N+1)4}X\right), \tag{3.71}$$

$$\omega_{22}^{\infty}(X,\zeta)=p_{41}\exp\left(s_{(N+1)2}X\right)+p_{42}\exp\left(s_{(N+1)4}X\right), \tag{3.72}$$

are obtained. In Eqs. (3.69)-(3.72), p_{ij}, i=1,…,4, j=1,2 are constant numbers which depend on the normalized punch speed and Kolosov's constant. Further manipulations about these constants will be given in the following steps. Euler Identity

$$\exp\left(-I\zeta\left(t-Y\right)\right)=\cos\left(\zeta\left(t-Y\right)\right)-I\sin\left(\zeta\left(t-Y\right)\right), \tag{3.73}$$

states the relation between exponential function and trigonometric functions, i.e., exp(-$I\zeta(t-Y)$) term is separated into even (cos($\zeta(t-Y)$)) and odd (sin($\zeta(t-Y)$)) parts. By utilizing the properties of even and odd functions,

$$\int_{-\infty}^{\infty} Even\ Function = 2\int_{0}^{\infty} Even\ Function,\ \int_{-\infty}^{\infty} Odd\ Function = 0. \tag{3.74}$$

$$\text{Even x Odd} = \text{Odd},\ \text{Even x Even} = \text{Even},\ \text{Odd x Odd} = \text{Even}, \tag{3.75}$$

Eqs. (3.69)-(3.72) are rewritten. Note that $\zeta/|\zeta|$ is an odd function. Two equations below are the sample calculations of the simplification procedure. These equations will directly be applied to Eqs. (3.69)-(3.72).

$$\int_{-\infty}^{\infty} I\frac{\zeta}{|\zeta|}\exp\left(-|\zeta|X\right)\exp\left(-I\zeta\left(t-Y\right)\right)d\zeta=2\int_{0}^{\infty}\exp\left(-\zeta X\right)\sin\left(\zeta\left(t-Y\right)\right)d\zeta, \tag{3.76}$$

$$\int_{-\infty}^{\infty} \exp\left(-|\zeta| X\right)\exp\left(-I\zeta\left(t-Y\right)\right)d\zeta = 2\int_{0}^{\infty} \exp\left(-\zeta X\right)\cos\left(\zeta\left(t-Y\right)\right)d\zeta. \quad (3.77)$$

Abramowitz and Stegun (1964) suggest the following relations in the calculation of infinite integrals.

$$\int_{0}^{\infty} \exp\left(-ax\right)\sin\left(bx\right)dx = \frac{b}{a^2+b^2}, \quad \int_{0}^{\infty} \exp\left(-ax\right)\cos\left(bx\right)dx = \frac{a}{a^2+b^2}. \quad (3.78)$$

Hence, one can adapt these relations to Eqs. (3.76) and (3.77) in the following way.

$$2\int_{0}^{\infty} \exp\left(-\zeta X\right)\sin\left(\zeta\left(t-Y\right)\right)d\zeta = \frac{2\left(t-Y\right)}{X^2+\left(t-Y\right)^2}, \quad X>0, \quad (3.79)$$

$$2\int_{0}^{\infty} \exp\left(-\zeta X\right)\cos\left(\zeta\left(t-Y\right)\right)d\zeta = \frac{2X}{X^2+\left(t-Y\right)^2}, \quad X>0. \quad (3.80)$$

After these mathematical procedures, asymptotic values of the kernels can be written.

$$\int_{-\infty}^{\infty} I\frac{\zeta}{|\zeta|}\exp\left(-\sqrt{1-\lambda_{(N+1)}^2}\,|\zeta| X\right)\exp\left(-I\zeta\left(t-Y\right)\right)d\zeta = \frac{2\left(t-Y\right)}{\left(1-\lambda_{(N+1)}^2\right)X^2+\left(t-Y\right)^2}, \quad (3.81)$$

$$\int_{-\infty}^{\infty} I\frac{\zeta}{|\zeta|}\exp\left(-\sqrt{1-\frac{\left(\kappa_{(N+1)}-1\right)}{\left(\kappa_{(N+1)}+1\right)}\lambda_{(N+1)}^2}\,|\zeta| X\right)\exp\left(-I\zeta\left(t-Y\right)\right)d\zeta = \frac{2\left(t-Y\right)}{\left(1-\frac{\left(\kappa_{(N+1)}-1\right)}{\left(\kappa_{(N+1)}+1\right)}\lambda_{(N+1)}^2\right)X^2+\left(t-Y\right)^2}, \quad (3.82)$$

$$\int_{-\infty}^{\infty} \exp\left(-\sqrt{1-\lambda_{(N+1)}^2}\,|\zeta| X\right)\exp\left(-I\zeta\left(t-Y\right)\right)d\zeta = \frac{2\sqrt{1-\lambda_{(N+1)}^2}\,X}{\left(1-\lambda_{(N+1)}^2\right)X^2+\left(t-Y\right)^2}, \quad (3.83)$$

$$\int_{-\infty}^{\infty} \exp\left(-\sqrt{1-\frac{\left(\kappa_{(N+1)}-1\right)}{\left(\kappa_{(N+1)}+1\right)}\lambda_{(N+1)}^{2}}\,|\zeta|\,X\right)\exp\left(-I\zeta\left(t-Y\right)\right)d\zeta = \frac{2\sqrt{1-\frac{\left(\kappa_{(N+1)}-1\right)}{\left(\kappa_{(N+1)}+1\right)}\lambda_{(N+1)}^{2}}\,X}{\left(1-\frac{\left(\kappa_{(N+1)}-1\right)}{\left(\kappa_{(N+1)}+1\right)}\lambda_{(N+1)}^{2}\right)X^{2}+\left(t-Y\right)^{2}}, \tag{3.84}$$

Limits of the kernels are calculated in the next step.

$$\lim_{X\to 0}\frac{2\left(t-Y\right)}{\left(1-\lambda_{(N+1)}^{2}\right)X^{2}+\left(t-Y\right)^{2}} = \lim_{X\to 0}\frac{2\left(t-Y\right)}{\left(1-\frac{\left(\kappa_{(N+1)}-1\right)}{\left(\kappa_{(N+1)}+1\right)}\lambda_{(N+1)}^{2}\right)X^{2}+\left(t-Y\right)^{2}} = \frac{2}{\left(t-Y\right)}, \tag{3.85}$$

$$\lim_{X\to 0}\frac{2\sqrt{1-\lambda_{(N+1)}^{2}}\,X}{\left(1-\lambda_{(N+1)}^{2}\right)X^{2}+\left(t-Y\right)^{2}} = \lim_{X\to 0}\frac{2\sqrt{1-\frac{\left(\kappa_{(N+1)}-1\right)}{\left(\kappa_{(N+1)}+1\right)}\lambda_{(N+1)}^{2}}\,X}{\left(1-\frac{\left(\kappa_{(N+1)}-1\right)}{\left(\kappa_{(N+1)}+1\right)}\lambda_{(N+1)}^{2}\right)X^{2}+\left(t-Y\right)^{2}} = 2\pi\delta\left(t-Y\right), \tag{3.86}$$

At the end, the coefficients of asymptotic analyses $\left(p_1, p_2, p_3, p_4\right)$ are found in terms of parameters in the model.

$$p_1 = p_{11} + p_{12}, \quad p_2 = p_{21} + p_{22}, \quad p_3 = p_{31} + p_{32}, \quad p_4 = p_{41} + p_{42}. \tag{3.87}$$

These coefficients are provided explicitly in Appendix B. Using the outputs of the asymptotic analyses, one can derive the singular integral equation and another integral equation that is necessary in the calculation of the lateral contact stress. In surface damages, the failure or deterioration is associated with the lateral stress. For this reason, examining the influences of lateral stress is indispensable in contact models so the lateral stress results are also provided in the present study.

$$p_2\eta S(Y)+\frac{1}{\pi}\int_0^b\left(\frac{p_1}{t-Y}+k_{11}(t,Y)+\eta k_{12}(t,Y)\right)S(t)\,dt = \mu_{(N+1)}\frac{\partial U_{(N+1)}(0,Y)}{\partial Y},\ -\infty<Y<\infty, \tag{3.88}$$

$$p_4 S(Y)+\frac{1}{\pi}\int_0^b\left(\frac{p_3\eta}{t-Y}+\eta k_{21}(t,Y)+k_{22}(t,Y)\right)S(t)\,dt = \mu_{(N+1)}\frac{\partial V_{(N+1)}(0,Y)}{\partial Y},\ -\infty<Y<\infty, \tag{3.89}$$

The kernels k_{ij}, i=1,2, j=1,2, are called as Fredholm kernels and written as

$$k_{11}(t,Y)=\int_0^\infty\left(h_{11}(\zeta)-p_1\right)\sin\left(\zeta(t-Y)\right)d\zeta, \tag{3.90}$$

$$k_{12}(t,Y)=\int_0^\infty\left(h_{12}(\zeta)-p_2\right)\cos\left(\zeta(t-Y)\right)d\zeta, \tag{3.91}$$

$$k_{21}(t,Y)=\int_0^\infty\left(h_{21}(\zeta)-p_3\right)\sin\left(\zeta(t-Y)\right)d\zeta, \tag{3.92}$$

$$k_{22}(t,Y)=\int_0^\infty\left(h_{22}(\zeta)-p_4\right)\cos\left(\zeta(t-Y)\right)d\zeta. \tag{3.93}$$

The integrands of the kernels of the singular integral equation are given by

$$h_{ij}(\zeta)=\lim_{X\to 0}\omega_{ij}(X,\zeta),\ i=1,2,\ j=1,2, \tag{3.94}$$

Integration end limits may be different points depending on the punch profile. For instance, the interval of the contact length for flat, triangular and semi-circular punch problems is $0 < Y < b$, whereas for circular punch problem, it is $-a < Y < b$. Then, one can define the equilibrium equation

$$\int_0^b S(t)\,dt=-P \tag{3.95}$$

which states that the total contact pressure is equal to the force exerted by the stamp. P is the compressive load exerted by the rigid punch per unit depth of the structure.

3.1.3 Derivation of Lateral Contact Stress on the Surface

The calculation of lateral contact stress is straight-forward if one obtains the normal contact stress. The derivation of lateral contact stress equation starts with three-dimensional Hooke's Law.

$$\varepsilon_{(N+1)XX} = \frac{1}{E_{(N+1)}}\left[\sigma_{(N+1)XX} - \nu_{(N+1)}\left(\sigma_{(N+1)YY} + \sigma_{(N+1)ZZ}\right)\right], \tag{3.96}$$

$$\varepsilon_{(N+1)YY} = \frac{1}{E_{(N+1)}}\left[\sigma_{(N+1)YY} - \nu_{(N+1)}\left(\sigma_{(N+1)XX} + \sigma_{(N+1)ZZ}\right)\right], \tag{3.97}$$

$$\varepsilon_{(N+1)ZZ} = \frac{1}{E_{(N+1)}}\left[\sigma_{(N+1)ZZ} - \nu_{(N+1)}\left(\sigma_{(N+1)XX} + \sigma_{(N+1)YY}\right)\right]. \tag{3.98}$$

For plane strain assumption, the strain in the Z-direction is taken as zero so the stress in the Z-direction is found from Eq. (3.98) and substituted into Eq. (3.97).

$$\sigma_{(N+1)ZZ} = \nu_{(N+1)}\left(\sigma_{(N+1)XX} + \sigma_{(N+1)YY}\right). \tag{3.99}$$

The strain in Y-direction is rewritten as below:

$$\varepsilon_{(N+1)YY} = \frac{1-\nu_{(N+1)}^2}{E_{(N+1)}}\sigma_{(N+1)YY} - \frac{\nu_{(N+1)}\left(1-\nu_{(N+1)}\right)}{E_{(N+1)}}\sigma_{(N+1)XX}, \tag{3.100}$$

Young's modulus and Poisson's ratio in Eq. (3.100) are replaced by shear modulus and Kolosov's constant and the strain in Y-direction is updated.

$$E_{(N+1)} = 2\left(1+\nu_{(N+1)}\right)\mu_{(N+1)}, \quad \nu_{(N+1)} = \frac{3-\kappa_{(N+1)}}{4}, \tag{3.101}$$

$$\varepsilon_{(N+1)YY} = \frac{\partial V_{(N+1)}(0,Y)}{\partial Y} = \frac{\kappa_{(N+1)}+1}{8\mu_{(N+1)}}\sigma_{(N+1)YY} - \frac{3-\kappa_{(N+1)}}{8\mu_{(N+1)}}\sigma_{(N+1)XX}, \tag{3.102}$$

Inserting Eq. (3.102) into Eq. (3.89) and performing some mathematical manipulations result in the following relation for lateral contact stress.

$$\begin{aligned}\sigma_{(N+1)YY}(0,Y) = {} & \frac{8p_3\eta}{\left(\kappa_{(N+1)}+1\right)\pi}\int_0^b \frac{S(t)}{t-Y}dt + \frac{8p_4+\left(3-\kappa_{(N+1)}\right)}{\left(\kappa_{(N+1)}+1\right)}S(Y) \\ & + \frac{8}{\left(\kappa_{(N+1)}+1\right)\pi}\int_0^b \left[\eta k_{21}(t,Y)+k_{22}(t,Y)\right]S(t)\,dt, \quad -\infty < Y < \infty.\end{aligned} \tag{3.103}$$

As expected, $\sigma_{(N+1)YY}(0,Y)$ is only dependent on the primary unknown of the contact problem, the normal contact stress $S(Y)$.

3.2 Multiferroic Structure

The moving contact problem of the multiferroic structure is shown in Figure 3.3. An arbitrarily shaped rigid loading agent is moving with a constant velocity V and is in contact with MEE coating of total thickness of h_c. The MEE coating is bonded to an elastic half-plane by utilizing elastic buffer layers. In the composite structure, the MEE coating and the buffer comprise N and M numbers of sub-layers, respectively. In the numbering of the layers, the counter, i=1, is reserved for the half-plane; i=2,…,M+1, stand for elastic buffer layers; and i=M+2,…,N+M+1, correspond to MEE layers. The composite medium is in a state of plane strain. Normal and tangential forces transferred by the contact are respectively denoted by P and Q.

It is assumed that Coulomb's friction law is applicable for the contact between the MEE coating and the punch. The tangential force, Q, is specified as ηP, η being the coefficient of friction. The entire surface z=0 is electrically and magnetically insulated. The coordinate system x-z is fixed, whereas the system X-Z is attached to the moving punch. In the moving coordinate system, the contact region extends from X=0 to X=b.

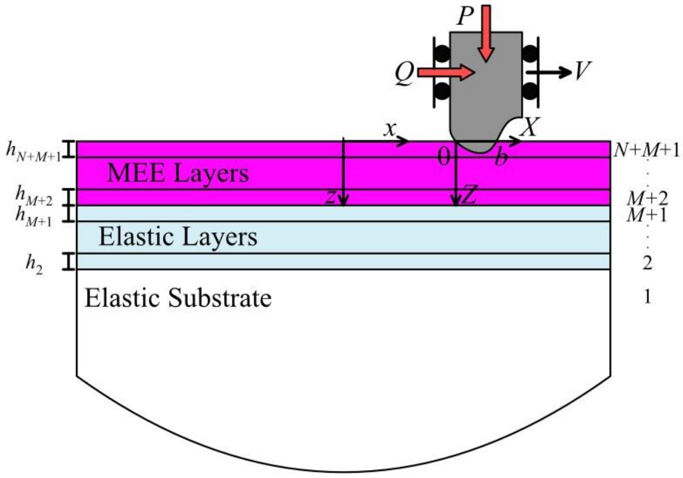

Figure 3.3. Geometry of general moving contact problem of multiferroic heterostructure.

All layers and the half-plane are assumed to be transversely isotropic with *z*-axis, i.e., *z* is the axis of symmetry and shows the poling direction. Constitutive relations for all MEE and elastic sub-layers and the substrate are expressed by the following representations:

$$\begin{Bmatrix} \sigma_{(i)xx} \\ \sigma_{(i)zz} \\ \sigma_{(i)xz} \end{Bmatrix} = \begin{bmatrix} c_{(i)11} & c_{(i)13} & 0 \\ c_{(i)13} & c_{(i)33} & 0 \\ 0 & 0 & c_{(i)44} \end{bmatrix} \begin{Bmatrix} \varepsilon_{(i)xx} \\ \varepsilon_{(i)zz} \\ 2\varepsilon_{(i)xz} \end{Bmatrix}, \quad i = 1, ..., M+1, \tag{3.104}$$

$$\begin{Bmatrix} \sigma_{(i)xx} \\ \sigma_{(i)zz} \\ \sigma_{(i)xz} \end{Bmatrix} = \begin{bmatrix} c_{(i)11} & c_{(i)13} & 0 \\ c_{(i)13} & c_{(i)33} & 0 \\ 0 & 0 & c_{(i)44} \end{bmatrix} \begin{Bmatrix} \varepsilon_{(i)xx} \\ \varepsilon_{(i)zz} \\ 2\varepsilon_{(i)xz} \end{Bmatrix} - \begin{bmatrix} 0 & e_{(i)31} \\ 0 & e_{(i)33} \\ e_{(i)15} & 0 \end{bmatrix} \begin{Bmatrix} E_{(i)x} \\ E_{(i)z} \end{Bmatrix} - \begin{bmatrix} 0 & f_{(i)31} \\ 0 & f_{(i)33} \\ f_{(i)15} & 0 \end{bmatrix} \begin{Bmatrix} H_{(i)x} \\ H_{(i)z} \end{Bmatrix},$$
$$i = M+2, \dots, N+M+1, \tag{3.105}$$

$$\begin{Bmatrix} D_{(i)x} \\ D_{(i)z} \end{Bmatrix} = \begin{bmatrix} 0 & 0 & e_{(i)15} \\ e_{(i)31} & e_{(i)33} & 0 \end{bmatrix} \begin{Bmatrix} \varepsilon_{(i)xx} \\ \varepsilon_{(i)zz} \\ 2\varepsilon_{(i)xz} \end{Bmatrix} + \begin{bmatrix} \beta_{(i)11} & 0 \\ 0 & \beta_{(i)33} \end{bmatrix} \begin{Bmatrix} E_{(i)x} \\ E_{(i)z} \end{Bmatrix} + \begin{bmatrix} g_{(i)11} & 0 \\ 0 & g_{(i)33} \end{bmatrix} \begin{Bmatrix} H_{(i)x} \\ H_{(i)z} \end{Bmatrix},$$
$$i = M+2,\ldots,N+M+1, \tag{3.106}$$

$$\begin{Bmatrix} B_{(i)x} \\ B_{(i)z} \end{Bmatrix} = \begin{bmatrix} 0 & 0 & f_{(i)15} \\ f_{(i)31} & f_{(i)33} & 0 \end{bmatrix} \begin{Bmatrix} \varepsilon_{(i)xx} \\ \varepsilon_{(i)zz} \\ 2\varepsilon_{(i)xz} \end{Bmatrix} + \begin{bmatrix} g_{(i)11} & 0 \\ 0 & g_{(i)33} \end{bmatrix} \begin{Bmatrix} E_{(i)x} \\ E_{(i)z} \end{Bmatrix} + \begin{bmatrix} \mu_{(i)11} & 0 \\ 0 & \mu_{(i)33} \end{bmatrix} \begin{Bmatrix} H_{(i)x} \\ H_{(i)z} \end{Bmatrix},$$
$$i = M+2,\ldots,N+M+1, \tag{3.107}$$

The variables, $\sigma_{(i)jk}$, $\varepsilon_{(i)jk}$, $E_{(i)j}$, $H_{(i)j}$, $D_{(i)j}$ and $B_{(i)j}$, respectively denote stress, strain, electric field, magnetic field, electric displacement and magnetic induction. The material parameters $c_{(i)jk}$, $e_{(i)jk}$, $f_{(i)jk}$, $g_{(i)jk}$, $\beta_{(i)jk}$ and $\mu_{(i)jk}$ stand for elastic, piezoelectric, piezomagnetic, and magnetoelectric constants, dielectric permittivities, and magnetic permeabilities. Strain, electric and magnetic fields can be written as

$$\varepsilon_{(i)xx} = \frac{\partial u_{(i)}}{\partial x}, \quad \varepsilon_{(i)zz} = \frac{\partial w_{(i)}}{\partial z}, \quad \varepsilon_{(i)xz} = \frac{1}{2}\left(\frac{\partial u_{(i)}}{\partial z} + \frac{\partial w_{(i)}}{\partial x}\right), \quad i = 1,\ldots,N+M+1, \tag{3.108}$$

$$E_{(i)x} = -\frac{\partial \phi_{(i)}}{\partial x}, \quad E_{(i)z} = -\frac{\partial \phi_{(i)}}{\partial z}, \quad H_{(i)x} = -\frac{\partial \psi_{(i)}}{\partial x}, \quad H_{(i)z} = -\frac{\partial \psi_{(i)}}{\partial z},$$
$$i = M+1,\ldots,N+M+1. \tag{3.109}$$

where $u_{(i)}$ and $w_{(i)}$ represent displacement components in x- and z-directions, respectively. The functions $\phi_{(i)}$ and $\psi_{(i)}$ are electric and magnetic potentials. The equilibrium equations for i^{th} layer are written as

$$\frac{\partial \sigma_{(i)xx}}{\partial x} + \frac{\partial \sigma_{(i)xz}}{\partial z} = \rho_{(i)} \frac{\partial^2 u_{(i)}}{\partial t^2}, \quad \frac{\partial \sigma_{(i)xz}}{\partial x} + \frac{\partial \sigma_{(i)zz}}{\partial z} = \rho_{(i)} \frac{\partial^2 w_{(i)}}{\partial t^2}, \quad i = 1,\ldots,N+M+1, \tag{3.110}$$

where ρ is density, t is time. Maxwell's electric and magnetic equations for MEE layers

$$\frac{\partial D_{(i)x}}{\partial x}+\frac{\partial D_{(i)z}}{\partial z}=0, \qquad \frac{\partial B_{(i)x}}{\partial x}+\frac{\partial B_{(i)z}}{\partial z}=0, \qquad i=M+2,\ldots,N+M+1. \tag{3.111}$$

are satisfied in terms of components of electric displacement, $D_{(i)j}$, and magnetic induction, $B_{(i)j}$. The governing partial differential equations (PDEs) are obtained by substitution of Eqs. (3.104)-(3.107) into Eqs. (3.110) and (3.111).

$$c_{(i)11}\frac{\partial^2 u_{(i)}}{\partial x^2}+c_{(i)44}\frac{\partial^2 u_{(i)}}{\partial z^2}+\left(c_{(i)13}+c_{(i)44}\right)\frac{\partial^2 w_{(i)}}{\partial x\partial z}=\rho_{(i)}\frac{\partial^2 u_{(i)}}{\partial t^2}, \quad i=1,\ldots,M+1, \tag{3.112}$$

$$\left(c_{(i)13}+c_{(i)44}\right)\frac{\partial^2 u_{(i)}}{\partial x\partial z}+c_{(i)44}\frac{\partial^2 w_{(i)}}{\partial x^2}+c_{(i)33}\frac{\partial^2 w_{(i)}}{\partial z^2}=\rho_{(i)}\frac{\partial^2 w_{(i)}}{\partial t^2}, \quad i=1,\ldots,M+1, \tag{3.113}$$

$$\begin{aligned}&c_{(i)11}\frac{\partial^2 u_{(i)}}{\partial x^2}+c_{(i)44}\frac{\partial^2 u_{(i)}}{\partial z^2}+\left(c_{(i)13}+c_{(i)44}\right)\frac{\partial^2 w_{(i)}}{\partial x\partial z}+\left(e_{(i)15}+e_{(i)31}\right)\frac{\partial^2 \phi_{(i)}}{\partial x\partial z}\\&\quad+\left(f_{(i)15}+f_{(i)31}\right)\frac{\partial^2 \psi_{(i)}}{\partial x\partial z}=\rho_{(i)}\frac{\partial^2 u_{(i)}}{\partial t^2}, \quad i=M+2,\ldots,N+M+1,\end{aligned} \tag{3.114}$$

$$\begin{aligned}&\left(c_{(i)13}+c_{(i)44}\right)\frac{\partial^2 u_{(i)}}{\partial x\partial z}+c_{(i)44}\frac{\partial^2 w_{(i)}}{\partial x^2}+c_{(i)33}\frac{\partial^2 w_{(i)}}{\partial z^2}+e_{(i)15}\frac{\partial^2 \phi_{(i)}}{\partial x^2}+e_{(i)33}\frac{\partial^2 \phi_{(i)}}{\partial z^2}\\&\quad+f_{(i)15}\frac{\partial^2 \psi_{(i)}}{\partial x^2}+f_{(i)33}\frac{\partial^2 \psi_{(i)}}{\partial z^2}=\rho_{(i)}\frac{\partial^2 w_{(i)}}{\partial t^2}, \quad i=M+2,\ldots,N+M+1,\end{aligned} \tag{3.115}$$

$$\begin{aligned}&\left(e_{(i)15}+e_{(i)31}\right)\frac{\partial^2 u_{(i)}}{\partial x\partial z}+e_{(i)15}\frac{\partial^2 w_{(i)}}{\partial x^2}+e_{(i)33}\frac{\partial^2 w_{(i)}}{\partial z^2}-\beta_{(i)11}\frac{\partial^2 \phi_{(i)}}{\partial x^2}\\&\quad-\beta_{(i)33}\frac{\partial^2 \phi_{(i)}}{\partial z^2}-g_{(i)11}\frac{\partial^2 \psi_{(i)}}{\partial x^2}-g_{(i)33}\frac{\partial^2 \psi_{(i)}}{\partial z^2}=0, \quad i=M+2,\ldots,N+M+1,\end{aligned} \tag{3.116}$$

$$\begin{aligned}&\left(f_{(i)15}+f_{(i)31}\right)\frac{\partial^2 u_{(i)}}{\partial x\partial z}+f_{(i)15}\frac{\partial^2 w_{(i)}}{\partial x^2}+f_{(i)33}\frac{\partial^2 w_{(i)}}{\partial z^2}-g_{(i)11}\frac{\partial^2 \phi_{(i)}}{\partial x^2}\\&\quad-g_{(i)33}\frac{\partial^2 \phi_{(i)}}{\partial z^2}-\mu_{(i)11}\frac{\partial^2 \psi_{(i)}}{\partial x^2}-\mu_{(i)33}\frac{\partial^2 \psi_{(i)}}{\partial z^2}=0, \quad i=M+2,\ldots,N+M+1.\end{aligned} \tag{3.117}$$

Due to the steady-state motion (constant speed) of the loading agent *V*, the model has become tractable by introducing Galilean transformation.

$$x = X + Vt, \quad z = Z. \tag{3.118}$$

In this step, it is appropriate to switch the moving coordinates by means of the functions below in order to eliminate time dependent terms in the governing PDEs.

$$u_{(i)}(x,z,t) = U_{(i)}(X,Z), \quad i = 1,\dots,N+M+1, \tag{3.119}$$

$$w_{(i)}(x,z,t) = W_{(i)}(X,Z), \quad i = 1,\dots,N+M+1, \tag{3.120}$$

$$\phi_{(i)}(x,z,t) = \Phi_{(i)}(X,Z), \quad i = M+2,\dots,N+M+1, \tag{3.121}$$

$$\psi_{(i)}(x,z,t) = \Psi_{(i)}(X,Z), \quad i = M+2,\dots,N+M+1, \tag{3.122}$$

$$\sigma_{(i)xx}(x,z,t) = \sigma_{(i)XX}(X,Z), \quad i = 1,\dots,N+M+1, \tag{3.123}$$

$$\sigma_{(i)zz}(x,z,t) = \sigma_{(i)ZZ}(X,Z), \quad i = 1,\dots,N+M+1, \tag{3.124}$$

$$\sigma_{(i)xz}(x,z,t) = \sigma_{(i)XZ}(X,Z), \quad i = 1,\dots,N+M+1, \tag{3.125}$$

$$D_{(i)x}(x,z,t) = D_{(i)X}(X,Z), \quad i = M+2,\dots,N+M+1, \tag{3.126}$$

$$D_{(i)z}(x,z,t) = D_{(i)Z}(X,Z), \quad i = M+2,\dots,N+M+1, \tag{3.127}$$

$$B_{(i)x}(x,z,t) = B_{(i)X}(X,Z), \quad i = M+2,\dots,N+M+1, \tag{3.128}$$

$$B_{(i)z}(x,z,t) = B_{(i)Z}(X,Z), \quad i = M+2,\dots,N+M+1. \tag{3.129}$$

One can then update the wave equations and Maxwell's equations in *X*-*Z* coordinate system utilizing the time independent unknown functions.

$$\left(c_{(i)11}-\lambda_{(i)}^2 c_{(i)44}\right)\frac{\partial^2 U_{(i)}}{\partial X^2}+c_{(i)44}\frac{\partial^2 U_{(i)}}{\partial Z^2}+\left(c_{(i)13}+c_{(i)44}\right)\frac{\partial^2 W_{(i)}}{\partial X\,\partial Z}=0,\ i=1,\dots,M+1, \tag{3.130}$$

$$\left(c_{(i)13}+c_{(i)44}\right)\frac{\partial^2 U_{(i)}}{\partial X\,\partial Z}+c_{(i)44}\left(1-\lambda_{(i)}^2\right)\frac{\partial^2 W_{(i)}}{\partial X^2}+c_{(i)33}\frac{\partial^2 W_{(i)}}{\partial Z^2}=0,\ i=1,\dots,M+1, \tag{3.131}$$

$$\begin{aligned}&\left(c_{(i)11}-\lambda_{(i)}^2 c_{(i)44}\right)\frac{\partial^2 U_{(i)}}{\partial X^2}+c_{(i)44}\frac{\partial^2 U_{(i)}}{\partial Z^2}+\left(c_{(i)13}+c_{(i)44}\right)\frac{\partial^2 W_{(i)}}{\partial X\,\partial Z}\\&\quad+\left(e_{(i)15}+e_{(i)31}\right)\frac{\partial^2 \Phi_{(i)}}{\partial X\,\partial Z}+\left(f_{(i)15}+f_{(i)31}\right)\frac{\partial^2 \Psi_{(i)}}{\partial X\,\partial Z}=0,\ i=M+2,\dots,N+M+1,\end{aligned} \tag{3.132}$$

$$\begin{aligned}&\left(c_{(i)13}+c_{(i)44}\right)\frac{\partial^2 U_{(i)}}{\partial X\,\partial Z}+c_{(i)44}\left(1-\lambda_{(i)}^2\right)\frac{\partial^2 W_{(i)}}{\partial X^2}+c_{(i)33}\frac{\partial^2 W_{(i)}}{\partial Z^2}+e_{(i)15}\frac{\partial^2 \Phi_{(i)}}{\partial X^2}\\&\quad+e_{(i)33}\frac{\partial^2 \Phi_{(i)}}{\partial Z^2}+f_{(i)15}\frac{\partial^2 \Psi_{(i)}}{\partial X^2}+f_{(i)33}\frac{\partial^2 \Psi_{(i)}}{\partial Z^2}=0,\ i=M+2,\dots,N+M+1,\end{aligned} \tag{3.133}$$

$$\begin{aligned}&\left(e_{(i)15}+e_{(i)31}\right)\frac{\partial^2 U_{(i)}}{\partial X\,\partial Z}+e_{(i)15}\frac{\partial^2 W_{(i)}}{\partial X^2}+e_{(i)33}\frac{\partial^2 W_{(i)}}{\partial Z^2}-\beta_{(i)11}\frac{\partial^2 \Phi_{(i)}}{\partial X^2}\\&\quad-\beta_{(i)33}\frac{\partial^2 \Phi_{(i)}}{\partial Z^2}-g_{(i)11}\frac{\partial^2 \Psi_{(i)}}{\partial X^2}-g_{(i)33}\frac{\partial^2 \Psi_{(i)}}{\partial Z^2}=0,\ i=M+2,\dots,N+M+1,\end{aligned} \tag{3.134}$$

$$\begin{aligned}&\left(f_{(i)15}+f_{(i)31}\right)\frac{\partial^2 U_{(i)}}{\partial X\,\partial Z}+f_{(i)15}\frac{\partial^2 W_{(i)}}{\partial X^2}+f_{(i)33}\frac{\partial^2 W_{(i)}}{\partial Z^2}-g_{(i)11}\frac{\partial^2 \Phi_{(i)}}{\partial X^2}\\&\quad-g_{(i)33}\frac{\partial^2 \Phi_{(i)}}{\partial Z^2}-\mu_{(i)11}\frac{\partial^2 \Psi_{(i)}}{\partial X^2}-\mu_{(i)33}\frac{\partial^2 \Psi_{(i)}}{\partial Z^2}=0,\ i=M+2,\dots,N+M+1,\end{aligned} \tag{3.135}$$

where $\lambda_{(i)}$ stands for the dimensionless punch speed relative to the i^{th} layer and it is specified as

$$\lambda_{(i)}=\frac{V}{\sqrt{c_{(i)44}/\rho_{(i)}}},\quad i=1,\dots,N+M+1. \tag{3.136}$$

Application of Fourier transformation in X-direction degrades the governing PDEs into ordinary differential equations and then, the general solutions of displacement, electric and magnetic fields

$$U_{(i)}\left(X,Z\right)=\frac{1}{2\pi}\int_{-\infty}^{\infty}\sum_{j=1}^{k}G_{(i)j}e^{\left(s_{(i)j}Z+I\zeta X\right)}d\zeta,\ -\infty<X<\infty,\quad \begin{array}{c} i=1,\ k=2, \\ i=2,...,M+1,\ k=4, \\ i=M+2,...,N+M+1,\ k=8, \end{array} \tag{3.137}$$

$$W_{(i)}\left(X,Z\right)=\frac{1}{2\pi}\int_{-\infty}^{\infty}\sum_{j=1}^{k}G_{(i)j}F_{(i)j}e^{\left(s_{(i)j}Z+I\zeta X\right)}d\zeta,\ -\infty<X<\infty,\quad \begin{array}{c} i=1,\ k=2, \\ i=2,...,M+1,\ k=4, \\ i=M+2,...,N+M+1,\ k=8, \end{array} \tag{3.138}$$

$$\Phi_{(i)}\left(X,Z\right)=\frac{1}{2\pi}\int_{-\infty}^{\infty}\sum_{j=1}^{k}G_{(i)j}R_{(i)j}e^{\left(s_{(i)j}Z+I\zeta X\right)}d\zeta,\ -\infty<X<\infty,\ i=M+2,...,N+M+1,\ k=8, \tag{3.139}$$

$$\Psi_{(i)}\left(X,Z\right)=\frac{1}{2\pi}\int_{-\infty}^{\infty}\sum_{j=1}^{k}G_{(i)j}Y_{(i)j}e^{\left(s_{(i)j}Z+I\zeta X\right)}d\zeta,\ -\infty<X<\infty,\ i=M+2,...,N+M+1,\ k=8, \tag{3.140}$$

are obtained. $s_{(i)j}$ are the j^{th} root of the characteristic equation of i^{th} layer and ζ is the transformation variable. Eqs. (3.130) and (3.131) are rewritten in the matrix form.

$$\begin{vmatrix} -\zeta^2(c_{(i)11}-\lambda_{(i)}^2c_{(i)44})+s_{(i)}^2c_{(i)44} & I\zeta s_{(i)}(c_{(i)13}+c_{(i)44}) \\ I\zeta s_{(i)}(c_{(i)13}+c_{(i)44}) & -\zeta^2c_{(i)44}(1-\lambda_{(i)}^2)+s_{(i)}^2c_{(i)33} \end{vmatrix}=0,\ i=1,...,M+1. \tag{3.141}$$

$s_{(i)j}$ for elastic layers are explicitly given by:

$$s_{(1)1}=-\frac{\sqrt{2}}{2}\frac{\sqrt{\varphi_{(1)1}+\sqrt{\varphi_{(1)2}}}}{\varphi_{(1)3}}\left|\zeta\right|,\ \ s_{(1)2}=-\frac{\sqrt{2}}{2}\frac{\sqrt{\varphi_{(1)1}-\sqrt{\varphi_{(1)2}}}}{\varphi_{(1)3}}\left|\zeta\right|, \tag{3.142}$$

$$s_{(i)1}=\frac{\sqrt{2}}{2}\frac{\sqrt{\varphi_{(i)1}+\sqrt{\varphi_{(i)2}}}}{\varphi_{(i)3}}|\zeta|,\ \ s_{(i)2}=-\frac{\sqrt{2}}{2}\frac{\sqrt{\varphi_{(i)1}+\sqrt{\varphi_{(i)2}}}}{\varphi_{(i)3}}|\zeta|,\ \ i=2,...,M+1, \quad (3.143)$$

$$s_{(i)3}=\frac{\sqrt{2}}{2}\frac{\sqrt{\varphi_{(i)1}-\sqrt{\varphi_{(i)2}}}}{\varphi_{(i)3}}|\zeta|,\ \ s_{(i)4}=-\frac{\sqrt{2}}{2}\frac{\sqrt{\varphi_{(i)1}-\sqrt{\varphi_{(i)2}}}}{\varphi_{(i)3}}|\zeta|,\ \ i=2,...,M+1, \quad (3.144)$$

$$\varphi_{(i)1}=-\lambda_{(i)}^2c_{(i)33}c_{(i)44}-\lambda_{(i)}^2c_{(i)44}^2+c_{(i)11}c_{(i)33}-c_{(i)13}^2-2c_{(i)13}c_{(i)44},\quad i=1,...,M+1, \quad (3.145)$$

$$\begin{aligned}\varphi_{(i)2}=&\ \lambda_{(i)}^4c_{(i)33}^2c_{(i)44}^2-2\lambda_{(i)}^4c_{(i)33}c_{(i)44}^3+\lambda_{(i)}^4c_{(i)44}^4-2\lambda_{(i)}^2c_{(i)11}c_{(i)33}^2c_{(i)44}+2\lambda_{(i)}^2c_{(i)11}c_{(i)33}c_{(i)44}^2\\&+4c_{(i)13}^2c_{(i)44}^2\ +2\lambda_{(i)}^2c_{(i)13}^2c_{(i)33}c_{(i)44}+2\lambda_{(i)}^2c_{(i)13}^2c_{(i)44}^2+4\lambda_{(i)}^2c_{(i)13}c_{(i)33}^2c_{(i)44}+4\lambda_{(i)}^2c_{(i)13}c_{(i)44}^3\\&+4\lambda_{(i)}^2c_{(i)33}c_{(i)44}^3+c_{(i)11}^2c_{i33}^2-2c_{(i)11}c_{(i)13}^2c_{(i)33}-4c_{(i)11}c_{(i)13}c_{(i)33}c_{(i)44}-4c_{(i)11}c_{(i)33}c_{(i)44}^2\\&+c_{(i)13}^4+4c_{(i)13}^3c_{(i)44},\ i=1,\ldots,M+1,\end{aligned}$$

(3.146)

$$\varphi_{(i)3}=\sqrt{c_{(i)33}c_{(i)44}},\quad i=1,...,M+1, \quad (3.147)$$

$$\Re\left(s_{11},s_{12}\right)<0,\ \Re\left(s_{i1},s_{i3}\right)>0,\ \Re\left(s_{i2},s_{i4}\right)<0,\quad i=2,...,M+1. \quad (3.148)$$

For MEE layers, Eqs. (3.132)-(3.135) in matrix form

$$\begin{vmatrix}-\zeta^2(c_{(i)11}-\lambda_{(i)}^2c_{(i)44})+s_{(i)}^2c_{(i)44} & I\zeta s_{(i)}(c_{(i)13}+c_{(i)44}) & I\zeta s_{(i)}(e_{(i)15}+e_{(i)31}) & I\zeta s_{(i)}(f_{(i)15}+f_{(i)31})\\ I\zeta s_{(i)}(c_{(i)13}+c_{(i)44}) & -\zeta^2c_{(i)44}(1-\lambda_{(i)}^2)+s_{(i)}^2c_{(i)33} & -\zeta^2e_{(i)15}+s_{(i)}^2e_{(i)33} & -\zeta^2f_{(i)15}+s_{(i)}^2f_{(i)33}\\ I\zeta s_{(i)}(e_{(i)15}+e_{(i)31}) & -\zeta^2e_{(i)15}+s_{(i)}^2e_{(i)33} & \zeta^2\beta_{(i)11}-s_{(i)}^2\beta_{(i)33} & \zeta^2g_{(i)11}-s_{(i)}^2g_{(i)33}\\ I\zeta s_{(i)}(f_{(i)15}+f_{(i)31}) & -\zeta^2f_{(i)15}+s_{(i)}^2f_{(i)33} & \zeta^2g_{(i)11}-s_{(i)}^2g_{(i)33} & \zeta^2\mu_{(i)11}-s_{(i)}^2\mu_{(i)33}\end{vmatrix}=0.$$

(3.149)

are provided and $s_{(i)j}$ for MEE layers are numerically calculated by inserting material properties. Note that the determinant of Eq. (3.149) leads to eight roots in total $s_{(i)j}$, (i=M+2,…,N+M+1, j=1,…,8) and the analyses on $s_{(i)j}$ reveal that there are three possibilities which may affect the displacement, electric and magnetic fields.

$$s_{i1}=n_{i1}|\zeta|,s_{i2}=-n_{i1}|\zeta|,s_{i3}=n_{i2}|\zeta|,s_{i4}=-n_{i2}|\zeta|,\ i=M+2,...,N+M+1, \quad (3.150)$$

$$s_{i5} = n_{i3}\left|\zeta\right|, s_{i6} = -n_{i3}\left|\zeta\right|, s_{i7} = n_{i4}\left|\zeta\right|, s_{i8} = -n_{i4}\left|\zeta\right|,\ i = M+2,...,N+M+1, \quad (3.151)$$

$$\Re\left(s_{(i)1}, s_{(i)3}, s_{(i)5}, s_{(i)7}\right) > 0,\ \Re\left(s_{(i)2}, s_{(i)4}, s_{(i)6}, s_{(i)8}\right) < 0,\ i = M+2,...,N+M+1. \quad (3.152)$$

These $s_{(i)j}$, (i=M+2,…,N+M+1, j=1,…,8) may be four pairs of opposite real roots, four pairs of complex conjugate roots or two pairs of opposite real roots and two pairs of complex conjugate roots depending on the properties of each MEE layer in practical computations and none of them are repeating roots (Zhou and Lee, 2012a).

The functions, $F_{(i)j}$, $R_{(i)j}$ and $Y_{(i)j}$

$$F_{(1)j} = -\frac{I\zeta s_{(1)j}\left(c_{(1)13}+c_{(1)44}\right)}{-\zeta^2 c_{(1)44}\left(1-\lambda_{(1)}^2\right)+s_{(1)j}^2 c_{(1)33}}, \quad j=1,2, \quad (3.153)$$

$$F_{(i)j} = -\frac{I\zeta s_{(i)j}\left(c_{(i)13}+c_{(i)44}\right)}{-\zeta^2 c_{(i)44}\left(1-\lambda_{(i)}^2\right)+s_{(i)j}^2 c_{(i)33}}, \quad i=2,...,M+1, \quad j=1,...,4, \quad (3.154)$$

$$\begin{Bmatrix} F_{(i)j} \\ R_{(i)j} \\ Y_{(i)j} \end{Bmatrix} = -A_{(i)j}^{-1} B_{(i)j}, \quad i = M+2,...,N+M+1, \ \ j=1,...,8. \quad (3.155)$$

$$A_{(i)j} = \begin{bmatrix} -\zeta^2 c_{(i)44}\left(1-\lambda_{(i)}^2\right)+s_{(i)j}^2 c_{(i)33} & -\zeta^2 e_{(i)15}+s_{(i)j}^2 e_{(i)33} & -\zeta^2 f_{(i)15}+s_{(i)j}^2 f_{(i)33} \\ -\zeta^2 e_{(i)15}+s_{(i)j}^2 e_{(i)33} & \zeta^2 \beta_{(i)11}-s_{(i)j}^2 \beta_{(i)33} & \zeta^2 g_{(i)11}-s_{(i)j}^2 g_{(i)33} \\ -\zeta^2 f_{(i)15}+s_{(i)j}^2 f_{(i)33} & \zeta^2 g_{(i)11}-s_{(i)j}^2 g_{(i)33} & \zeta^2 \mu_{(i)11}-s_{(i)j}^2 \mu_{(i)33} \end{bmatrix},$$

(3.156)

$$B_{(i)j} = \begin{Bmatrix} I\zeta s_{(i)j}\left(c_{(i)13}+c_{(i)44}\right) \\ I\zeta s_{(i)j}\left(e_{(i)15}+e_{(i)31}\right) \\ I\zeta s_{(i)j}\left(f_{(i)15}+f_{(i)31}\right) \end{Bmatrix}. \quad (3.157)$$

are calculated. Note that the number of roots, $s_{(i)j}$, is equal to 2, 4 and 8 for elastic substrate, i=1, elastic buffer layers, i=2,…,M+1, and MEE layers, i=M+2,…,N+M+1, respectively. Hence, the total number of unknown functions, $G_{(i)j}$ is 8N+4M+2. These functions are determined by using the interface and boundary conditions in the next section.

3.2.1 Interface Continuity and Boundary Conditions

The aim in this section is to find $G_{(i)j}$ functions in terms of $P(\zeta)$ and $Q(\zeta)$. To do that, interface continuity equations and boundary conditions are handled. As mentioned, the conditions must be equal to the number of unknown $G_{(i)j}$ which is 8N+4M+2. Between elastic layers, there is no condition for electric and magnetic fields. Hence, the continuity is assured for solely displacements and stress fields. MEE layers, on the other hand, possess electro-magnetic fields in addition to displacement and stress fields so the number of conditions at each interface is not equal.

3.2.1.1 Continuity Conditions along the Interfaces

In this part, we initially impose the continuity conditions along each interface . These continuity conditions

$$U_{(i)}\left(X, d_{(i)}\right) = U_{(i+1)}\left(X, d_{(i)}\right),\ i = 1,...,N+M,\ -\infty < X < \infty, \tag{3.158}$$

$$W_{(i)}\left(X, d_{(i)}\right) = W_{(i+1)}\left(X, d_{(i)}\right),\ i = 1,...,N+M,\ -\infty < X < \infty, \tag{3.159}$$

$$\sigma_{(i)ZZ}\left(X, d_{(i)}\right) = \sigma_{(i+1)ZZ}\left(X, d_{(i)}\right),\ i = 1,...,N+M,\ -\infty < X < \infty, \tag{3.160}$$

$$\sigma_{(i)XZ}\left(X, d_{(i)}\right) = \sigma_{(i+1)XZ}\left(X, d_{(i)}\right),\ i = 1,...,N+M,\ -\infty < X < \infty, \tag{3.161}$$

$$\Phi_{(i)}\left(X, d_{(i)}\right) = \Phi_{(i+1)}\left(X, d_{(i)}\right),\ i = M+2,...,N+M,\ -\infty < X < \infty, \tag{3.162}$$

$$\Psi_{(i)}\left(X,d_{(i)}\right)=\Psi_{(i+1)}\left(X,d_{(i)}\right),\ i=M+2,...,N+M,\ -\infty<X<\infty, \tag{3.163}$$

$$D_{(M+2)Z}\left(X,d_{(M+1)}\right)=0,\ B_{(M+2)Z}\left(X,d_{(M+1)}\right)=0,\ -\infty<X<\infty, \tag{3.164}$$

$$D_{(i)Z}\left(X,d_{(i)}\right)=D_{(i+1)Z}\left(X,d_{(i)}\right),\ i=M+2,...,N+M,\ -\infty<X<\infty, \tag{3.165}$$

$$B_{(i)Z}\left(X,d_{(i)}\right)=B_{(i+1)Z}\left(X,d_{(i)}\right),\ i=M+2,...,N+M,\ -\infty<X<\infty, \tag{3.166}$$

$$d_{(i)}=\sum_{j=i+1}^{N+M+1}h_j,\ i=1,...,N+M. \tag{3.167}$$

are satisfied in the solution. Note that, Eq. (3.164) retains the continuity in $D_{(M+2)Z}$ and $B_{(M+2)Z}$, when switching from elastic layers to MEE layers. Both quantities are equated to zero since they do not exist in elastic layers. 8N+4M unknown $G_{(i)j}$ functions are found by applying Eqs. (3.158)-(3.166) . The formulation in this section is quite different than the one in Section 3.1.1.1. Normalized unknown functions with '*' symbol as superscript are defined.

$$G^*_{(1)1}=G_{(1)1}e^{s_{(1)1}d_{(1)}},\quad G^*_{(1)2}=G_{12}e^{s_{(1)2}d_{(1)}}, \tag{3.168}$$

$$G^*_{(i+1)j}=G_{(i+1)j}e^{s_{(i+1)j}d_{(i)}},\quad i=1,...,M,\quad j=1,...,4, \tag{3.169}$$

$$G^*_{(i)j}=G_{(i)j}e^{s_{(i)j}d_{(i)}},\quad i=2,...,M,\quad j=1,...,4, \tag{3.170}$$

$$G^*_{(M+1)j}=G_{(M+1)j}e^{s_{(M+1)j}d_{(M+1)}},\quad j=1,...,4, \tag{3.171}$$

$$G^*_{(i+1)j}=G_{(i+1)j}e^{s_{(i+1)j}d_{(i)}},\quad i=M+1,...,N+M,\quad j=1,...,8, \tag{3.172}$$

$$G^*_{(i)j}=G_{(i)j}e^{s_{(i)j}d_{(i)}},\quad i=M+2,...,N+M,\quad j=1,...,8. \tag{3.173}$$

Displacements and stresses between 1st and 2nd layers are equated each other and $\{G^*_{(2)1}\quad G^*_{(2)3}\}^T$ is related to $\{G^*_{(2)2}\quad G^*_{(2)4}\}^T$.

$$\begin{Bmatrix} G^*_{(1)1} \\ G^*_{(1)2} \end{Bmatrix} = \begin{bmatrix} 1 & 1 \\ F_{(1)1} & F_{(1)2} \end{bmatrix}^{-1} \begin{bmatrix} 1 & 1 & 1 & 1 \\ F_{(2)1} & F_{(2)2} & F_{(2)3} & F_{(2)4} \end{bmatrix} \begin{Bmatrix} G^*_{(2)1} \\ G^*_{(2)2} \\ G^*_{(2)3} \\ G^*_{(2)4} \end{Bmatrix}, \tag{3.174}$$

$$\begin{bmatrix} I\zeta c_{(1)13} + s_{(1)1} F_{(1)1} c_{(1)33} & I\zeta c_{(1)13} + s_{(1)2} F_{(1)2} c_{(1)33} \\ c_{(1)44}\left(s_{(1)1} + I\zeta F_{(1)1}\right) & c_{(1)44}\left(s_{(1)2} + I\zeta F_{(1)2}\right) \end{bmatrix} \begin{Bmatrix} G^*_{(1)1} \\ G^*_{(1)2} \end{Bmatrix} = \left[r_{(2)} \right] \begin{Bmatrix} G^*_{(2)1} \\ G^*_{(2)2} \\ G^*_{(2)3} \\ G^*_{(2)4} \end{Bmatrix}, \tag{3.175}$$

$$\left[r_{(2)} \right] = \begin{bmatrix} r_{(2)1} & r_{(2)2} & r_{(2)3} & r_{(2)4} \\ r_{(2)5} & r_{(2)6} & r_{(2)7} & r_{(2)8} \end{bmatrix}, \tag{3.176}$$

$$r_{(2)1} = I\zeta c_{(2)13} + s_{(2)1} F_{(2)1} c_{(2)33},\ r_{(2)2} = I\zeta c_{(2)13} + s_{(2)2} F_{(2)2} c_{(2)33}, \tag{3.177}$$

$$r_{(2)3} = I\zeta c_{(2)13} + s_{(2)3} F_{(2)3} c_{(2)33},\ r_{(2)4} = I\zeta c_{(2)13} + s_{(2)4} F_{(2)4} c_{(2)33}, \tag{3.178}$$

$$r_{(2)5} = c_{(2)44}\left(s_{(2)1} + I\zeta F_{(2)1}\right),\ r_{(2)6} = c_{(2)44}\left(s_{(2)2} + I\zeta F_{(2)2}\right), \tag{3.179}$$

$$r_{(2)7} = c_{(2)44}\left(s_{(2)3} + I\zeta F_{(2)3}\right),\ r_{(2)8} = c_{(2)44}\left(s_{(2)4} + I\zeta F_{(2)4}\right). \tag{3.180}$$

Among $G^*_{(1)1}$, $G^*_{(1)2}$, $G^*_{(2)1}$, $G^*_{(2)2}$, $G^*_{(2)3}$ and $G^*_{(2)4}$, one can extinguish $G^*_{(1)1}$ and $G^*_{(1)2}$ and express $\{G^*_{(2)1} \quad G^*_{(2)3}\}^T$ in the form dependent on $\{G^*_{(2)2} \quad G^*_{(2)4}\}^T$, using four conditions in Eqs. (3.174) and (3.175).

$$\left[q_{(2)} \right] = \begin{bmatrix} I\zeta c_{(1)13} + s_{(1)1} F_{(1)1} c_{(1)33} & I\zeta c_{(1)13} + s_{(1)2} F_{(1)2} c_{(1)33} \\ c_{(1)44}\left(s_{(1)1} + I\zeta F_{(1)1}\right) & c_{(1)44}\left(s_{(1)2} + I\zeta F_{(1)2}\right) \end{bmatrix} \begin{bmatrix} 1 & 1 \\ F_{(1)1} & F_{(1)2} \end{bmatrix}^{-1} \begin{bmatrix} 1 & 1 & 1 & 1 \\ F_{(2)1} & F_{(2)2} & F_{(2)3} & F_{(2)4} \end{bmatrix}, \tag{3.181}$$

$$\left[q_{(2)} \right] = \begin{bmatrix} q_{(2)1} & q_{(2)2} & q_{(2)3} & q_{(2)4} \\ q_{(2)5} & q_{(2)6} & q_{(2)7} & q_{(2)8} \end{bmatrix}, \tag{3.182}$$

$$\begin{bmatrix} w_{(2)1} & w_{(2)2} \\ w_{(2)3} & w_{(2)4} \end{bmatrix} = \begin{bmatrix} q_{(2)1} - r_{(2)1} & q_{(2)3} - r_{(2)3} \\ q_{(2)5} - r_{(2)5} & q_{(2)7} - r_{(2)7} \end{bmatrix}^{-1} \begin{bmatrix} r_{(2)2} - q_{(2)2} & r_{(2)4} - q_{(2)4} \\ r_{(2)6} - q_{(2)6} & r_{(2)8} - q_{(2)8} \end{bmatrix}, \tag{3.183}$$

$$\begin{Bmatrix} G^*_{(2)1} \\ G^*_{(2)3} \end{Bmatrix} = \begin{bmatrix} e^{s_{(2)1}\left(d_{(2)}-d_{(1)}\right)} & 0 \\ 0 & e^{s_{(2)3}\left(d_{(2)}-d_{(1)}\right)} \end{bmatrix} \begin{bmatrix} w_{(2)1} & w_{(2)2} \\ w_{(2)3} & w_{(2)4} \end{bmatrix} \begin{bmatrix} e^{s_{(2)2}\left(d_{(1)}-d_{(2)}\right)} & 0 \\ 0 & e^{s_{(2)4}\left(d_{(1)}-d_{(2)}\right)} \end{bmatrix} \begin{Bmatrix} G^*_{(2)2} \\ G^*_{(2)4} \end{Bmatrix}. \tag{3.184}$$

The relation between $\{G^*_{(2)1} \quad G^*_{(2)3}\}^T$ and $\{G^*_{(2)2} \quad G^*_{(2)4}\}^T$ is derived with this way.

$$\begin{Bmatrix} G^*_{(2)1} \\ G^*_{(2)3} \end{Bmatrix} = \begin{bmatrix} z_{(2)1} & z_{(2)2} \\ z_{(2)3} & z_{(2)4} \end{bmatrix} \begin{Bmatrix} G^*_{(2)2} \\ G^*_{(2)4} \end{Bmatrix}, \tag{3.185}$$

Then, we follow the algorithm below until we reach MEE layers. At first, the displacement components are equated at the interfaces.

$$\left[K_{(i)}\right] \begin{Bmatrix} G^*_{(i)1} \\ G^*_{(i)3} \end{Bmatrix} + \left[L_{(i)}\right] \begin{Bmatrix} G^*_{(i)2} \\ G^*_{(i)4} \end{Bmatrix} = \left[M_{(i)}\right] \begin{Bmatrix} G^*_{(i+1)1} \\ G^*_{(i+1)3} \end{Bmatrix} + \left[N_{(i)}\right] \begin{Bmatrix} G^*_{(i+1)2} \\ G^*_{(i+1)4} \end{Bmatrix}, \; i = 2, ..., M, \tag{3.186}$$

$$\left[K_{(i)}\right] = \begin{bmatrix} 1 & 1 \\ F_{(i)1} & F_{(i)3} \end{bmatrix}, \; \left[L_{(i)}\right] = \begin{bmatrix} 1 & 1 \\ F_{(i)2} & F_{(i)4} \end{bmatrix}, \; i = 2, ..., M, \tag{3.187}$$

$$\left[M_{(i)}\right] = \begin{bmatrix} 1 & 1 \\ F_{(i+1)1} & F_{(i+1)3} \end{bmatrix}, \; \left[N_{(i)}\right] = \begin{bmatrix} 1 & 1 \\ F_{(i+1)2} & F_{(i+1)4} \end{bmatrix}, \; i = 2, ..., M, \tag{3.188}$$

Matrix inversion is applied in order to express $\{G^*_{(i)2} \quad G^*_{(i)4}\}^T$.

$$\begin{Bmatrix} G^*_{(i)2} \\ G^*_{(i)4} \end{Bmatrix} = \left[O_{(i)}\right]^{-1} \left[M_{(i)}\right] \begin{Bmatrix} G^*_{(i+1)1} \\ G^*_{(i+1)3} \end{Bmatrix} + \left[O_{(i)}\right]^{-1} \left[N_{(i)}\right] \begin{Bmatrix} G^*_{(i+1)2} \\ G^*_{(i+1)4} \end{Bmatrix}, \; i = 2, ..., M, \tag{3.189}$$

$$\left[O_{(i)}\right] = \left[\left[K_{(i)}\right] \begin{bmatrix} z_{(i)1} & z_{(i)2} \\ z_{(i)3} & z_{(i)4} \end{bmatrix} + \left[L_{(i)}\right] \right], \; i = 2, ..., M, \tag{3.190}$$

Secondly, the stress components are equated.

$$\left[P_{(i)}\right]\begin{Bmatrix} G^*_{(i)1} \\ G^*_{(i)3} \end{Bmatrix}+\left[R_{(i)}\right]\begin{Bmatrix} G^*_{(i)2} \\ G^*_{(i)4} \end{Bmatrix}=\left[S_{(i)}\right]\begin{Bmatrix} G^*_{(i+1)1} \\ G^*_{(i+1)3} \end{Bmatrix}+\left[T_{(i)}\right]\begin{Bmatrix} G^*_{(i+1)2} \\ G^*_{(i+1)4} \end{Bmatrix}, \quad i=2,...,M, \tag{3.191}$$

$$\left[P_{(i)}\right]=\begin{bmatrix} I\zeta c_{(i)13}+s_{(i)1}F_{(i)1}c_{(i)33} & I\zeta c_{(i)13}+s_{(i)3}F_{(i)3}c_{(i)33} \\ c_{(i)44}\left(s_{(i)1}+I\zeta F_{(i)1}\right) & c_{(i)44}\left(s_{(i)3}+I\zeta F_{(i)3}\right) \end{bmatrix}, \quad i=2,...,M, \tag{3.192}$$

$$\left[R_{(i)}\right]=\begin{bmatrix} I\zeta c_{(i)13}+s_{(i)2}F_{(i)2}c_{(i)33} & I\zeta c_{(i)13}+s_{(i)4}F_{(i)4}c_{(i)33} \\ c_{(i)44}\left(s_{(i)2}+I\zeta F_{(i)2}\right) & c_{(i)44}\left(s_{(i)4}+I\zeta F_{(i)4}\right) \end{bmatrix}, \quad i=2,...,M, \tag{3.193}$$

$$\left[S_{(i)}\right]=\begin{bmatrix} I\zeta c_{(i+1)13}+s_{(i+1)1}F_{(i+1)1}c_{(i+1)33} & I\zeta c_{(i+1)13}+s_{(i+1)3}F_{(i+1)3}c_{(i+1)33} \\ c_{(i+1)44}\left(s_{(i+1)1}+I\zeta F_{(i+1)1}\right) & c_{(i+1)44}\left(s_{(i+1)3}+I\zeta F_{(i+1)3}\right) \end{bmatrix}, \quad i=2,...,M, \tag{3.194}$$

$$\left[T_{(i)}\right]=\begin{bmatrix} I\zeta c_{(i+1)13}+s_{(i+1)2}F_{(i+1)2}c_{(i+1)33} & I\zeta c_{(i+1)13}+s_{(i+1)4}F_{(i+1)4}c_{(i+1)33} \\ c_{(i+1)44}\left(s_{(i+1)2}+I\zeta F_{(i+1)2}\right) & c_{(i+1)44}\left(s_{(i+1)4}+I\zeta F_{(i+1)4}\right) \end{bmatrix}, \quad i=2,...,M, \tag{3.195}$$

$$\begin{Bmatrix} G^*_{(i+1)1} \\ G^*_{(i+1)3} \end{Bmatrix}=\left[\left[U_{(i)}\right]-\left[S_{(i)}\right]\right]^{-1}\left[\left[T_{(i)}\right]-\left[V_{(i)}\right]\right]\begin{Bmatrix} G^*_{(i+1)2} \\ G^*_{(i+1)4} \end{Bmatrix}, \quad i=2,...,M, \tag{3.196}$$

$$\left[U_{(i)}\right]=\left[\left[P_{(i)}\right]\begin{bmatrix} z_{(i)1} & z_{(i)2} \\ z_{(i)3} & z_{(i)4} \end{bmatrix}+\left[R_{(i)}\right]\right]\left[O_{(i)}\right]^{-1}\left[M_{(i)}\right], \quad i=2,...,M, \tag{3.197}$$

$$\left[V_{(i)}\right]=\left[\left[P_{(i)}\right]\begin{bmatrix} z_{(i)1} & z_{(i)2} \\ z_{(i)3} & z_{(i)4} \end{bmatrix}+\left[R_{(i)}\right]\right]\left[O_{(i)}\right]^{-1}\left[N_{(i)}\right], \quad i=2,...,M, \tag{3.198}$$

At this point, $\{G^*_{(i+1)1} \quad G^*_{(i+1)3}\}^T$ is found in terms of $\{G^*_{(i+1)2} \quad G^*_{(i+1)4}\}^T$.

$$\left[W_{(i)}\right]=\left[\left[U_{(i)}\right]-\left[S_{(i)}\right]\right]^{-1}\left[\left[T_{(i)}\right]-\left[V_{(i)}\right]\right], \tag{3.199}$$

$$\begin{bmatrix} z_{(i+1)1} & z_{(i+1)2} \\ z_{(i+1)3} & z_{(i+1)4} \end{bmatrix} = \begin{bmatrix} e^{s_{(i+1)1}\left(d_{(i+1)}-d_{(i)}\right)} & 0 \\ 0 & e^{s_{(i+1)3}\left(d_{(i+1)}-d_{(i)}\right)} \end{bmatrix} \begin{bmatrix} W_{(i)} \end{bmatrix} \begin{bmatrix} e^{s_{(i+1)2}\left(d_{(i)}-d_{(i+1)}\right)} & 0 \\ 0 & e^{s_{(i+1)4}\left(d_{(i)}-d_{(i+1)}\right)} \end{bmatrix}, \tag{3.200}$$

$$\begin{Bmatrix} G^*_{(i+1)1} \\ G^*_{(i+1)3} \end{Bmatrix} = \begin{bmatrix} z_{(i+1)1} & z_{(i+1)2} \\ z_{(i+1)3} & z_{(i+1)4} \end{bmatrix} \begin{Bmatrix} G^*_{(i+1)2} \\ G^*_{(i+1)4} \end{Bmatrix}, \quad i = 2,...,M, \tag{3.201}$$

When the last conditions between elastic layers are involved in the algorithm, the operations change significantly. Since there are eight roots for MEE layers, eight unknown functions present in the right-hand sides of Eqs. (3.202) and (3.205). With these equations, the displacement and stress field become continuous.

$$\begin{aligned} &\begin{bmatrix} 1 & 1 \\ F_{(M+1)1} & F_{(M+1)3} \end{bmatrix} \begin{Bmatrix} G^*_{(M+1)1} \\ G^*_{(M+1)3} \end{Bmatrix} + \begin{bmatrix} 1 & 1 \\ F_{(M+1)2} & F_{(M+1)4} \end{bmatrix} \begin{Bmatrix} G^*_{(M+1)2} \\ G^*_{(M+1)4} \end{Bmatrix} = \\ &\begin{bmatrix} 1 & 1 & 1 & 1 \\ F_{(M+2)1} & F_{(M+2)3} & F_{(M+2)5} & F_{(M+2)7} \end{bmatrix} \begin{Bmatrix} G^*_{(M+2)1} \\ G^*_{(M+2)3} \\ G^*_{(M+2)5} \\ G^*_{(M+2)7} \end{Bmatrix} \\ &+ \begin{bmatrix} 1 & 1 & 1 & 1 \\ F_{(M+2)2} & F_{(M+2)4} & F_{(M+2)6} & F_{(M+2)8} \end{bmatrix} \begin{Bmatrix} G^*_{(M+2)2} \\ G^*_{(M+2)4} \\ G^*_{(M+2)6} \\ G^*_{(M+2)8} \end{Bmatrix}, \end{aligned} \tag{3.202}$$

$$\begin{Bmatrix} G^*_{(M+1)2} \\ G^*_{(M+1)4} \end{Bmatrix} = [O]^{-1} \begin{bmatrix} 1 & 1 & 1 & 1 \\ F_{(M+2)1} & F_{(M+2)3} & F_{(M+2)5} & F_{(M+2)7} \end{bmatrix} \begin{Bmatrix} G^*_{(M+2)1} \\ G^*_{(M+2)3} \\ G^*_{(M+2)5} \\ G^*_{(M+2)7} \end{Bmatrix} + [O]^{-1} \begin{bmatrix} 1 & 1 & 1 & 1 \\ F_{(M+2)1} & F_{(M+2)3} & F_{(M+2)5} & F_{(M+2)7} \end{bmatrix} \begin{Bmatrix} G^*_{(M+2)2} \\ G^*_{(M+2)4} \\ G^*_{(M+2)6} \\ G^*_{(M+2)8} \end{Bmatrix}, \tag{3.203}$$

where the matrix $[O]$ appears in displacement continuity relation and defined by

$$[O] = \left[\begin{bmatrix} 1 & 1 \\ F_{(M+1)1} & F_{(M+1)3} \end{bmatrix} \begin{bmatrix} z_{(M+1)1} & z_{(M+1)2} \\ z_{(M+1)3} & z_{(M+1)4} \end{bmatrix} + \begin{bmatrix} 1 & 1 \\ F_{(M+1)2} & F_{(M+1)4} \end{bmatrix} \right], \tag{3.204}$$

At this point, one needs stress continuity relation

$$[P] \begin{Bmatrix} G^*_{(M+1)1} \\ G^*_{(M+1)3} \end{Bmatrix} + [R] \begin{Bmatrix} G^*_{(M+1)2} \\ G^*_{(M+1)4} \end{Bmatrix} = [S] \begin{Bmatrix} G^*_{(M+2)1} \\ G^*_{(M+2)3} \\ G^*_{(M+2)5} \\ G^*_{(M+2)7} \end{Bmatrix} + [T] \begin{Bmatrix} G^*_{(M+2)2} \\ G^*_{(M+2)4} \\ G^*_{(M+2)6} \\ G^*_{(M+2)8} \end{Bmatrix}, \tag{3.205}$$

between the last elastic layer and the first MEE layer. The matrices in Eq. (3.205) $[P]$, $[R]$, $[S]$ and $[T]$ are found as follows:

$$[P] = \begin{bmatrix} I\zeta c_{(M+1)13} + s_{(M+1)1} F_{(M+1)1} c_{(M+1)33} & I\zeta c_{(M+1)13} + s_{(M+1)3} F_{(M+1)3} c_{(M+1)33} \\ c_{(M+1)44} \left(s_{(M+1)1} + I\zeta F_{(M+1)1} \right) & c_{(M+1)44} \left(s_{(M+1)3} + I\zeta F_{(M+1)3} \right) \end{bmatrix}, \tag{3.206}$$

$$[R] = \begin{bmatrix} I\zeta c_{(M+1)13} + s_{(M+1)2} F_{(M+1)2} c_{(M+1)33} & I\zeta c_{(M+1)13} + s_{(M+1)4} F_{(M+1)4} c_{(M+1)33} \\ c_{(M+1)44} \left(s_{(M+1)2} + I\zeta F_{(M+1)2} \right) & c_{(M+1)44} \left(s_{(M+1)4} + I\zeta F_{(M+1)4} \right) \end{bmatrix}, \tag{3.207}$$

$$[S] = \begin{bmatrix} S_{11} & S_{13} & S_{15} & S_{17} \\ S_{21} & S_{23} & S_{25} & S_{27} \end{bmatrix}, \quad [T] = \begin{bmatrix} T_{12} & T_{14} & T_{16} & T_{18} \\ T_{22} & T_{24} & T_{26} & T_{28} \end{bmatrix}, \tag{3.208}$$

$$S_{1i}=I\zeta c_{(M+2)13}+s_{(M+2)i}\left(F_{(M+2)i}c_{(M+2)33}+R_{(M+2)i}e_{(M+2)33}+Y_{(M+2)i}f_{(M+2)33}\right),\quad i=1,3,5,7. \tag{3.209}$$

$$S_{2i}=s_{(M+2)i}c_{(M+2)44}+I\zeta\left(F_{(M+2)i}c_{(M+2)44}+R_{(M+2)i}e_{(M+2)15}+Y_{(M+2)i}f_{(M+2)15}\right),\quad i=1,3,5,7. \tag{3.210}$$

$$T_{1i}=I\zeta c_{(M+2)13}+s_{(M+2)i}\left(F_{(M+2)i}c_{(M+2)33}+R_{(M+2)i}e_{(M+2)33}+Y_{(M+2)i}f_{(M+2)33}\right),\quad i=2,4,6,8. \tag{3.211}$$

$$T_{2i}=s_{(M+2)i}c_{(M+2)44}+I\zeta\left(F_{(M+2)i}c_{(M+2)44}+R_{(M+2)i}e_{(M+2)15}+Y_{(M+2)i}f_{(M+2)15}\right),\quad i=2,4,6,8. \tag{3.212}$$

Here, our purpose is to get a connection between $G^*_{(M+2)j}$, j=1,…,8.

$$[U]\begin{Bmatrix}G^*_{(M+2)1}\\G^*_{(M+2)3}\\G^*_{(M+2)5}\\G^*_{(M+2)7}\end{Bmatrix}+[V]\begin{Bmatrix}G^*_{(M+2)2}\\G^*_{(M+2)4}\\G^*_{(M+2)6}\\G^*_{(M+2)8}\end{Bmatrix}=[S]\begin{Bmatrix}G^*_{(M+2)1}\\G^*_{(M+2)3}\\G^*_{(M+2)5}\\G^*_{(M+2)7}\end{Bmatrix}+[T]\begin{Bmatrix}G^*_{(M+2)2}\\G^*_{(M+2)4}\\G^*_{(M+2)6}\\G^*_{(M+2)8}\end{Bmatrix}, \tag{3.213}$$

$$[U]=\left[[P]\begin{bmatrix}z_{(M+1)1}&z_{(M+1)2}\\z_{(M+1)3}&z_{(M+1)4}\end{bmatrix}+[R]\right][O]^{-1}[M], \tag{3.214}$$

$$[V]=\left[[P]\begin{bmatrix}z_{(M+1)1}&z_{(M+1)2}\\z_{(M+1)3}&z_{(M+1)4}\end{bmatrix}+[R]\right][O]^{-1}[N], \tag{3.215}$$

Now, it is time to apply Eq. (3.164) by defining [W] and [X] matrices.

$$\begin{bmatrix}[U]-[S]\\ [W]\end{bmatrix}\begin{Bmatrix}G^*_{(M+2)1}\\G^*_{(M+2)3}\\G^*_{(M+2)5}\\G^*_{(M+2)7}\end{Bmatrix}=\begin{bmatrix}[T]-[V]\\ -[X]\end{bmatrix}\begin{Bmatrix}G^*_{(M+2)2}\\G^*_{(M+2)4}\\G^*_{(M+2)6}\\G^*_{(M+2)8}\end{Bmatrix}, \tag{3.216}$$

Note that the order of two matrices in Eq. (3.216) becomes 4x4 after the latest manipulation. [W] and [X] matrices are explicitly provided as below.

$$[W]=\begin{bmatrix} W_{11} & W_{13} & W_{15} & W_{17} \\ W_{21} & W_{23} & W_{25} & W_{27} \end{bmatrix}, \quad [X]=\begin{bmatrix} X_{12} & X_{14} & X_{16} & X_{18} \\ X_{22} & X_{24} & X_{26} & X_{28} \end{bmatrix}, \tag{3.217}$$

$$W_{1i}=I\zeta e_{(M+2)31}+s_{(M+2)i}\left(F_{(M+2)i}e_{(M+2)33}-R_{(M+2)i}\beta_{(M+2)33}-Y_{(M+2)i}g_{(M+2)33}\right), \quad i=1,3,5,7. \tag{3.218}$$

$$W_{2i}=I\zeta f_{(M+2)31}+s_{(M+2)i}\left(F_{(M+2)i}f_{(M+2)33}-R_{(M+2)i}g_{(M+2)33}-Y_{(M+2)i}\mu_{(M+2)33}\right), \quad i=1,3,5,7. \tag{3.219}$$

$$X_{1i}=I\zeta e_{(M+2)31}+s_{(M+2)i}\left(F_{(M+2)i}e_{(M+2)33}-R_{(M+2)i}\beta_{(M+2)33}-Y_{(M+2)i}g_{(M+2)33}\right), \quad i=2,4,6,8. \tag{3.220}$$

$$X_{2i}=I\zeta f_{(M+2)31}+s_{(M+2)i}\left(F_{(M+2)i}f_{(M+2)33}-R_{(M+2)i}g_{(M+2)33}-Y_{(M+2)i}\mu_{(M+2)33}\right), \quad i=2,4,6,8. \tag{3.221}$$

Before jumping to the next interface, the regular manipulation is done below. Eventually, our goal of writing $\{G^*_{(M+2)1} \quad G^*_{(M+2)3} \quad G^*_{(M+2)5} \quad G^*_{(M+2)7}\}^T$ in terms of $\{G^*_{(M+2)2} \quad G^*_{(M+2)4} \quad G^*_{(M+2)6} \quad G^*_{(M+2)8}\}^T$ is accomplished. $[Z_{(M+2)}]$ is the connective matrix of these two vectors.

$$[\varsigma_1]=\begin{bmatrix} e^{s_{(M+2)1}\left(d_{(M+2)}-d_{(M+1)}\right)} & 0 & 0 & 0 \\ 0 & e^{s_{(M+2)3}\left(d_{(M+2)}-d_{(M+1)}\right)} & 0 & 0 \\ 0 & 0 & e^{s_{(M+2)5}\left(d_{(M+2)}-d_{(M+1)}\right)} & 0 \\ 0 & 0 & 0 & e^{s_{(M+2)7}\left(d_{(M+2)}-d_{(M+1)}\right)} \end{bmatrix}, \tag{3.222}$$

$$[\varsigma_2]=\begin{bmatrix} e^{s_{(M+2)2}\left(d_{(M+1)}-d_{(M+2)}\right)} & 0 & 0 & 0 \\ 0 & e^{s_{(M+2)4}\left(d_{(M+1)}-d_{(M+2)}\right)} & 0 & 0 \\ 0 & 0 & e^{s_{(M+2)6}\left(d_{(M+1)}-d_{(M+2)}\right)} & 0 \\ 0 & 0 & 0 & e^{s_{(M+2)8}\left(d_{(M+1)}-d_{(M+2)}\right)} \end{bmatrix}. \tag{3.223}$$

$$\left[Z_{(M+2)}\right]=[\varsigma_1]\begin{bmatrix}[U]-[S]\\ [W]\end{bmatrix}^{-1}\begin{bmatrix}[T]-[V]\\ -[X]\end{bmatrix}[\varsigma_2], \tag{3.224}$$

$$\begin{Bmatrix} G^*_{(M+2)1} \\ G^*_{(M+2)3} \\ G^*_{(M+2)5} \\ G^*_{(M+2)7} \end{Bmatrix}=\left[Z_{(M+2)}\right]\begin{Bmatrix} G^*_{(M+2)2} \\ G^*_{(M+2)4} \\ G^*_{(M+2)6} \\ G^*_{(M+2)8} \end{Bmatrix}, \tag{3.225}$$

After this point, the continuousness of the displacement field and electro-magnetic potentials are maintained by Eq. (3.226). The interface condition algorithm proceeds for each MEE layer as follows:

$$\left[K_{(i)}\right]\begin{Bmatrix} G^*_{(i)1} \\ G^*_{(i)3} \\ G^*_{(i)5} \\ G^*_{(i)7} \end{Bmatrix}+\left[L_{(i)}\right]\begin{Bmatrix} G^*_{(i)2} \\ G^*_{(i)4} \\ G^*_{(i)6} \\ G^*_{(i)8} \end{Bmatrix}=\left[M_{(i)}\right]\begin{Bmatrix} G^*_{(i+1)1} \\ G^*_{(i+1)3} \\ G^*_{(i+1)4} \\ G^*_{(i+1)7} \end{Bmatrix}+\left[N_{(i)}\right]\begin{Bmatrix} G^*_{(i+1)2} \\ G^*_{(i+1)4} \\ G^*_{(i+1)6} \\ G^*_{(i+1)8} \end{Bmatrix}, \quad i=M+2,\ldots,N+M, \tag{3.226}$$

where $[K_{(i)}]$, $[L_{(i)}]$, $[M_{(i)}]$ and $[N_{(i)}]$ matrices are acquired as

$$\left[K_{(i)}\right]=\begin{bmatrix} 1 & 1 & 1 & 1 \\ F_{(i)1} & F_{(i)3} & F_{(i)5} & F_{(i)7} \\ R_{(i)1} & R_{(i)3} & R_{(i)5} & R_{(i)7} \\ Y_{(i)1} & Y_{(i)3} & Y_{(i)5} & Y_{(i)7} \end{bmatrix}, \quad i=M+2,\ldots,N+M, \tag{3.227}$$

$$\left[L_{(i)}\right]=\begin{bmatrix}1 & 1 & 1 & 1\\ F_{(i)2} & F_{(i)4} & F_{(i)6} & F_{(i)8}\\ R_{(i)2} & R_{(i)4} & R_{(i)6} & R_{(i)8}\\ Y_{(i)2} & Y_{(i)4} & Y_{(i)6} & Y_{(i)8}\end{bmatrix},\ i=M+2,...,N+M, \tag{3.228}$$

$$\left[M_{(i)}\right]=\begin{bmatrix}1 & 1 & 1 & 1\\ F_{(i+1)1} & F_{(i+1)3} & F_{(i+1)5} & F_{(i+1)7}\\ R_{(i+1)1} & R_{(i+1)3} & R_{(i+1)5} & R_{(i+1)7}\\ Y_{(i+1)1} & Y_{(i+1)3} & Y_{(i+1)5} & Y_{(i+1)7}\end{bmatrix},\ i=M+2,...,N+M, \tag{3.229}$$

$$\left[N_{(i)}\right]=\begin{bmatrix}1 & 1 & 1 & 1\\ F_{(i+1)2} & F_{(i+1)4} & F_{(i+1)6} & F_{(i+1)8}\\ R_{(i+1)2} & R_{(i+1)4} & R_{(i+1)6} & R_{(i+1)8}\\ Y_{(i+1)2} & Y_{(i+1)4} & Y_{(i+1)6} & Y_{(i+1)8}\end{bmatrix},\ i=M+2,...,N+M, \tag{3.230}$$

Another matrix manipulation is done at this step in order to get rid of $\{G^*_{(i)2} \quad G^*_{(i)4} \quad G^*_{(i)6} \quad G^*_{(i)8}\}^T$ vector.

$$\begin{Bmatrix}G^*_{(i)2}\\ G^*_{(i)4}\\ G^*_{(i)6}\\ G^*_{(i)8}\end{Bmatrix}=\left[O_{(i)}\right]^{-1}\left[M_{(i)}\right]\begin{Bmatrix}G^*_{(i+1)1}\\ G^*_{(i+1)3}\\ G^*_{(i+1)5}\\ G^*_{(i+1)7}\end{Bmatrix}+\left[O_{(i)}\right]^{-1}\left[N_{(i)}\right]\begin{Bmatrix}G^*_{(i+1)2}\\ G^*_{(i+1)4}\\ G^*_{(i+1)6}\\ G^*_{(i+1)8}\end{Bmatrix},\quad i=M+2,...,N+M, \tag{3.231}$$

$$\left[O_{(i)}\right]=\left[\left[K_{(i)}\right]\left[Z_{(i)}\right]+\left[L_{(i)}\right]\right],\ \ i=M+2,...,N+M, \tag{3.232}$$

The final continuity conditions for normal and shear stresses, electric displacement and magnetic induction in *Z*-direction are given by

$$\left[P_{(i)}\right]\begin{Bmatrix}G^*_{(i)1}\\G^*_{(i)3}\\G^*_{(i)5}\\G^*_{(i)7}\end{Bmatrix}+\left[R_{(i)}\right]\begin{Bmatrix}G^*_{(i)2}\\G^*_{(i)4}\\G^*_{(i)6}\\G^*_{(i)8}\end{Bmatrix}=\left[S_{(i)}\right]\begin{Bmatrix}G^*_{(i+1)1}\\G^*_{(i+1)3}\\G^*_{(i+1)5}\\G^*_{(i+1)7}\end{Bmatrix}+\left[T_{(i)}\right]\begin{Bmatrix}G^*_{(i+1)2}\\G^*_{(i+1)4}\\G^*_{(i+1)6}\\G^*_{(i+1)8}\end{Bmatrix},\quad i=M+2,...,N+M,\tag{3.233}$$

where $[P_{(i)}]$, $[R_{(i)}]$, $[S_{(i)}]$ and $[T_{(i)}]$ are introduced by

$$\left[P_{(i)}\right]=\begin{bmatrix}I\zeta c_{(i)13}+s_{(i)1}\left(F_{(i)1}c_{(i)33}+R_{(i)1}e_{(i)33}+Y_{(i)1}f_{(i)33}\right) & ... & ... & ...\\ s_{(i)1}c_{(i)44}+I\zeta\left(F_{(i)1}c_{(i)44}+R_{(i)1}e_{(i)15}+Y_{(i)1}f_{(i)15}\right) & ... & ... & ...\\ I\zeta e_{(i)31}+s_{(i)1}\left(F_{(i)1}e_{(i)33}-R_{(i)1}\beta_{(i)33}-Y_{(i)1}g_{(i)33}\right) & ... & ... & ...\\ I\zeta f_{(i)31}+s_{(i)1}\left(F_{(i)1}f_{(i)33}-R_{(i)1}g_{(i)33}-Y_{(i)1}\mu_{(i)33}\right) & ... & ... & ...\end{bmatrix}, i=M+2,...,N+M,\tag{3.234}$$

$$\left[R_{(i)}\right]=\begin{bmatrix}I\zeta c_{(i)13}+s_{(i)2}\left(F_{(i)2}c_{(i)33}+R_{(i)2}e_{(i)33}+Y_{(i)2}f_{(i)33}\right) & ... & ... & ...\\ s_{(i)2}c_{(i)44}+I\zeta\left(F_{(i)2}c_{(i)44}+R_{(i)2}e_{(i)15}+Y_{(i)2}f_{(i)15}\right) & ... & ... & ...\\ I\zeta e_{(i)31}+s_{(i)2}\left(F_{(i)2}e_{(i)33}-R_{(i)2}\beta_{(i)33}-Y_{(i)2}g_{(i)33}\right) & ... & ... & ...\\ I\zeta f_{(i)31}+s_{(i)2}\left(F_{(i)2}f_{(i)33}-R_{(i)2}g_{(i)33}-Y_{(i)2}\mu_{(i)33}\right) & ... & ... & ...\end{bmatrix}, i=M+2,...,N+M,\tag{3.235}$$

$$\left[S_{(i-1)}\right]=\begin{bmatrix}I\zeta c_{(i)13}+s_{(i)1}\left(F_{(i)1}c_{(i)33}+R_{(i)1}e_{(i)33}+Y_{(i)1}f_{(i)33}\right) & ... & ... & ...\\ s_{(i)1}c_{(i)44}+I\zeta\left(F_{(i)1}c_{(i)44}+R_{(i)1}e_{(i)15}+Y_{(i)1}f_{(i)15}\right) & ... & ... & ...\\ I\zeta e_{(i)31}+s_{(i)1}\left(F_{(i)1}e_{(i)33}-R_{(i)1}\beta_{(i)33}-Y_{(i)1}g_{(i)33}\right) & ... & ... & ...\\ I\zeta f_{(i)31}+s_{(i)1}\left(F_{(i)1}f_{(i)33}-R_{(i)1}g_{(i)33}-Y_{(i)1}\mu_{(i)33}\right) & ... & ... & ...\end{bmatrix}, i=M+3,...,N+M+1,\tag{3.236}$$

$$\left[T_{(i-1)}\right]=\begin{bmatrix} I\zeta c_{(i)13}+s_{(i)2}\left(F_{(i)2}c_{(i)33}+R_{(i)2}e_{(i)33}+Y_{(i)2}f_{(i)33}\right) & \dots & \dots & \dots \\ s_{(i)2}c_{(i)44}+I\zeta\left(F_{(i)2}c_{(i)44}+R_{(i)2}e_{(i)15}+Y_{(i)2}f_{(i)15}\right) & \dots & \dots & \dots \\ I\zeta e_{(i)31}+s_{(i)2}\left(F_{(i)2}e_{(i)33}-R_{(i)2}\beta_{(i)33}-Y_{(i)2}g_{(i)33}\right) & \dots & \dots & \dots \\ I\zeta f_{(i)31}+s_{(i)2}\left(F_{(i)2}f_{(i)33}-R_{(i)2}g_{(i)33}-Y_{(i)2}\mu_{(i)33}\right) & \dots & \dots & \dots \end{bmatrix}, i=M+3,...,N+M+1, \tag{3.237}$$

In Eqs. (3.234)-(3.237), only the first columns of the matrices are written for brevity. When writing the second, third and fourth columns of $\left[P_{(i)}\right]$ and $\left[S_{(i)}\right]$ the second subscripts in $s_{(i)1}$, $F_{(i)1}$, $R_{(i)1}$ and $Y_{(i)1}$ in the first column will simply be replaced by 3, 5 and 7, respectively. Similarly, the second subscripts in $s_{(i)2}$, $F_{(i)2}$, $R_{(i)2}$ and $Y_{(i)2}$ in the first column in $\left[R_{(i)}\right]$ and $\left[T_{(i)}\right]$ are switched out with 4, 6 and 8 for the second, third and fourth columns. The last matrix manipulations are completed to further simplify Eqs. (3.226) and (3.233).

$$\left[U_{(i)}\right]\begin{Bmatrix} G^*_{(i+1)1} \\ G^*_{(i+1)3} \\ G^*_{(i+1)5} \\ G^*_{(i+1)7} \end{Bmatrix}+\left[V_{(i)}\right]\begin{Bmatrix} G^*_{(i+1)2} \\ G^*_{(i+1)4} \\ G^*_{(i+1)6} \\ G^*_{(i+1)8} \end{Bmatrix}=\left[S_{(i)}\right]\begin{Bmatrix} G^*_{(i+1)1} \\ G^*_{(i+1)3} \\ G^*_{(i+1)5} \\ G^*_{(i+1)7} \end{Bmatrix}+\left[T_{(i)}\right]\begin{Bmatrix} G^*_{(i+1)2} \\ G^*_{(i+1)4} \\ G^*_{(i+1)6} \\ G^*_{(i+1)8} \end{Bmatrix}, i=M+2,...,N+M, \tag{3.238}$$

$$\left[U_{(i)}\right]=\left[\left[P_{(i)}\right]\left[Z_{(i)}\right]+\left[R_{(i)}\right]\right]\left[O_{(i)}\right]^{-1}\left[M_{(i)}\right],\ i=M+2,...,N+M, \tag{3.239}$$

$$\left[V_{(i)}\right]=\left[\left[P_{(i)}\right]\left[Z_{(i)}\right]+\left[R_{(i)}\right]\right]\left[O_{(i)}\right]^{-1}\left[N_{(i)}\right],\ i=M+2,...,N+M, \tag{3.240}$$

$$\begin{Bmatrix} G^*_{(i+1)1} \\ G^*_{(i+1)3} \\ G^*_{(i+1)5} \\ G^*_{(i+1)7} \end{Bmatrix}=\left[W_{(i)}\right]\begin{Bmatrix} G^*_{(i+1)2} \\ G^*_{(i+1)4} \\ G^*_{(i+1)6} \\ G^*_{(i+1)8} \end{Bmatrix},\quad i=M+2,...,N+M, \tag{3.241}$$

$$\left[W_{(i)}\right]=\left[\left[U_{(i)}\right]-\left[S_{(i)}\right]\right]^{-1}\left[\left[T_{(i)}\right]-\left[V_{(i)}\right]\right], \quad i=M+2,\ldots,N+M, \tag{3.242}$$

Here, the normalized unknown functions with '*' superscripts are transformed one last time.

$$\left[\varsigma_{(i)1}\right]=\begin{bmatrix} e^{s_{(i+1)1}\left(d_{(i+1)}-d_{(i)}\right)} & 0 & 0 & 0 \\ 0 & e^{s_{(i+1)3}\left(d_{(i+1)}-d_{(i)}\right)} & 0 & 0 \\ 0 & 0 & e^{s_{(i+1)5}\left(d_{(i+1)}-d_{(i)}\right)} & 0 \\ 0 & 0 & 0 & e^{s_{(i+1)7}\left(d_{(i+1)}-d_{(i)}\right)} \end{bmatrix}, \; i=M+2,\ldots,N+M, \tag{3.243}$$

$$\left[\varsigma_{(i)2}\right]=\begin{bmatrix} e^{s_{(i+1)2}\left(d_{(i)}-d_{(i+1)}\right)} & 0 & 0 & 0 \\ 0 & e^{s_{(i+1)4}\left(d_{(i)}-d_{(i+1)}\right)} & 0 & 0 \\ 0 & 0 & e^{s_{(i+1)6}\left(d_{(i)}-d_{(i+1)}\right)} & 0 \\ 0 & 0 & 0 & e^{s_{(i+1)8}\left(d_{(i)}-d_{(i+1)}\right)} \end{bmatrix}, \; i=M+2,\ldots,N+M, \tag{3.244}$$

$$\left[Z_{(i+1)}\right]=\left[\varsigma_{(i)1}\right]\left[W_{(i)}\right]\left[\varsigma_{(i)2}\right], \quad i=M+2,\ldots,N+M, \tag{3.245}$$

$$\begin{Bmatrix} G^*_{(i+1)1} \\ G^*_{(i+1)3} \\ G^*_{(i+1)5} \\ G^*_{(i+1)7} \end{Bmatrix}=\left[Z_{(i+1)}\right]\begin{Bmatrix} G^*_{(i+1)2} \\ G^*_{(i+1)4} \\ G^*_{(i+1)6} \\ G^*_{(i+1)8} \end{Bmatrix}, \quad i=M+2,\ldots,N+M. \tag{3.246}$$

The algorithm ends when the counter *i* equals to *N+M*. Up to this point, the number of unknown functions is successfully dropped to four which will be determined by boundary conditions.

3.2.1.2 Boundary Conditions

The surface of the coating is exposed to air except for the contact region of the punch. Both the surface exposed to air and the contact surface are assumed to be electrically and magnetically insulated. With this assumption, the distribution of the normal stress in contact region $S(X)$ has become our only point of interest.

$$\sigma_{(N+M+1)ZZ}\left(X,0\right)=\begin{cases} S\left(X\right),\ 0<X<b, \\ 0,\ X<0,\ b<X, \end{cases} \tag{3.247}$$

$$\sigma_{(N+M+1)XZ}\left(X,0\right)=\begin{cases} \eta S\left(X\right),\ 0<X<b, \\ 0,\ X<0,\ b<X, \end{cases} \tag{3.248}$$

$$D_{(N+M+1)Z}\left(X,0\right)=0,\ \ -\infty<X<\infty, \tag{3.249}$$

$$B_{(N+M+1)Z}\left(X,0\right)=0,\ \ -\infty<X<\infty. \tag{3.250}$$

Similar to Section 3.1.1.2, $P(\zeta)$ and $Q(\zeta)$ terms are introduced and the unknown functions are written in terms of them.

$$\int_0^b S\left(t\right)\exp\left(-I\zeta t\right)dt=P\left(\zeta\right),\quad \int_0^b \eta S\left(t\right)\exp\left(-I\zeta t\right)dt=Q\left(\zeta\right). \tag{3.251}$$

$$\begin{Bmatrix} G_{(N+M+1)2} \\ G_{(N+M+1)4} \\ G_{(N+M+1)6} \\ G_{(N+M+1)8} \end{Bmatrix}=\left[\Theta\right]\begin{Bmatrix} P\left(\zeta\right) \\ Q\left(\zeta\right) \\ 0 \\ 0 \end{Bmatrix}, \tag{3.252}$$

where the matrix $[\Theta]$ is obtained as

$$\left[\Theta\right]=\left[\left[R_{(N+M+1)}\right]+\left[P_{(N+M+1)}\right]\left[Z_{(N+M+1)}\right]\right]^{-1}, \tag{3.253}$$

$$\left[P_{(i)}\right]=\begin{bmatrix} I\zeta c_{(i)13}+s_{(i)1}\left(F_{(i)1}c_{(i)33}+R_{(i)1}e_{(i)33}+Y_{(i)1}f_{(i)33}\right) & \ldots & \ldots & \ldots \\ s_{(i)1}c_{(i)44}+I\zeta\left(F_{(i)1}c_{(i)44}+R_{(i)1}e_{(i)15}+Y_{(i)1}f_{(i)15}\right) & \ldots & \ldots & \ldots \\ I\zeta e_{(i)31}+s_{(i)1}\left(F_{(i)1}e_{(i)33}-R_{(i)1}\beta_{(i)33}-Y_{(i)1}g_{(i)33}\right) & \ldots & \ldots & \ldots \\ I\zeta f_{(i)31}+s_{(i)1}\left(F_{(i)1}f_{(i)33}-R_{(i)1}g_{(i)33}-Y_{(i)1}\mu_{(i)33}\right) & \ldots & \ldots & \ldots \end{bmatrix},\ i=N+M+1, \tag{3.254}$$

$$\left[R_i\right]=\begin{bmatrix} I\zeta c_{(i)13}+s_{(i)2}\left(F_{(i)2}c_{(i)33}+R_{(i)2}e_{(i)33}+Y_{(i)2}f_{(i)33}\right) & \ldots & \ldots & \ldots \\ s_{(i)2}c_{(i)44}+I\zeta\left(F_{(i)2}c_{(i)44}+R_{(i)2}e_{(i)15}+Y_{(i)2}f_{(i)15}\right) & \ldots & \ldots & \ldots \\ I\zeta e_{(i)31}+s_{(i)2}\left(F_{(i)2}e_{(i)33}-R_{(i)2}\beta_{(i)33}-Y_{(i)2}g_{(i)33}\right) & \ldots & \ldots & \ldots \\ I\zeta f_{(i)31}+s_{(i)2}\left(F_{(i)2}f_{(i)33}-R_{(i)2}g_{(i)33}-Y_{(i)2}\mu_{(i)33}\right) & \ldots & \ldots & \ldots \end{bmatrix},\ i=N+M+1. \tag{3.255}$$

All $G_{(i)j}$ functions are attained in terms of $P(\zeta)$ and $Q(\zeta)$ at this stage.

3.2.2 Derivation of the Singular Integral Equation of Multiferroic Structure

The formulation in this section starts with the derivatives of displacements and electrical and magnetic potentials with respect to X-coordinate.

$$\lim_{Z\to 0}\frac{\partial W_{(N+M+1)}(X,Z)}{\partial X}=\lim_{Z\to 0}\frac{1}{2\pi}\int_{-\infty}^{\infty} I\zeta\sum_{j=1}^{8}G_{(N+M+1)j}F_{(N+M+1)j}\exp\left(s_{(N+M+1)j}Z+I\zeta X\right)d\zeta, \tag{3.256}$$

$$\lim_{Z\to 0}\frac{\partial U_{(N+M+1)}(X,Z)}{\partial X}=\lim_{Z\to 0}\frac{1}{2\pi}\int_{-\infty}^{\infty} I\zeta\sum_{j=1}^{8}G_{(N+M+1)j}\exp\left(s_{(N+M+1)j}Z+I\zeta X\right)d\zeta, \tag{3.257}$$

$$\lim_{Z\to 0}\frac{\partial \Phi_{(N+M+1)}(X,Z)}{\partial X}=\lim_{Z\to 0}\frac{1}{2\pi}\int_{-\infty}^{\infty} I\zeta\sum_{j=1}^{8}G_{(N+M+1)j}R_{(N+M+1)j}\exp\left(s_{(N+M+1)j}Z+I\zeta X\right)d\zeta, \tag{3.258}$$

$$\lim_{Z\to 0}\frac{\partial \Psi_{(N+M+1)}(X,Z)}{\partial X}=\lim_{Z\to 0}\frac{1}{2\pi}\int_{-\infty}^{\infty} I\zeta\sum_{j=1}^{8}G_{(N+M+1)j}Y_{(N+M+1)j}\exp\left(s_{(N+M+1)j}Z+I\zeta X\right)d\zeta. \tag{3.259}$$

Further refinements are made in Eqs. (3.256)-(3.259) as follows:

$$\lim_{Z\to 0}2\pi\frac{\partial W_{(N+M+1)}(X,Z)}{\partial X}=\int_{-\infty}^{\infty} J_{11}(X,Z,t)S(t)\,dt+\int_{-\infty}^{\infty}\eta J_{12}(X,Z,t)S(t)\,dt, \tag{3.260}$$

$$\lim_{Z\to 0}2\pi\frac{\partial U_{(N+M+1)}(X,Z)}{\partial X}=\int_{-\infty}^{\infty}\eta J_{21}(X,Z,t)S(t)\,dt+\int_{-\infty}^{\infty} J_{22}(X,Z,t)S(t)\,dt, \tag{3.261}$$

$$\lim_{Z\to 0}2\pi\frac{\partial \Phi_{(N+M+1)}(X,Z)}{\partial X}=\int_{-\infty}^{\infty} J_{31}(X,Z,t)S(t)\,dt+\int_{-\infty}^{\infty}\eta J_{32}(X,Z,t)S(t)\,dt, \tag{3.262}$$

$$\lim_{Z\to 0}2\pi\frac{\partial \Psi_{(N+M+1)}(X,Z)}{\partial X}=\int_{-\infty}^{\infty} J_{41}(X,Z,t)S(t)\,dt+\int_{-\infty}^{\infty}\eta J_{42}(X,Z,t)S(t)\,dt, \tag{3.263}$$

where the functions J_{ij}, i=1,…,4, j=1,2, are defined as

$$J_{ij}(X,Z,t)=\lim_{Z\to 0}\int_{-\infty}^{\infty}\omega_{ij}(\zeta,Z)\exp\left(-I\zeta(t-Z)\right)d\zeta,\quad i=1,...,4,\quad j=1,2, \tag{3.264}$$

where $\omega_{ij}(\zeta,Z)$, i=1,…,4, j=1,2, are provided as

$$\omega_{11}(\zeta,Z)=\text{coeff}\left(I\zeta\sum_{i=1}^{8}G_{(N+M+1)i}F_{(N+M+1)i}e^{s_{(N+M+1)i}Z},P\right), \tag{3.265}$$

$$\omega_{12}(\zeta,Z)=\text{coeff}\left(I\zeta\sum_{i=1}^{8}G_{(N+M+1)i}F_{(N+M+1)i}e^{s_{(N+M+1)i}Z},Q\right), \tag{3.266}$$

$$\omega_{21}(\zeta,Z)=\text{coeff}\left(I\zeta\sum_{i=1}^{8}G_{(N+M+1)i}e^{s_{(N+M+1)i}Z},Q\right), \tag{3.267}$$

$$\omega_{22}(\zeta,Z)=\text{coeff}\left(I\zeta\sum_{i=1}^{8}G_{(N+M+1)i}e^{s_{(N+M+1)i}Z},P\right), \tag{3.268}$$

$$\omega_{31}(\zeta,Z)=\operatorname{coeff}\left(I\zeta\sum_{i=1}^{8}G_{(N+M+1)i}R_{(N+M+1)i}e^{s_{(N+M+1)i}Z},P\right),\tag{3.269}$$

$$\omega_{32}(\zeta,Z)=\operatorname{coeff}\left(I\zeta\sum_{i=1}^{8}G_{(N+M+1)i}R_{(N+M+1)i}e^{s_{(N+M+1)i}Z},Q\right),\tag{3.270}$$

$$\omega_{41}(\zeta,Z)=\operatorname{coeff}\left(I\zeta\sum_{i=1}^{8}G_{(N+M+1)i}Y_{(N+M+1)i}e^{s_{(N+M+1)i}Z},P\right),\tag{3.271}$$

$$\omega_{42}(\zeta,Z)=\operatorname{coeff}\left(I\zeta\sum_{i=1}^{8}G_{(N+M+1)i}Y_{(N+M+1)i}e^{s_{(N+M+1)i}Z},Q\right).\tag{3.272}$$

The functions in Eqs. (3.265)-(3.272) are evaluated as $\zeta\to\infty$. The results of the asymptotic analyses are as follows:

$$\omega_{i1}^{\infty}(\zeta,Z)=I\frac{\zeta}{|\zeta|}\sum_{j=1}^{4}p_{\{2i-1\}\{j\}}\exp\left(s_{(N+M+1)(2j)}Z\right),\quad i=1,\ldots,4,\tag{3.273}$$

$$\omega_{i2}^{\infty}(\zeta,Z)=\sum_{j=1}^{4}p_{\{2i\}\{j\}}\exp\left(s_{(N+M+1)(2j)}Z\right),\quad i=1,\ldots,4,\tag{3.274}$$

$$p_i=\sum_{j=1}^{4}p_{\{i\}\{j\}},\quad i=1,\ldots,8.\tag{3.275}$$

where p_i, i=1,…,8, are the asymptotic coefficients which are calculated numerically. After performing homologous calculations explained in Section 3.1.2, four integral equations are derived. Among them, Eq. (3.276) is solved for the normal contact stress $S(X)$. Lateral contact stress $\sigma_{(N+M+1)XX}$ is evaluated by utilizing Eq. (3.277) and constitutive relations. Electric displacement and magnetic induction outputs are computed using Eqs. (3.278) and (3.279) and shear stress definition.

$$p_2\eta S(X)+\frac{1}{\pi}\int_0^b\left(\frac{p_1}{t-X}+k_{11}(t,X)+\eta k_{12}(t,X)\right)S(t)\,dt=\frac{\partial W_{(N+M+1)}(X,0)}{\partial X},\quad -\infty<X<\infty,\tag{3.276}$$

$$p_4 S(X)+\frac{1}{\pi}\int_0^b\left(\frac{p_3\eta}{t-X}+\eta k_{21}(t,X)+k_{22}(t,X)\right)S(t)\,dt = \frac{\partial U_{(N+M+1)}(X,0)}{\partial X},\ -\infty < X < \infty, \tag{3.277}$$

$$p_6\eta S(X)+\frac{1}{\pi}\int_0^b\left(\frac{p_5}{t-X}+k_{31}(t,X)+\eta k_{32}(t,X)\right)S(t)\,dt = \frac{\partial \Phi_{(N+M+1)}(X,0)}{\partial X},\ -\infty < X < \infty, \tag{3.278}$$

$$p_8\eta S(X)+\frac{1}{\pi}\int_0^b\left(\frac{p_7}{t-X}+k_{41}(t,X)+\eta k_{42}(t,X)\right)S(t)\,dt = \frac{\partial \Psi_{(N+M+1)}(X,0)}{\partial X},\ -\infty < X < \infty, \tag{3.279}$$

The kernels k_{ij}, i=1,…,4, j=1,2, are called as Fredholm kernels and written as

$$k_{11}(t,X)=\int_0^\infty\left(h_{11}(\zeta)-p_1\right)\sin\left(\zeta(t-X)\right)d\zeta, \tag{3.280}$$

$$k_{12}(t,Y)=\int_0^\infty\left(h_{12}(\zeta)-p_2\right)\cos\left(\zeta(t-Y)\right)d\zeta, \tag{3.281}$$

$$k_{21}(t,Y)=\int_0^\infty\left(h_{21}(\zeta)-p_3\right)\sin\left(\zeta(t-Y)\right)d\zeta, \tag{3.282}$$

$$k_{22}(t,Y)=\int_0^\infty\left(h_{22}(\zeta)-p_4\right)\cos\left(\zeta(t-Y)\right)d\zeta. \tag{3.283}$$

$$k_{31}(t,X)=\int_0^\infty\left(h_{31}(\zeta)-p_5\right)\sin\left(\zeta(t-X)\right)d\zeta, \tag{3.284}$$

$$k_{32}(t,Y)=\int_0^\infty\left(h_{32}(\zeta)-p_6\right)\cos\left(\zeta(t-Y)\right)d\zeta, \tag{3.285}$$

$$k_{41}(t,Y)=\int_0^{\infty}\left(h_{41}(\zeta)-p_7\right)\sin\left(\zeta(t-Y)\right)d\zeta, \tag{3.286}$$

$$k_{42}(t,Y)=\int_0^{\infty}\left(h_{42}(\zeta)-p_8\right)\cos\left(\zeta(t-Y)\right)d\zeta. \tag{3.287}$$

The integrands of the kernels of the singular integral equation are given by

$$h_{ij}(\zeta)=\lim_{Z\to 0}\omega_{ij}(\zeta,Z),\ i=1,\ldots,4,\ j=1,2, \tag{3.288}$$

The impact of punch profile on the contact region is critical. Flat, triangular and semi-circular punches lead contact region to restrict in $0 < Y < b$, while for circular punch problem, the region is squeezed in $-a < Y < b$. The punch force equilibrium equation

$$\int_0^{b} S(t)\,dt=-P \tag{3.289}$$

is also implemented in the formulation since it is an essential condition in fulfilling the physical requirements.

3.2.3 Derivation of Lateral Contact Stress, Electric Displacement and Magnetic Induction

In order to obtain $\sigma_{(N+M+1)XX}$, $D_{(N+M+1)X}$ and $B_{(N+M+1)X}$, the following calculations are done as separate parts. The calculation steps of lateral stress are primarily summarized below.

$$\begin{aligned}\sigma_{(N+M+1)XX}(X,0)=&\,c_{(N+M+1)11}\frac{\partial U_{(N+M+1)}}{\partial X}+c_{(N+M+1)13}\frac{\partial W_{(N+M+1)}}{\partial Z}\\&+e_{(N+M+1)31}\frac{\partial \Phi_{(N+M+1)}}{\partial Z}+f_{(N+M+1)31}\frac{\partial \Psi_{(N+M+1)}}{\partial Z},\end{aligned} \tag{3.290}$$

$$\sigma_{(N+M+1)ZZ}\left(X,0\right)=c_{(N+M+1)13}\frac{\partial U_{(N+M+1)}}{\partial X}+c_{(N+M+1)33}\frac{\partial W_{(N+M+1)}}{\partial Z} \\ +e_{(N+M+1)33}\frac{\partial \Phi_{(N+M+1)}}{\partial Z}+f_{(N+M+1)33}\frac{\partial \Psi_{(N+M+1)}}{\partial Z}, \tag{3.291}$$

$$D_{(N+M+1)Z}\left(X,0\right)=e_{(N+M+1)31}\frac{\partial U_{(N+M+1)}}{\partial X}+e_{(N+M+1)33}\frac{\partial W_{(N+M+1)}}{\partial Z} \\ -\beta_{(N+M+1)33}\frac{\partial \Phi_{(N+M+1)}}{\partial Z}-g_{(N+M+1)33}\frac{\partial \Psi_{(N+M+1)}}{\partial Z}, \tag{3.292}$$

$$B_{(N+M+1)Z}\left(X,0\right)=f_{(N+M+1)31}\frac{\partial U_{(N+M+1)}}{\partial X}+f_{(N+M+1)33}\frac{\partial W_{(N+M+1)}}{\partial Z} \\ -g_{(N+M+1)33}\frac{\partial \Phi_{(N+M+1)}}{\partial Z}-\mu_{(N+M+1)33}\frac{\partial \Psi_{(N+M+1)}}{\partial Z}. \tag{3.293}$$

where $\sigma_{(N+M+1)ZZ}(X,0)$ and $\partial U_{(N+M+1)}/\partial X$ are known from the numerical solution of the singular integral equation and Eq. (3.277), respectively. At the coating surface, electro-magnetic insulation occurs owing to $D_{(N+M+1)Z}(X,0)=B_{(N+M+1)Z}(X,0)=0$ conditions. Thus, one can write these relations in matrix form.

$$\begin{Bmatrix} \dfrac{\partial W_{(N+M+1)}}{\partial Z} \\ \dfrac{\partial \Phi_{(N+M+1)}}{\partial Z} \\ \dfrac{\partial \Psi_{(N+M+1)}}{\partial Z} \end{Bmatrix}=\begin{bmatrix} c_{(N+M+1)33} & e_{(N+M+1)33} & f_{(N+M+1)33} \\ e_{(N+M+1)33} & -\beta_{(N+M+1)33} & -g_{(N+M+1)33} \\ f_{(N+M+1)33} & -g_{(N+M+1)33} & -\mu_{(N+M+1)33} \end{bmatrix}^{-1}\begin{Bmatrix} \sigma_{(N+M+1)ZZ}\left(X,0\right) \\ 0 \\ 0 \end{Bmatrix} \\ -\begin{bmatrix} c_{(N+M+1)33} & e_{(N+M+1)33} & f_{(N+M+1)33} \\ e_{(N+M+1)33} & -\beta_{(N+M+1)33} & -g_{(N+M+1)33} \\ f_{(N+M+1)33} & -g_{(N+M+1)33} & -\mu_{(N+M+1)33} \end{bmatrix}^{-1}\begin{Bmatrix} c_{(N+M+1)13} \\ e_{(N+M+1)31} \\ f_{(N+M+1)31} \end{Bmatrix}\begin{Bmatrix} \dfrac{\partial U_{(N+M+1)}}{\partial X} \end{Bmatrix}. \tag{3.294}$$

The terms in $\{\partial W_{(N+M+1)}/\partial Z \quad \partial \Phi_{(N+M+1)}/\partial Z \quad \partial \Psi_{(N+M+1)}/\partial Z\}^T$ are computed utilizing Eq. (3.294) as dependent on $\sigma_{(N+M+1)ZZ}(X,0)$ and $\partial U_{(N+M+1)}/\partial X$ and the stress in X-direction in Eq. (3.290) is updated as below.

$$\sigma_{(N+M+1)XX}\left(X,0\right)=\frac{p_3 p_{10}\eta}{\pi}\int_{-1}^{1}\frac{S_{ZZ}\left(t\right)}{t-X}dt+\left(p_9+p_4 p_{10}\right)S_{ZZ}\left(X\right)$$
$$+\frac{p_{10}}{\pi}\int_{-1}^{1}\left[\eta K_{21}\left(t,X\right)+K_{22}\left(t,X\right)\right]S_{ZZ}\left(t\right)dt,\ \ -\infty<X<\infty, \tag{3.295}$$

where p_9 and p_{10} are defined as

$$p_9=c_{(N+M+1)13}\Delta_{111}+e_{(N+M+1)31}\Delta_{121}+f_{(N+M+1)31}\Delta_{131}, \tag{3.296}$$

$$p_{10}=c_{(N+M+1)11}-c_{(N+M+1)13}\Delta_{21}-e_{(N+M+1)31}\Delta_{22}-f_{(N+M+1)31}\Delta_{23}, \tag{3.297}$$

$$\begin{bmatrix}\Delta_{111} & \Delta_{112} & \Delta_{113}\\ \Delta_{121} & \Delta_{122} & \Delta_{123}\\ \Delta_{131} & \Delta_{132} & \Delta_{133}\end{bmatrix}=\begin{bmatrix}c_{(N+M+1)33} & e_{(N+M+1)33} & f_{(N+M+1)33}\\ e_{(N+M+1)33} & -\beta_{(N+M+1)33} & -g_{(N+M+1)33}\\ f_{(N+M+1)33} & -g_{(N+M+1)33} & -\mu_{(N+M+1)33}\end{bmatrix}^{-1}, \tag{3.298}$$

$$\begin{Bmatrix}\Delta_{21}\\ \Delta_{22}\\ \Delta_{23}\end{Bmatrix}=\begin{bmatrix}c_{(N+M+1)33} & e_{(N+M+1)33} & f_{(N+M+1)33}\\ e_{(N+M+1)33} & -\beta_{(N+M+1)33} & -g_{(N+M+1)33}\\ f_{(N+M+1)33} & -g_{(N+M+1)33} & -\mu_{(N+M+1)33}\end{bmatrix}^{-1}\begin{Bmatrix}c_{(N+M+1)13}\\ e_{(N+M+1)31}\\ f_{(N+M+1)31}\end{Bmatrix}. \tag{3.299}$$

Electro-magnetic outputs are found from another set of equations as explained by the procedures below.

$$D_{(N+M+1)X}\left(X,0\right)=e_{(N+M+1)15}\left(\frac{\partial U_{(N+M+1)}}{\partial Z}+\frac{\partial W_{(N+M+1)}}{\partial X}\right)-\beta_{(N+M+1)11}\frac{\partial \Phi_{(N+M+1)}}{\partial X}$$
$$-g_{(N+M+1)11}\frac{\partial \Psi_{(N+M+1)}}{\partial X}, \tag{3.300}$$

$$B_{(N+M+1)X}\left(X,0\right)=f_{(N+M+1)15}\left(\frac{\partial U_{(N+M+1)}}{\partial Z}+\frac{\partial W_{(N+M+1)}}{\partial X}\right)-g_{(N+M+1)11}\frac{\partial \Phi_{(N+M+1)}}{\partial X}$$
$$-\mu_{(N+M+1)11}\frac{\partial \Psi_{(N+M+1)}}{\partial X}. \tag{3.301}$$

Here, electric displacement and magnetic induction are defined by Eqs. (3.300) and

(3.301). The only unknown term in these equations is $\partial U_{(N+M+1)}/\partial Z$ and this term is found from shear stress equation below.

$$\begin{aligned}\sigma_{(N+M+1)XZ}(X,0)&=c_{(N+M+1)44}\left(\frac{\partial U_{(N+M+1)}}{\partial Z}+\frac{\partial W_{(N+M+1)}}{\partial X}\right)+e_{(N+M+1)15}\frac{\partial \Phi_{(N+M+1)}}{\partial X}\\&+f_{(N+M+1)15}\frac{\partial \Psi_{(N+M+1)}}{\partial X}=\eta\sigma_{(N+M+1)ZZ}(X,0)\end{aligned}\tag{3.302}$$

Since shear stress acting on the contact region is related to normal stress through Coulomb's friction law $\left(\sigma_{(N+M+1)XZ}(X,0)=\eta\sigma_{(N+M+1)ZZ}(X,0)\right)$, one can write the following relation.

$$\begin{aligned}\frac{\partial U_{(N+M+1)}}{\partial Z}&=\frac{\eta\sigma_{(N+M+1)ZZ}}{c_{(N+M+1)44}}-\frac{\partial W_{(N+M+1)}}{\partial X}-\frac{e_{(N+M+1)15}}{c_{(N+M+1)44}}\frac{\partial \Phi_{(N+M+1)}}{\partial X}\\&-\frac{f_{(N+M+1)15}}{c_{(N+M+1)44}}\frac{\partial \Psi_{(N+M+1)}}{\partial X}.\end{aligned}\tag{3.303}$$

When Eq. (3.303) is substituted in Eqs. (3.300) and (3.301), electro-magnetic outputs are derived.

$$\begin{aligned}D_{(N+M+1)X}(X,0)&=-\frac{(p_{12}p_5+p_{13}p_7)p_{16}}{\pi}\int_{-1}^{1}\frac{S_{ZZ}(t)}{t-X}dt\\&+\eta p_{16}(p_{11}-p_{12}p_6-p_{13}p_8)S_{ZZ}(X)\\&-\frac{p_{12}p_{16}}{\pi}\int_{-1}^{1}\left[K_{31}(t,X)+\eta K_{32}(t,X)\right]S_{ZZ}(t)dt\\&-\frac{p_{13}p_{16}}{\pi}\int_{-1}^{1}\left[K_{41}(t,X)+\eta K_{42}(t,X)\right]S_{ZZ}(t)dt,\quad -\infty<X<\infty,\end{aligned}\tag{3.304}$$

$$\begin{aligned}B_{(N+M+1)X}(X,0)&=-\frac{(p_{13}p_5+p_{15}p_7)p_{17}}{\pi}\int_{-1}^{1}\frac{S_{ZZ}(t)}{t-X}dt\\&+\eta p_{17}(p_{14}-p_{13}p_6-p_{15}p_8)S_{ZZ}(X)\\&-\frac{p_{13}p_{17}}{\pi}\int_{-1}^{1}\left[K_{31}(t,X)+\eta K_{32}(t,X)\right]S_{ZZ}(t)dt\\&-\frac{p_{15}p_{17}}{\pi}\int_{-1}^{1}\left[K_{41}(t,X)+\eta K_{42}(t,X)\right]S_{ZZ}(t)dt,\quad -\infty<X<\infty.\end{aligned}\tag{3.305}$$

where the constants, p_i, i=11,…,15, are provided as

$$p_{11} = \frac{e_{(N+M+1)15}}{c_{(N+M+1)44}},\ p_{12} = \frac{e^2_{(N+M+1)15}}{c_{(N+M+1)44}} + \beta_{(N+M+1)11}, \tag{3.306}$$

$$p_{13} = \frac{e_{(N+M+1)15} f_{(N+M+1)15}}{c_{(N+M+1)44}} + g_{(N+M+1)11},\ p_{14} = \frac{f_{(N+M+1)15}}{c_{(N+M+1)44}}, \tag{3.307}$$

$$p_{15} = \frac{f^2_{(N+M+1)15}}{c_{(N+M+1)44}} + \mu_{(N+M+1)11}. \tag{3.308}$$

CHAPTER 4

NUMERICAL SOLUTION OF SINGULAR INTEGRAL EQUATION

In this chapter, our focus is on the numerical methods for the solutions of different punch problems. Orthogonal polynomial expansions by favour of Jacobi polynomials with appropriate weight functions are described for four punch profiles. In what follows, a collocation tecnique is applied to calculate the coefficients of orthogonal polynomial expansion.

4.1 Flat Punch Problem

Underneath the flat punch, normal displacement remains constant in the moving coordinate. The derivative of the normal displacement then becomes zero in the contact region. At both end points, we observe sharp peaks in the displacement of the uppermost layer.

4.1.1 Multi-layer Model

Figure 4.1 depicts the elastic structure loaded by moving flat punch. The problem is also called as complete contact problem as the contact region is not affected by the applied force.

$$\frac{\partial U_{(N+1)}\left(0,Y\right)}{\partial Y}=0, \quad 0<Y<b. \tag{4.1}$$

In the solution of singular integral equation, we first normalize the interval in Y-coordinate to -1 and 1. Variables and functions are also affected by this normalization. New variables and functions are provided below.

$$Y=\frac{b}{2}s+\frac{b}{2},\ t=\frac{b}{2}r+\frac{b}{2},\ K_{ij}\left(r,s\right)=\frac{b}{2}k_{ij}\left(\frac{b}{2}r+\frac{b}{2},\frac{b}{2}s+\frac{b}{2}\right),\ i=1,2,\ j=1,2, \quad (4.2)$$

$$\frac{S\left(Y\right)}{P/b}=\frac{S\left(\frac{b}{2}s+\frac{b}{2}\right)}{P/b}=S_{XX}\left(s\right). \quad (4.3)$$

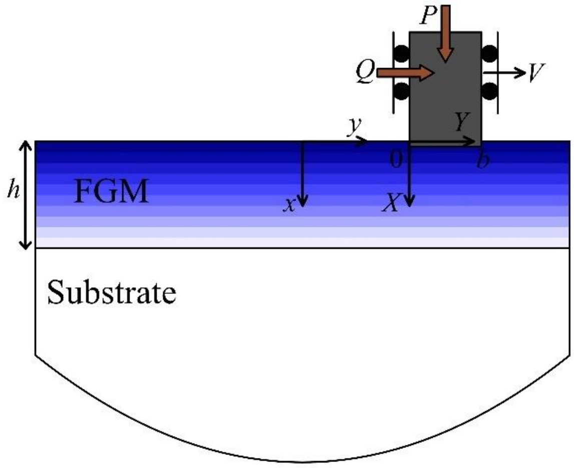

Figure 4.1. A moving rigid flat punch on FGM coating with arbitrary spatial variations of material properties.

These normalized quantities form the new version of singular integral equation.

$$\eta p_2 S_{XX}\left(s\right)+\frac{1}{\pi}\int_{-1}^{1}\left(\frac{p_1}{r-s}+K_{11}\left(r,s\right)+\eta K_{12}\left(r,s\right)\right)S_{XX}\left(r\right)dr=0,\quad -1<s<1. \quad (4.4)$$

Equilibrium equation is also updated as below:

$$\int_{-1}^{1}S_{XX}\left(r\right)dr=-2. \quad (4.5)$$

According to the function theoretic analysis (Dag, 2001), the unknown normal stress is expanded into the series of Jacobi polynomials.

$$S_{XX}\left(s\right)=w\left(s\right)\sum_{n=0}^{\infty}A_n P_n^{(\alpha_1,\alpha_2)}(s),\quad -1<s<1, \quad (4.6)$$

$$w(s)=(1-s)^{\alpha_1}(1+s)^{\alpha_2}. \tag{4.7}$$

where A_n represents the unknown coefficients, $P_n^{(\alpha_1,\alpha_2)}(s)$ is the n^{th} order Jacobi polynomial, and $w(s)$ is the weight function. The normal stress $S_{XX}(s)$ possesses singularities at the end points. The powers of the stress singularities are obtained by function theoretic method (Erdogan, 1978).

$$\alpha_1=\frac{1}{\pi}\operatorname{arccot}\left(-\frac{\eta p_2}{p_1}\right),\ \alpha_2=\frac{1}{\pi}\operatorname{arccot}\left(\frac{\eta p_2}{p_1}\right). \tag{4.8}$$

Note that both α_1 and α_2 are negative and in between $-1 < (\alpha_1,\alpha_2) < 0$ because of the sharp end points of the flat punch. When Eq. (4.6) is substituted into the normalized singular integral equation, the following functional expression is found.

$$\sum_{n=0}^{\infty}A_n\left\{-\frac{p_1}{2\sin(\pi\alpha_1)}P_{n-1}^{(-\alpha_1,-\alpha_2)}(s)+\frac{1}{\pi}\left[Z_{1n}(s)+Z_{2n}(s)\right]\right\}=0,\ -1<s<1, \tag{4.9}$$

$$Z_{1n}(s)=\int_{-1}^{1}K_{11}(r,s)w(r)P_n^{(\alpha_1,\alpha_2)}(r)dr,\ Z_{2n}(s)=\eta\int_{-1}^{1}K_{12}(r,s)w(r)P_n^{(\alpha_1,\alpha_2)}(r)dr. \tag{4.10}$$

Using orthogonality properties of Jacobi polynomials and Eq. (4.5), we calculate the first coefficient of expansion A_0.

$$A_0=-\frac{2\sin\left(\pi(1+\alpha_1)\right)}{\pi}. \tag{4.11}$$

Inserting the collocation points below into Eq. (4.9) and changing the upper limit of summation symbol with N_t convert the functional equation into a linear system in terms of unknown coefficients of expansion. Then, matrix inversion is applied and the coefficients are obtained that means all quantities can be calculated.

$$s_i=\cos\left(\frac{(2i-1)\pi}{2N_t}\right),\ \ i=1,\dots,N_t. \tag{4.12}$$

At the ends of the rigid flat punch, mode-I stress intensity factors can be calculated as

$$k_I(0) = \lim_{Y\to 0} \frac{-\sigma_{(N+1)XX}(0,Y)}{2^{\alpha_1} Y^{\alpha_2}}, \; k_I(b) = \lim_{Y\to b} \frac{-\sigma_{(N+1)XX}(0,Y)}{2^{\alpha_2}(b-Y)^{\alpha_1}}. \tag{4.13}$$

In the nondimensional form, they are expressed by

$$K_I(0) = \frac{\left(b/2\right)^{\alpha_2}}{2(P/b)} k_I(0) = -\frac{1}{2}\sum_{n=0}^{N_t} A_n P_n^{(\alpha_1,\alpha_2)}(-1), \tag{4.14}$$

$$K_I(b) = \frac{\left(b/2\right)^{\alpha_1}}{2(P/b)} k_I(b) = -\frac{1}{2}\sum_{n=0}^{N_t} A_n P_n^{(\alpha_1,\alpha_2)}(1). \tag{4.15}$$

Recall that the lateral contact stress expressed by Eq. (3.103) should be normalized in the following form.

$$\begin{aligned} S_{YY}(s) = \frac{\sigma_{(N+1)YY}(0,s)}{P/b} &= \frac{8p_3\eta}{\left(\kappa_{(N+1)}+1\right)\pi}\int_{-1}^{1}\frac{S_{XX}(r)}{r-s}dr + \frac{8p_4+\left(3-\kappa_{(N+1)}\right)}{\left(\kappa_{N+1}+1\right)} S_{XX}(s) \\ &+ \frac{8}{\left(\kappa_{(N+1)}+1\right)\pi}\int_{-1}^{1}\left[\eta K_{21}(r,s)+K_{22}(r,s)\right]S_{XX}(r)\,dr, \quad -\infty < s < \infty. \end{aligned} \tag{4.16}$$

4.1.2 Multiferroic Structure

In this section, the numerical solution procedures for multiferroic structure loaded by the flat punch are outlined. The displacement derivative dictated by the rigid flat punch is equated to Eq. (3.276). The schematic of the problem is illustrated in Figure 4.2.

$$\frac{\partial W_{(N+M+1)}(X,0)}{\partial X} = 0, \quad 0 < X < b. \tag{4.17}$$

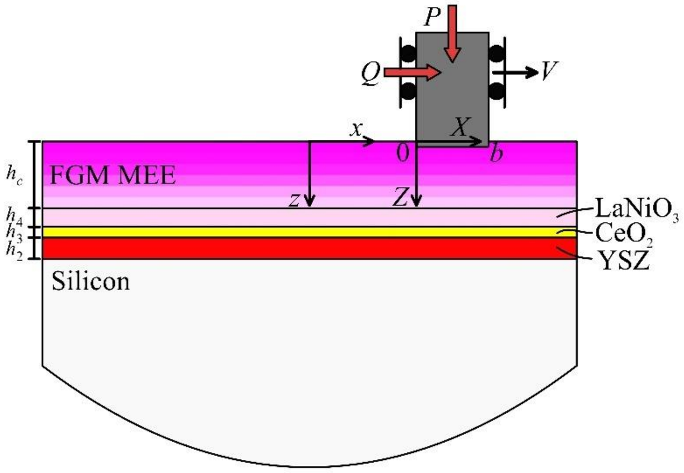

Figure 4.2. A moving rigid flat punch on FGM MEE coating with arbitrary spatial variations of material properties.

It is required to normalize the interval in X-direction from $(0,b)$ to $(-1,1)$.

$$X = \frac{b}{2}s + \frac{b}{2},\ t = \frac{b}{2}r + \frac{b}{2},\ K_{ij}(r,s) = \frac{b}{2}k_{ij}\left(\frac{b}{2}r + \frac{b}{2}, \frac{b}{2}s + \frac{b}{2}\right),\ i = 1,...,4,\ j = 1,2, \tag{4.18}$$

$$\frac{S(X)}{P/b} = \frac{S\left(\frac{b}{2}s + \frac{b}{2}\right)}{P/b} = S_{ZZ}(s). \tag{4.19}$$

The updated singular integral equation and equilibrium equation

$$\eta p_2 S_{ZZ}(s) + \frac{1}{\pi}\int_{-1}^{1}\left(\frac{p_1}{r-s} + K_{11}(r,s) + \eta K_{12}(r,s)\right)S_{ZZ}(r)\,dr = 0,\ \ -1 < s < 1. \tag{4.20}$$

$$\int_{-1}^{1} S_{ZZ}(r)\,dr = -2. \tag{4.21}$$

are provided. The normalized contact stress

$$S_{ZZ}(s) = w(s)\sum_{n=0}^{\infty} A_n P_n^{(\alpha_1,\alpha_2)}(s),\ \ -1 < s < 1. \tag{4.22}$$

is represented by the orthogonal series expansion of Jacobi polynomials. The procedures (the stress singularities, determination of A_0 and the collocation points) explained in Section 4.1.1 by Eqs. (4.7)-(4.12) are directly applied. Similar to elastic structure problem, stress intensity factors are given by the following relations.

$$k_I\left(0\right)=\lim_{X\to 0}\frac{-\sigma_{(N+M+1)ZZ}\left(X,0\right)}{2^{\alpha_1}X^{\alpha_2}},\ k_I\left(b\right)=\lim_{X\to b}\frac{-\sigma_{(N+M+1)ZZ}\left(X,0\right)}{2^{\alpha_2}\left(b-X\right)^{\alpha_1}}. \tag{4.23}$$

Recall that the only difference in stress intensity factors is caused by the usage of different coordinates and normalized versions of them are exactly the same as Eqs. (4.14) and (4.15). For multiferroic structures, electric displacement and magnetic induction are calculated in addition to lateral contact stress.

$$\begin{aligned}S_{XX}\left(s\right)&=\frac{\sigma_{(N+M+1)XX}\left(X,0\right)}{P/b}=\frac{p_3p_{10}\eta}{\pi}\int_{-1}^{1}\frac{S_{ZZ}\left(r\right)}{r-s}dr+\left(p_9+p_4p_{10}\right)S_{ZZ}\left(s\right)\\&+\frac{p_{10}}{\pi}\int_{-1}^{1}\left[\eta K_{21}\left(r,s\right)+K_{22}\left(r,s\right)\right]S_{ZZ}\left(r\right)dr,\ -\infty<s<\infty,\end{aligned} \tag{4.24}$$

$$\begin{aligned}\Omega_X\left(s\right)&=\frac{D_{(N+M+1)X}\left(X,0\right)}{P/\left(p_{16}b\right)}=-\frac{\left(p_{12}p_5+p_{13}p_7\right)p_{16}}{\pi}\int_{-1}^{1}\frac{S_{ZZ}\left(r\right)}{r-s}dr\\&+\eta p_{16}\left(p_{11}-p_{12}p_6-p_{13}p_8\right)S_{ZZ}\left(s\right)\\&-\frac{p_{12}p_{16}}{\pi}\int_{-1}^{1}\left[K_{31}\left(r,s\right)+\eta K_{32}\left(r,s\right)\right]S_{ZZ}\left(r\right)dr\\&-\frac{p_{13}p_{16}}{\pi}\int_{-1}^{1}\left[K_{41}\left(r,s\right)+\eta K_{42}\left(r,s\right)\right]S_{ZZ}\left(r\right)dr,\ -\infty<s<\infty,\end{aligned} \tag{4.25}$$

$$\begin{aligned}\Gamma_X\left(s\right)&=\frac{B_{(N+M+1)X}\left(X,0\right)}{P/\left(p_{17}b\right)}=-\frac{\left(p_{13}p_5+p_{15}p_7\right)p_{17}}{\pi}\int_{-1}^{1}\frac{S_{ZZ}\left(r\right)}{r-s}dr\\&+\eta p_{17}\left(p_{14}-p_{13}p_6-p_{15}p_8\right)S_{ZZ}\left(s\right)\\&-\frac{p_{13}p_{17}}{\pi}\int_{-1}^{1}\left[K_{31}\left(r,s\right)+\eta K_{32}\left(r,s\right)\right]S_{ZZ}\left(r\right)dr\\&-\frac{p_{15}p_{17}}{\pi}\int_{-1}^{1}\left[K_{41}\left(r,s\right)+\eta K_{42}\left(r,s\right)\right]S_{ZZ}\left(r\right)dr,\ -\infty<s<\infty.\end{aligned} \tag{4.26}$$

where p_{16} and p_{17} are the normalization constants and defined as

$$p_{16} = c_{33}(0)/e_{33}(0), \quad p_{17} = c_{33}(0)/f_{33}(0). \tag{4.27}$$

4.2 Triangular Punch Problem

The normal displacement on the uppermost layer in contact with the triangular puch is a linear function of the inclination angle of the punch in the moving coordinate. For the very reason, the displacement derivative is shown up as constant. Triangular punch indentation creates an apex in the normal displacement at the trailing end whereas the displacement at the leading end is smoothened by the inclined shape of the punch.

4.2.1 Multi-layer Model

Figure 4.3 shows the corresponding problem indented by the moving triangular shaped loading agent. The displacement derivative on the surface of the uppermost layer is given by

$$\frac{\partial U_{(N+1)}(0,Y)}{\partial Y} = -\tan(\theta), \quad 0 < Y < b. \tag{4.28}$$

where θ is the inclination angle of the punch.

The normalizations are done through the following substitutions.

$$Y = \frac{b}{2}s + \frac{b}{2},\ t = \frac{b}{2}r + \frac{b}{2},\ K_{ij}(r,s) = \frac{b}{2}k_{ij}\left(\frac{b}{2}r + \frac{b}{2}, \frac{b}{2}s + \frac{b}{2}\right),\ i = 1,2,\ j = 1,2, \tag{4.29}$$

$$\frac{S(Y)}{\mu_{(N+1)}\tan(\theta)} = \frac{S\left(\frac{b}{2}s + \frac{b}{2}\right)}{\mu_{(N+1)}\tan(\theta)} = S_{XX}(s). \tag{4.30}$$

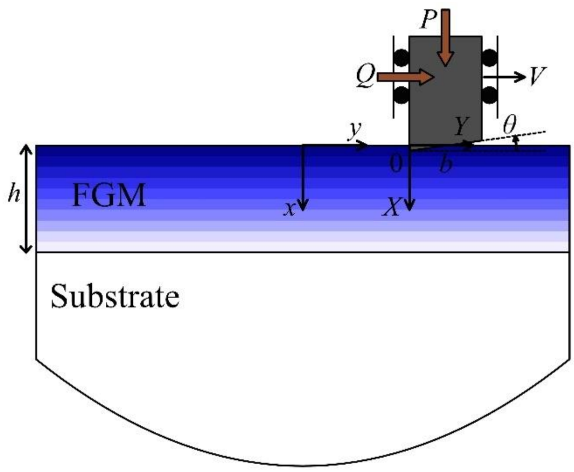

Figure 4.3. A moving rigid triangular punch on FGM coating with arbitrary spatial variations of material properties.

Singular integral equation

$$\eta p_2 S_{XX}(s)+\frac{1}{\pi}\int_{-1}^{1}\left(\frac{p_1}{r-s}+K_{11}(r,s)+\eta K_{12}(r,s)\right)S_{XX}(r)\,dr=-1,\ \ -1<s<1. \quad (4.31)$$

is rewritten in the common form. Note that the right-hand side of Eq. (4.31) is equal to -1. Then, the total punch force

$$\int_{-1}^{1} S_{XX}(r)\,dr=-\frac{2P}{\mu_{(N+1)}\tan(\theta)b}. \quad (4.32)$$

is updated. Eq. (4.32) proves that the problem is an incomplete contact, i.e., the contact length b is affected by normal punch force P. In this step, S_{XX} is expanded with Eqs. (4.6) and (4.7) but the strength of singularity at the leading end is in between $0 < \alpha_1 < 1$ this time. Because, the transition of the displacement caused by the punch indentation at the leading end is smooth. The strength of singularity at the trailing end is chosen as $\alpha_2 = -\alpha_1$. Therefore, the functional form of the integral equation turns out to be

$$\sum_{0}^{\infty} A_n \left\{ -\frac{p_1}{\sin(\pi\psi_1)} P_n^{(-\alpha_1,-\alpha_2)}(s) + \frac{1}{\pi}\left[Z_{1n}(s) + Z_{2n}(s) \right] \right\} = -1, \quad -1 < s < 1. \tag{4.33}$$

where $Z_{1n}(s)$ and $Z_{2n}(s)$ are given by Eq. (4.10). The collocation points for triangular punch indentation differ as shown below since the equilibrium equation does not provide a coefficient of expansion as it does for flat punch problem. Hence, the number of collocation points must be N_t+1.

$$s_i = \cos\left(\frac{(2i-1)\pi}{2(N_t+1)} \right), \quad i = 1,\ldots, N_t + 1. \tag{4.34}$$

Once the infinite terms in Jacobi polynomial expansion are cut at N_t and the collocation points are substituted to s terms in Eq. (4.33), the coefficients of expansion, A_n, n=0,…,N_t, are calculated. Contact stress and punch force are modified using shear modulus at the coating surface $\mu(0)$ for the last time.

$$\frac{S_{XX}(s)}{\mu(0)\tan(\theta)} = \frac{\mu_{(N+1)}}{\mu(0)}(1-s)^{\alpha_1}(1+s)^{\alpha_2}\sum_{n=0}^{N_t} A_n P_n^{(\alpha_1,\alpha_2)}(s), \tag{4.35}$$

$$\frac{P}{\mu(0)\tan(\theta)b} = \frac{\mu_{(N+1)} A_0 \pi \alpha_1}{\mu(0)\sin(\pi(1+\alpha_1))}. \tag{4.36}$$

Stress intensification occurs only at the sharp corner at Y=0 and is defined as follows:

$$k_I(0) = \lim_{Y\to 0}\left(-Y^{\alpha_1}\sigma_{(N+1)XX}(0,Y) \right) = -\mu_{(N+1)}\tan(\theta)\left(\frac{b}{2}\right)^{\alpha_1} \lim_{s\to -1}(1-s)^{\alpha_1}\sum_{n=0}^{N_t} A_n P_n^{(\alpha_1,\alpha_2)}(s). \tag{4.37}$$

The normalized version of $k_I(0)$ is found below.

$$K_I(0) = \frac{k_I(0)}{\mu(0)\tan(\theta)b^{\alpha_1}} = -\frac{\mu_{(N+1)}}{\mu(0)}\sum_{n=0}^{N_t} A_n P_n^{(\alpha_1,\alpha_2)}(-1). \tag{4.38}$$

Remember the last output of the analysis which should be obtained is the lateral contact stress in normalized form.

$$
\begin{aligned}
S_{YY}(s) = \frac{\sigma_{(N+1)YY}(0,s)}{\mu(0)\tan(\theta)} &= \frac{8p_3\eta\mu_{(N+1)}}{\left(\kappa_{(N+1)}+1\right)\pi\mu(0)}\int_{-1}^{1}\frac{S_{XX}(r)}{r-s}dr \\
&+\frac{8p_4+\left(3-\kappa_{N+1}\right)}{\left(\kappa_{(N+1)}+1\right)}\frac{\mu_{(N+1)}}{\mu(0)}S_{XX}(s) \\
&+\frac{8\mu_{(N+1)}}{\left(\kappa_{(N+1)}+1\right)\pi\mu(0)}\int_{-1}^{1}\left[\eta K_{21}(r,s)+K_{22}(r,s)\right]S_{XX}(r)dr, \quad -\infty<s<\infty.
\end{aligned}
\tag{4.39}
$$

4.2.2 Multiferroic Structure

The schematic illustration of the contact problem of multiferroic structure is shown in Figure 4.4. The displacement derivative enforced by the triangular punch

$$
\frac{\partial W_{(N+M+1)}(X,0)}{\partial X} = -\tan(\theta), \quad 0<X<b, \tag{4.40}
$$

is written and equated to Eq. (3.276). After that step, normalized variables and functions are stated as usual.

$$
X=\frac{b}{2}s+\frac{b}{2},\ t=\frac{b}{2}r+\frac{b}{2},\ K_{ij}(r,s)=\frac{b}{2}k_{ij}\left(\frac{b}{2}r+\frac{b}{2},\frac{b}{2}s+\frac{b}{2}\right),\ i=1,\ldots,4,\ j=1,2, \tag{4.41}
$$

$$
\frac{S(X)}{c_{44}(0)\tan(\theta)} = \frac{S\left(\frac{b}{2}s+\frac{b}{2}\right)}{c_{44}(0)\tan(\theta)} = S_{ZZ}(s), \tag{4.42}
$$

Singular integral equation of the triangular punch problem is normalized in the following form.

$$
\eta p_2 S_{ZZ}(s)+\frac{1}{\pi}\int_{-1}^{1}\left(\frac{p_1}{r-s}+K_{11}(r,s)+\eta K_{12}(r,s)\right)S_{ZZ}(r)dr = -\frac{1}{c_{44}(0)}, \quad -1<s<1, \tag{4.43}
$$

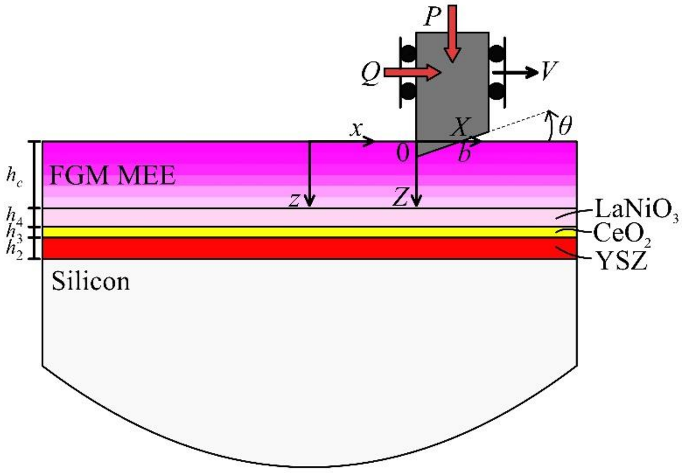

Figure 4.4. A moving rigid triangular punch on FGM MEE coating with arbitrary spatial variations of material properties.

In the next task, the punch force transferred to the multiferroic structure

$$\int_{-1}^{1} S_{ZZ}(r)\,dr = -\frac{2P}{c_{44}(0)\tan(\theta)b}, \tag{4.44}$$

is attained. After following Jacobi polynomial expansion procedures mentioned in Section 4.2.1 (recasting the normal stress using Jacobi polynomials and determination of index of singular integral equation), we are ready to reconstitute the functional form of the singular integral equation.

$$\sum_{n=0}^{\infty} A_n \left\{ -\frac{p_1}{\sin(\pi\alpha_1)} P_n^{(-\alpha_1,-\alpha_2)}(s) + \frac{1}{\pi}\left[Z_{1n}(s) + Z_{2n}(s) \right] \right\} = -\frac{1}{c_{44}(0)}, \quad -1 < s < 1. \tag{4.45}$$

Note that $c_{44}(0)$ appears as a divider in the right-hand side of Eq. (4.45). In elastic structure formulation, we do not encounter with a corresponding term. The reason is that the coefficients of integrands are taken into account considering $P/\mu_{(N+1)}$ and $Q/\mu_{(N+1)}$ terms as multipliers in elastic structure as given by Eqs. (3.65)-(3.68) whereas the formulation reckons P and Q for multiferroic structure in Eqs. (3.265)-(3.272). The definitions of $Z_{1n}(s)$ and $Z_{2n}(s)$ in this section are same as the ones given by Eq. (4.10). The relationship between the punch force and contact length is calculated utilizing orthogonal properties of Jacobi polynomials and Eq. (4.44).

$$\frac{P}{c_{44}\left(0\right)\tan\left(\theta\right)b}=\frac{A_0\pi\alpha_1}{\sin\left(\pi\left(1+\alpha_1\right)\right)}. \tag{4.46}$$

The intensity of mode-I stress caused by S_{ZZ}

$$k_I\left(0\right)=\lim_{X\to 0}\left(-X^{\alpha_1}\sigma_{(N+M+1)ZZ}\left(X,0\right)\right), \tag{4.47}$$

is conventionally quantified and updated in non-dimensional form.

$$K_I\left(-1\right)=\frac{k_I\left(0\right)}{c_{44}\left(0\right)\tan\left(\theta\right)b^{\alpha_1}}=-\sum_{n=0}^{N_t}A_n P_n^{(\alpha_1,\alpha_2)}(-1). \tag{4.48}$$

Eventually, mechanic, electric and magnetic outputs in the lateral direction representing the contact response of multiferroic heterostructures are expressed in the non-dimensional manner.

$$\begin{aligned}S_{XX}\left(s\right)&=\frac{\sigma_{(N+M+1)XX}\left(X,0\right)}{c_{44}\left(0\right)\tan\left(\theta\right)}=\frac{p_3p_{10}\eta}{\pi}\int_{-1}^{1}\frac{S_{ZZ}\left(r\right)}{r-s}dr+\left(p_9+p_4p_{10}\right)S_{ZZ}\left(s\right)\\&+\frac{p_{10}}{\pi}\int_{-1}^{1}\left[\eta K_{21}\left(r,s\right)+K_{22}\left(r,s\right)\right]S_{ZZ}\left(r\right)dr,\ -\infty<s<\infty,\end{aligned} \tag{4.49}$$

$$\begin{aligned}\Omega_X\left(s\right)&=\frac{D_{(N+M+1)X}\left(X,0\right)}{c_{44}\left(0\right)\tan\left(\theta\right)/p_{16}}=-\frac{\left(p_{12}p_5+p_{13}p_7\right)p_{16}}{\pi}\int_{-1}^{1}\frac{S_{ZZ}\left(r\right)}{r-s}dr\\&+\eta p_{16}\left(p_{11}-p_{12}p_6-p_{13}p_8\right)S_{ZZ}\left(s\right)\\&-\frac{p_{12}p_{16}}{\pi}\int_{-1}^{1}\left[K_{31}\left(r,s\right)+\eta K_{32}\left(r,s\right)\right]S_{ZZ}\left(r\right)dr\\&-\frac{p_{13}p_{16}}{\pi}\int_{-1}^{1}\left[K_{41}\left(r,s\right)+\eta K_{42}\left(r,s\right)\right]S_{ZZ}\left(r\right)dr,\ -\infty<s<\infty,\end{aligned} \tag{4.50}$$

$$\Gamma_X(s) = \frac{B_{(N+M+1)X}(X,0)}{c_{44}(0)\tan(\theta)/p_{17}} = -\frac{(p_{13}p_5 + p_{15}p_7)p_{17}}{\pi}\int_{-1}^{1}\frac{S_{ZZ}(r)}{r-s}dr$$
$$+\eta p_{17}(p_{14} - p_{13}p_6 - p_{15}p_8)S_{ZZ}(s)$$
$$-\frac{p_{13}p_{17}}{\pi}\int_{-1}^{1}\left[K_{31}(r,s)+\eta K_{32}(r,s)\right]S_{ZZ}(r)dr \tag{4.51}$$
$$-\frac{p_{15}p_{17}}{\pi}\int_{-1}^{1}\left[K_{41}(r,s)+\eta K_{42}(r,s)\right]S_{ZZ}(r)dr, \quad -\infty < s < \infty.$$

4.3 Semi-Circular Punch Problem

Normal displacement caused by semi-circular and circular punches on the surface of the coating is a quadratic function of lateral coordinate. Hence, the displacement derivative turns out to be a linear function. Note that this assumption is based on Hertzian contact theory that is valid when the length of the contact zone is considerably smaller than the punch radius *R*. Semi-circular punch creates a sharp point at the trailing end and a smooth point at the leading end.

4.3.1 Multi-layer Model

Figure 4.5 illustrates the semi-circular punch problem for elastic heterogeneous structure. Numerical solution starts with the definition of displacement derivative induced by semi-circular punch.

$$\frac{\partial U_{(N+1)}(0,Y)}{\partial Y} = -\frac{Y}{R}, \quad 0 < Y < b. \tag{4.52}$$

The formulation proceeds with the identification of normalization functions and parameters.

$$Y = \frac{b}{2}s + \frac{b}{2},\ t = \frac{b}{2}r + \frac{b}{2},\ K_{ij}(r,s) = \frac{b}{2}k_{ij}\left(\frac{b}{2}r + \frac{b}{2}, \frac{b}{2}s + \frac{b}{2}\right),\ i = 1,2,\ j = 1,2, \tag{4.53}$$

$$\frac{S(Y)}{\mu_{(N+1)}} = \frac{S\left(\frac{b}{2}s + \frac{b}{2}\right)}{\mu_{(N+1)}} = S_{XX}(s). \tag{4.54}$$

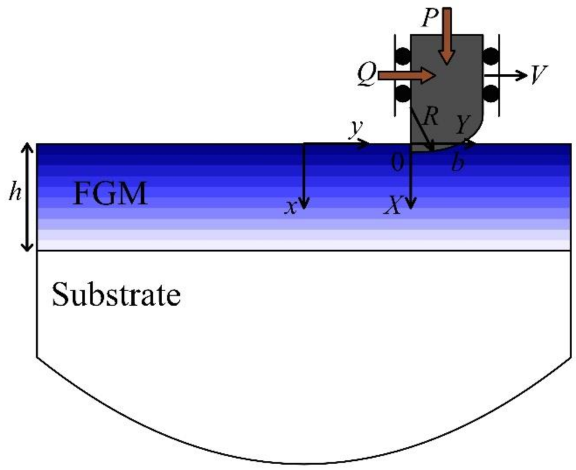

Figure 4.5. A moving rigid semi-circular punch on FGM coating with arbitrary spatial variations of material properties.

After that step, the normalized SIE and total punch force relation are derived.

$$\eta p_2 S_{XX}(s) + \frac{1}{\pi}\int_{-1}^{1}\left(\frac{p_1}{r-s} + K_{11}(r,s) + \eta K_{12}(r,s)\right)S_{XX}(r)\,dr = -\frac{b}{2R}(s+1), \quad -1 < s < 1. \tag{4.55}$$

$$\int_{-1}^{1} S_{XX}(r)\,dr = -\frac{2P}{\mu_{(N+1)}b}. \tag{4.56}$$

Determination of the index of the singular integral equation depends on the end points of the contact led by the shape of the punch. Due to the physical shape of the punch, the strength of singularity at the leading α_1 and the trailing α_2 ends become positive and negative, respectively. They also meet $\alpha_2 = -\alpha_1$, $0 < \alpha_1 < 1$ and $-1 < \alpha_2 < 0$ conditions. Then, enforcing Eq. (4.6) expands the normalized contact stress. The singular integral equation is subsequently recast into the functional form.

$$\sum_{0}^{\infty} A_n \left\{ -\frac{p_1}{\sin\left(\pi\psi_1\right)} P_n^{(-\alpha_1,-\alpha_2)}\left(s\right) + \frac{1}{\pi}\left[Z_{1n}\left(s\right) + Z_{2n}\left(s\right) \right] \right\} = -\frac{b}{2R}\left(s+1\right), \quad -1 < s < 1.$$

(4.57)

The functions $Z_{1n}(s)$ and $Z_{2n}(s)$ in functional equation are precisely identical to Eq. (4.10). Note that parameters in the right-hand side of Eq. (4.57) are the entries in the analyses. N_t is chosen to be upper limit of Jacobi polynomial expansion. Hence, N_t+1 number of collocation points as given by Eq. (4.34) must be inserted to Eq. (4.57). Then, A_n, n=0,…,N_t, are calculated using the inversion of (N_t+1)x(N_t+1) matrix. Normalized contact stress and punch force are reshaped into the conclusive form.

$$\frac{S_{XX}\left(s\right)}{\mu(0)} = \frac{\mu_{(N+1)}}{\mu(0)}\left(1-s\right)^{\alpha_1}\left(1+s\right)^{\alpha_2}\sum_{n=0}^{N_t} A_n P_n^{(\alpha_1,\alpha_2)}(s), \tag{4.58}$$

$$\frac{P}{\mu(0)R} = \frac{\mu_{(N+1)} A_0 \pi \alpha_1 b}{\mu(0)\sin\left(\pi\left(1+\alpha_1\right)\right)R}. \tag{4.59}$$

Singularity at the trailing end leads to stress concentration in mode-I. This intensification is specified as follows:

$$k_I\left(0\right) = \lim_{Y\to 0}\left(-Y^{\alpha_1}\sigma_{(N+1)XX}\left(0,Y\right)\right) = -\frac{\mu_{(N+1)}}{\mu\left(0\right)}\left(\frac{b}{2}\right)^{\alpha_1}\lim_{s\to -1}\left(1-s\right)^{\alpha_1}\sum_{n=0}^{N_t} A_n P_n^{(\alpha_1,\alpha_2)}(s). \tag{4.60}$$

Mode-I stress intensity factor is normalized and determined in the form below.

$$K_I\left(0\right) = \frac{k_I\left(0\right)}{\mu(0)b^{\alpha_1}} = -\frac{\mu_{(N+1)}}{\mu(0)}\sum_{n=0}^{N_t} A_n P_n^{(\alpha_1,\alpha_2)}(-1). \tag{4.61}$$

Finally, the stress in Y-direction is provided in the normalized form.

$$S_{YY}(s)=\frac{\sigma_{(N+1)YY}(0,s)}{\mu(0)}=\frac{8p_3\eta\mu_{(N+1)}}{\left(\kappa_{(N+1)}+1\right)\pi\mu(0)}\int_{-1}^{1}\frac{S_{XX}(r)}{r-s}dr$$

$$+\frac{8p_4+\left(3-\kappa_{(N+1)}\right)}{\left(\kappa_{(N+1)}+1\right)}\frac{\mu_{(N+1)}}{\mu(0)}S_{XX}(s) \tag{4.62}$$

$$+\frac{8\mu_{(N+1)}}{\left(\kappa_{(N+1)}+1\right)\pi\mu(0)}\int_{-1}^{1}\left[\eta K_{21}(r,s)+K_{22}(r,s)\right]S_{XX}(r)dr,\quad -\infty<s<\infty.$$

4.3.2 Multiferroic Structure

Multiferroic structure under the effect of moving semi-circular punch is demonstrated in Figure 4.6.

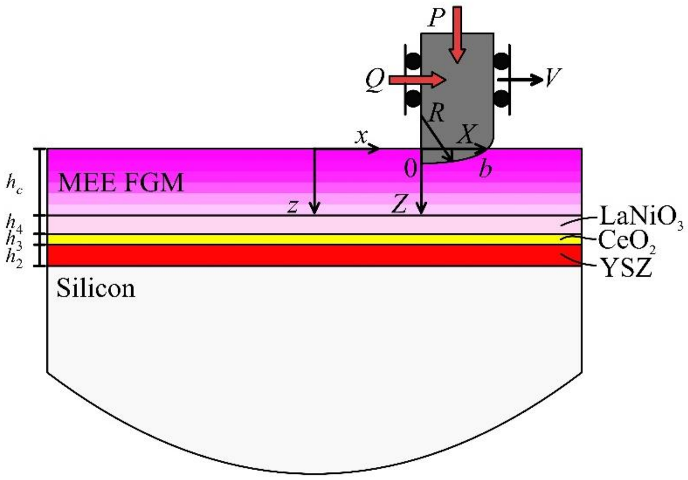

Figure 4.6. A moving rigid semi-circular punch on FGM MEE coating with arbitrary spatial variations of material properties.

The derivative of $W_{(N+M+1)}(X,0)$ with respect to spatial X-coordinate is provided below.

$$\frac{\partial W_{(N+M+1)}(X,0)}{\partial X}=-\frac{X}{R},\quad 0<X<b. \tag{4.63}$$

The parameters and functions in SIE should be modified in order to make the limits of the integral -1 and 1 so that the numerical methods become applicable.

$$X=\frac{b}{2}s+\frac{b}{2},\ t=\frac{b}{2}r+\frac{b}{2},\ K_{ij}\left(r,s\right)=\frac{b}{2}k_{ij}\left(\frac{b}{2}r+\frac{b}{2},\frac{b}{2}s+\frac{b}{2}\right),\ i=1,...,4,\ j=1,2,\quad (4.64)$$

$$\frac{S\left(X\right)}{c_{44}\left(0\right)}=\frac{S\left(\frac{b}{2}s+\frac{b}{2}\right)}{c_{44}\left(0\right)}=S_{ZZ}\left(s\right),\qquad (4.65)$$

Eqs. (4.64) and (4.65) are inserted to singular integral equation and punch force equilibrium equation.

$$\begin{aligned}\eta p_2 S_{ZZ}\left(s\right)+\frac{1}{\pi}\int_{-1}^{1}\left\{\frac{p_1}{r-s}+K_{11}\left(r,s\right)+\eta K_{12}\left(r,s\right)\right\}S_{ZZ}\left(r\right)dr=\\ -\frac{b}{2Rc_{44}\left(0\right)}\left(s+1\right),\ \ -1<s<1,\end{aligned}\qquad (4.66)$$

$$\int_{-1}^{1}S_{ZZ}\left(r\right)dr=-\frac{2P}{c_{44}\left(0\right)b}.\qquad (4.67)$$

In the right-hand side of Eq. (4.66), normalized contact length b/R appears as multiplier that is selected numerically as an input in MAPLE codes. The normal stress is discretized by means of orthogonal Jacobi polynomials as $S_{ZZ}(s)=w(s)\sum_{n=0}^{\infty}A_nP_n^{(\alpha_1,\alpha_2)}(s)$, $-1<s<1$. The index of singular integral equation is found in a similar manner explained in Section 4.3.1.

$$\sum_{n=0}^{\infty}A_n\left\{-\frac{p_1}{\sin\left(\pi\alpha_1\right)}P_n^{(-\alpha_1,-\alpha_2)}\left(s\right)+\frac{1}{\pi}\left[Z_{1n}\left(s\right)+Z_{2n}\left(s\right)\right]\right\}=-\frac{b}{2Rc_{44}\left(0\right)}\left(s+1\right),\ \ -1<s<1,\qquad (4.68)$$

The normalized parameter s in the above equation is replaced by s_i, i=1,…,N_t+1, in Eq. (4.34). A vector comprised of the coefficients of Jacobi polynomial expansion $\mathrm{A}=\{A_0 \quad \cdots \quad A_{N_t}\}^T$, is left alone in the left hand side by inverting (N_t+1)x(N_t+1) matrix attained from Eq. (4.68). With this way, the coefficients of expansion are found and the punch force equilibrium

$$\frac{P}{c_{44}(0)R}=\frac{A_0\pi\alpha_1 b}{\sin\left(\pi\left(1+\alpha_1\right)\right)R}, \tag{4.69}$$

is satisfied. At the trailing end *X*=0, we define the stress intensification as

$$k_I(0)=\lim_{X\to 0}\left(-X^{\alpha_1}\sigma_{(N+M+1)ZZ}(X,0)\right), \tag{4.70}$$

and normalize this quantity at $s=-1$ as below.

$$K_I(-1)=\frac{k_I(0)}{c_{44}(0)b^{\alpha_1}}=-\sum_{n=0}^{N_t}A_n P_n^{(\alpha_1,\alpha_2)}(-1). \tag{4.71}$$

And last but not the least, magneto-electro-elastic response of the structure in *X*-direction is obtained by the formulae below.

$$\begin{aligned}S_{XX}(s)=\frac{\sigma_{(N+M+1)XX}(X,0)}{c_{44}(0)}&=\frac{p_3 p_{10}\eta}{\pi}\int_{-1}^{1}\frac{S_{ZZ}(r)}{r-s}dr+\left(p_9+p_4 p_{10}\right)S_{ZZ}(s)\\&+\frac{p_{10}}{\pi}\int_{-1}^{1}\left[\eta K_{21}(r,s)+K_{22}(r,s)\right]S_{ZZ}(r)dr,\ -\infty<s<\infty,\end{aligned} \tag{4.72}$$

$$\begin{aligned}\Omega_X(s)=\frac{D_{(N+M+1)X}(X,0)}{c_{44}(0)/p_{16}}&=-\frac{\left(p_{12}p_5+p_{13}p_7\right)p_{16}}{\pi}\int_{-1}^{1}\frac{S_{ZZ}(r)}{r-s}dr\\&+\eta p_{16}\left(p_{11}-p_{12}p_6-p_{13}p_8\right)S_{ZZ}(s)\\&-\frac{p_{12}p_{16}}{\pi}\int_{-1}^{1}\left[K_{31}(r,s)+\eta K_{32}(r,s)\right]S_{ZZ}(r)dr\\&-\frac{p_{13}p_{16}}{\pi}\int_{-1}^{1}\left[K_{41}(r,s)+\eta K_{42}(r,s)\right]S_{ZZ}(r)dr,\ -\infty<s<\infty,\end{aligned} \tag{4.73}$$

$$\Gamma_X(s) = \frac{B_{(N+M+1)X}(X,0)}{c_{44}(0)/p_{17}} = -\frac{(p_{13}p_5 + p_{15}p_7)\,p_{17}}{\pi}\int_{-1}^{1}\frac{S_{ZZ}(r)}{r-s}dr$$
$$+\eta p_{17}(p_{14} - p_{13}p_6 - p_{15}p_8)S_{ZZ}(s)$$
$$-\frac{p_{13}p_{17}}{\pi}\int_{-1}^{1}\left[K_{31}(r,s)+\eta K_{32}(r,s)\right]S_{ZZ}(r)\,dr \tag{4.74}$$
$$-\frac{p_{15}p_{17}}{\pi}\int_{-1}^{1}\left[K_{41}(r,s)+\eta K_{42}(r,s)\right]S_{ZZ}(r)\,dr,\quad -\infty < s < \infty.$$

4.4 Circular Punch Problem

Normal displacement arisen by the indentation of circular punch is same as the one for the semi-circular punch. On the other hand, the moving coordinate is connected to a point on the centerline of the circular punch. Thus, the trailing end is located at a negative point ($-a$) in the lateral direction. At both end points, circular punch leads to fairly blunt transition in normal displacement at the topmost layer.

4.4.1 Multi-layer Model

In this section, a periodic coating model suggested by Penkov et al. (2015) and an FGM coating model are investigated. Penkov et al. (2015) state that the usage of the periodic multi-layer coating demonstrated in Figure 4.7 provides high wear resistance to the structure. The examined FGM coating model is depicted in Figure 4.8. It is also known that FGM structures decrease the failure problems at the interfaces and increase the resistance against environmental stimulus effects such as thermal, corrosive and impact. In both problems, the formulation is exactly the same.

The displacement derivative is written as follows:

$$\frac{\partial U_{(N+1)}(0,Y)}{\partial Y} = -\frac{Y}{R},\quad -a < Y < b. \tag{4.75}$$

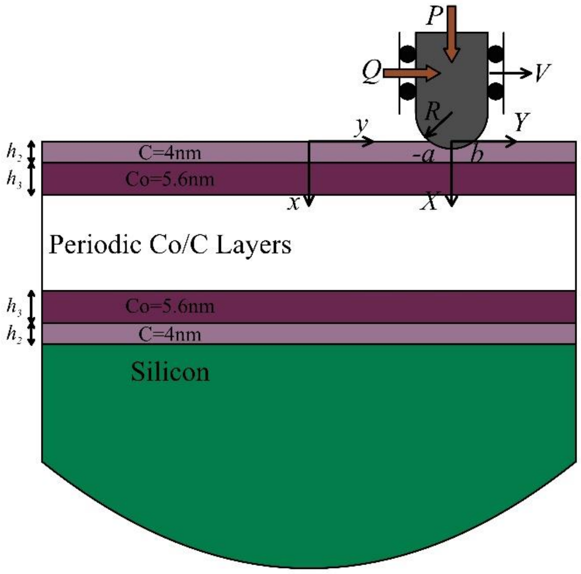

Figure 4.7. A moving rigid circular punch on periodic Co/C coating.

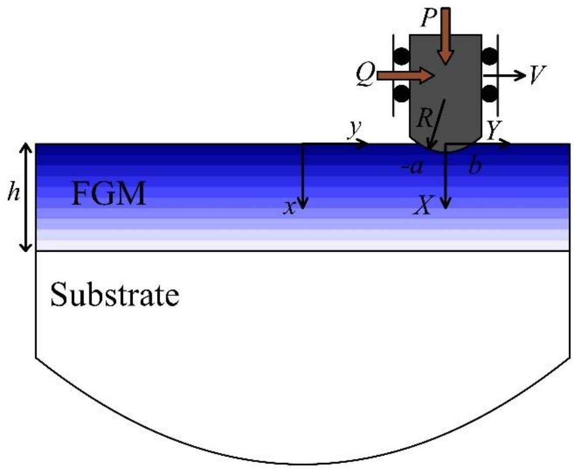

Figure 4.8. A moving rigid circular punch on FGM coating with arbitrary spatial variations of material properties.

Remember that the trailing end is placed at $Y = -a$ point as different from other punch problems. For this reason, the interval of displacement derivative in Eq. (4.75) and the lower limits of the integrals in the integral equations vary in circular punch problem. The normalization variables and functions are also affected by this incident.

$$Y=\frac{b+a}{2}s+\frac{b-a}{2},\;\; t=\frac{b+a}{2}r+\frac{b-a}{2}, \tag{4.76}$$

$$K_{ij}\left(r,s\right)=\frac{b+a}{2}k_{ij}\left(\frac{b+a}{2}r+\frac{b-a}{2},\frac{b+a}{2}s+\frac{b-a}{2}\right), i=1,2, j=1,2, \tag{4.77}$$

$$\frac{S\left(Y\right)}{\mu_{(N+1)}}=\frac{S\left(\frac{b+a}{2}s+\frac{b-a}{2}\right)}{\mu_{(N+1)}}=S_{XX}\left(s\right). \tag{4.78}$$

In the next stage, the normalized SIE is derived by using the transformations in Eqs. (4.76)-(4.78).

$$\begin{gathered}\eta p_2 S_{XX}\left(s\right)+\frac{1}{\pi}\int_{-1}^{1}\left(\frac{p_1}{r-s}+K_{11}\left(r,s\right)+\eta K_{12}\left(r,s\right)\right)S_{XX}\left(r\right)dr=\\ -\frac{\left(b+a\right)s}{2R}-\frac{\left(b-a\right)}{2R},\;\; -1<s<1.\end{gathered} \tag{4.79}$$

By carrying out function-theoretic analysis, the unknown of the singular integral equation $S_{XX}(s)$ is expanded by means of Eq. (4.6). Both exponents α_1 and α_2 in the weight function $w(s)$ are determined between the interval 0 and 1. They must also satisfy $\alpha_1+\alpha_2=1$ relation because of the physics of the problem, i.e., the smooth transition end points are originated by the nature of circular punch.

Hertzian contact problem in this section is an incomplete one which means the total contact size is strongly associated with the applied force. This phenomenon brings an additional parameter which is the position of the trailing end. Therefore, an additional relation between a, b and $S_{XX}(s)$ must exist. This condition is called as the consistency equation and it is obtained by multiplying each term in Eq. (4.79) by $(1-s)^{-\alpha_1}(1+s)^{-\alpha_2}$ and integrating the variable s from -1 to 1. Once the necessary simplifications are done utilizing the orthogonality properties of Jacobi polynomials, the punch eccentricity (punch position) parameter $(b-a)/R$ is written in terms of the normalized total contact size $(b+a)/R$ and the normalized contact stress S_{XX}.

$$\frac{(b-a)}{R}=\frac{(b+a)}{R}(1-2\alpha_1)$$
$$-\frac{2\sin(\pi\alpha_1)}{\pi^2}\int_{-1}^{1}\left\{\int_{-1}^{1}\left[K_{11}(r,s)+\eta K_{12}(r,s)\right]S_{XX}(r)dr\right\}(1-s)^{-\alpha_1}(1+s)^{-\alpha_2}\,ds \tag{4.80}$$

Note that s is replaced by $2P_1^{(-\alpha_1,-\alpha_2)}(s)+(\alpha_1-\alpha_2)$ in Eq. (4.79) and the following relation is useful in the calculation of Eq. (4.80).

$$\int_{-1}^{1}(1-s)^{-\alpha_1}(1+s)^{-\alpha_2}\,ds=\frac{\pi}{\sin(\pi\alpha_1)},\quad \text{if}\quad \alpha_1+\alpha_2=1. \tag{4.81}$$

Now, substitution of $(b-a)/R$ into Eq. (4.79) gives the final form of integral equation.

$$\eta p_2 S_{XX}(s)+\frac{1}{\pi}\int_{-1}^{1}\left(\frac{p_1}{r-s}+K_{11}(r,s)+\eta K_{12}(r,s)\right)S_{XX}(r)dr$$
$$-\frac{\sin(\pi\psi_1)}{\pi^2}\int_{-1}^{1}\left\{\int_{-1}^{1}\left[K_{11}(r,s)+\eta K_{12}(r,s)\right]S_{XX}(r)dr\right\}(1-s)^{-\alpha_1}(1+s)^{-\alpha_2}\,ds= \tag{4.82}$$
$$-\frac{(b+a)P_1^{(-\alpha_1,-\alpha_2)}(s)}{R},\ -1<s<1$$

Punch equilibrium equation

$$\int_{-1}^{1}S_{XX}(r)dr=-\frac{2P}{\mu_{(N+1)}(b+a)}. \tag{4.83}$$

is modified, too. Jacobi polynomial expansion of normal stress is inserted to Eq. (4.82) and the functional equation below is obtained.

$$\sum_{n=0}^{\infty}A_n\left\{-\frac{2p_1}{\sin(\pi\alpha_1)}P_{n+1}^{(-\alpha_1,-\alpha_2)}(s)+\frac{1}{\pi}\left[Z_{1n}(s)+Z_{2n}(s)\right]+C\right\}=-\frac{(b+a)P_1^{(-\alpha_1,-\alpha_2)}(s)}{R},\ -1<s<1 \tag{4.84}$$

where C in the above equation is computed as

$$C=-\frac{\sin(\pi\alpha_1)}{\pi^2}\int_{-1}^{1}\left\{\int_{-1}^{1}\left[K_{11}(r,s)+\eta K_{12}(r,s)\right]S_{XX}(r)dr\right\}(1-s)^{-\alpha_1}(1+s)^{-\alpha_2}\,ds. \tag{4.85}$$

The upper limit in the summation symbol in Eq. (4.84) is truncated at N_t and the collocation points in Eq. (4.34) are employed in the calculation of the coefficients of expansion A_n. Hence, the final versions of contact stress and punch force are written below.

$$\frac{S_{XX}(s)}{\mu(0)} = \frac{\mu_{(N+1)}}{\mu(0)}(1-s)^{\alpha_1}(1+s)^{\alpha_2}\sum_{n=0}^{N_t} A_n P_n^{(\alpha_1,\alpha_2)}(s), \tag{4.86}$$

$$\frac{P}{\mu(0)(b+a)} = -\frac{\mu_{(N+1)}A_0\pi\alpha_1(\alpha_1-1)}{\mu(0)\sin(\pi(\alpha_1+1))}. \tag{4.87}$$

At the last step, the lateral contact stress formula

$$\begin{aligned} S_{YY}(s) = \frac{\sigma_{(N+1)YY}(0,s)}{\mu(0)} &= \frac{8p_3\eta\mu_{(N+1)}}{\left(\kappa_{(N+1)}+1\right)\pi\mu(0)}\int_{-1}^{1}\frac{S_{XX}(r)}{r-s}dr \\ &+ \frac{8p_4+\left(3-\kappa_{(N+1)}\right)}{\left(\kappa_{(N+1)}+1\right)}\frac{\mu_{(N+1)}}{\mu(0)}S_{XX}(s) \\ &+ \frac{8\mu_{(N+1)}}{\left(\kappa_{(N+1)}+1\right)\pi\mu(0)}\int_{-1}^{1}\left[\eta K_{21}(r,s)+K_{22}(r,s)\right]S_{XX}(r)dr, \quad -\infty<s<\infty. \end{aligned} \tag{4.88}$$

is noted.

4.4.2 Multiferroic Structure

The numerical solution of multiferroic structure indented by a moving circular punch is presented in this section. The corresponding problem is illustrated in Figure 4.9. The displacement derivative is written as below.

$$\frac{\partial W_{(N+M+1)}(X,0)}{\partial X} = -\frac{X}{R}, \quad -a<X<b. \tag{4.89}$$

The normalized variables and functions are introduced.

$$X = \frac{b+a}{2}s + \frac{b-a}{2}, \quad t = \frac{b+a}{2}r + \frac{b-a}{2}, \tag{4.90}$$

$$K_{ij}(r,s) = \frac{b+a}{2}k_{ij}\left(\frac{b+a}{2}r + \frac{b-a}{2}, \frac{b+a}{2}s + \frac{b-a}{2}\right), \; i = 1,...,4, \; j = 1,2, \tag{4.91}$$

$$\frac{S(X)}{c_{44}(0)} = \frac{S\left(\frac{b+a}{2}s + \frac{b-a}{2}\right)}{c_{44}(0)} = S_{ZZ}(s). \tag{4.92}$$

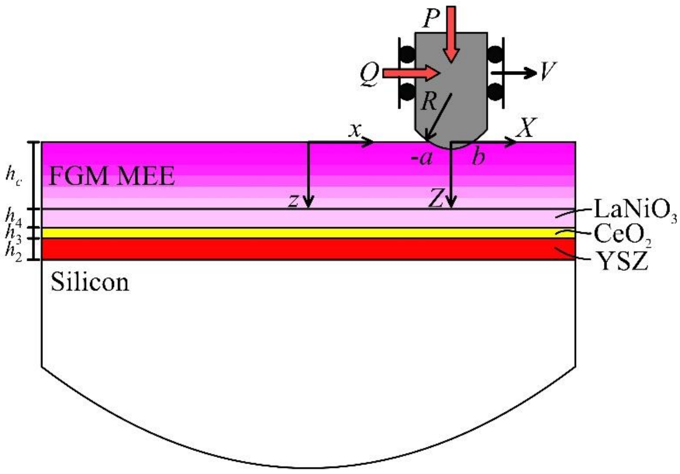

Figure 4.9. A moving rigid circular punch on FGM MEE coating with arbitrary spatial variations of material properties.

Normalized terms are inserted into the singular integral equation and the punch force equilibrium equation.

$$\begin{gathered}\eta p_2 S_{ZZ}(s) + \frac{1}{\pi}\int_{-1}^{1}\left\{\frac{p_1}{r-s} + K_{11}(r,s) + \eta K_{12}(r,s)\right\}S_{ZZ}(r)dr = \\ -\frac{(b+a)s}{2Rc_{44}(0)} - \frac{(b-a)}{2Rc_{44}(0)}, \quad -1 < s < 1,\end{gathered} \tag{4.93}$$

$$\int_{-1}^{1} S_{ZZ}(r)dr = -\frac{2P}{c_{44}(0)(b+a)}. \tag{4.94}$$

The consistency condition reveals the relation between punch eccentricity parameter and total contact length and normal contact stress.

$$\frac{b-a}{R}=\frac{b+a}{R}\left(1-2\alpha_1\right)$$
$$-\frac{2c_{44}\left(0\right)\sin\left(\pi\alpha_1\right)}{\pi^2}\int_{-1}^{1}\left\{\int_{-1}^{1}\left[K_{11}\left(r,s\right)+\eta K_{12}\left(r,s\right)\right]S_{ZZ}\left(r\right)dr\right\}\left(1-s\right)^{-\alpha_1}\left(1+s\right)^{-\alpha_2}ds. \tag{4.95}$$

Eq, (4.95) is substituted back into Eq. (4.93) and singular integral equation takes the final form.

$$\begin{aligned}&\eta p_2 S_{ZZ}\left(s\right)+\frac{1}{\pi}\int_{-1}^{1}\left(\frac{p_1}{r-s}+K_{11}\left(r,s\right)+\eta K_{12}\left(r,s\right)\right)S_{ZZ}\left(r\right)dr\\&-\frac{\sin\left(\pi\psi_1\right)}{\pi^2}\int_{-1}^{1}\left\{\int_{-1}^{1}\left[K_{11}\left(r,s\right)+\eta K_{12}\left(r,s\right)\right]S_{ZZ}\left(r\right)dr\right\}\left(1-s\right)^{-\alpha_1}\left(1+s\right)^{-\alpha_2}ds\\&=-\frac{\left(b+a\right)P_1^{\left(-\alpha_1,-\alpha_2\right)}\left(s\right)}{Rc_{44}\left(0\right)},\ -1<s<1.\end{aligned} \tag{4.96}$$

As always, $S_{ZZ}(s)$ is expanded utilizing orthogonal Jacobi polynomials and the usual expansion-collocation technique given by Eq. (4.22) and Eq. (4.34) is applied to form and solve the functional equation.

$$\sum_{n=0}^{\infty}A_n\left\{-\frac{2p_1}{\sin\left(\pi\alpha_1\right)}P_{n+1}^{\left(-\alpha_1,-\alpha_2\right)}\left(s\right)+\frac{1}{\pi}\left[Z_{1n}\left(s\right)+Z_{2n}\left(s\right)\right]+C\right\}=-\frac{\left(b+a\right)P_1^{\left(-\alpha_1,-\alpha_2\right)}\left(s\right)}{Rc_{44}\left(0\right)},\ -1<s<1. \tag{4.97}$$

where C contains the double integral term in SIE.

$$C=-\frac{\sin\left(\pi\alpha_1\right)}{\pi^2}\int_{-1}^{1}\left\{\int_{-1}^{1}\left[K_{11}\left(r,s\right)+\eta K_{12}\left(r,s\right)\right]S_{ZZ}\left(r\right)dr\right\}\left(1-s\right)^{-\alpha_1}\left(1+s\right)^{-\alpha_2}ds. \tag{4.98}$$

Normalized punch force can be evaluated using the first coefficient of the expansion A_0.

$$\frac{P}{c_{44}\left(0\right)\left(b+a\right)}=-\frac{A_0\pi\alpha_1\left(\alpha_1-1\right)}{\sin\left(\pi\left(\alpha_1+1\right)\right)}. \tag{4.99}$$

In this very last step, normalized lateral stress, electric displacement and magnetic induction functions are derived.

$$S_{XX}(s)=\frac{\sigma_{(N+M+1)XX}(X,0)}{c_{44}(0)}=\frac{p_3 p_{10}\eta}{\pi}\int_{-1}^{1}\frac{S_{ZZ}(r)}{r-s}dr+\left(p_9+p_4 p_{10}\right)S_{ZZ}(s)$$
$$+\frac{p_{10}}{\pi}\int_{-1}^{1}\left[\eta K_{21}(r,s)+K_{22}(r,s)\right]S_{ZZ}(r)dr,\ -\infty<s<\infty, \tag{4.100}$$

$$\Omega_X(s)=\frac{D_{(N+M+1)X}(X,0)}{c_{44}(0)/p_{16}}=-\frac{\left(p_{12}p_5+p_{13}p_7\right)p_{16}}{\pi}\int_{-1}^{1}\frac{S_{ZZ}(r)}{r-s}dr$$
$$+\eta p_{16}\left(p_{11}-p_{12}p_6-p_{13}p_8\right)S_{ZZ}(s)$$
$$-\frac{p_{12}p_{16}}{\pi}\int_{-1}^{1}\left[K_{31}(r,s)+\eta K_{32}(r,s)\right]S_{ZZ}(r)dr \tag{4.101}$$
$$-\frac{p_{13}p_{16}}{\pi}\int_{-1}^{1}\left[K_{41}(r,s)+\eta K_{42}(r,s)\right]S_{ZZ}(r)dr,\ -\infty<s<\infty,$$

$$\Gamma_X(s)=\frac{B_{(N+M+1)X}(X,0)}{c_{44}(0)/p_{17}}=-\frac{\left(p_{13}p_5+p_{15}p_7\right)p_{17}}{\pi}\int_{-1}^{1}\frac{S_{ZZ}(r)}{r-s}dr$$
$$+\eta p_{17}\left(p_{14}-p_{13}p_6-p_{15}p_8\right)S_{ZZ}(s)$$
$$-\frac{p_{13}p_{17}}{\pi}\int_{-1}^{1}\left[K_{31}(r,s)+\eta K_{32}(r,s)\right]S_{ZZ}(r)dr \tag{4.102}$$
$$-\frac{p_{15}p_{17}}{\pi}\int_{-1}^{1}\left[K_{41}(r,s)+\eta K_{42}(r,s)\right]S_{ZZ}(r)dr,\ -\infty<s<\infty.$$

CHAPTER 5

NUMERICAL RESULTS

In this chapter, the results obtained by utilizing the procedures explained in Chapters 3 and 4 are demonstrated in tables and figures. Among the significant outputs of the problems, the normal and the lateral contact stresses for all problems, the punch force for incomplete contact problems, mode-I stress intensity factors at the sharp end points, the punch eccentricity parameter for circular punch indentation and electric displacement and magnetic induction for multiferroic structures are discussed in detail. Note that most of the results in this chapter is published in international journals or presented in conferences.

This section is mainly divided into 4 parts. In the first part, the results associated with the flat and triangular punch indentations are presented in Figure 5.1-Figure 5.18 and Table 5.1-Table 5.13. The following subsection examines the contact problems involving semi-circular shaped loading agent in Figure 5.19-Figure 5.27 and Table 5.14-Table 5.26. In the next section, Figure 5.28-Figure 5.40 and Table 5.27-Table 5.44 show the results regarding the loading cases by circular punch. Additional analyses on elastic multi-layer structures are presented in Figure 5.41-Figure 5.43 and Table 5.45 and Table 5.46.

The examined problems are clarified in details as below.

- The pure elastic multi-layer problems are divided into three groups.
    1. The elastic FGM coating problems involve only two materials. The metal substrate is covered by ceramic&metal FGM coating.
    2. The periodic elastic coating structure, on the other hand, is formed by a silicon substrate that is protected by repeating Co/C multilayers.

3. In the multi-layer elastic coating problem, a storage device which combines diamond like carbon coating (DLC), magnetic layer (MAG), intermediate layer (IL), soft magnetic underlayer (SUL) and Ni-P substrate is studied.

- The multiferroic structure comprises a silicon substrate. On top of that, a buffer composed of three elastic layers is deposited and FGM MEE layer is placed at the topmost.

For the elastic and multiferroic FGM problems, the variation of any property is defined by power law functions.

$$\Lambda(X) = \Lambda_0 + (\Lambda_h - \Lambda_0)(X/h)^{\gamma}, \; 0 < X < h, \text{ for elastic structures,} \tag{5.1}$$

$$\Lambda(Z) = \Lambda_0 + (\Lambda_h - \Lambda_0)(Z/h_c)^{\gamma}, \; 0 < Z < h_c, \text{ for multiferroic structures.} \tag{5.2}$$

Λ_h&Λ_0 indicate the properties at X=h and X=0 for multi-layer model and Z=h_c and Z=0 for multiferroic structure. γ symbolizes the power exponent.

5.1 Numerical Results for Flat and Triangular Punches

This section is published by the author collaborating with his supervisor in two separate articles for multi-layer model and multiferroic structure, respectively. (Toktas and Dag, 2022a; 2023a).

5.1.1 Multi-layer Model

Elastic structure under the effect of flat and triangular punch indentation is investigated in this section. Nickel and zirconia are chosen as substrate-coating pair. Note that the coating made of zirconia creates less stiff coating, i.e., shear modulus of zirconia is less than the one for nickel.

5.1.1.1 Verification

In order to verify the developed analytical and numerical procedures, the comparisons are presented with the results available for limiting cases in the literature. The first set of comparisons is generated by considering the contact problem solved by Eringen and Suhubi (1975). This book presents closed form solutions for the contact problem involving a homogeneous half plane and a flat punch moving with a constant velocity *V*. The comparisons of the normalized contact stresses are provided in Figure 5.1. Normal and lateral contact stresses are presented with respect to the normalized coordinate *s* for four different values of the normalized punch velocity λ, which is defined by

$$\lambda = \frac{V}{\sqrt{\mu/\rho}}. \tag{5.3}$$

In modelling, the number of coating layers *N* is taken as 1. The single-layer coating and the bonded half-plane are specified as if they possess the identical physical properties. The homogeneous elastic body is assumed to be in a state of plane strain. It can be seen that our results for both the normal stress S_{XX} and the lateral stress S_{YY} are in excellent agreement with those provided by Eringen and Suhubi (1975) for all considered dimensionless punch velocity values. Hence, this is deemed to be a verification of the contact mechanics solution procedures, that are based on elastodynamic equations and Galilean transformation.

A second set of comparisons is generated by considering the contact stresses computed by Ke and Wang (2007) for a static flat punch (λ=0) in frictional contact with a functionally graded coating. The comparisons are shown in Figure 5.2. Referring to Figure 4.1, the shear modulus variation of the coating is expressed as follows:

$$\mu(x) = \mu(h) + \left(\mu(0) - \mu(h)\right)\left(\frac{h-X}{h}\right)^{\gamma}, \quad 0 < X < h. \tag{5.4}$$

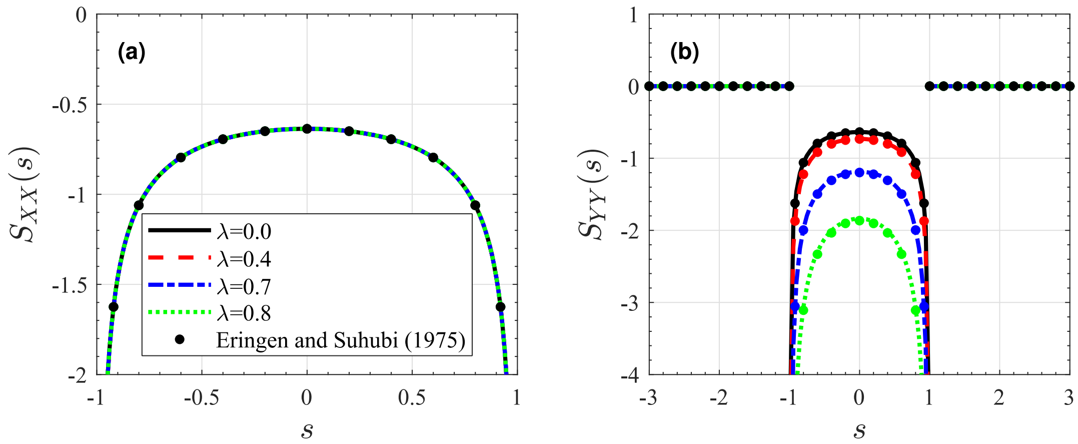

Figure 5.1. Comparison of contact stresses for an isotropic half-plane in contact with a moving flat punch to those given by Eringen and Suhubi (1975) (a) normal stress; (b) normal stress in lateral direction. η=0.0.

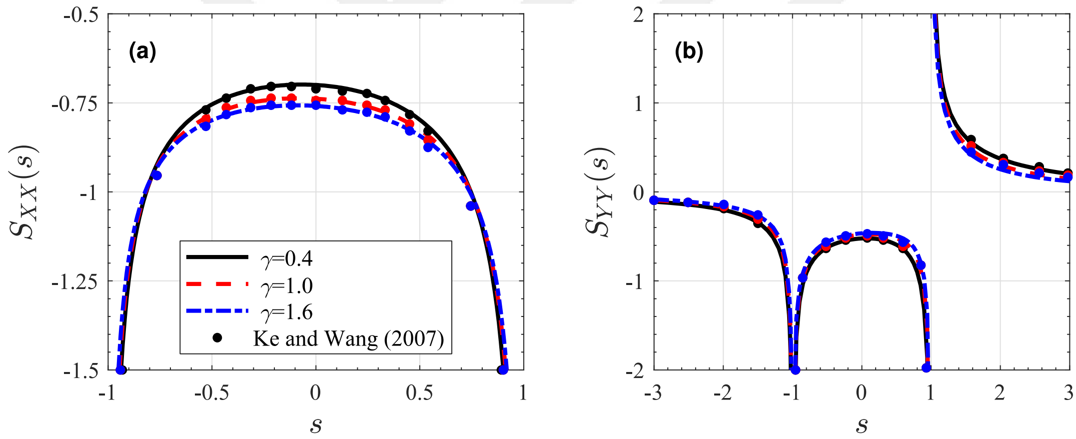

Figure 5.2. Comparison of contact stresses for a graded coating whose properties are varying with power functions in contact with a stationary flat punch to those given by Ke and Wang (2007): (a) normal stress; (b) normal stress in lateral direction. b/h=0.2, η=−0.5, κ=1.8, $\mu(h)/\mu(0)$=8.

Poisson's ratio is assumed to be constant, and material properties are continuous at the interface. The composite medium is in a state of plane strain. Total number of sub-layers (N) used in the computations is chosen as 150. It can be seen that there is an excellent agreement in the results generated for both of the contact stresses S_{XX} and S_{YY}. Thus, our model is capable of producing highly accurate results for FGM coatings possessing any kind of shear modulus variation, including exponential and power function type variations.

A final set of comparisons is generated by considering the numerical results by Balci and Dag (2020), who solved moving contact problems involving exponentially graded materials. The problem solved by Balci and Dag (2020) consists of a single FGM coating bonded to a homogeneous substrate. Shear modulus and density of the FGM coating are proportionally varied, and Poisson's ratio is assumed to be a constant to be able to make the problem analytically tractable. The material property variations of the coating are represented as follows:

$$\mu(X)=\mu(0)\exp(\gamma X), \quad \rho(X)=\rho(0)\exp(\gamma X), \quad 0<X<h. \tag{5.5}$$

The properties are assumed to be continuous at the interface of the coating and the substrate. In accordance with the model developed by Balci and Dag (2020), the dimensionless punch speed λ is specified same for all the layers and the substrate. For each sub-layer in the graded coating, the variable properties μ and ρ are specified at the mid-section in our model. The comparisons of our numerical results for a flat punch are provided in Figure 5.3 for different values of λ. It can be seen that our results agree quite well with those provided by Balci and Dag (2020). The number of layers used in the coating N is 150. This number is determined through a convergence analysis, whose results are tabulated in Table 5.1. Approximate error function is introduced in order to check the convergence of the results. In Table 5.1, the value of N is continuously increased until the error function drops under certain value.

$$\varepsilon_a=\left|\frac{\text{current value}-\text{previous value}}{\text{current value}}\right|\times 100. \tag{5.6}$$

The optimum value of N is determined as 150 since the approximate error is less than 1% for both of the stress components in Table 5.1. In order to save time in the analyses, the number of collocation points N_t is chosen as 20. Convergence can also be checked comparing the first A_0 and the last coefficient of expansion A_{N_t}. If the ratio of these coefficients (A_0/A_{N_t}) is greater than 50, it means that the necessary level of convergence is reached.

Table 5.1. Number of layers, stresses, and percent approximate errors computed at s=0 for a graded coating whose properties are varying with exponential functions in contact with a moving flat punch. b/h=0.4, η=0.3, κ=1.8, $\mu(h)/\mu(0)$=1/6, $\rho(h)/\rho(0)$=1/6, λ=0.4.

N	$S_{XX}(0)$	ε_a	$S_{YY}(0)$	ε_a
10	-0.4450	-	-1.4012	-
50	-0.4348	2.35	-1.5498	9.59
100	-0.4335	0.30	-1.5714	1.37
150	-0.4330	0.10	-1.5787	0.46
200	-0.4328	0.05	-1.5823	0.23

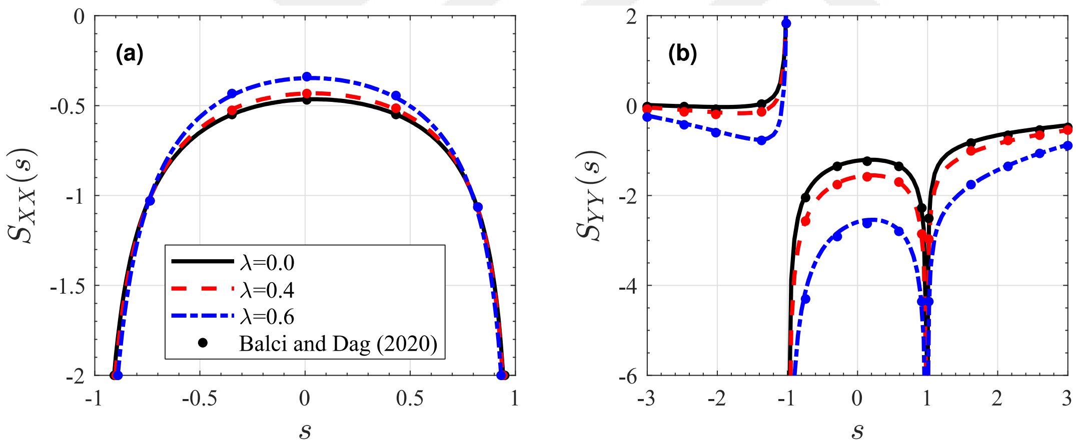

Figure 5.3. Comparison of contact stresses for a graded coating whose properties are varying with exponential functions in contact with a moving flat punch to those given by Balci and Dag (2020): (a) normal stress; (b) normal stress in lateral direction. b/h=0.4, η=0.3, κ=1.8, $\mu(h)/\mu(0)$=1/6, $\rho(h)/\rho(0)$=1/6.

Comparisons of our results to those computed for a triangular punch by Balci and Dag (2020) are given in Figure 5.4. Again, there is a very good agreement. Hence, the developed procedures lead to numerical results with a high degree of accuracy.

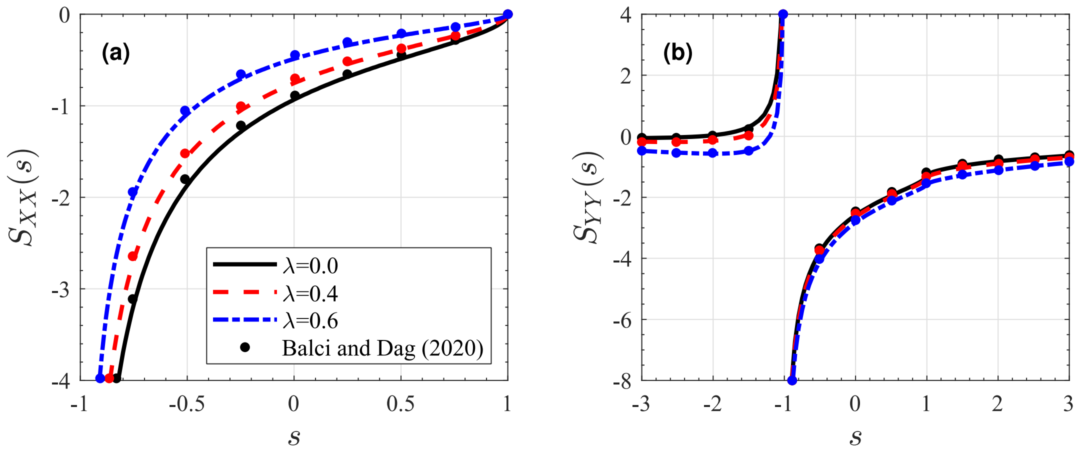

Figure 5.4. Comparison of contact stresses for a graded coating whose properties are varying with exponential functions in contact with a moving triangular punch to those given by Balci and Dag (2020): (a) normal stress; (b) normal stress in lateral direction. b/h=0.2, η=0.3, κ=1.8, $\mu(h)/\mu(0)$=1/6, $\rho(h)/\rho(0)$=1/6.

5.1.1.2 Parametric Analyses

To prove the superiority of the multi-layer model in the present study over the single exponential layer model by Balci and Dag (2020), Figure 5.5 is presented for elastic structure in Figure 4.1 loaded by a frictional moving flat punch. In this set, the model parameters are taken as b/h=0.2 and η=0.3. Both $\mu(X)$ and $\rho(X)$ vary exponentially as given by Eq. (5.5) in the single-layer model, whereas the multi-layer model is more proficient and is able to take care of more general distributions given below. Notice that three exponents, γ_i, (i=1,2,3), are unequal that indicates nonproportional variations. In addition, the variation of Poisson's ratio is incorporated into the model.

$$\mu(X)=\mu(0)\exp(\gamma_1 X), \quad 0<X<h, \tag{5.7}$$

$$\rho(X)=\rho(0)\exp(\gamma_2 X), \quad 0<X<h, \tag{5.8}$$

$$\nu(X)=\nu(0)\exp(\gamma_3 X), \quad 0<X<h. \tag{5.9}$$

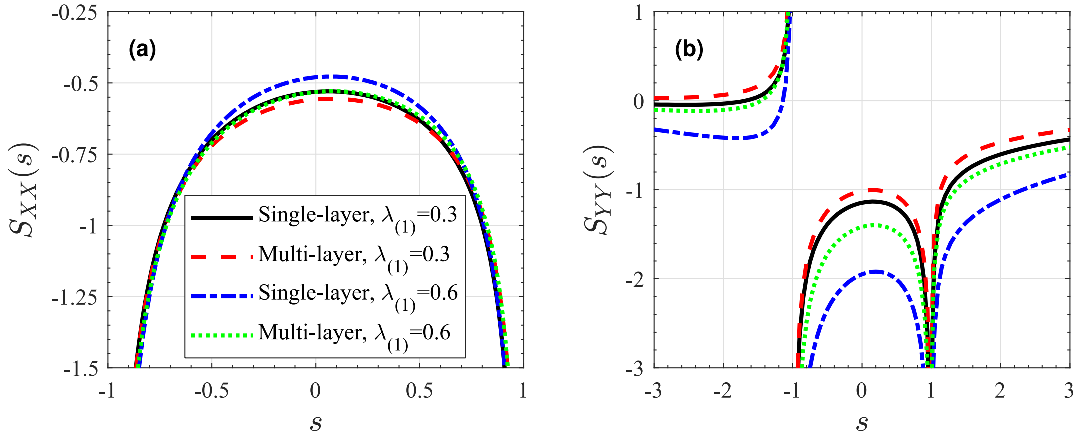

Figure 5.5. Comparison of the stresses generated by single- and multi-layer models in contact with a moving flat punch. b/h=0.2, η=0.3. (a) normal stress; (b) normal stress in lateral direction. Single-layer model: $\mu(h)/\mu(0)=1/6$, $\rho(h)/\rho(0)=1/6$, $\kappa=1.4$; multi-layer model: $\nu(h)/\nu(0)=5$, $\mu(h)/\mu(0)=1/6$, $\rho(h)/\rho(0)=1/3$.

The stress results obtained by two models are compared for an intermediate level punch speed $\lambda_{(1)}$=0.3 and a high-level punch speed $\lambda_{(1)}$=0.6. In both punch speeds, one can observe substantial discrepancy in normal and lateral stress curves as shown in Figure 5.5. The conclusion understood from this comparison is that the multi-layer model is superior compared to single-layer exponential model and should be applied in nonproportionally graded structures. Nonproportional variation is very common due to processing techniques employed in manufacturing of FGMs whereas proportional variation can only occur as an exception. Thus, multi-layer modelling technique is more realistic whenever nonproportionality exists.

Referring to Figure 4.1, the properties of the functionally graded coating are expressed in Eq. (5.1) in the new sets. The FGM coating is assumed to be 100% Zirconia at the exposed surface X=0 and 100% Nickel at the interface $X=h$. Hence, the properties become continuous and uninterrupted at the interface. The material properties are tabulated in Table 5.2. Three properties including Poisson's ratio vary by power law functions and there are no restrictions especially proportionality constraint in the variations. The power law exponents γ_i, (i=1,2,3), are intentionally defined as different from each other so that nonproportionality is reached. These exponents are presented in Table 5.3.

Table 5.2. Properties of Ni and ZrO_2 (Abdullaev et al., 2015; Dag, 2007; Opalinska et al., 2015).

	E(GPa)	ρ(kg/m^3)	ν
Nickel	175.8	8902	0.25
Zirconia	116.4	5680	0.33

Table 5.3. Exponents used in parametric analyses for the functionally graded coatings.

	Metal-rich coating (MR)	Linear coating (LN)	Ceramic-rich coating (CR)	Ceramic coating (H)
γ_1	0.3	1	3	∞
γ_2	0.4	1	4	∞
γ_3	0.5	1	5	∞

Depending on the choice of the exponents, four coatings namely ceramic-rich (CR), metal-rich (MR), linear (LN), and homogeneous ceramic (H) are considered in the analyses. The selection of power law exponents is a critical matter because it determines the coating type. Now, consider a case in which all properties are squeezed between zero and one, $(0 < \gamma_i < 1,\ i{=}1{,}2{,}3)$. The coating under these circumstances becomes MR type. Profile variations and the coating are linear (LN) only if $\gamma_1{=}\gamma_2{=}\gamma_3{=}\,1$. The condition regarding the exponents for obtaining a CR coating is choosing all of them greater than one $(1 < \gamma_i,\ i{=}1{,}2{,}3)$. Lastly, all exponents must be infinity in order to vanish (X/h) term in Eq. (5.1). Therefore, the properties at everywhere in the coating is equal to the ones of ceramic, $\Lambda(X){=}\Lambda_0,\ 0 < X < h$, because $(X/h)^{\infty}{=}0$ when the interval of X/h is between zero and one.

Numerical results concerning the coating types exposed to the contact loading by flat punch are illustrated in Figure 5.6 and Figure 5.7. Convergence analysis whose results are given in Table 5.4 is carried out for the CR coating. Homogenization of CR coating with 100 layers restrains the approximate errors under 1% at the center point of the contact, s=0. For this reason, utilization of 100 for N reveals accurate results in this section.

Table 5.4. Number of layers, stresses, and percent approximate errors computed at s=0 for a CR coating in contact with a moving flat punch. b/h=1, η=0.4, $\lambda_{(1)}$=0.6.

N	$S_{XX}(0)$	ε_a	$S_{YY}(0)$	ε_a
10	-0.6991	-	-0.8329	-
50	-0.6996	0.08	-0.8438	1.30
100	-0.6997	0.01	-0.8454	0.18
150	-0.6997	0.00	-0.8459	0.06

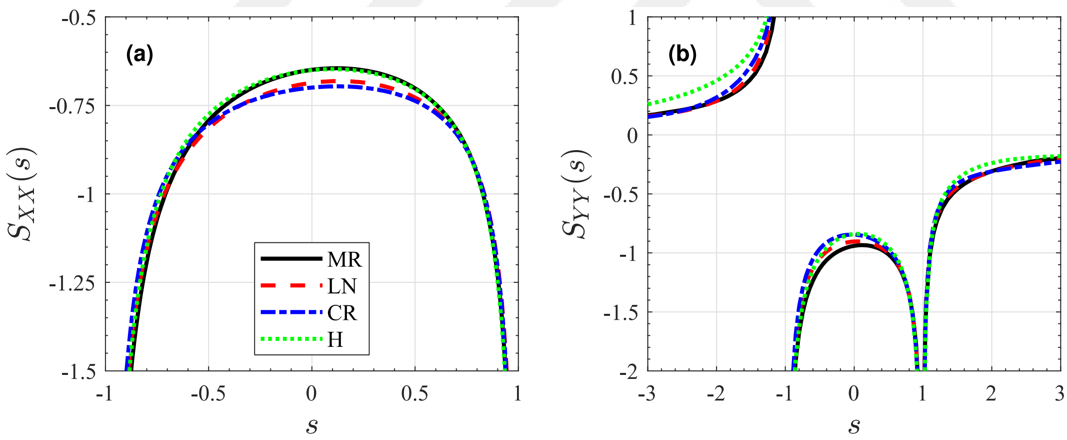

Figure 5.6. Contact stresses computed by considering FGM coatings in contact with a moving flat punch: (a) normal stress; (b) normal stress in lateral direction. b/h=1, η=0.4, $\lambda_{(1)}$=0.6.

As seen in Figure 5.6, S_{XX} of CR coating is a bit large in magnitude in the central part of the contact zone. The largest tensile lateral stress is computed for H coating near the trailing end. Figure 5.7 indicates the alteration of dimensionless SIFs with

$\lambda_{(1)}$. Independent of the end point, the largest SIFs are computed for H coating. That is deemed to be a proof of the material gradation lowers SIFs and the chance of failure due to high stress concentration. LN coating seems to cause relatively smaller SIFs. In all cases, it is found that SIFs can be lowered when the structure is exposed to a punch having a higher $\lambda_{(1)}$ value.

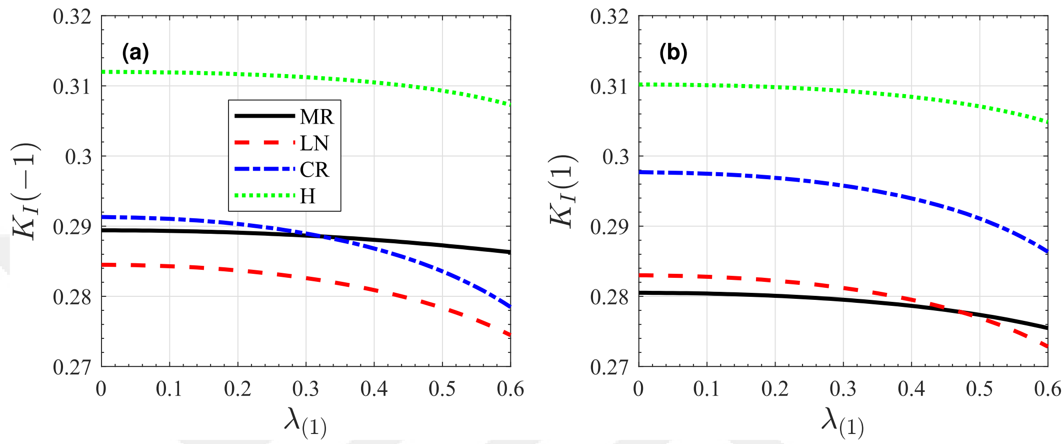

Figure 5.7. Stress intensity factors computed by considering FGM coatings in contact with a moving flat punch: (a) $K_I(-1)$ (b) $K_I(1)$. b/h=1, η=0.4.

The impact of punch speed on stresses is shown in Figure 5.8 for a CR coating loaded by triangular punch referring to Figure 4.3. Dimensionless punch speed is especially effectual on normal contact stress S_{XX}. A significant drop in the magnitude is observed when $\lambda_{(1)}$ is increased from 0.0 to 0.7. Lateral stress is also affected by the punch speed in the same way to a lesser extent. The variations of SIF at $s=-1$ and normalized punch force are depicted in Figure 5.9 for several values of the coefficient of friction. It is worthy to mention that SIF and punch force are inversely correlated with $\lambda_{(1)}$. The competing effect of η on SIF and punch force can also be observed in Figure 5.9. SIF and punch force respond differently to the change in the coefficient of friction. When η is increased from frictionless case to a highly frictional punch, SIF drops whereas the punch force enlarges its magnitude.

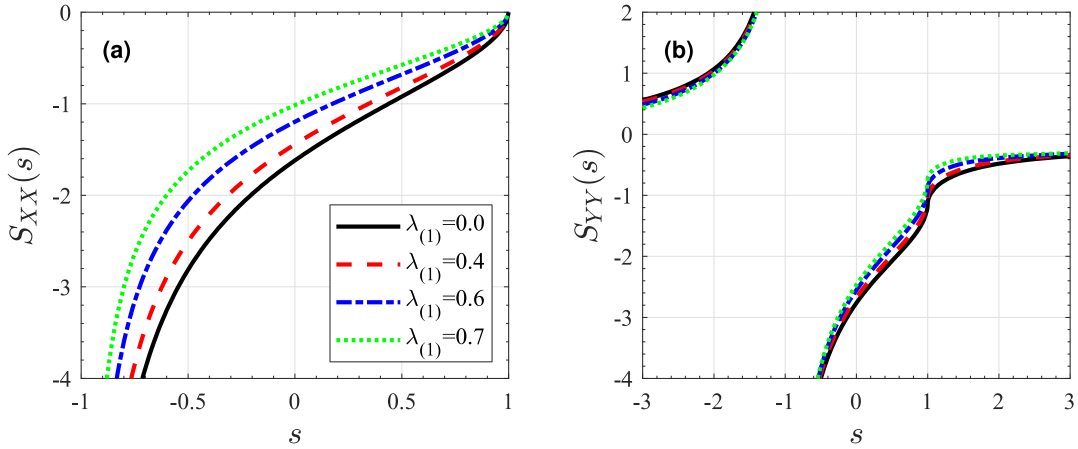

Figure 5.8. Contact stresses computed by considering a CR coating in contact with a moving triangular punch for various values of $\lambda_{(1)}$: (a) normal stress; (b) normal stress in lateral direction. b/h=0.5, η=0.4.

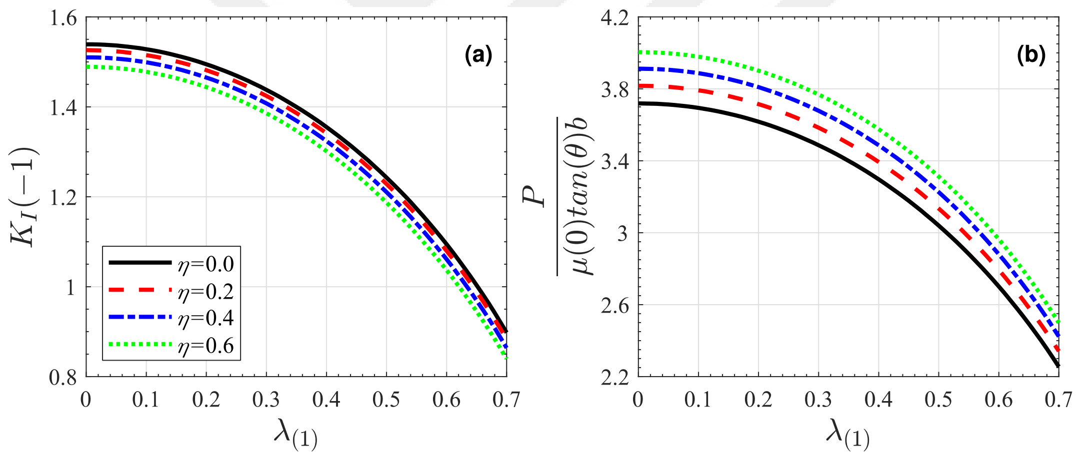

Figure 5.9. Stress intensity factor and normalized punch force computed by considering a CR coating in contact with a moving triangular punch for various values of η. b/h=0.5.

The last parameter examined in this part is relative contact length (contact length to coating thickness ratio, b/h). It is known that this parameter has a vital importance in the contact models. The depiction of numerical results which shows the influence of this parameter is presented in Figure 5.10 and Figure 5.11 for a ceramic-rich coating under the effect of flat punch indentation. The magnitude of S_{XX} evaluated for a large value of b/h is more than one calculated for a smaller ratio as understood from green and black curves in Figure 5.10.

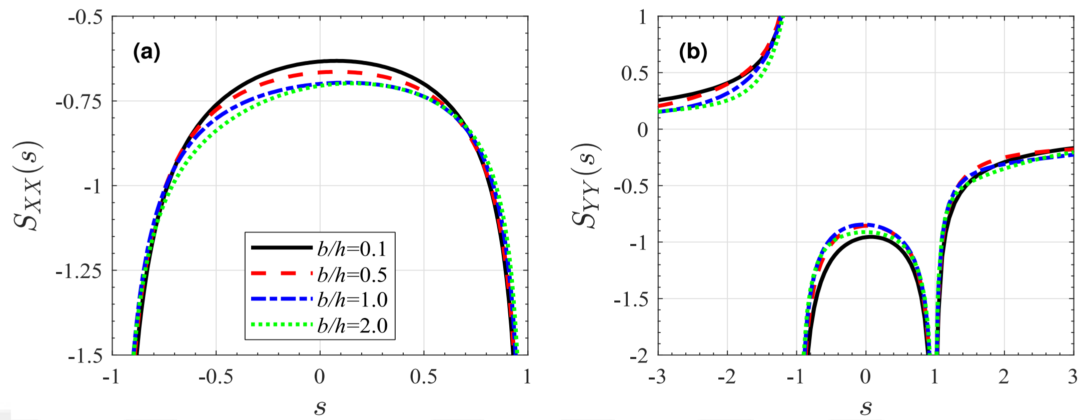

Figure 5.10. Contact stresses computed by considering a CR coating in contact with a moving flat punch for various values of b/h: (a) normal stress; (b) normal stress in lateral direction. η=0.4, $\lambda_{(1)}$=0.6.

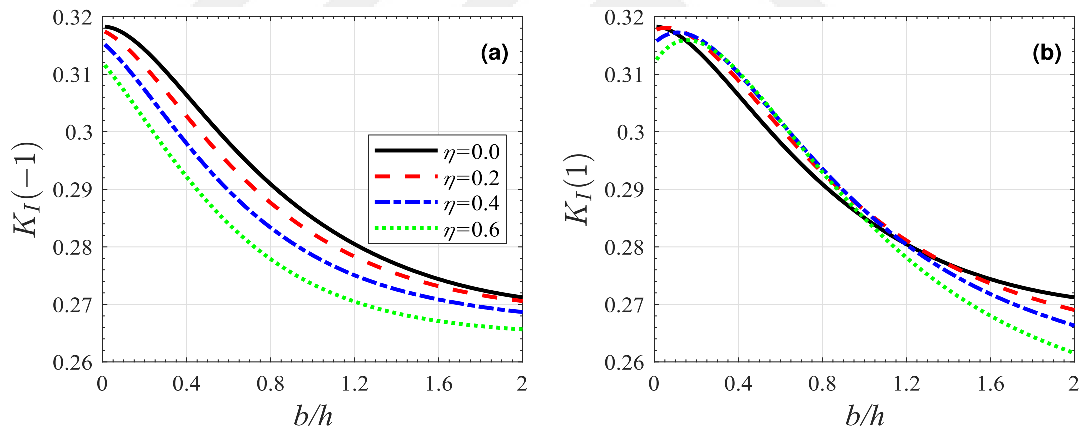

Figure 5.11. Stress intensity factors computed by considering a CR coating in contact with a moving flat punch for various values of η. $\lambda_{(1)}$=0.6.

Figure 5.11 displays the combined influences of b/h and η on mode-I stress intensity factors. Except for the frictionless case, the curves associated with $K_I(1)$ goes through a maximum level at certain b/h value between 0.1 and 0.3. As b/h is further increased, we observe that $K_I(1)$ decreases for all η values. $K_I(-1)$, on the other hand, is perpetually decreasing as a function of b/h ratio inside the examined interval.

5.1.2 Multiferroic Structure

In all multiferroic structures, the material model proposed by Scigaj et al. (2016) is selected. The half-plane material is chosen as silicon like in most device application. MEE material is the combination of $BaTiO_3$ and $CoFe_2O_4$. The buffer layers between the half-plane and the MEE coating are yttria-stabilized zirconia (YSZ), ceric oxide (CeO_2) and $LaNiO_3$. This buffer not only acts like a bonding material but also protects the silicon half-plane from the electro and magnetic fields. Thus, preserving the silicon by creating electro-magnetic insulation is another service of the buffer. Note that silicon, YSZ, and CeO_2 are isotropic; $LaNiO_3$ is cubic; and the $BaTiO_3$-$CoFe_2O_4$ composite is transversely isotropic. The relative layer thicknesses are h_2/b=0.5, h_3/b=0.25, and h_4/b=0.4375, as proposed by Scigaj et al. (2016). In this section, the coating is assumed to be equally weighted (%50-%50) in volume fraction of $BaTiO_3$ and $CoFe_2O_4$.

Referring to Figure 4.2, the properties of multiferroic coating are expressed in Eqs. (5.2). Multiferroic coating is assumed to be 100% $BaTiO_3$-$CoFe_2O_4$ composite at the exposed surface X=0 and 100% $LaNiO_3$ at the interface X=h_c. Gradation functions ensure the continuity in all properties at the interface. Note that all properties about electromagnetism are equal to zero for $LaNiO_3$. Thus, there is no jump in these properties, too. Material parameters of each layer in the FGM MEE coating are calculated in the mid-section of the corresponding sub-layer using the exact gradation functions. The properties of materials in the structure are given in Table 5.5. In the parametric analyses, four coating types namely FGM1 (linear), FGM2 (MEE rich), and FGM3 (MEE richer than FGM2) and H (pure MEE coating) are considered. The exponents of these coatings γ_i, i=1,…,17, are tabulated in Table 5.6.

5.1.2.1 Verification

To begin with, unprecedented procedures and methods in the present study are verified through the results of limiting cases of the original problem in the literature.

Zhou and Lee (2012b) considered homogeneous $BaTiO_3$-$CoFe_2O_4$ half-plane that is in contact with a frictionless moving flat punch possessing a constant speed V or a nondimensional speed $\lambda=V/\sqrt{c_{44}/\rho}$. The results in the present study are in good accordance with the ones provided by Zhou and Lee (2012b). The comparison is shown in Figure 5.12.

Table 5.5. Material properties used in the parametric analyses (set-1) (Annamalai et al., 2018; Elloumi et al., 2013; Giraud and Canel, 2008; Golalikhani et al., 2018; Masys and Jonauskas, 2015; MEMSnet, 2023; Suzuki et al., 2019).

Property	Silicon	YSZ	CeO_2	$LaNiO_3$	$BaTiO_3$-$CoFe_2O_4$
c_{11}(GPa)	188.37	284.14	286.93	405.5	226
c_{13}(GPa)	53.13	127.66	128.91	119.2	124
c_{33}(GPa)	188.37	284.14	286.93	405.5	216
c_{44}(GPa)	67.62	78.24	79.01	103.6	44
e_{15}(C/m^2)	-	-	-	-	5.8
e_{31}(C/m^2)	-	-	-	-	-2.2
e_{33}(C/m^2)	-	-	-	-	9.3
f_{15}(N/Am)	-	-	-	-	275
f_{31}(N/Am)	-	-	-	-	290.2
f_{33}(N/Am)	-	-	-	-	350
$\beta_{11}\left(10^{-9}\mathrm{C}^2/\mathrm{Nm}^2\right)$	-	-	-	-	5.64
$\beta_{33}\left(10^{-9}\mathrm{C}^2/\mathrm{Nm}^2\right)$	-	-	-	-	6.35
$\mu_{11}\left(10^{-6}\mathrm{Ns}^2/\mathrm{C}^2\right)$	-	-	-	-	297
$\mu_{33}\left(10^{-6}\mathrm{Ns}^2/\mathrm{C}^2\right)$	-	-	-	-	83.5
ρ(kg/m^3)	2330	6090	7215	7200	5550
$g_{11}\left(10^{-12}\mathrm{Ns/VC}\right)$	-	-	-	-	5.367
$g_{33}\left(10^{-12}\mathrm{Ns/VC}\right)$	-	-	-	-	2737.5

Table 5.6. Exponents used in the parametric analyses (set-1).

Property	Exponent	FGM1	FGM2	FGM3	H
c_{11}	γ_1	1	1.5	3.0	∞
c_{13}	γ_2	1	1.5	3.0	∞
c_{33}	γ_3	1	1.5	3.0	∞
c_{44}	γ_4	1	1.5	3.0	∞
e_{15}	γ_5	1	1.5	3.0	∞
e_{31}	γ_6	1	1.5	3.0	∞
e_{33}	γ_7	1	1.5	3.0	∞
f_{15}	γ_8	1	1.6	3.2	∞
f_{31}	γ_9	1	1.6	3.2	∞
f_{33}	γ_{10}	1	1.6	3.2	∞
β_{11}	γ_{11}	1	1.6	3.2	∞
β_{33}	γ_{12}	1	1.6	3.2	∞
μ_{11}	γ_{13}	1	1.8	3.6	∞
μ_{33}	γ_{14}	1	1.8	3.6	∞
ρ	γ_{15}	1	2.0	4.0	∞
g_{11}	γ_{16}	1	2.0	4.0	∞
g_{33}	γ_{17}	1	2.0	4.0	∞

Note that the dots are taken from the study by Zhou and Lee (2012b) whereas the curves are plotted using the programs special to the present study. The model in Figure 4.2 gives us the opportunity to calculate contact stresses for homogeneous MEE half-plane only if a sufficiently large thickness is chosen for MEE coating. Thus, coating thickness-to-contact size ratio (h_c/b) is equated to 10 so that the effects of other layers are minimized. In Maple code, N and M values are assigned as 1 and 3, respectively. Zhou and Lee (2012b) found that normal stress is not affected by the variation punch speed whereas a rise in the magnitude of the lateral stress is observed in the contact region. The results of these findings are confirmed by our model, too.

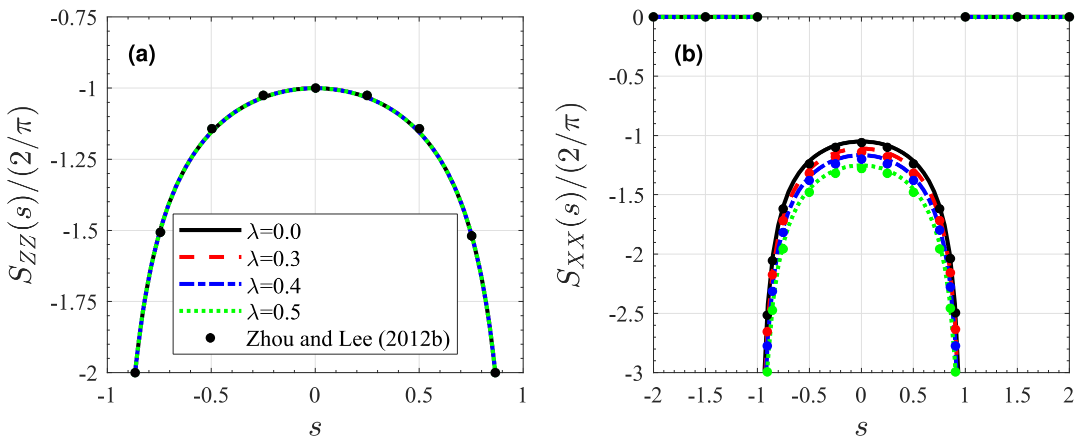

Figure 5.12. Comparisons of contact stresses for an MEE half-plane in contact with a moving flat punch to those given by Zhou and Lee (2012b): (a) normal stress in *Z*-direction; (b) normal stress in *X*-direction. η=0, h_2/b=0.5, h_3/b=0.25, h_4/b=0.4375, h_c/b=10.

5.1.2.2 Parametric Analyses

This section starts with a new convergence analysis for FGM MEE coatings. In order to determine the optimum number of MEE layers *N*, the analysis is performed by comparing not only mechanical stresses but also electric displacement and magnetic induction. The schematic given by Figure 4.2 is studied for FGM2 coating in the convergence analysis. Both kinetic friction coefficient and normalized punch speed are set as 0.3. Table 5.7 clarifies that convergence for electro-magnetic outputs is reached slower compared to mechanical stresses and all approximate percent errors fall below 0.5% when *N*=100. In conclusion, this is the optimized value used in the analyses in this section.

Figure 5.13 explains the effects of coating type on stresses and electro-magnetic results. In the central contact region, the smallest normal stress S_{ZZ} is calculated for H coating as shown in Figure 5.13(a). Yet, near the wake of the contact, the lateral stress S_{XX} is obtained as tension and the biggest magnitude of the lateral stress is found for H coating. Normalized electric displacement and magnetic induction in *X*-

direction are illustrated in Figure 5.13(c)-(d). The magnitude order of Ω_X and Γ_X is FGM1<FGM2<FGM3<H for $1<|s|$. In the contact zone, the magnitudes of electro-magnetic outputs fluctuate. Stress intensity factors for this analysis are stated in Table 5.8. $K_I(-1)$ and $K_I(1)$ designate that the lowest values are obtained for FGM1 (linear) coating which possess the lowest MEE content in itself. SIFs at the leading end is greater than the ones at the trailing end for all coatings which indicate that failure is more likely to occur near the leading end.

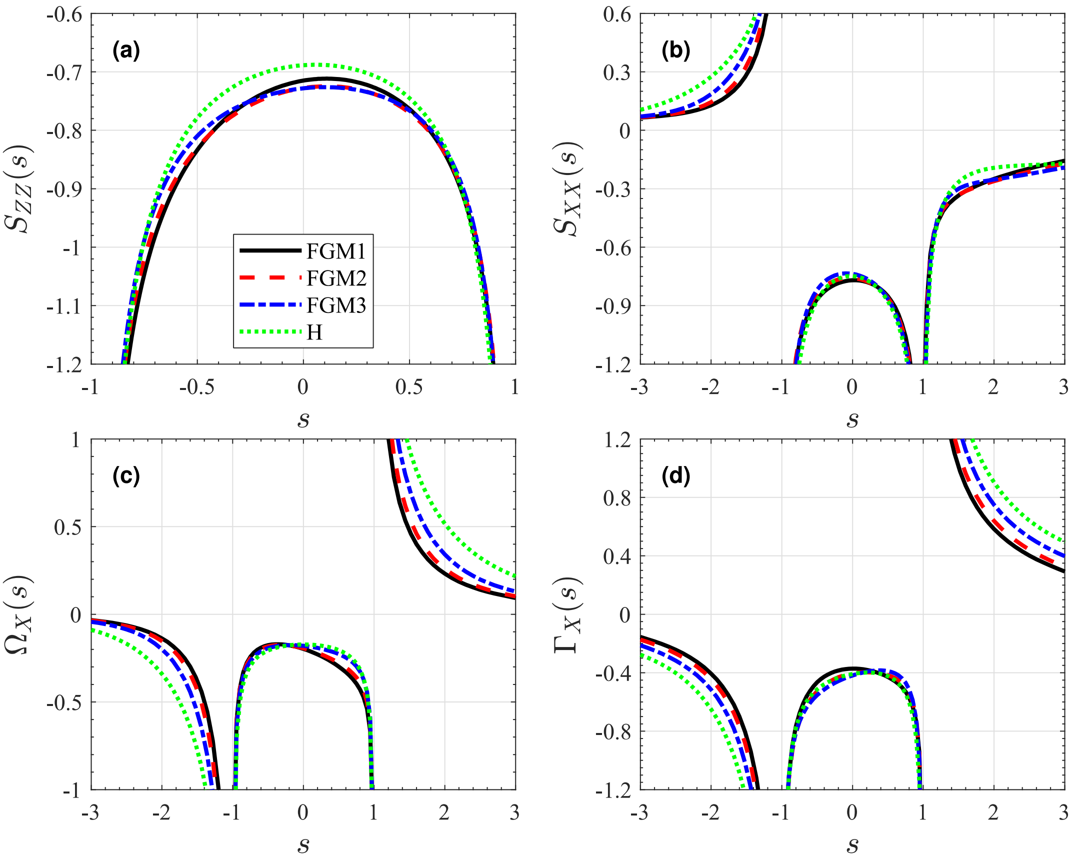

Figure 5.13. Mechanic and electro-magnetic results computed for different MEE coatings in contact with a moving flat punch: (a) normal stress in Z-direction; (b) normal stress in X-direction; (c) electric displacement in X-direction; (d) magnetic induction in X-direction. h_2/b=0.5, h_3/b=0.25, h_4/b=0.4375, h_c/b=1, η=0.3, $\lambda_{(1)}$=0.3.

Table 5.7. Number of layers, stresses, electric displacement, magnetic induction and percent approximate errors computed at s=0 for an FGM2 coating in contact with a moving flat punch. h_2/b=0.5, h_3/b=0.25, h_4/b=0.4375, h_c/b=1, η=0.3, $\lambda_{(1)}$=0.3.

N	$S_{ZZ}(0)$	ε_a	$S_{XX}(0)$	ε_a	$\Omega_X(0)$	ε_a	$\Gamma_X(0)$	ε_a
10	-0.7272	-	-0.7611	-	-0.1834	-	-0.3901	-
50	-0.7276	0.05	-0.7588	0.30	-0.1934	5.17	-0.4036	3.34
100	-0.7277	0.01	-0.7587	0.01	-0.1941	0.36	-0.4045	0.22
150	-0.7277	0.00	-0.7587	0.00	-0.1943	0.10	-0.4047	0.05

Table 5.8. Stress intensity factors computed for different MEE coatings in contact with a moving flat punch. h_2/b=0.5, h_3/b=0.25, h_4/b=0.4375, h_c/b=1, η=0.3, $\lambda_{(1)}$=0.3.

	FGM1	FGM2	FGM3	H
$K_I(-1)$	0.2475	0.2538	0.2664	0.2867
$K_I(1)$	0.2481	0.2577	0.2746	0.2980

The punch speed is another parameter that has a bearing on the response of the coating. In this set, the coating length to contact size ratio and kinetic coefficient of friction are chosen as 1 and 0.3, respectively. The influence of punch speed is especially crucial in contact stresses of FGM2 coating as illustrated in Figure 5.14. The tendency of both stress components is to expand its magnitude in the mid-section of the contact zone. It is also detected that electric displacement and magnetic induction are not responsive and vulnerable to the change in punch speed. Table 5.9 implies that $K_I(-1)$ and $K_I(1)$ become really close to each other for quasi-static punch case. However, this situation is not valid for moving punches. Another conclusion from Table 5.9 is that both mode-I SIFs tend to lessen as $\lambda_{(1)}$ increases. In short, consideration of punch speed in contact problems is obligatory for obtaining especially accurate mechanical results.

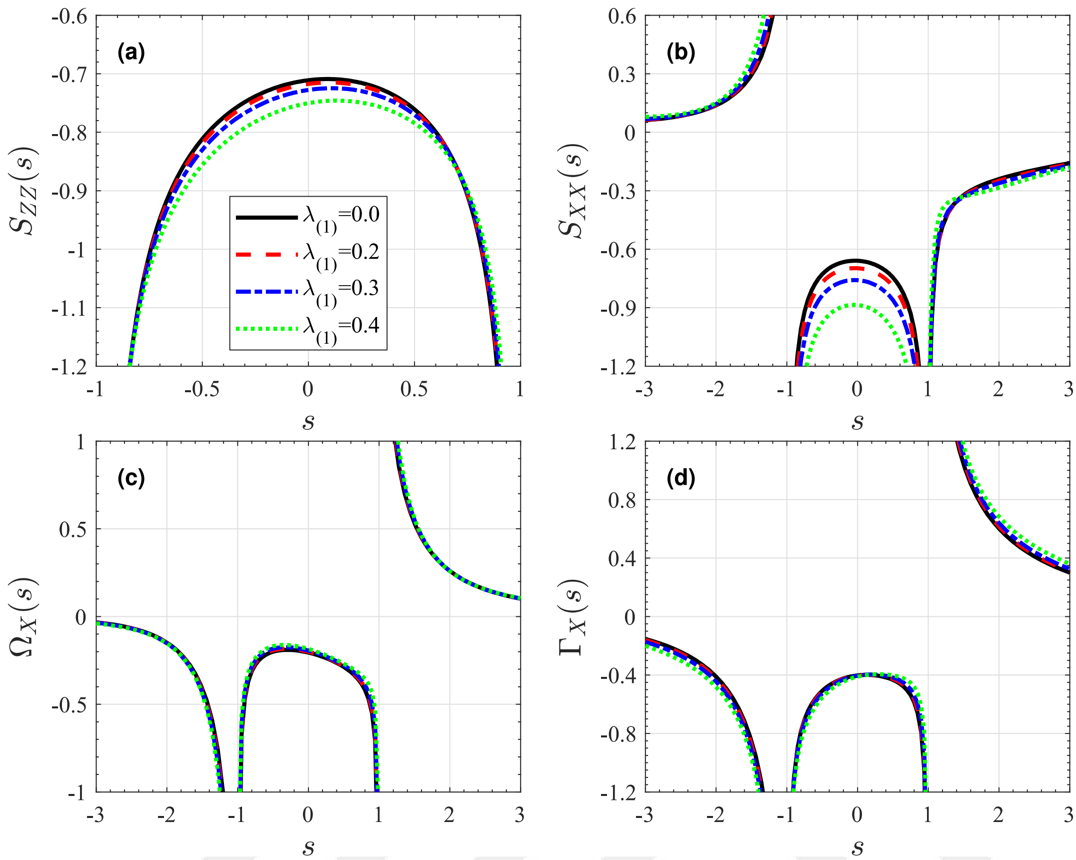

Figure 5.14. Mechanic and electro-magnetic results computed by considering an FGM2 coating in contact with a moving flat punch for various values of $\lambda_{(1)}$: (a) normal stress in Z-direction; (b) normal stress in X-direction; (c) electric displacement in X-direction; (d) magnetic induction in X-direction. h_2/b=0.5, h_3/b=0.25, h_4/b=0.4375, h_c/b=1, η=0.3.

Table 5.9. Stress intensity factors computed for an FGM2 coating in contact with a moving flat punch for various values of $\lambda_{(1)}$. h_2/b=0.5, h_3/b=0.25, h_4/b=0.4375, h_c/b=1, η=0.3.

	$\lambda_{(1)}$			
	0.0	0.2	0.3	0.4
$K_I(-1)$	0.2699	0.2639	0.2538	0.2305
$K_I(1)$	0.2695	0.2651	0.2577	0.2401

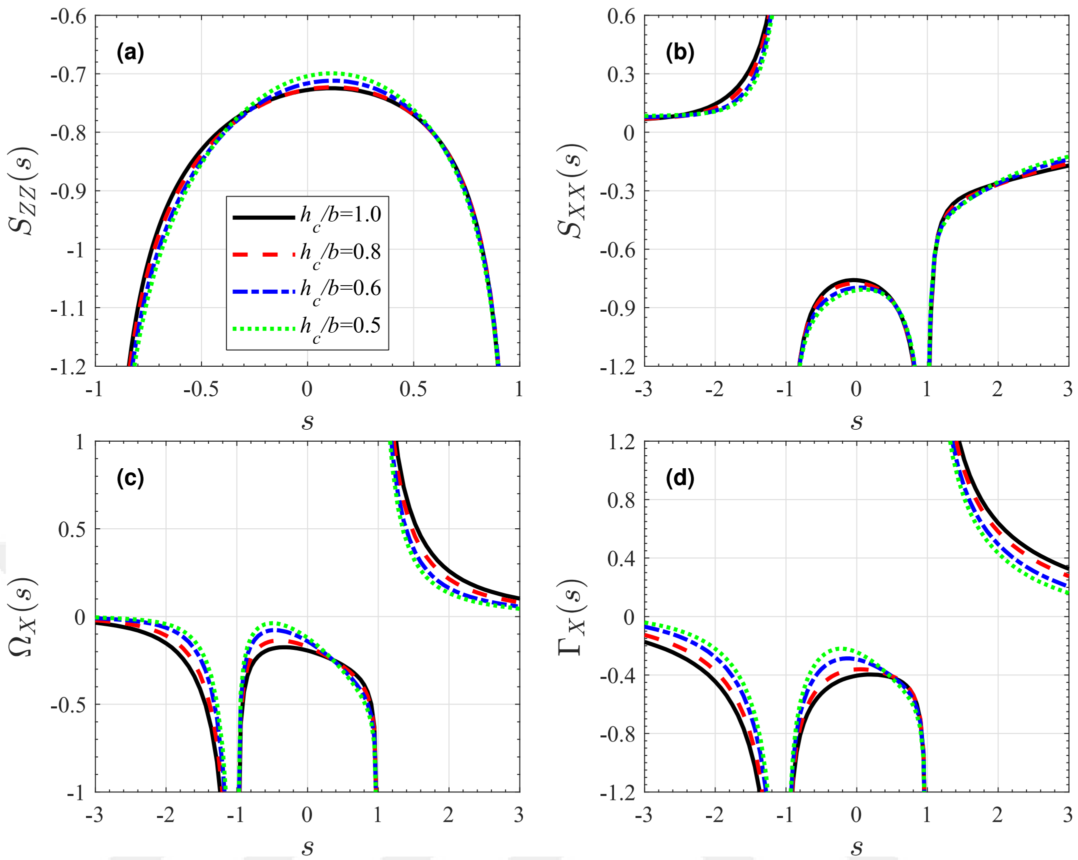

Figure 5.15. Mechanic and electro-magnetic results computed by considering an FGM2 coating in contact with a moving flat punch for various values of h_c/b: (a) normal stress in Z-direction; (b) normal stress in X-direction; (c) electric displacement in X-direction; (d) magnetic induction in X-direction. h_2/b=0.5, h_3/b=0.25, h_4/b=0.4375, η=0.3, $\lambda_{(1)}$=0.3.

In Figure 5.15 and Table 5.10, the impact of thinner and thicker coatings is investigated considering h_c/b ratio. Again, FGM2 coating is preferred in this set. Also note that, both the friction coefficient of Coulomb's law and normalized punch speed of the first layer are chosen as 0.3. The center zone in the contact stresses is affected by the change in the coating size. The amplitude of normal contact stress S_{ZZ} is directly proportionate to the h_c/b ratio but one can observe the inverse of this behavior for lateral contact stress in the contact region. The general tendency of the curves of the electric displacement and magnetic induction is notably same. The relevancy between h_c/b ratio and electromagnetism is noteworthy as the electro-magnetic reaction of the structure against the contact loading become larger with a corresponding increase in h_c/b ratio in almost everywhere. SIFs in Table 5.10 indicate that MEE rich structures (thicker coatings) lead to greater stress intensifications at the sharp end points of the contact. This incident is also confirmed in Table 5.8.

Table 5.10. Stress intensity factors computed for an FGM2 coating in contact with a moving flat punch for various values of h_c/b. h_2/b=0.5, h_3/b=0.25, h_4/b=0.4375, η=0.3, $\lambda_{(1)}$=0.3.

	h_c/b			
	0.5	0.6	0.8	1.0
$K_I(-1)$	0.2443	0.2458	0.2496	0.2538
$K_I(1)$	0.2412	0.2443	0.2511	0.2577

Figure 4.4 depicts the triangular punch sliding with constant speed V over MEE multi-layer system and the pertaining results are given in Figure 5.16-Figure 5.18 and Table 5.11-Table 5.13. Due to the physics of the problem, singularity occurs at s=−1 whereas transition at s=1 is smooth and the results converge to finite values. Figure 5.16 analyzes the influence of the coating type on the results. Normal contact stress S_{ZZ} and lateral contact stress S_{XX} when $-1 < s$ seem to inversely affected by the content of MEE material in the coating. On the other hand, S_{XX} spikes to tensile infinity behind the wake of the punch and the sharpest peak occurs for H coating. Both electric displacement Ω_X and magnetic induction Γ_X shoot to negative infinity at s=−1 and reach maximum apexes at s=1. Among four coatings, utilization of H and FGM3 coatings end up with largest electric displacement and magnetic induction at s=1, respectively. It is inferred from Table 5.11 that lesser punch force and SIF occur in H coating. The greatest magnitudes are evaluated for FGM1 coating that is the poorest in MEE content among FGM coatings.

Dimensionless punch speed has striking effect solely on normal contact stress for FGM2 coating as shown in Figure 5.17. A rise in $\lambda_{(1)}$ fetches up with drop in S_{ZZ}. From the same figure, it is also drawn conclusion that the peaks of electric displacement and magnetic induction lessen as the dimensionless punch speed is boosted from 0 to 0.4. Similarly, Table 5.12 remarks that the punch speed diminishes the punch force and SIF. Hence, one can say that the punch speed has extenuative effects on every result as a conclusion.

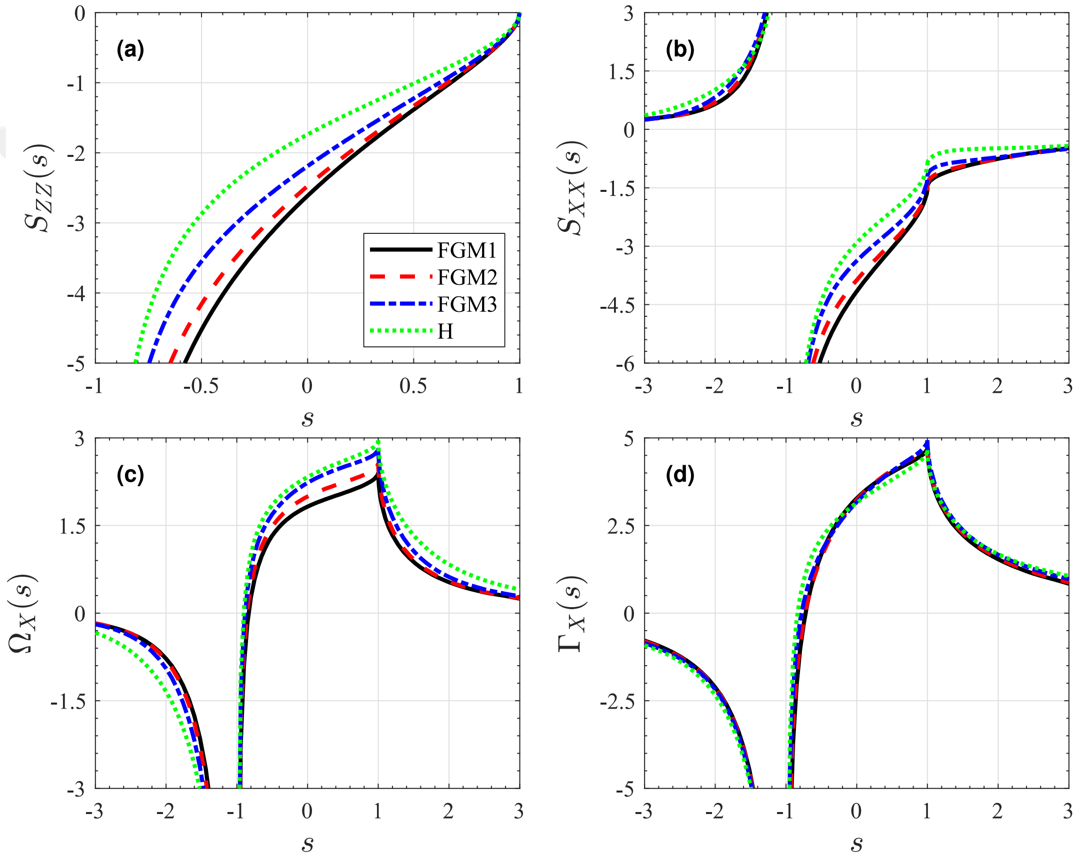

Figure 5.16. Mechanic and electro-magnetic results computed for different MEE coatings in contact with a moving triangular punch: (a) normal stress in Z-direction; (b) normal stress in X-direction; (c) electric displacement in X-direction; (d) magnetic induction in X-direction. h_2/b=0.5, h_3/b=0.25, h_4/b=0.4375, h_c/b=1, η=0.3, $\lambda_{(1)}$=0.3.

Table 5.11. Stress intensity factor and contact force computed for different MEE coatings in contact with a moving triangular punch. h_2/b=0.5, h_3/b=0.25, h_4/b=0.4375, h_c/b=1, η=0.3, $\lambda_{(1)}$=0.3.

	FGM1	FGM2	FGM3	H
$K_I(-1)$	1.7536	1.6754	1.5713	1.4481
$P/(c_{44}(0)\tan(\theta)b)$	3.8019	3.5235	3.1171	2.6415

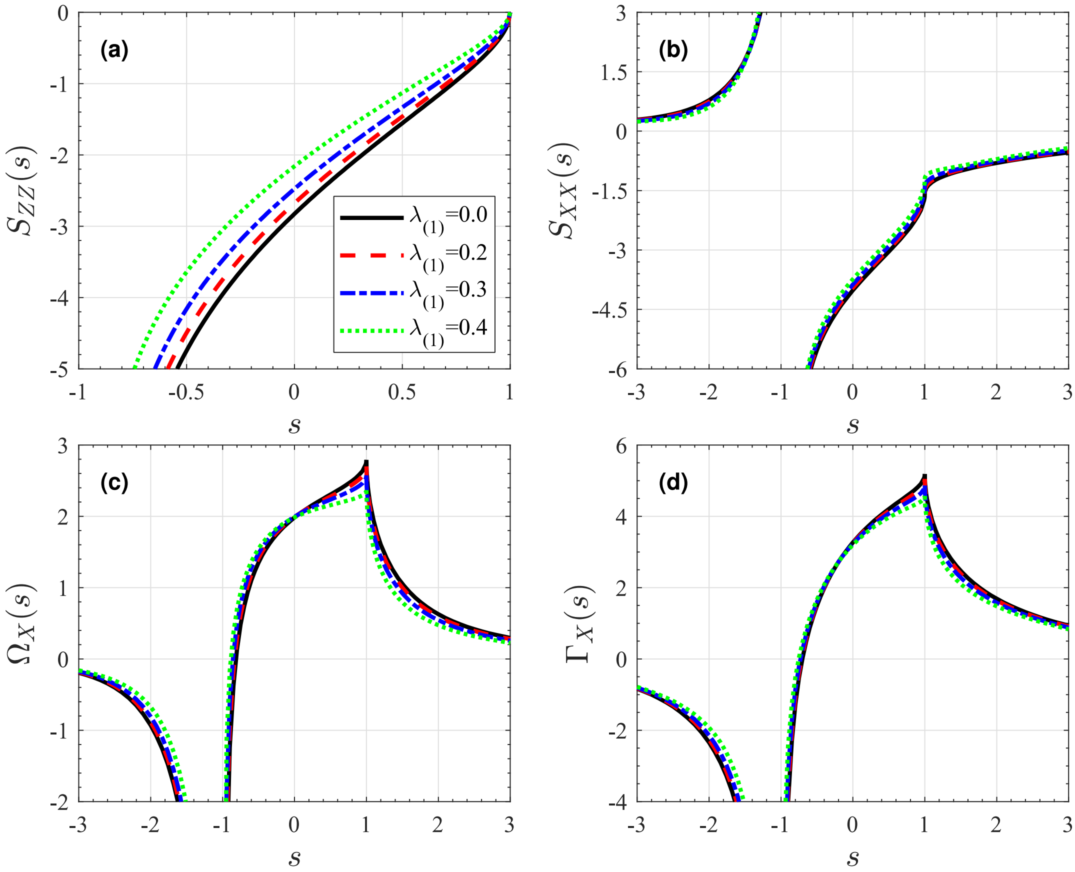

Figure 5.17. Mechanic and electro-magnetic results computed by considering an FGM2 coating in contact with a moving triangular punch for various values of $\lambda_{(1)}$: (a) normal stress in Z-direction; (b) normal stress in X-direction; (c) electric displacement in X-direction; (d) magnetic induction in X-direction. h_2/b=0.5, h_3/b=0.25, h_4/b=0.4375, h_c/b=1, η=0.3.

Table 5.12. Stress intensity factor and contact force computed for an FGM2 coating in contact with a moving triangular punch for various values of $\lambda_{(1)}$. h_2/b=0.5, h_3/b=0.25, h_4/b=0.4375, h_c/b=1, η=0.3.

	$\lambda_{(1)}$			
	0.0	0.2	0.3	0.4
$K_I(-1)$	2.0882	1.9142	1.6754	1.2844
$P/(c_{44}(0)\tan(\theta)b)$	4.1003	3.8555	3.5235	2.9932

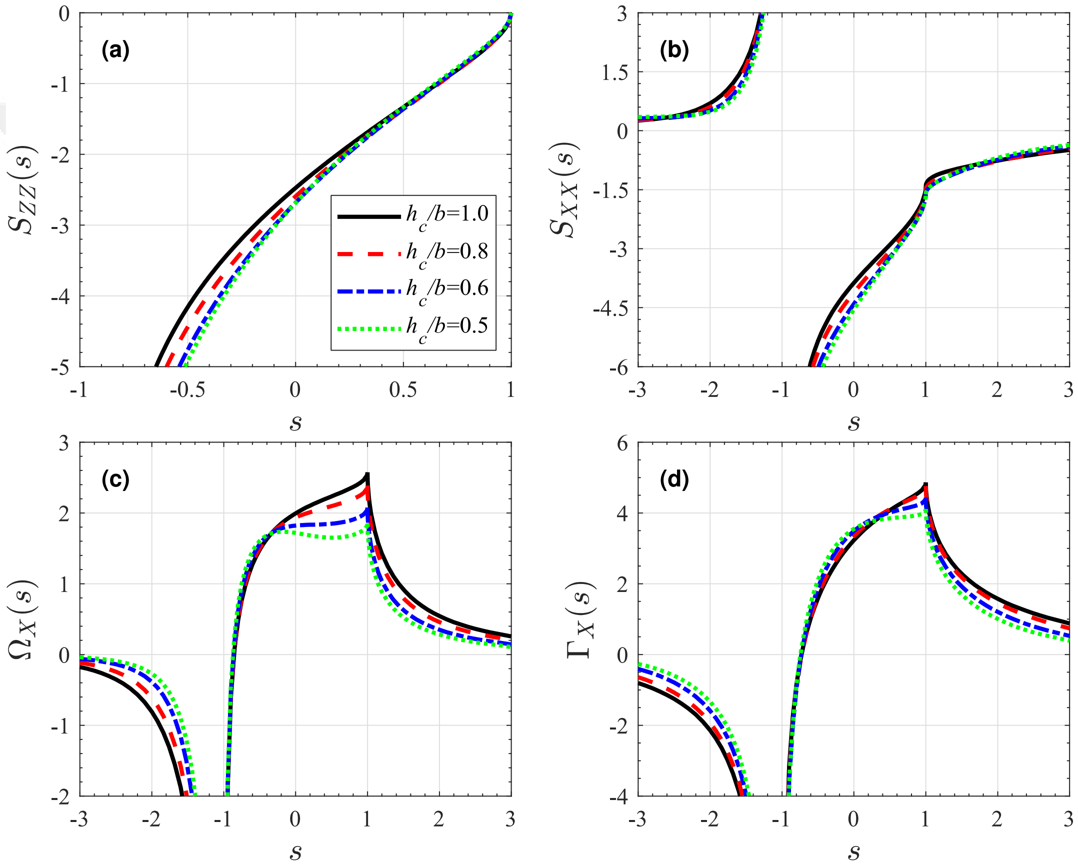

Figure 5.18. Mechanic and electro-magnetic results computed by considering an FGM2 coating in contact with a moving triangular punch for various values of h_c/b: (a) normal stress in Z-direction; (b) normal stress in X-direction; (c) electric displacement in X-direction; (d) magnetic induction in X-direction. h_2/b=0.5, h_3/b=0.25, h_4/b=0.4375, η=0.3, $\lambda_{(1)}$=0.3.

The influence of relative coating thickness, h_c/b, is examined considering FGM2 coating in Figure 5.18 and Table 5.13. Inside the contact zone, both contact stresses are inclined to decrease their magnitudes as the coating becomes thicker. Substantial changes in electric displacement and magnetic induction are observed with the variation of coating size. Thicker coatings induce greater electro-magnetic outputs in almost everywhere. The peak at s=1 for electric displacement is more sensitive to h_c/b ratio than the one for magnetic induction. Table 5.13 draws attention to the variation of SIF and punch force with respect to h_c/b. Both examined functions in Table 5.13 are decreasing functions of coating thickness to contact size ratio. In short, it is concluded that the energy transformed by the contact to the structure shifts to electro-magnetic fields as the coating becomes thicker.

Table 5.13 Stress intensity factor and contact force computed for an FGM2 coating in contact with a moving triangular punch for various values of h_c/b. h_2/b=0.5, h_3/b=0.25, h_4/b=0.4375, η=0.3, $\lambda_{(1)}$=0.3.

	h_c/b			
	0.5	0.6	0.8	1.0
$K_I(-1)$	1.7907	1.7681	1.7200	1.6754
$P/(c_{44}(0)\tan(\theta)b)$	3.9714	3.8862	3.6988	3.5235

5.2 Numerical Results for Semi-Circular Punch

This section is presented by the author collaborating with his supervisor in Contact Mechanics International Symposium (CMIS 2022) in Lausanne, Switzerland and 23th National Mechanics Congress in Konya, Türkiye for multi-layer model and multiferroic structure, respectively (Toktas and Dag, 2022b; 2023b).

5.2.1 Multi-layer Model

Stiffer coatings are generally encountered in applications. These coatings show more resistance against the failures caused by wear. One commonly used material as stiffer coating is silicon carbide which offers desirable hardness while being relatively light weighted. In this section, such a system formed by aluminum substrate and silicon carbide is exposed to semi-circular punch indentation in the contact problem. Note that Young's modulus of silicon carbide is six times greater than Young's modulus of aluminum.

5.2.1.1 Verification

Similar to Section 5.1.1.1, the model is verified through the contact analyses of exponentially graded coatings done by Balci and Dag (2018b). Figure 5.19 presents contact stresses originating from the indentation of semi-circular punch. Dotted data is directly taken from the results provided by Balci and Dag (2018b), whereas the results shown by curves belong to the present study. In this analysis, proportional gradation is compulsorily thought and shear modulus and density of the structure are six times higher at X=0 than the ones at X=h. Kolosov's constant is accepted as an unvarying property and other parameters are provided in the figure cation. N is found as 150 from Table 5.14 by conducting a convergence analysis similar to previous sections. Although there is a slight deviation in lateral stress results caused by the highest punch speed λ=0.7, the other results match perfectly.

Table 5.14. Number of layers, stresses, and percent approximate errors computed at s=0 for a graded coating whose properties are varying with exponential functions in contact with a moving semi-circular punch. b/R=0.01, b/h=1, η=0.3, κ=2, $\mu(h)/\mu(0)$=1/6, $\rho(h)/\rho(0)$=1/6, λ=0.4.

N	$S_{XX}(0)$	ε_a	$S_{YY}(0)$	ε_a
10	-0.00849900	-	-0.02042753	-
50	-0.00850562	0.08	-0.02191909	6.80
100	-0.00850368	0.02	-0.02214929	1.04
150	-0.00850272	0.01	-0.02222764	0.35
200	-0.00850222	0.01	-0.02226687	0.18

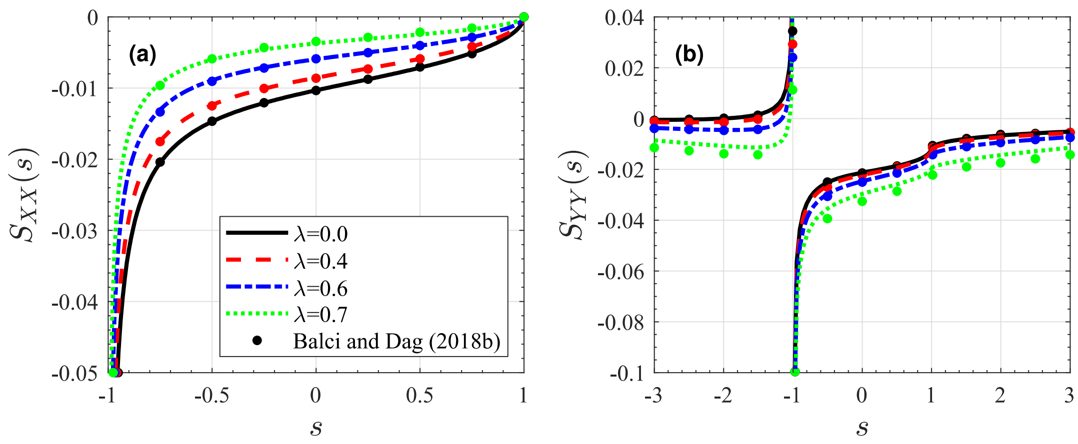

Figure 5.19. Comparison of contact stresses for a graded coating whose properties are varying with exponential functions in contact with a moving semi-circular punch to those given by Balci and Dag (2018b): (a) normal stress; (b) normal stress in lateral direction. b/R=0.01, b/h=0.2, η=0.3, κ=2, $\mu(h)/\mu(0)$=1/6, $\rho(h)/\rho(0)$=1/6.

5.2.1.2 Parametric Analyses

Based on Figure 4.5, Eq. (5.1) defines the properties of the structure and removes all restrictions about the property gradations. The FGM coating is 100% ceramic (SiC) at the exposed surface X=0 and 100% metal (Al) at the interface $X=h$. Table 5.15 informs us about the properties of SiC and Al used in the analyses. The power-law exponents are tabulated in Table 5.3. Note that, material properties are continuous at the interface.

Table 5.15. Properties of silicon carbide and aluminum (Eshraghi and Dag, 2018).

	E(GPa)	ρ(kg/m^3)	v
Silicon Carbide (SiC)	427	3100	0.17
Aluminum (Al)	70	2702	0.30

Firstly, the analyses should start with a convergence analysis on a coating whose gradation is more severe. As a sample, CR coating is preferred and the model parameters represent relatively harsher conditions as shown in the caption of Table

5.16. Our findings manifest that the convergence is attained in the last row of the convergence table when N=250 since the percent error ε_a does not reduce to the desired level under 1% until the last row. Compared to the other sections in this study, the convergence is assured at a relatively high value of N. This is due to the huge gradation ratio of shear modulus of ceramic and metal pair used in the analyses. Therefore, one may conclude that the most powerful factor affecting the optimum value of N is the choice of pair in the structure.

Table 5.16. Number of layers, stresses, and approximate errors computed at s=0 for a CR coating in contact with a moving semi-circular punch. b/R=0.01, b/h=1, η=0.3, $\lambda_{(1)}$=0.4.

N	$S_{XX}(0)$	ε_a	$S_{YY}(0)$	ε_a
10	-0.00781299	-	-0.01695857	-
50	-0.00569280	37.24	-0.01731098	2.04
100	-0.00531441	7.12	-0.01730294	0.05
150	-0.00518106	2.57	-0.01729517	0.04
200	-0.00511298	1.33	-0.01729021	0.03
250	-0.00507169	0.81	-0.01728687	0.02

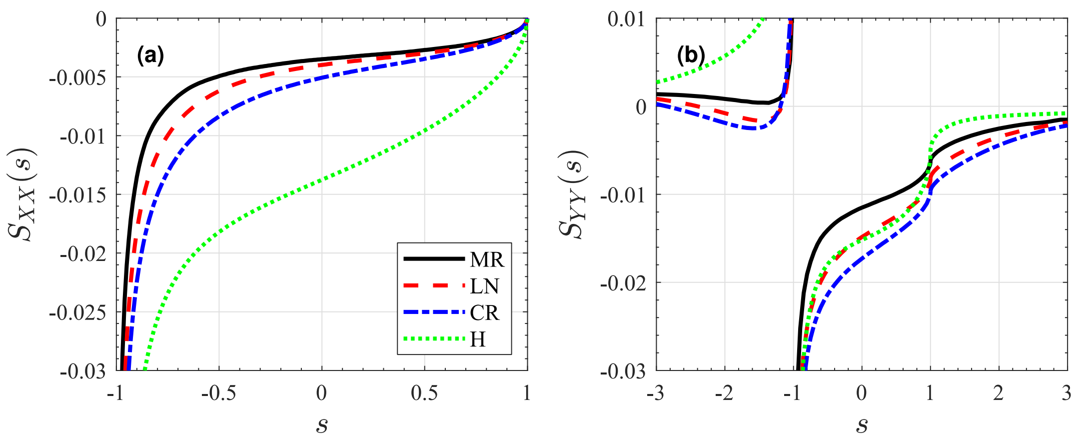

Figure 5.20. Contact stresses computed by considering FGM coatings in contact with a moving semi-circular punch: (a) normal stress; (b) normal stress in lateral direction. b/R=0.01, b/h=1, η=0.3, $\lambda_{(1)}$=0.4.

In Figure 5.20, the comparisons of stress distributions for four coating types are illustrated. Model parameters are given in the captions. By examining S_{XX} distributions, one may see that the homogeneous ceramic coating (H) possesses the largest normal stress magnitude in the contact area. The values calculated for the FGM coatings are considerably small and closer to zero. Comparatively higher tensile stresses are computed for the homogeneous coating near the trailing end. On the contrary, the magnitude of the stress component S_{YY} is lower near the leading end of the contact when the coating is homogeneous. From Table 5.17, it is found that as the ceramic content in the coating increases, both normalized punch force and punch stress intensity factor increase.

Table 5.17. Contact force and stress intensity factor computed for FGM coatings in contact with a moving semi-circular punch. b/R=0.01, b/h=1, η=0.3, $\lambda_{(1)}$=0.4.

	$P/(\mu(0)R)$	$K_I(-1)$
MR	0.00004726	0.00313765
LN	0.00006649	0.00402368
CR	0.00008270	0.00459226
H	0.00016631	0.00637512

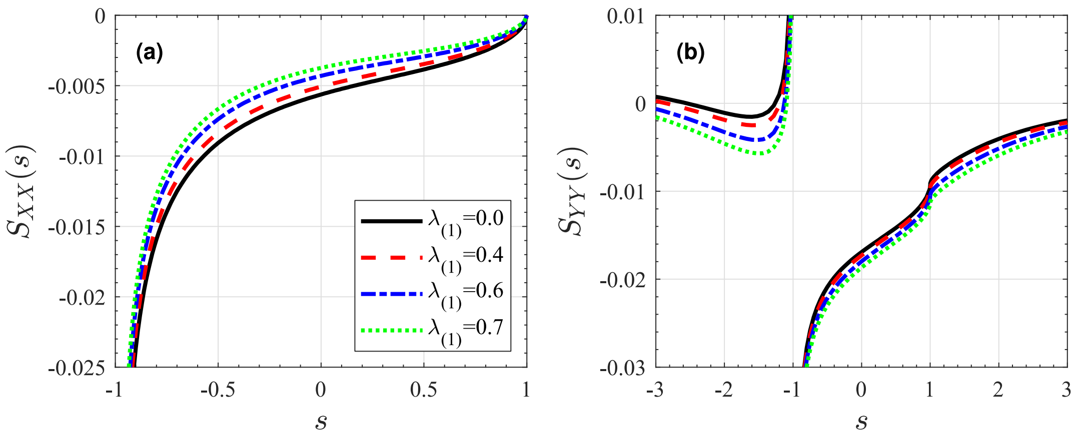

Figure 5.21. Contact stresses computed by considering a CR coating in contact with a moving semi-circular punch for various values of $\lambda_{(1)}$: (a) normal stress; (b) normal stress in lateral direction. b/R=0.01, b/h=1, η=0.3.

In Figure 5.21, the influence of punch speed is demonstrated for CR coating. Lateral stress becomes greater as the dimensionless punch speed increases except for a narrow region near $s = -1^{-}$. On the other hand, opposite behavior is observed for the normal contact stress. As shown in Table 5.18, a rise in the normalized punch speed causes a drop in both normalized punch force and SIF.

Table 5.18. Contact force and stress intensity factor computed for a CR coating in contact with a moving semi-circular punch for various values of $\lambda_{(1)}$. b/R=0.01, b/h=1, η=0.3.

$\lambda_{(1)}$	$P/(\mu(0)R)$	$K_I(-1)$
0.0	0.00008893	0.00480585
0.4	0.00008270	0.00459226
0.6	0.00007402	0.00429787
0.7	0.00006764	0.00408402

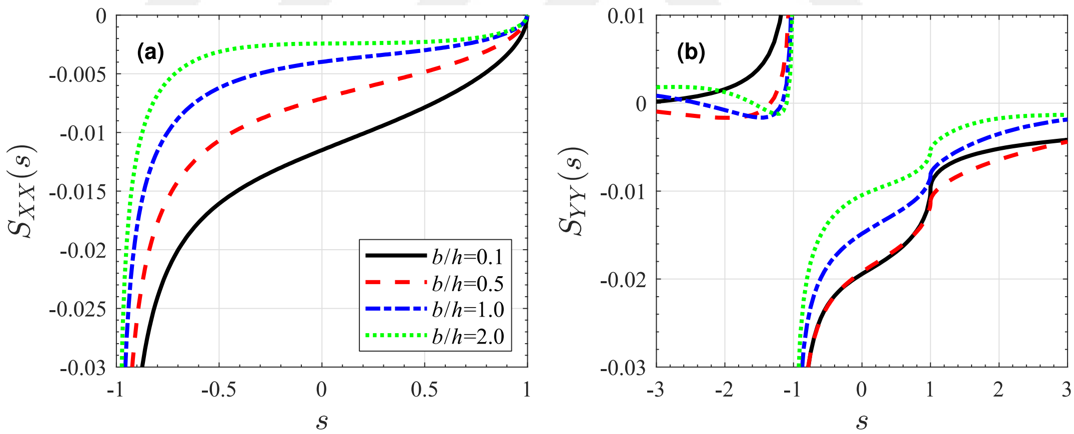

Figure 5.22. Contact stresses computed by considering an LN coating in contact with a moving semi-circular punch for various values of b/h: (a) normal stress; (b) normal stress in lateral direction. b/R=0.01, η=0.3, $\lambda_{(1)}$=0.4.

Another set of results is presented for the variation of contact size-to-coating thickness ratio for LN coating in Figure 5.22 and Table 5.19. As the contact length-to-coating thickness ratio b/h is increased from 0.1 to 2.0, the magnitude of the normalized stress S_{XX} becomes smaller. The effect on the stress in Y-direction is also seen to be significant. Largest positive peak at the trailing end of the contact is calculated when b/h=0.1 (the thickest coating). It is found that both the contact force and punch stress intensity factor are found to be decreasing functions of b/h ratio.

Table 5.19. Contact force and stress intensity factor computed for an LN coating in contact with a moving semi-circular punch for various values of b/h. b/R=0.01, η=0.3, $\lambda_{(1)}$=0.4.

b/h	$P/(\mu(0)R)$	$K_I(-1)$
0.1	0.00014872	0.00639009
0.5	0.00010356	0.00531043
1	0.00006649	0.00402368
2	0.00004332	0.00312038

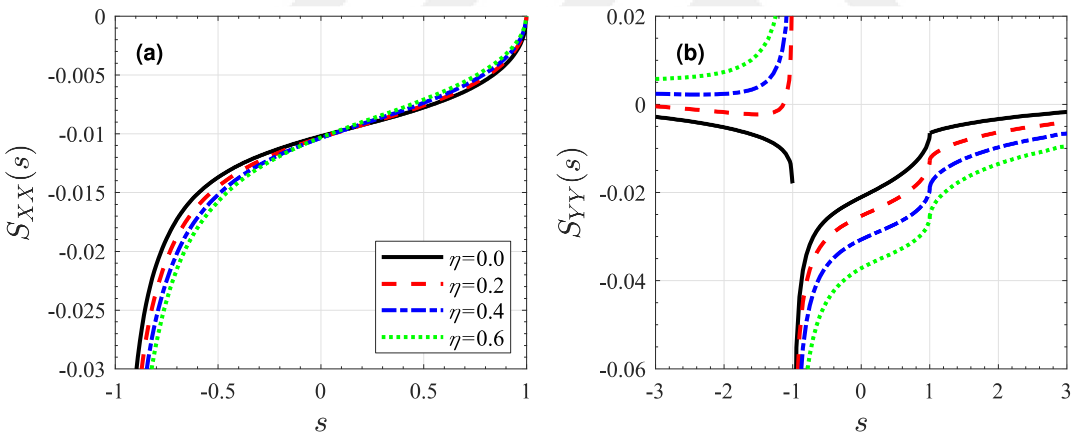

Figure 5.23. Contact stresses computed by considering an MR coating in contact with a moving semi-circular punch for various values of η: (a) normal stress; (b) normal stress in lateral direction. b/R=0.02, b/h=0.5, $\lambda_{(1)}$=0.4.

In Figure 5.23, we show the influence of the kinetic coefficient of friction η on the normalized contact stresses for MR coating. The effect of friction on especially contact stress in lateral direction is quite impressive. Lateral stress is negative for all values of s when frictionless contact is assumed. Black curve for frictionless contact in Figure 5.23(b) seems like as if it stops around -0.019 at $s=-1^{-}$, however, it must approach to infinity if one inserts a very close number to minus one into Eq. (4.62). As η is increased, tensile peak at the trailing end becomes positive and culminates greater amplitudes. Lateral stress inside the contact region and ahead of the leading end is always found as negative and the magnitude increases with friction. Finally, the increase in the coefficient of friction leads to a corresponding increase in normalized punch force and stress intensity factor.

Table 5.20. Contact force and stress intensity factor computed for an MR coating in contact with a moving semi-circular punch for various values of η. b/R=0.02, b/h=0.5, $\lambda_{(1)}$=0.4.

η	$P/(\mu(0)R)$	$K_I(-1)$
0.0	0.00023567	0.00693993
0.2	0.00025430	0.00744500
0.4	0.00027399	0.00791598
0.6	0.00029467	0.00834619

5.2.2 Multiferroic Structure

In this section, the MEE material in the coating is assumed to be unequally weighted in the favor of $CoFe_2O_4$ (%40-%60) considering volume fractions of piezoelectric and magnetostrictive constituents based on Figure 4.6.

5.2.2.1 Parametric Analyses

Table 5.21 specifies all material properties of the heterogeneous multiferroic structure used in the analyses. Since the volume fractions of $BaTiO_3$ and $CoFe_2O_4$ are not identical, another convergence analysis is required. Note that the exponents of FGM MEE coatings are taken as the ones in Table 5.6. The obtained results of the convergence analysis are tabulated for FGM2 coating in Table 5.22. All approximate errors ε_a for normal and lateral stresses, electric displacement and magnetic induction are below 0.4% when N is equated to 100.

Table 5.21. Material properties used in the parametric analyses (set-2) (Ajdour et al., 2016; Annamalai et al., 2018; Elloumi et al., 2013; Giraud and Canel, 2008; Golalikhani et al., 2018; Masys and Jonauskas, 2015; MEMSnet, 2023; Suzuki et al., 2019).

	Silicon	YSZ	CeO_2	$LaNiO_3$	$BaTiO_3$-$CoFe_2O_4$
c_{11}(GPa)	188.37	284.14	286.93	405.5	238
c_{13}(GPa)	53.13	127.66	128.91	119.2	133.5
c_{33}(GPa)	188.37	284.14	286.93	405.5	226.5
c_{44}(GPa)	67.62	78.24	79.01	103.6	44.38
ρ(kg/m^3)	2330	6090	7215	7200	5500

$BaTiO_3$-$CoFe_2O_4$					
e_{15}(C/m^2)	4.64	f_{31}(N/Am)	348.18	$\mu_{11}\left(10^{-6}\text{Ns}^2/\text{C}^2\right)$	356
e_{31}(C/m^2)	-1.76	f_{33}(N/Am)	419.82	$\mu_{33}\left(10^{-6}\text{Ns}^2/\text{C}^2\right)$	98.2
e_{33}(C/m^2)	7.44	$\beta_{11}\left(10^{-9}\text{C}^2/\text{Nm}^2\right)$	4.528	$g_{11}\left(10^{-12}\text{Ns/VC}\right)$	4.546
f_{15}(N/Am)	330	$\beta_{33}\left(10^{-9}\text{C}^2/\text{Nm}^2\right)$	5.096	$g_{33}\left(10^{-12}\text{Ns/VC}\right)$	2769.7

Table 5.22. Number of layers, stresses, and approximate errors computed at s=0 for an FGM2 coating in contact with a moving semi-circular punch. b/R=0.01, h_2/b=0.5, h_3/b=0.25, h_4/b=0.4375, h_c/b=1, η=0.3, $\lambda_{(1)}$=0.3.

N	$S_{ZZ}(0)$	ε_a	$S_{XX}(0)$	ε_a	$\Omega_X(0)$	ε_a	$\Gamma_X(0)$	ε_a
10	-0.02290	-	-0.03101	-	0.00661	-	0.00933	-
50	-0.02290	0.00	-0.03087	0.45	0.00641	3.12	0.00904	3.21
100	-0.02290	0.00	-0.03086	0.03	0.00639	0.31	0.00903	0.11
150	-0.02290	0.00	-0.03086	0.00	0.00639	0.00	0.00902	0.11

As comprehended from the convergence analysis, N is selected as 100 in order to produce the output functions correctly. The results pertaining four different coating types (FGM1, FGM2, FGM3 and H coatings) are generated as below. Figure 5.24 and Table 5.23 presents the impact of coatings on mechanic and electro-magnetic results. In this set, thin coatings $(h_c/b=1)$, are assessed for intermediate coefficient of friction and normalized punch speed (η=0.3, $\lambda_{(1)}$=0.3). It is established from Figure 5.24 that normal stress in Z-direction for H coating is significantly lower than the ones for FGM MEE coatings. For less stiff coatings like the one examined in this section, this is an expected issue. Because the coating becomes softer as it switches to MEE rich medium. The greatest normal stress S_{ZZ} is obtained for FGM1 coating. MEE rich coatings also leads to lessening in S_{XX} for $-1 < s$. Electric displacement and magnetic induction reach to their peak levels at s=1. It is found that the maximum electric displacement and magnetic induction are calculated for H and FGM2 coatings, respectively. According to Table 5.23, the biggest SIF and punch force occur for FGM1 coating.

The influence of punch speed on FGM1 coating is demonstrated in Figure 5.25 and Table 5.24. It is observed that a reduction in dimensionless punch speed causes normal stress S_{XX} to magnify. Electro-magnetic outputs taken place for quasi-static case $\left(\lambda_{(1)}=0\right)$ at s=1 are found as the supreme values among the ones calculated for four normalized punch speeds. In addition to these, enhancing $\lambda_{(1)}$ level lowers both dimensionless punch force and SIF.

It should be noted that the normalized coating length parameter (h_c/b) plays a critical role in contact analyses. The results associated with this ratio are reported in Figure 5.26 and Table 5.25. Relatively thinner coatings amplify the stress components in contact zone $-1 < s < 1$. The exact opposite of this behavior is exhibited for electro-magnetic results almost in the entire interval. In other words, electro-magnetic activity of thinner coatings is limited with respect to thicker coatings. It is apperceived from Table 5.25 that the coating thickness affects punch force and SIF adversely.

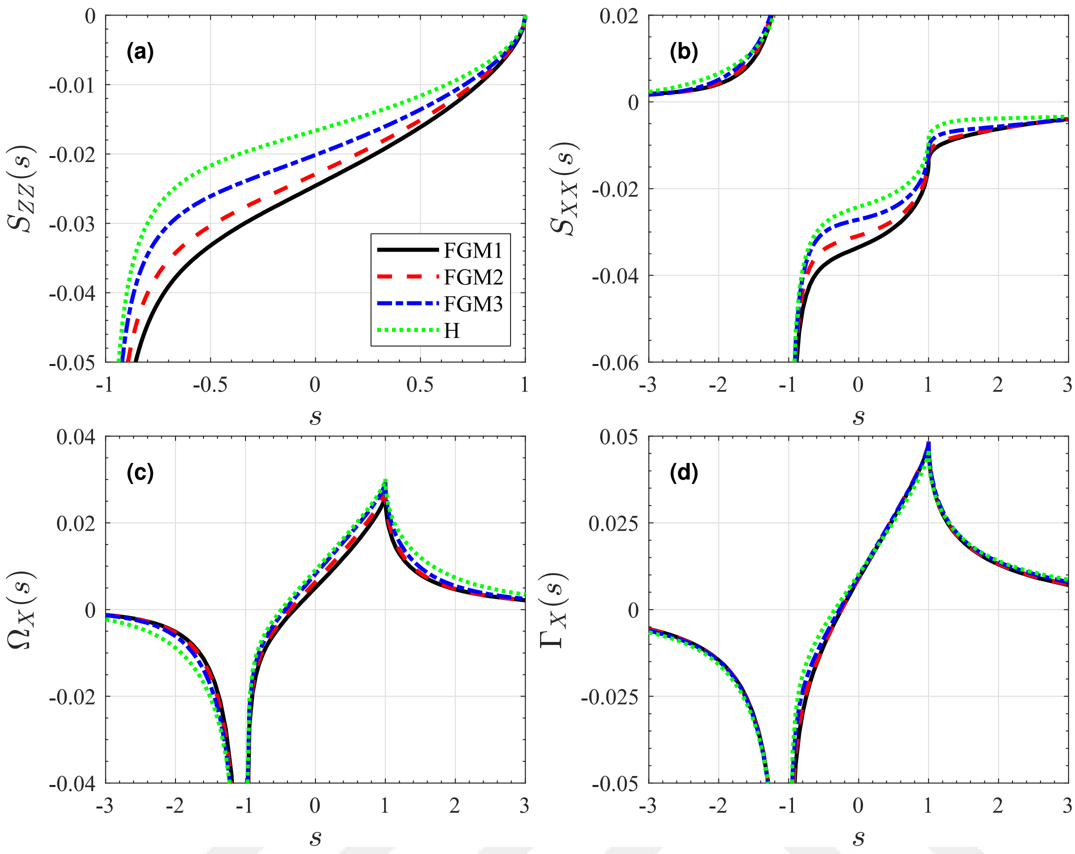

Figure 5.24. Mechanic and electro-magnetic results computed for different MEE coatings in contact with a moving semi-circular punch: (a) normal stress in Z-direction; (b) normal stress in X-direction; (c) electric displacement in X-direction; (d) magnetic induction in X-direction. b/R=0.01, h_2/b=0.5, h_3/b=0.25, h_4/b=0.4375, h_c/b=1, η=0.3, $\lambda_{(1)}$=0.3.

Table 5.23. Contact force and stress intensity factor computed for different MEE coatings in contact with a moving semi-circular punch. b/R=0.01, h_2/b=0.5, h_3/b=0.25, h_4/b=0.4375, h_c/b=1, η=0.3, $\lambda_{(1)}$=0.3.

	FGM1	FGM2	FGM3	H
$K_I(-1)$	0.009281	0.008824	0.008230	0.007576
$P/(c_{44}(0)R)$	0.000282	0.000260	0.000230	0.000197

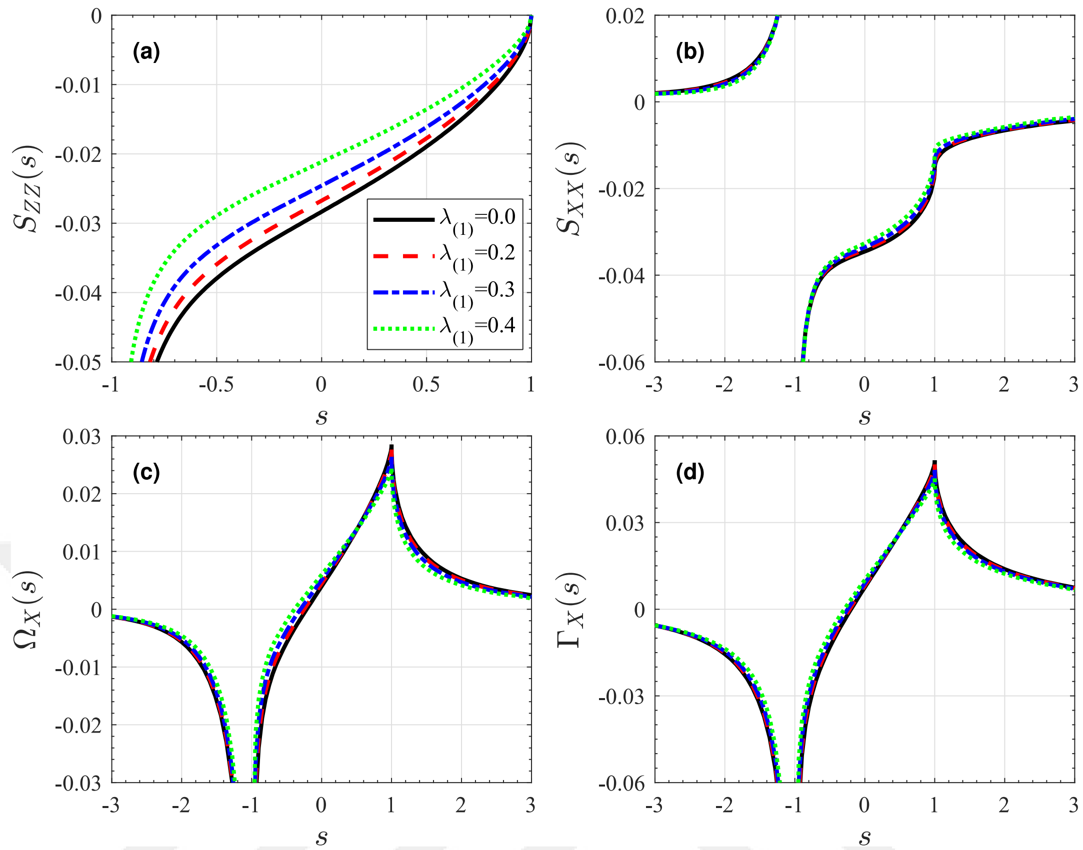

Figure 5.25. Mechanic and electro-magnetic results computed by considering an FGM1 coating in contact with a moving semi-circular punch for various values of $\lambda_{(1)}$: (a) normal stress in Z-direction; (b) normal stress in X-direction; (c) electric displacement in X-direction; (d) magnetic induction in X-direction. b/R=0.01, h_2/b=0.5, h_3/b=0.25, h_4/b=0.4375, h_c/b=1, η=0.3.

Table 5.24. Contact force and stress intensity factor computed for an FGM1 coating in contact with a moving semi-circular punch for various values of $\lambda_{(1)}$. b/R=0.01, h_2/b=0.5, h_3/b=0.25, h_4/b=0.4375, h_c/b=1, η=0.3.

	$\lambda_{(1)}$			
	0.0	0.2	0.3	0.4
$K_I(-1)$	0.011453	0.010541	0.009281	0.007197
$P/(c_{44}(0)R)$	0.000327	0.000308	0.000282	0.000241

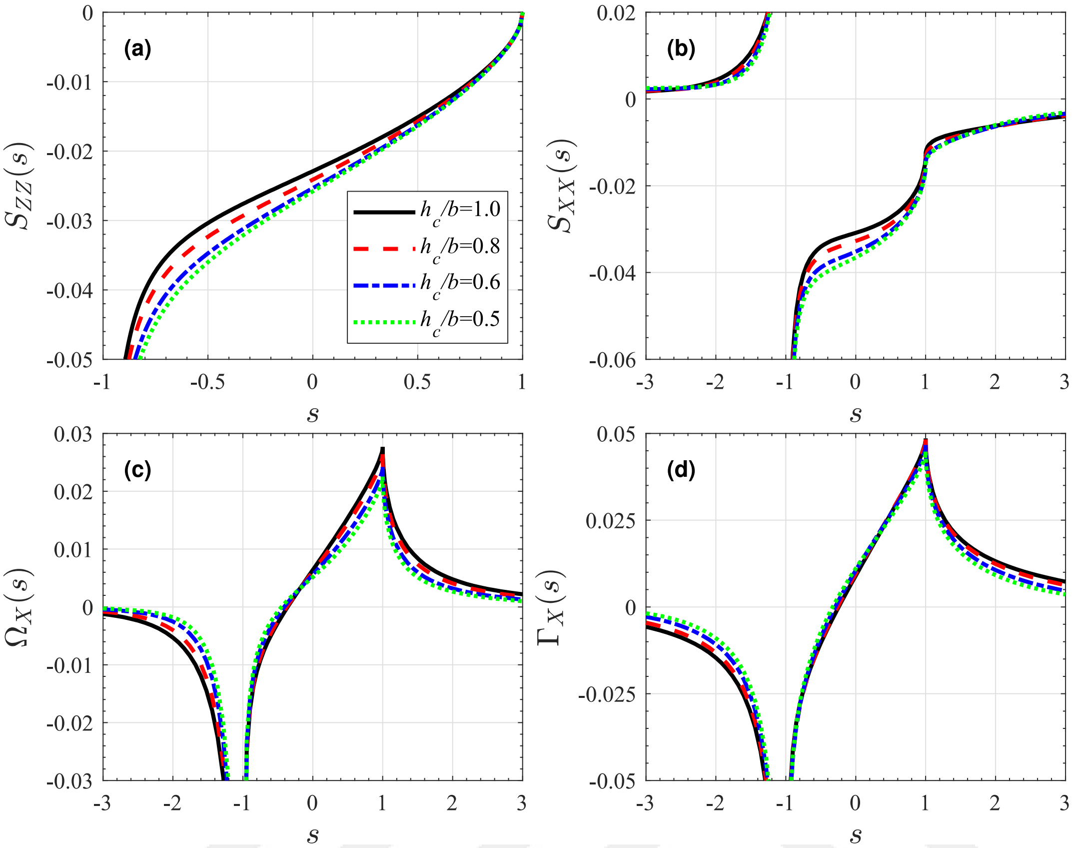

Figure 5.26. Mechanic and electro-magnetic results computed by considering an FGM2 coating in contact with a moving semi-circular punch for various values of h_c/b: (a) normal stress in Z-direction; (b) normal stress in X-direction; (c) electric displacement in X-direction; (d) magnetic induction in X-direction. b/R=0.01, h_2/b=0.5, h_3/b=0.25, h_4/b=0.4375, η=0.3, $\lambda_{(1)}$=0.3.

Table 5.25. Contact force and stress intensity factor computed for an FGM2 coating in contact with a moving semi-circular punch for various values of h_c/b. b/R=0.01, h_2/b=0.5, h_3/b=0.25, h_4/b=0.4375, η=0.3, $\lambda_{(1)}$=0.3.

	h_c/b			
	0.5	0.6	0.8	1.0
$K_I(-1)$	0.009542	0.009391	0.009089	0.008824
$P/(c_{44}(0)R)$	0.000297	0.000289	0.000274	0.000260

Another parameter which has a key importance on the response of the structure against contact loading is the friction coefficient. It is seen from Figure 5.27 and Table 5.26 that each output function is affected by the variation of η. In this set, frictionless contact is not considered and the lowest value starts from 0.1 as shown in the legend of Figure 5.27. The absolute values of both stress components are increasing functions of η. The peak levels of electric displacement and magnetic induction at s=1 belong to green curves which correspond η=0.7 case. Table 5.26 points out higher levels of friction originate greater $P/(c_{44}(0)R)$ and $K_I(-1)$.

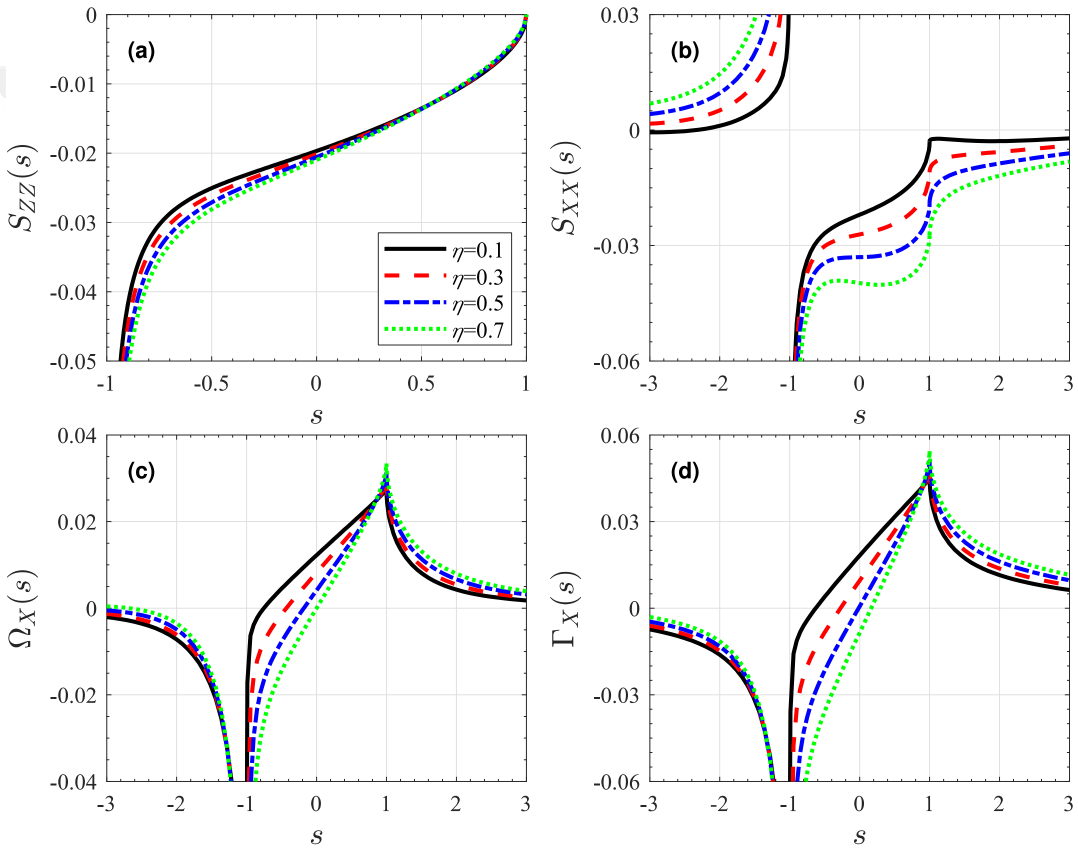

Figure 5.27. Mechanic and electro-magnetic results computed by considering an FGM3 coating in contact with a moving semi-circular punch for various values of η: (a) normal stress in Z-direction; (b) normal stress in X-direction; (c) electric displacement in X-direction; (d) magnetic induction in X-direction. b/R=0.01, h_2/b=0.5, h_3/b=0.25, h_4/b=0.4375, h_c/b=1, $\lambda_{(1)}$=0.3.

Table 5.26. Contact force and stress intensity factor computed for an FGM3 coating in contact with a moving semi-circular punch for various values of η. b/R=0.01, h_2/b=0.5, h_3/b=0.25, h_4/b=0.4375, h_c/b=1, $\lambda_{(1)}$=0.3.

	η			
	0.1	0.3	0.5	0.7
$K_I(-1)$	0.008094	0.008230	0.008337	0.008415
$P/(c_{44}(0)R)$	0.000219	0.000230	0.000240	0.000251

5.3 Numerical Results for Circular Punch

Two articles regarding multi-layer model and multiferroic structure sections are added to the literature by the author collaborating with his supervisor. (Toktas and Dag, 2022c; 2024).

5.3.1 Multi-layer Model

Circular shaped punch is analyzed as the loading agent in this section. The underlayer of the examined periodic coating is made of a silicon half-plane. Repeating Co/C layers are placed on top of silicon as suggested by Penkov et al. (2015). In total, 21 C and 20 Co layers are deposited. Hence, total number of layers equal to 42 in this problem as shown in Figure 4.7. The FGM coating, on the other hand, is made of silicon carbide coating and aluminum substrate referring to Figure 4.8. Material properties of SiC and Al employed in the analyses of FGM coatings are stated in Table 5.15 and Table 5.3 itemizes the coating types and the power-law exponents.

5.3.1.1 Verification

The problem considered by Balci and Dag (2019a) consists of an FGM coating, that possesses proportional and exponential variations in shear modulus and density. The same exponent is selected for both the shear modulus and density. That makes λ

constant at everywhere in the structure. Kolosov's constant is assumed to be constant. Between FGM coating and substrate at $X=h$, all mechanical properties are continuous. Considering plane strain situation, FGM coating is modelled by employing HMLM method, i.e., N number of sublayers succeeds FGM coating. For each particular layer, the properties are read at the centroid using Eq. (5.1).

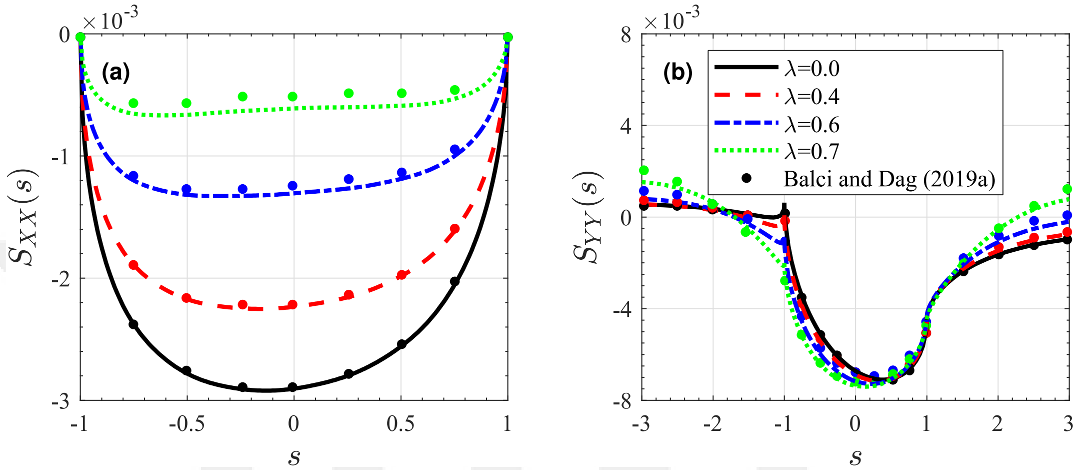

Figure 5.28. Comparison of contact stresses for a graded coating whose properties are varying with exponential functions in contact with a circular punch to those given by Balci and Dag (2019a): (a) normal stress; (b) normal stress in lateral direction. $(b+a)/R=0.01$, $(b+a)/h=1$, $\eta=0.3$, $\kappa=2$, $\mu(h)/\mu(0)=1/6$, $\rho(h)/\rho(0)=1/6$.

In Figure 5.28, obtained dimensionless contact stresses are compared with the ones provided by Balci and Dag (2019a). The variation ratio of properties between the surface of the structure and the interface equals to six. From black to green curve, nondimensional punch speed changes from stationary case $\lambda=0.0$, to high-speed situation $\lambda=0.7$. An intermediate level of friction ($\eta=0.3$) is chosen for identical contact size and coating length in the comparison. According to Table 5.27, the optimized value of N is determined as 150. Even though there exist insignificant differences in green curve and dotted data ($\lambda=0.7$), the results in both studies agree well for $\lambda \leq 0.6$. To sum up, HMLM is applicable to any heterogeneous structure to identify its contact response.

Table 5.27. Number of layers, stresses, and approximate errors computed at s=0 for a graded coating whose properties are varying with exponential functions in contact with a moving circular punch. $(b+a)/R$=0.01, $(b+a)/h$=1, η=0.3, κ=2, $\mu(h)/\mu(0)$=1/6, $\rho(h)/\rho(0)$=1/6, λ=0.4.

N	$S_{XX}(0)$	ε_a	$S_{YY}(0)$	ε_a
10	-0.002331		-0.006283	
50	-0.002249	3.62	-0.006802	7.62
100	-0.002238	0.50	-0.006872	1.03
150	-0.002234	0.17	-0.006897	0.35
200	-0.002232	0.09	-0.006909	0.18

5.3.1.2 Parametric Analyses

The initial problem solved in the parametric analyses concerns periodic coating put forward by Penkov et al. (2015). Figure 4.7 depicts the schematic of the moving contact problem. Consecutive Co/C nanolayers are deposited over a silicon half-plane. This coating suggested by Penkov et al. (2015) is known to offer incredible resistance against micro and nano level wear and surface deformation in the absence of lubrication. The layer thicknesses of Co are specified as 5.6 nm whereas even thinner carbon layers of 4 nm are stacked between Co layers. The total contact size $(b+a)$ is specified as 245 nm. Mechanical properties of components forming this heterogeneous structure are written in Table 5.28.

Figure 5.29 displays normalized contact stresses versus dimensionless punch speed $\lambda_{(1)}$. A motionless punch $\left(\lambda_{(1)}=0.0\right)$ and three moving punch cases $\left(\lambda_{(1)}>0.0\right)$ are taken into consideration. The deduction from other sections about the effects of punch speed was the weakening of contact stress S_{XX}. Same behavior is found in Figure 5.29. S_{YY} curves belong to separate $\lambda_{(1)}$ values seem close to each other. Behind the trailing end of the contact zone, S_{YY} for each punch speed remains as tensile and positive peaks happen at $s=-1$. It is perceived from Table 5.29 that both normalized contact force and punch eccentricity parameter are decaying functions of punch speed. The mid-point of the contact deviates slightly left from the centerline of the circular punch as $(b-a)/R < 0$ and $a > b$. Faster punches lead this deviation to be greater as expected. Overall conclusion from this set is that the dynamic effects of the punch cannot be neglected and the implementation of punch speed by keeping the time dependent differential terms in PDEs of contact models is essential.

Table 5.28. Material properties and thicknesses used in the solution of the periodic multi-layer coating problem (AZO Materials, 2023; Bhattarai et al., 2018; MEMSnet, 2023; Penkov et al., 2015; Suk et al., 2012).

	E(GPa)	ρ(kg/m^3)	ν	Thickness (nm)
Cobalt	211	8800	0.32	5.6
Amorphous carbon	180	2270	0.25	4
Silicon	165	2330	0.22	N/A

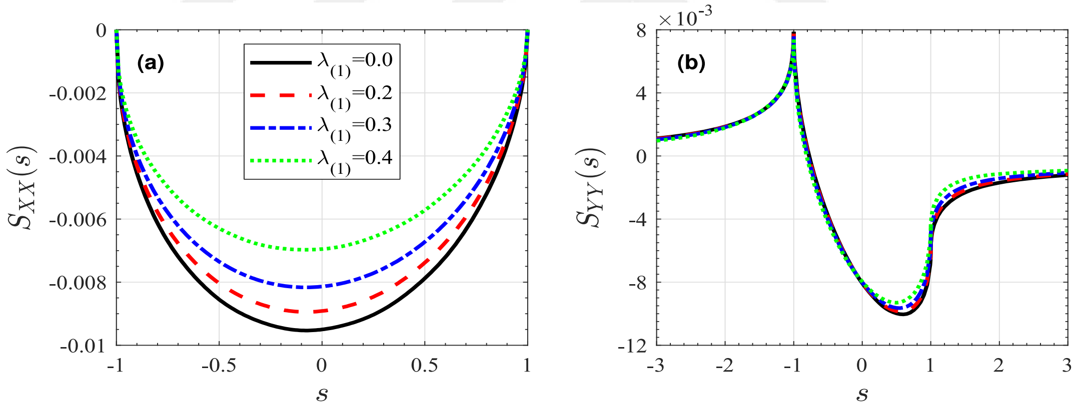

Figure 5.29. Contact stresses computed by considering a periodic multi-layer coating in contact with a moving circular punch for various values of $\lambda_{(1)}$: (a) normal stress; (b) normal stress in lateral direction. $(b+a)/R$=0.0125, η=0.4.

Table 5.29. Contact force and punch position parameter computed for a periodic multi-layer coating in contact with a moving circular punch for various values of $\lambda_{(1)}$. $(b+a)/R$=0.0125, η=0.4.

$\lambda_{(1)}$	$P/(\mu(0)(b+a))$	$(b-a)/R$
0.0	0.007444	-0.000922
0.2	0.006990	-0.000948
0.3	0.006386	-0.000981
0.4	0.005460	-0.001026

In Figure 5.30, four curves are plotted to show stress distributions in periodic multi-layer coating in contact with a moving circular punch for different values of kinetic coefficient of friction η. With the increase in η, S_{XX} loses certain amount of amplitude when $0 < s < 1$ while it potentiates its magnitude in the rest of the interval. It is monitored that the lateral stress S_{YY} heavily depends on the coefficient of friction. The peak tensile point in curves at $s=-1$ becomes a sharper apex when more shear stress S_{XY} is involved in the model.

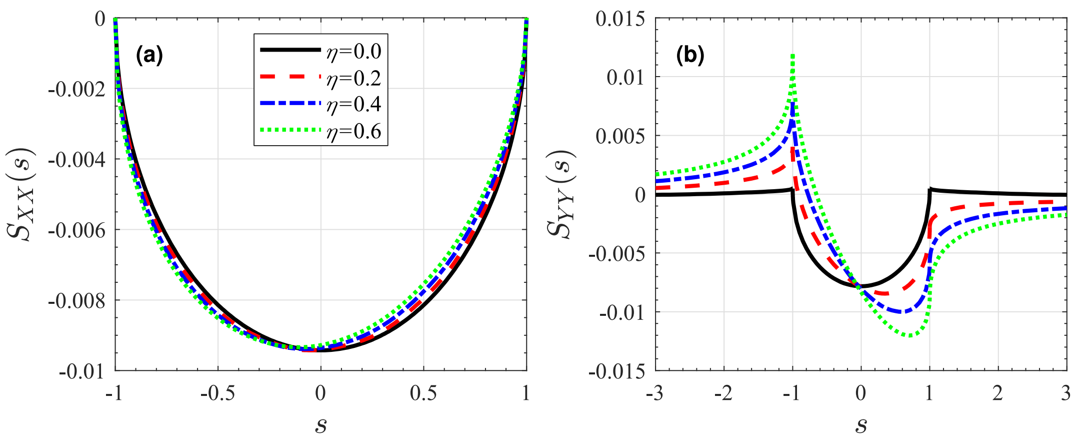

Figure 5.30. Contact stresses computed by considering a periodic multi-layer coating in contact with a moving circular punch for various values of η: (a) normal stress; (b) normal stress in lateral direction. $(b+a)/R$=0.0125, $\lambda_{(1)}$=0.1.

Table 5.30 lists normalized contact force and punch eccentricity parameters versus friction. Certain level of decrements in both parameters are detected as more friction is incorporated in the model. Recall from Eq. (4.80) and Eq. (4.8) that the strength of singularity of stress at the leading end (α_1) is 0.5 for frictionless contact (η=0.0). That makes the punch eccentricity zero, i.e., the punch centerline is vertically aligned with the mid-point of the contact. For frictional cases, the punch eccentricity parameter is negative and $a > b$. Also note that the greatest punch force is calculated for frictionless contact when $a = b$.

Table 5.30. Contact force and punch position parameter computed for a periodic multi-layer coating in contact with a moving circular punch for various values of η. $(b+a)/R$=0.0125, $\lambda_{(1)}$=0.1.

η	$P/(\mu(0)(b+a))$	$(b-a)/R$
0.0	0.007376	0.000000
0.2	0.007366	-0.000466
0.4	0.007333	-0.000928
0.6	0.007281	-0.001384

Figure 5.31 illustrates stress outputs for four FGM coatings defined by power law exponents. In this set, a medium level coefficient of friction η=0.4 and a relatively low punch speed $\lambda_{(1)}$=0.1 are chosen. The corresponding convergence analysis of a CR coating is inscrolled in Table 5.31. This time, number of sub-layers is set as 200 as it limits the percent error at the needed level. It is understood that all FGM coatings generate S_{XX} lower than the one calculated for H coating. It concludes that material gradation has a positive effect in diminishing contact stress. The same consequence can be comprehended from the peak level of lateral stress at the trailing end. The value of the green curve belonging to H coating at the tensile peak is more than three times of its nearest challenger's value shown by black curve of MR coating. In Table 5.32, the contact forces for FGM coatings are considerably smaller than the one for H coating. In brief, the suppression capacity of material gradation upon stresses in

FGM coatings is enormously impressive. Due to friction, the end points of the contact are found as unsymmetrical with respect to the centerline of the punch.

Table 5.31. Number of layers, stresses, and approximate errors computed at s=0 for a CR coating in contact with a moving circular punch. $(b+a)/R$=0.01, $(b+a)/h$=1, η=0.4, $\lambda_{(1)}$=0.1.

N	$S_{XX}(0)$	ε_a	$S_{YY}(0)$	ε_a
10	-0.004742	-	-0.006642	-
50	-0.004113	15.29	-0.007110	6.59
100	-0.003994	2.98	-0.007191	1.12
150	-0.003952	1.08	-0.007219	0.40
200	-0.003930	0.56	-0.007234	0.20
250	-0.003917	0.34	-0.007243	0.12

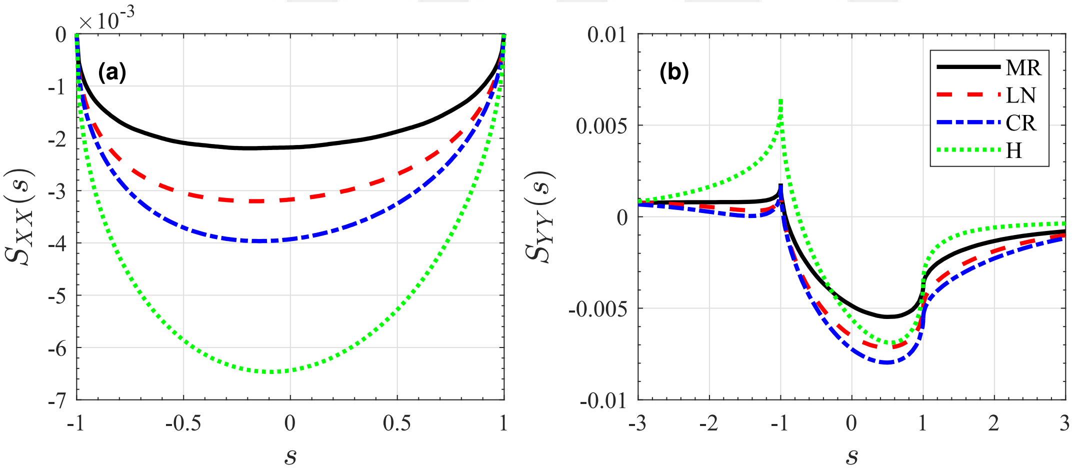

Figure 5.31. Contact stresses computed by considering FGM coatings in contact with a moving circular punch: (a) normal stress; (b) normal stress in lateral direction. $(b+a)/R$=0.01, $(b+a)/h$=1, η=0.4, $\lambda_{(1)}$=0.1.

Figure 5.32 and Figure 5.33 present contact stress curves versus punch speed in the legend considering CR and MR coatings, respectively. The model parameters $(b+a)/h$ and $(b+a)/R$ are equated to 1.25 and 0.0125. Shear stress is equal to forty percent of the normal stress in the contact region. The increment in punch speed lessens the normal stresses in both considered coatings. Despite similar trends in S_{YY} curves, zooming in the vicinity of $s=-1$ clarifies that punch speed reduces the intensity of lateral stress. According to Table 5.33 and Table 5.34, both punch force and punch eccentricity parameter depreciate as normalized punch speed rises.

Table 5.32. Contact force and punch position parameter computed for FGM coatings in contact with a moving circular punch. $(b+a)/R$=0.01, $(b+a)/h$=1, η=0.4, $\lambda_{(1)}$=0.1.

	$P/(\mu(0)(b+a))$	$(b-a)/R$
MR	0.001813	-0.001069
LN	0.002608	-0.001286
CR	0.003157	-0.001445
H	0.005054	-0.000720

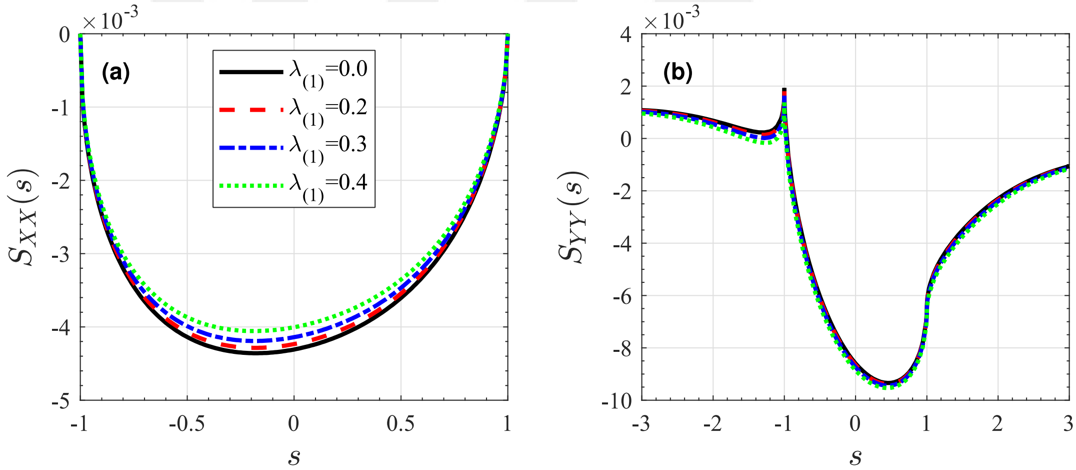

Figure 5.32. Contact stresses computed by considering a CR coating in contact with a moving circular punch for various values of $\lambda_{(1)}$: (a) normal stress; (b) normal stress in lateral direction. $(b+a)/R$=0.0125, $(b+a)/h$=1.25, η=0.4.

Table 5.33. Contact force and punch position parameter computed for a CR coating in contact with a moving circular punch for various values of $\lambda_{(1)}$. $(b+a)/R$=0.0125, $(b+a)/h$=1.25, η=0.4.

$\lambda_{(1)}$	$P/(\mu(0)(b+a))$	$(b-a)/R$
0.0	0.003513	-0.001677
0.2	0.003455	-0.001698
0.3	0.003382	-0.001726
0.4	0.003277	-0.001770

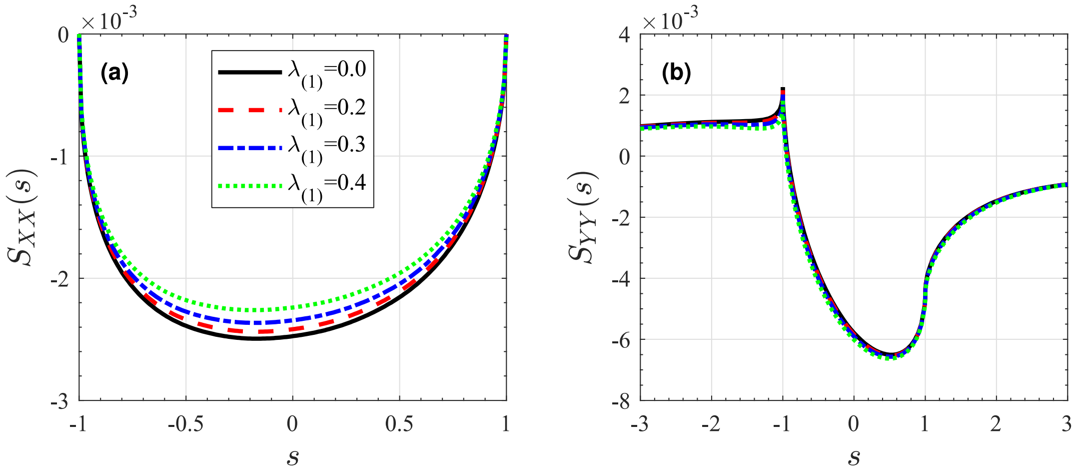

Figure 5.33. Contact stresses computed by considering an MR coating in contact with a moving circular punch for various values of $\lambda_{(1)}$: (a) normal stress; (b) normal stress in lateral direction. $(b+a)/R$=0.0125, $(b+a)/h$=1.25, η=0.4.

Table 5.34. Contact force and punch position parameter computed for an MR coating in contact with a moving circular punch for various values of $\lambda_{(1)}$. $(b+a)/R$=0.0125, $(b+a)/h$=1.25, η=0.4.

$\lambda_{(1)}$	$P/(\mu(0)(b+a))$	$(b-a)/R$
0.0	0.002083	-0.001255
0.2	0.002038	-0.001273
0.3	0.001980	-0.001299
0.4	0.001898	-0.001338

In Figure 5.34, the contact stresses for ceramic rich coating are plotted by examining the relative contact size in legend. Normalized punch speed $\lambda_{(1)}$ and friction coefficient are taken as 0.1 and 0.4, respectively. As $(b+a)/h$ ratio is ascending from 0.1 to 2.0, i.e., the coating length is shortening, lower normalized contact stresses S_{XX} are calculated. Except for trailing end, S_{YY} fluctuates with the variation of $(b+a)/h$ in the rest of the examined interval. The peak point at $s=-1$, on the other hand, is steadily diminishing as the analysis is conducted with thinner coatings. Table 5.35 reveals that normalized punch force is a decreasing function of $(b+a)/h$ ratio. However, the change in $(b-a)/R$ due to $(b+a)/h$ ratio is not a monotonous trend. There is a minimum value of punch eccentricity parameter somewhere in between $0.1< (b+a)/h <1.0$.

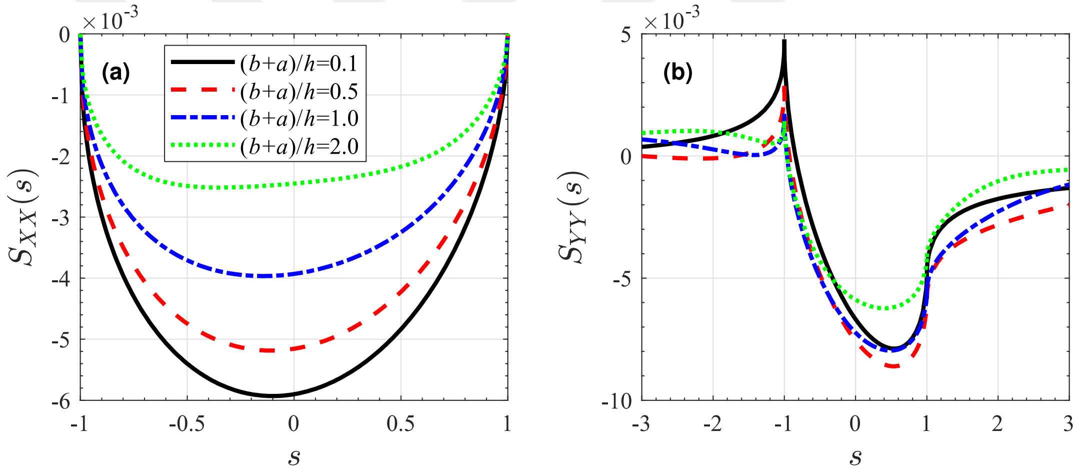

Figure 5.34. Contact stresses computed by considering a CR coating in contact with a moving circular punch for various values of $(b+a)/h$: (a) normal stress; (b) normal stress in lateral direction. $(b+a)/R=0.01$, $\eta=0.4$, $\lambda_{(1)}=0.1$.

Figure 5.35 demonstrates the effects of shear stress induced in the contact region for a CR coating and $(b+a)/h=0.8$ ratio by altering the coefficient of friction in the legend. Although this figure shows similarities in S_{XX} with Figure 5.30, the lateral stress curves shift downwards in the entire range. That means the lateral stress turns into compressive stress especially for $\eta=0.0$ and $\eta=0.2$, shown by black and red curves, respectively when CR coating is considered instead of periodic coating. As shear stress or η is further increased, the lateral stress changes sign and becomes tensile for $s \leq -1$. It is perceived that the tensile peak at the trailing end still occurs at high friction conditions in spite of the presence of CR coating. Table 5.36 summarizes contact force and punch position parameter calculations of this set. Symmetric orientation is unsurprisingly found for frictionless case. The required contact force and punch eccentricity parameter are inclined to decay as shear stress increases.

Table 5.35. Contact force and punch position parameter computed for a CR coating in contact with a moving circular punch for various values of $(b+a)/h$. $(b+a)/R$=0.01, η=0.4, $\lambda_{(1)}$=0.1.

$(b+a)/h$	$P/(\mu(0)(b+a))$	$(b-a)/R$
0.1	0.004645	-0.001162
0.5	0.004070	-0.001502
1.0	0.003157	-0.001445
2.0	0.002117	-0.001073

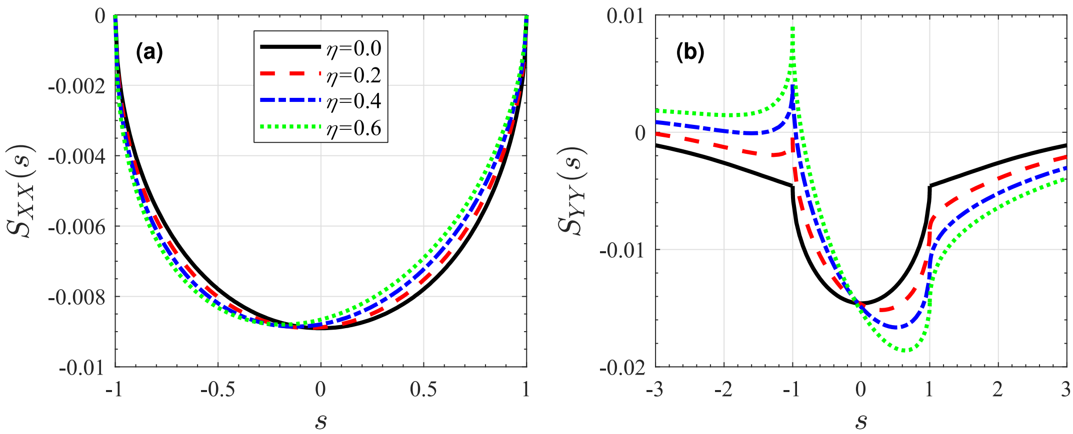

Figure 5.35. Contact stresses computed by considering a CR coating in contact with a moving circular punch for various values of η: (a) normal stress; (b) normal stress in lateral direction. $(b+a)/R$=0.02, $(b+a)/h$=0.8, $\lambda_{(1)}$=0.1.

Table 5.36. Contact force and punch position parameter computed for a CR coating in contact with a moving circular punch for various values of η. $(b+a)/R$=0.02, $(b+a)/h$=0.8, $\lambda_{(1)}$=0.1.

η	$P/(\mu(0)(b+a))$	$(b-a)/R$
0.0	0.007066	0.000000
0.2	0.007049	-0.001514
0.4	0.006998	-0.003009
0.6	0.006915	-0.004469

5.3.2 Multiferroic Structure

The property profile of MEE material in this section is considered as 50% $BaTiO_3$-50% $CoFe_2O_4$ in volume fraction.

5.3.2.1 Verification

A verification is carried out in order to comprehend the correctness of the developed procedures and the accuracy of the numerical findings. One may consider a homogeneous MEE half-plane subjected to the indentation of circular shaped loading agent, a special case of our problem. In Figure 5.36, the closed form solutions provided in Appendix E for contact problem of MEE half-plane are compared by our numerical results. The effects of punch velocity and friction are tested; i.e., the punch velocity and the coefficient of friction are non-zero. In the closed form solution, MEE half-plane is assumed to be barium titanate ($BaTiO_3$) - cobalt ferrite ($CoFe_2O_4$) composite and in a state of plane strain. In our results, the relative thickness parameter, $h_c/(b+a)$ is selected as 10, a sufficiently large value for the relative coating thickness parameter so that the outputs in our model recover the closed form solutions. Homogeneous MEE coating is modelled by equating N as 1. Number of elastic buffer layers, M, is chosen as 3. Figure 5.36 shows comparisons of the contact stresses, electric displacement and magnetic induction for a circular punch indentation computed by considering four different values of λ which is defined by

$$\lambda = V \Big/ \sqrt{c_{44}/\rho}\,. \tag{5.10}$$

Besides, numerical results of punch force and eccentricity parameter are listed in Table 5.37. As shown in Figure 5.36 and Table 5.37, there is an excellent agreement between the two sets of outputs, which is an indication of the high degree of accuracy in our results.

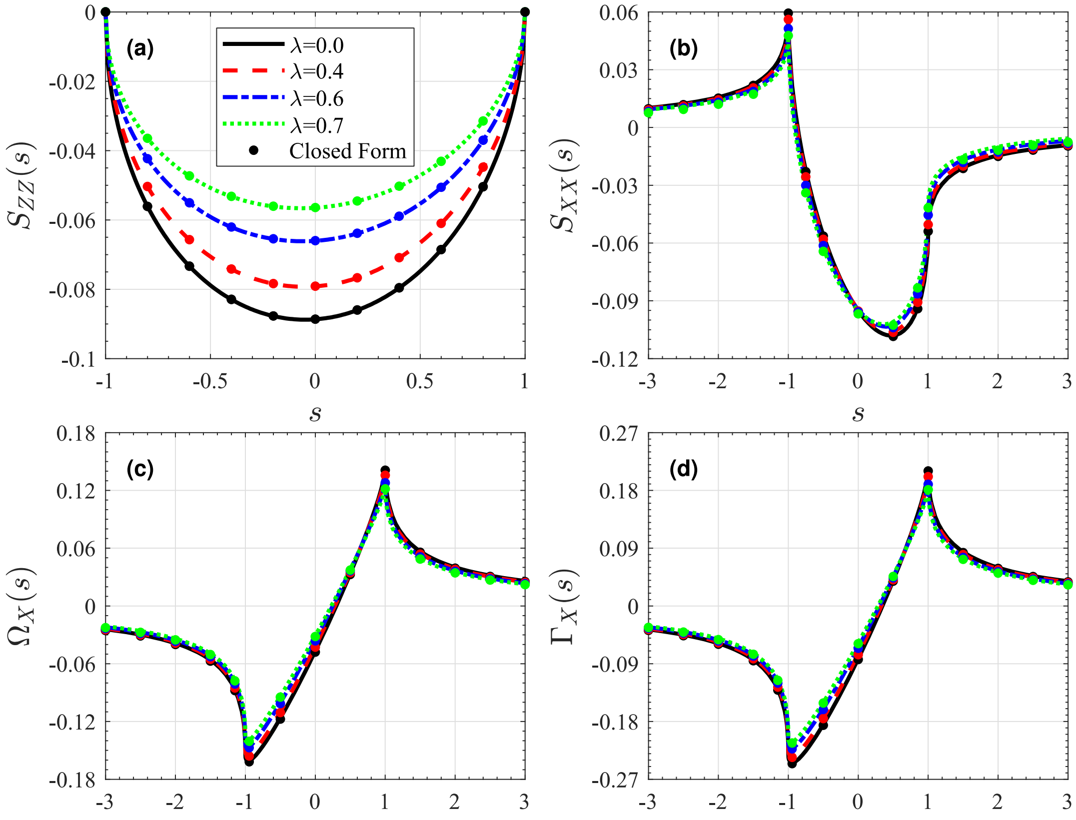

Figure 5.36. Comparisons of contact stresses for an MEE half-plane in contact with a moving circular punch to closed form solutions for various values of λ: (a) normal stress in Z-direction; (b) normal stress in X-direction; (c) electric displacement in X-direction; (d) magnetic induction in X-direction. η=0.3, $h_2/(b+a)$=0.5, $h_3/(b+a)$=0.25, $h_4/(b+a)$=0.4375, $h_c/(b+a)$=10, $R/(b+a)$=10.

Table 5.37. Comparisons of contact force and punch position parameter for a homogeneous MEE half-plane in contact with a moving circular punch. η=0.3, $h_2/(b+a)$ =0.5, $h_3/(b+a)$ =0.25, $h_4/(b+a)$ =0.4375, $h_c/(b+a)$=10, $R/(b+a)$=10.

	$P/(c_{44}(b+a))$				$(b-a)/R$			
	λ=0.0	λ=0.4	λ=0.6	λ=0.7	λ=0.0	λ=0.4	λ=0.6	λ=0.7
Numerical	0.06968	0.06221	0.05190	0.04442	-0.00478	-0.00523	-0.00591	-0.00645
Closed-form	0.06964	0.06218	0.05186	0.04436	-0.00486	-0.00535	-0.00611	-0.00673

5.3.2.2 Parametric Analyses

The abbreviations for the considered coatings and their exponents are given in Table 5.38. In this set, the exponents of FGM coatings are chosen as a bit lower in order to see the effects of gradation better. By comparing the convergence analyses done in Sections 5.2.1 and 5.3.1, it is concluded that convergence for circular punch results takes place at lower values of N when the same structure is exposed to the contact loading. Recall that the number of layers used in semi-circular punch problem is greater than the one in circular punch problem for elastic structures ($N_{\text{S-cir}}$=250>N_{Cir}=200). We observe the same situation in Table 5.39, too. The results are not changing too much after N=25 which corresponds to the fastest convergence. In the preparation of the results in this section, N=25 provides the desired accuracy and there is no need to more powerful homogenization of FGM MEE coating. Lastly, normalized punch force and eccentricity values are listed in Table 5.40 for N=25 which guarantees the convergence.

The numerical analyses are performed by considering the problem in Figure 4.9. The parametric analyses focus on influences of coating type, punch speed, kinetic friction coefficient, and relative coating thickness on magneto-electro-elastic response of the structure. Radius of circular punch is assumed as 10 times bigger than the total contact size.

Table 5.38. Exponents used in the parametric analyses (set-2).

Property	Exponent	FGM1	FGM2	LN	H
c_{11}	γ_1	1.3	1.8	1.0	∞
c_{13}	γ_2	1.3	1.8	1.0	∞
c_{33}	γ_3	1.3	1.8	1.0	∞
c_{44}	γ_4	1.3	1.8	1.0	∞
e_{15}	γ_5	1.4	1.9	1.0	∞
e_{31}	γ_6	1.4	1.9	1.0	∞
e_{33}	γ_7	1.4	1.9	1.0	∞
f_{15}	γ_8	1.5	2.0	1.0	∞
f_{31}	γ_9	1.5	2.0	1.0	∞
f_{33}	γ_{10}	1.5	2.0	1.0	∞
β_{11}	γ_{11}	1.6	2.1	1.0	∞
β_{33}	γ_{12}	1.6	2.1	1.0	∞
μ_{11}	γ_{13}	1.7	2.2	1.0	∞
μ_{33}	γ_{14}	1.7	2.2	1.0	∞
ρ	γ_{15}	1.4	1.6	1.0	∞
g_{11}	γ_{16}	1.8	2.3	1.0	∞
g_{33}	γ_{17}	1.8	2.3	1.0	∞

The results belonging to different types of coatings are provided in Figure 5.37. Model parameters are written in the caption. It is found that MEE rich coatings lower the contact stress S_{ZZ}. Thus, the maximum S_{ZZ} is computed for LN coating. The lateral stress S_{XX} hits the maximum level again for LN coating. S_{XX} behaves like S_{ZZ} for $s > 0$. The curves of electromagnetic functions plotted for different coatings are usually close. However, the magnitude of electric displacement in $|s| > 1$, is larger for H coating. Table 5.41 tabulates normalized punch force and eccentricity parameters for the examined coatings. The coating types differ particularly the punch force. LN coating possesses the greatest force. Insignificant variations in $(b-a)/R$ can be seen in Table 5.41.

Table 5.39. Number of layers, stresses, electric displacement, magnetic induction and percent approximate errors computed at s=0 for an FGM1 in contact with a moving circular punch. $h_2/(b+a)$=0.5, $h_3/(b+a)$=0.25, $h_4/(b+a)$=0.4375, $h_c/(b+a)$=2, $R/(b+a)$=10, η=0.4, $\lambda_{(1)}$=0.4.

N	$S_{ZZ}(0)$	ε_a	$S_{XX}(0)$	ε_a	$\Omega_X(0)$	ε_a	$\Gamma_X(0)$	ε_a
5	-0.06996	-	-0.09655	-	-0.03854	-	-0.07756	-
10	-0.06987	0.14	-0.09498	1.65	-0.04102	6.05	-0.08099	4.24
15	-0.06981	0.08	-0.09463	0.38	-0.04188	2.07	-0.08199	1.22
20	-0.06979	0.03	-0.09445	0.18	-0.04232	1.04	-0.08250	0.61
25	-0.06978	0.01	-0.09435	0.11	-0.04258	0.61	-0.08280	0.36
30	-0.06977	0.01	-0.09429	0.07	-0.04275	0.39	-0.08299	0.23

Table 5.40. Contact force and punch position parameter for the coating FGM1 in contact with circular punch. $h_2/(b+a)$=0.5, $h_3/(b+a)$=0.25, $h_4/(b+a)$=0.4375, $h_c/(b+a)$=2, $R/(b+a)$=10, η=0.4, $\lambda_{(1)}$=0.4.

	$P/(c_{44}(0)(b+a))$	$(b-a)/R$
N=25	0.053375	-0.007119

Second set of numerical results given in Figure 5.38 and Table 5.42 looks into the impact of punch speed on contact stresses and electromagnetism for FGM1 coating. Contact stress S_{ZZ} tends to drop as $\lambda_{(1)}$ changes from 0.0 to 0.4. Extenuative effect of punch speed on contact stress S_{XX} is especially distinguished for s > 0. Zooming into both positive and negative peaks of electromagnetic response elucidates that the largest values of electric displacement and magnetic induction are generated for the elastostatic case shown by black curve. The final remark regarding this set is that both quantities in Table 5.42 show decaying trend with $\lambda_{(1)}$.

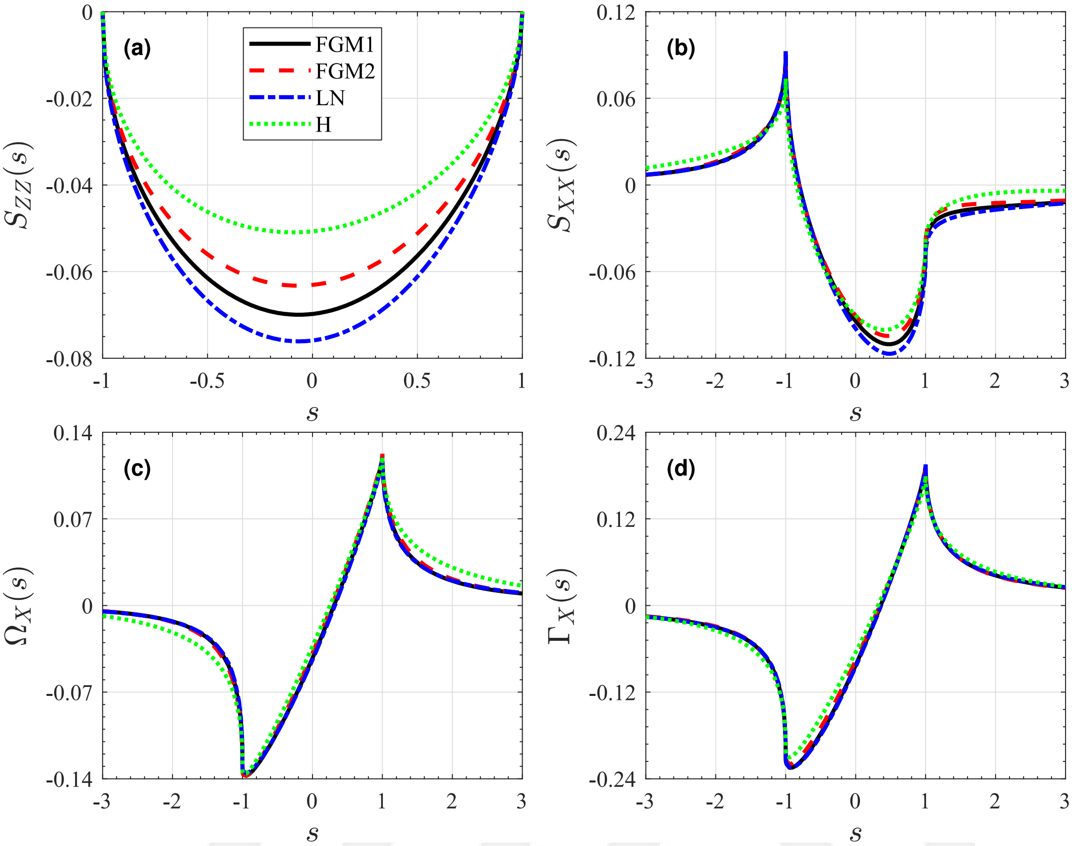

Figure 5.37. Mechanic and electro-magnetic results computed for different MEE coatings in contact with a moving circular punch: (a) normal stress in Z-direction; (b) normal stress in X-direction; (c) electric displacement in X-direction; (d) magnetic induction in X-direction. $h_2/(b+a)=0.5$, $h_3/(b+a)=0.25$, $h_4/(b+a)=0.4375$, $h_c/(b+a)=2$, $R/(b+a)=10$, $\eta=0.4$, $\lambda_{(1)}=0.4$.

Table 5.41. Contact force and punch position parameter computed for different MEE coatings in contact with a moving circular punch. $h_2/(b+a)=0.5$, $h_3/(b+a)=0.25$, $h_4/(b+a)=0.4375$, $h_c/(b+a)=2$, $R/(b+a)=10$, $\eta=0.4$, $\lambda_{(1)}=0.4$.

	FGM1	FGM2	LN	H
$P/(c_{44}(0)(b+a))$	0.053375	0.048619	0.057840	0.039881
$(b-a)/R$	-0.007119	-0.006934	-0.007427	-0.007637

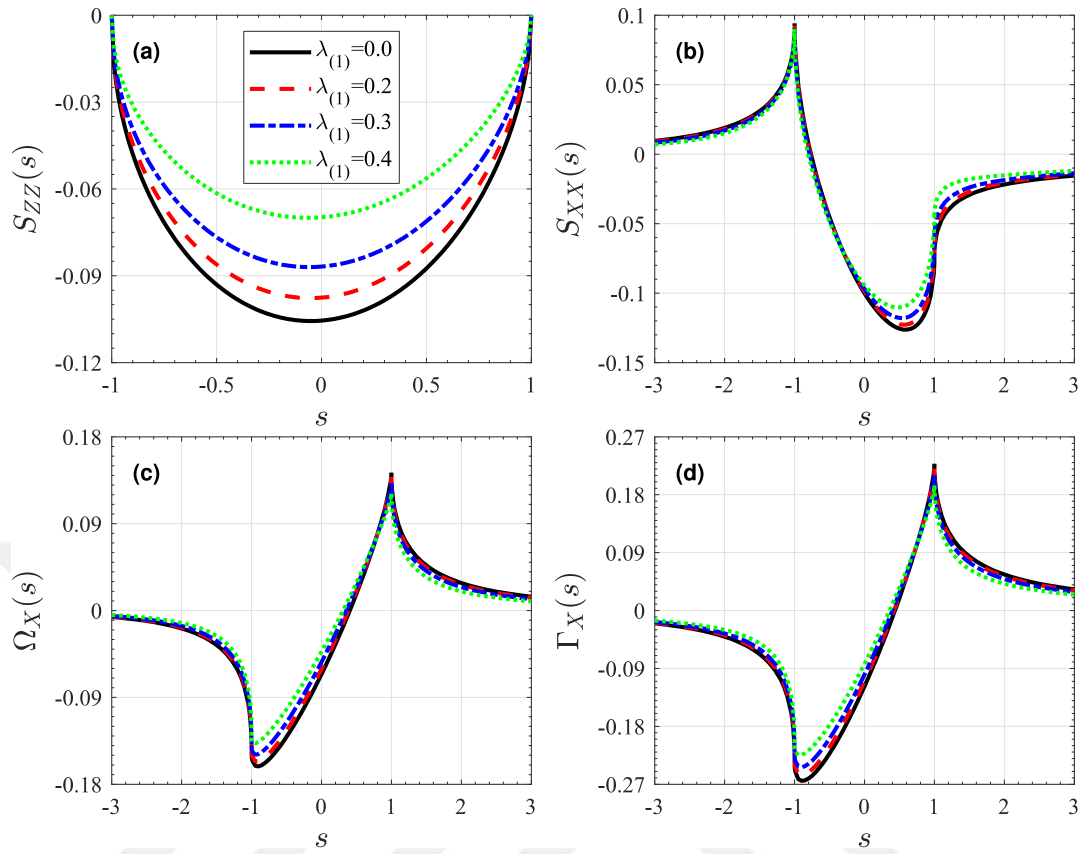

Figure 5.38. Mechanic and electro-magnetic results computed for an FGM1 coating in contact with a moving circular punch for various values of $\lambda_{(1)}$: (a) normal stress in Z-direction; (b) normal stress in X-direction; (c) electric displacement in X-direction; (d) magnetic induction in X-direction. $h_2/(b+a)$ =0.5, $h_3/(b+a)$ =0.25, $h_4/(b+a)$ =0.4375, $h_c/(b+a)$=2, $R/(b+a)$=10, η=0.4.

Table 5.42. Contact force and punch position parameter computed for an FGM1 coating in contact with a moving circular punch for various values of $\lambda_{(1)}$. $h_2/(b+a)$ =0.5, $h_3/(b+a)$ =0.25, $h_4/(b+a)$ =0.4375, $h_c/(b+a)$=2, $R/(b+a)$=10, η=0.4.

	$\lambda_{(1)}$			
	0.0	0.2	0.3	0.4
$P/(c_{44}(0)(b+a))$	0.081830	0.075533	0.067001	0.053375
$(b-a)/R$	-0.005688	-0.006009	-0.006450	-0.007119

Another main parameter whose influences are inspected is the coating thickness. Figure 5.39 and Table 5.43 exhibit the impact of the relative MEE coating thickness, $h_c/(b+a)$. The coating choice here is again FGM1. The other parameters η and $\lambda_{(1)}$ are set as 0.4. Decreasing $h_c/(b+a)$ from 3.0 to 0.5 results in larger S_{XX} and S_{ZZ} magnitudes in the contact region. Ahead of the leading end, the largest S_{XX} magnitude is calculated for $h_c/(b+a)$=0.5 shown by black curve. Examining the region around $s=-1$ in Figure 5.39(b) in the expanded version clarifies that the maximum peak occurs for red curve. The coating thickness is coupled with electric displacement more compared to magnetic induction. One may observe that more differences exist between the curves in Figure 5.39(c) compared to the curves in Figure 5.39(d) which advocates the last remark. Table 5.43 shows that the thicker coatings decrease the punch force yet increase the punch eccentricity parameter.

The final factor that has a worth to analyze is the kinetic coefficient of friction η. Carried out analyses are relayed necessary information about indentation of FGM1 coating with Figure 5.40 and Table 5.44 for four different values of the friction coefficient. As seen, all outputs in X-direction are influenced by the variation of η. Surprisingly, tensile peaks for S_{XX} occurs at both ends at $s=-1$ and $s=1$ for frictionless contact. Although the positive peaks at $s=1$ for electromagnetic results seem very close, negative maximum levels near $s=-1$ are magnified by higher friction. It is deducted from Table 5.44 that higher shear stress has a decreasing effect on punch force and eccentricity parameter.

Table 5.43. Contact force and punch position parameter computed for an FGM1 coating in contact with a moving circular punch for various values of $h_c/(b+a)$. $h_2/(b+a)=0.5$, $h_3/(b+a)=0.25$, $h_4/(b+a)=0.4375$, $R/(b+a)=10$, $\eta=0.4$, $\lambda_{(1)}=0.4$.

	$h_c/(b+a)$			
	0.5	1.0	2.0	3.0
$P/(c_{44}(0)(b+a))$	0.073836	0.063634	0.053375	0.048782
$(b-a)/R$	-0.009541	-0.007966	-0.007119	-0.007065

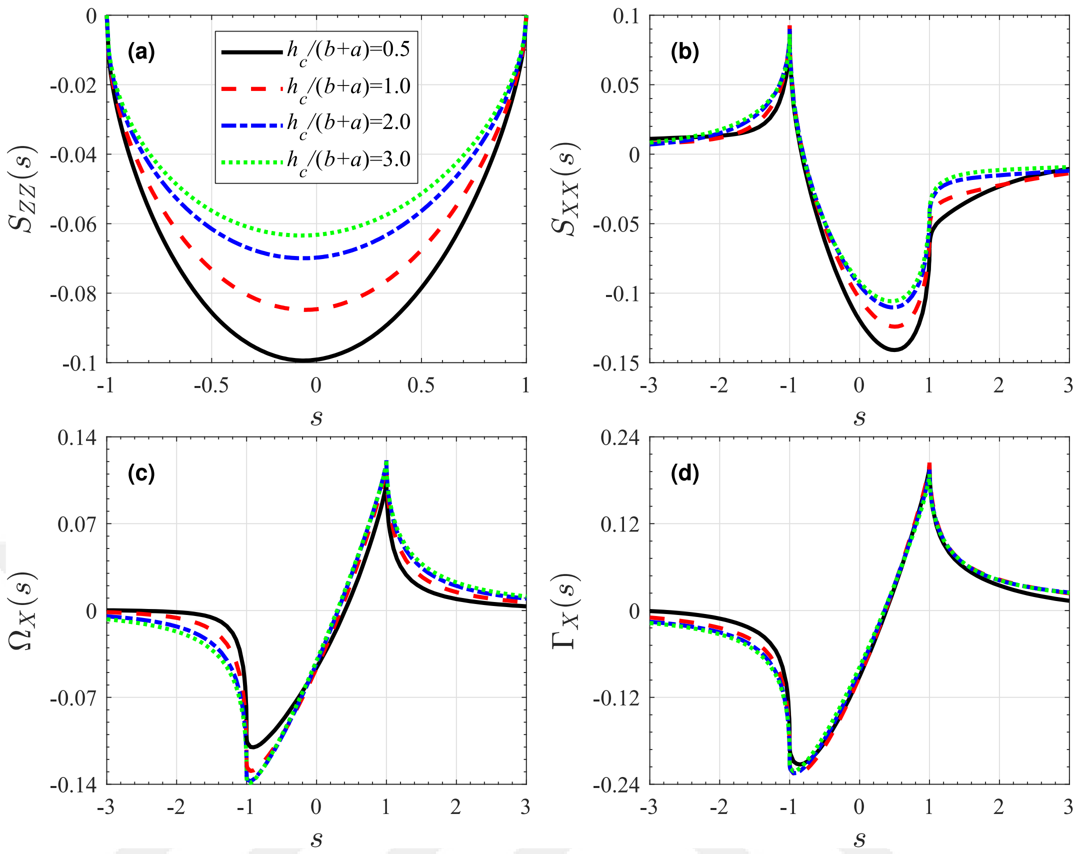

Figure 5.39. Mechanic and electro-magnetic results computed for an FGM1 coating in contact with a moving circular punch for various values of $h_c/(b+a)$: (a) normal stress in Z-direction; (b) normal stress in X-direction; (c) electric displacement in X-direction; (d) magnetic induction in X-direction. $h_2/(b+a)$=0.5, $h_3/(b+a)$=0.25, $h_4/(b+a)$=0.4375, $R/(b+a)$=10, η=0.4, $\lambda_{(1)}$=0.4.

Table 5.44. Contact force and punch position parameter computed for an FGM1 coating in contact with a moving circular punch for various values of η. $h_2/(b+a)$=0.5, $h_3/(b+a)$=0.25, $h_4/(b+a)$=0.4375, $R/(b+a)$=10, $h_c/(b+a)$=1 $\lambda_{(1)}$=0.3.

	η			
	0.0	0.2	0.4	0.6
$P/(c_{44}(0)(b+a))$	0.077221	0.077130	0.076859	0.076415
$(b-a)/R$	0.000000	-0.003608	-0.007195	-0.010741

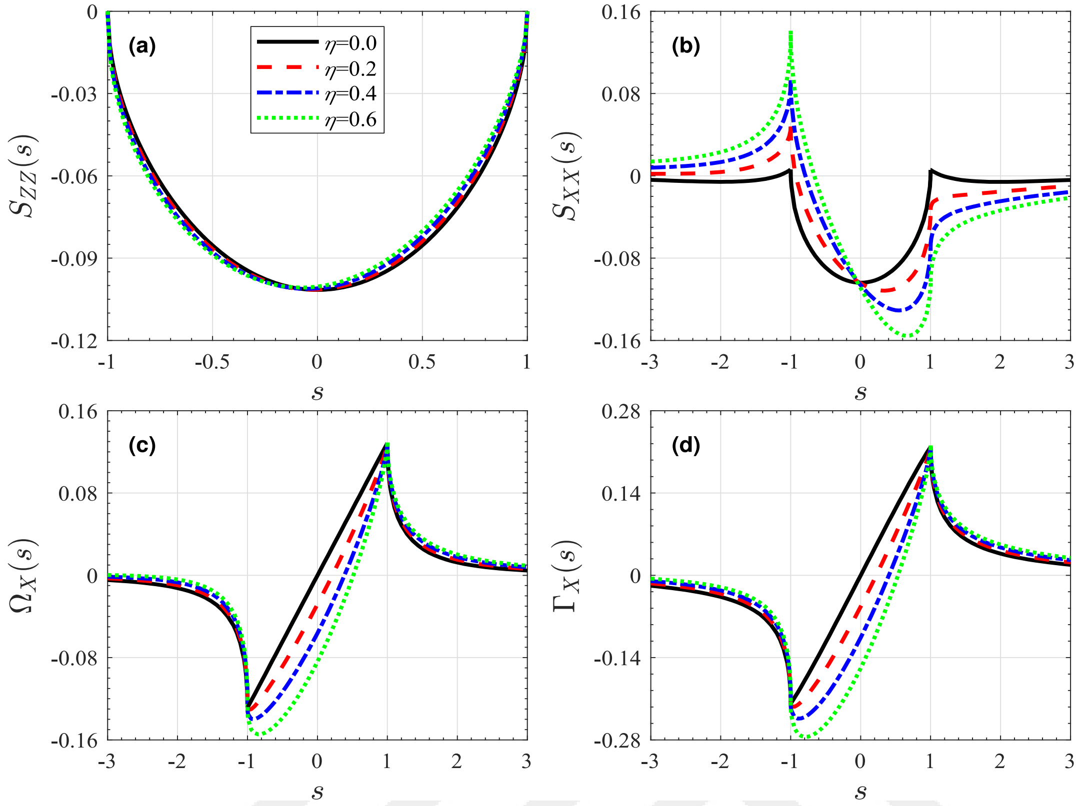

Figure 5.40. Mechanic and electro-magnetic results computed for an FGM1 coating in contact with a moving circular punch for various values of η: (a) normal stress in Z-direction; (b) normal stress in X-direction; (c) electric displacement in X-direction; (d) magnetic induction in X-direction. $h_2/(b+a)$=0.5, $h_3/(b+a)$=0.25, $h_4/(b+a)$=0.4375, $R/(b+a)$=10, $h_c/(b+a)$=1, $\lambda_{(1)}$=0.3.

5.4 Additional Numerical Results

This section is unique to this dissertation and not published in anywhere else. A multi-layer coating in sliding contact with a rigid frictional punch is examined in detail. Problem geometry is depicted in Figure 5.41 which shows a magnetic storage device in contact with a moving flat or triangular punch. The magnetic storage device comprises four different thin films, namely diamond like carbon (DLC), magnetic layer (MAG), intermediate layer (IL), and soft magnetic underlayer (SUL). The multi-layer coating is bonded to a nickel-phosphorous substrate (Ni-P), modelled as a half-plane. The thickness of each layer is provided by Katta et al. (2009), and shown in Figure 5.41. Utilizing the data given by Katta et al. (2009), the relative dimensions are specified as

$$\frac{b}{h_2}=\frac{140}{64},\quad \frac{b}{h_3}=\frac{140}{28},\quad \frac{b}{h_4}=\frac{140}{16},\quad \frac{b}{h_5}=\frac{140}{4}. \tag{5.11}$$

Elastic properties, density, and thickness of each film and the substrate are tabulated in Table 5.45. Figure 5.42 shows contact stresses computed by considering a moving flat punch. The results in Figure 5.42 are generated for η=0.4. The curves are obtained for four different values of the dimensionless punch speed $\lambda_{(1)}$, where the subscript 1 stands for the semi-infinite Ni-P substrate. Around the mid-section of the contact zone, the magnitude of the normal contact stress S_{XX} is seen to decrease as the dimensionless velocity $\lambda_{(1)}$ is increased from 0.0 to 0.7. Reverse variation is observed for S_{YY} in the contact zone, i.e., the increase in $\lambda_{(1)}$ leads to a corresponding increase in the stress magnitude in the contact zone. Normal stress in the lateral direction S_{YY} becomes tensile and approaches to infinity near the trailing end of contact ($s\to -1^-$), whereas it is negative at the leading end $(s\to 1^+)$.

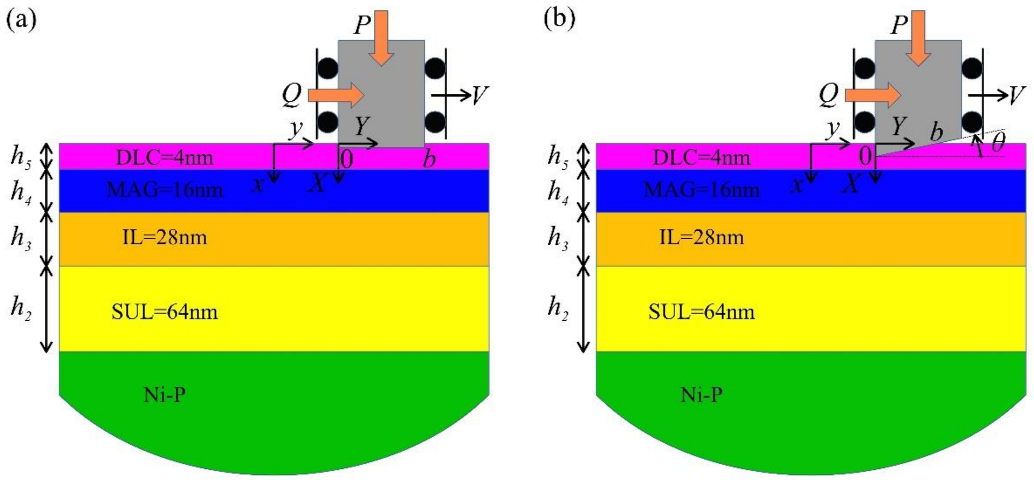

Figure 5.41. The moving rigid punches on multi-layer storage device: (a) flat punch; (b) triangular punch.

Table 5.45. Material properties and thicknesses of a magnetic storage device (Katta et al., 2009).

	E(GPa)	ρ(kg/m^3)	ν	Thickness (nm)
Diamond like carbon (DLC)	250	1900	0.24	4
Magnetic layer (MAG)	150	7900	0.30	16
Intermediate layer (IL)	135	7900	0.30	28
Soft magnetic underlayer (SUL)	120	7900	0.30	64
Ni-P layer	114	9000	0.31	-

Normalized stress intensity factors at the sharp corners of the flat punch, $K_I(-1)$ and $K_I(1)$ are tabulated in Table 5.46. Stress intensity factors at both ends are found to be increasing functions of $\lambda_{(1)}$. Note that $\lambda_{(1)}$=0.0 corresponds to the case of the stationary punch. Significant differences are seen between SIFs calculated for larger $\lambda_{(1)}$ values and $\lambda_{(1)}$=0.0. These results imply that the assumption of statically applied punch loading will not lead to sufficiently accurate results if the punch possesses a velocity.

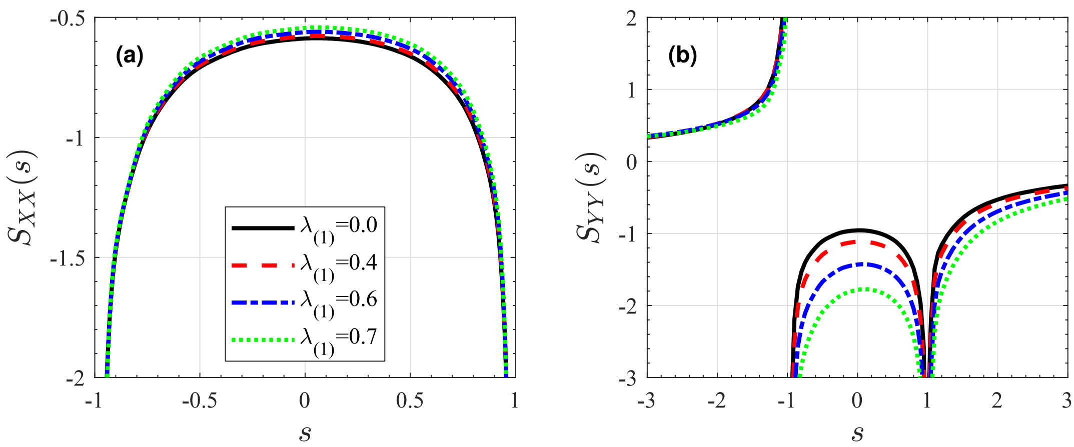

Figure 5.42. Contact stresses computed by considering a magnetic storage device (Katta et al., 2009) in contact with a moving flat punch. (a) Normal stress; (b) normal stress in lateral direction. η=0.4.

Contact stresses calculated considering a moving triangular punch are presented in Figure 5.43 for friction coefficient value of 0.4. For the triangular punch, the normal contact stress is singular at the sharp corner $s=-1$, and zero at the point of smooth contact $s=1$. Note that contact is not complete in the case of the triangular punch, and the force P is a function of the length of the contact zone b. Figure 5.43 shows that magnitude of normal contact stress gets smaller as the dimensionless punch speed $\lambda_{(1)}$ increases from 0.0 to 0.7. Influence of dimensionless speed on normal stress in Y-direction, on the other hand, is significant especially near the trailing end of the contact zone. Normalized contact forces and SIFs at $s=-1$ corresponding to the cases studied are tabulated in Table 5.46. Normalized force and SIF at $s=-1$ are decreasing functions of punch velocity as presented in Table 5.46. There is again a significant degree of differences between the values calculated for a statically applied punch $(\lambda_{(1)}=0.0)$ and those computed for a dynamic punch $(\lambda_{(1)}>0.0)$. Hence, it is imperative that governing equations of elastodynamics be employed in the study of contact mechanics of a multi-layer coating loaded by a moving punch.

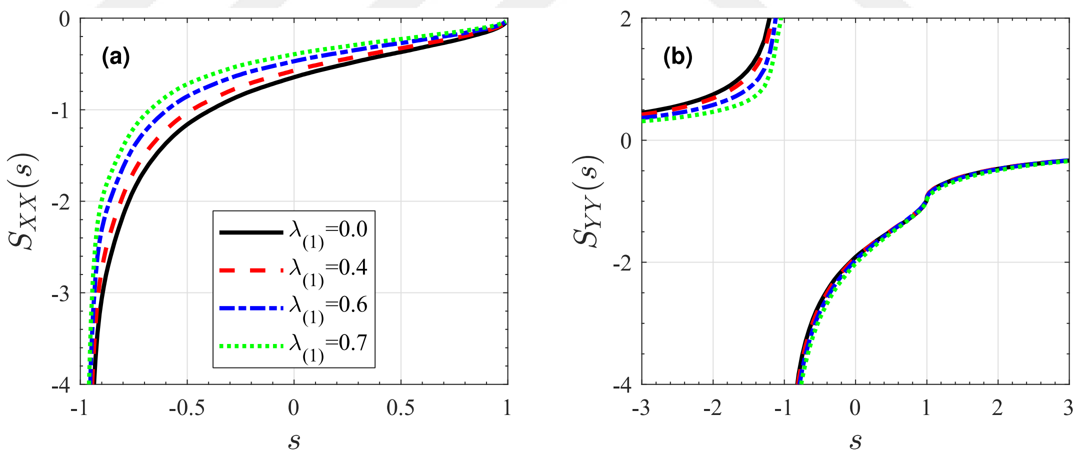

Figure 5.43. Contact stresses computed by considering a magnetic storage device (Katta et al., 2009) in contact with a moving triangular punch. (a) Normal stress; (b) normal stress in lateral direction. η=0.4.

Table 5.46. Stress intensity factors and contact force computed for a magnetic storage device in contact with a punch. η=0.4.

	Flat Punch		Triangular Punch	
$\lambda_{(1)}$	$K_I(-1)$	$K_I(1)$	$K_I(-1)$	$P/(\mu(0)\tan(\theta)b)$
0.0	0.418691	0.443971	0.926035	1.557544
0.4	0.444158	0.459161	0.885296	1.413050
0.6	0.489623	0.485101	0.825875	1.209438
0.7	0.534056	0.509196	0.779246	1.057259

CHAPTER 6

CONCLUSIONS AND FUTURE WORK

Integral transform technique-based solutions for dynamic contact problems of elastic and multiferroic FGM coatings of arbitrary property variation that is perfectly bonded to isotropic homogeneous inter-layers and substrates are developed in the present study. In the method, the most critical issue is the derivation of SIE. In the numerical homogenization of the graded layers, one should be conscientious since a skipped step in the numerical algorithm may result in the failure of entire solution method. Another point one must be careful is that normalized punch speed parameter is only defined for the substrate in the algorithm. Inside the structure, normalized punch speed varies depending on the properties of corresponding layers, however, this parameter cannot be greater than 1 for subsonic speeds. In order to keep this parameter lower than 1, the maximum limit of normalized punch speed for the first layer must be limited at certain levels such as 0.4 or 0.7 depending on certain structures.

In the parametric analyses, both complete and incomplete contact conditions are examined. Exponents of the weight function in Jacobi polynomial expansion depend on the material properties, the coefficient of friction and the punch speed. Rigid loading agent assumption is applied in order to estimate the normal displacement of the uppermost layer. Coulomb's friction law assists to relate shear and normal stresses in the contact region. The discussed procedures and presented results are verified through comparisons with the models in the literature for elementary cases. The comparisons in Chapter 5 indicate the accuracy, validity and superiority of the model in this study.

The framework of this dissertation is as follows: Chapter 1 describes the general information about multi-layer models, FGMs, multiferroics and their applications in devices and components. Chapter 2 summarizes the previous studies in the literature concerning the homogenization approaches of hetero-structures, the classes of examined materials and the homogenized solid mechanics models. Chapter 3 informs about the essential steps in the formulation of contact problems. Chapter 4 examines the numerical approaches for four loading punch profiles. In Chapter 5, verifications and novel results are provided in figures and tables. Chapter 6 finalizes the dissertation with conclusions, remarks and suggestions.

6.1 Concluding Remarks

The main conclusions drawn from the analyses in the present study can be summarized in six groups.

- Elastic Less Stiff Coating (Flat and Triangular Punches)
  1. Material gradation lessens the lateral stress S_{YY} near the wake of the punch and SIFs compared to H coating.
  2. Normalized punch speed $\lambda_{(1)}$ lowers the contact stress S_{XX}, the punch force $P/(\mu(0)\tan(\theta)b)$ and SIF $K_I(-1)$.
  3. More friction in the contact originates greater punch force and smaller SIF.
  4. Thicker coatings generate a decrease in S_{XX} yet an increase in SIFs in general.
- Elastic Stiffer Coating (Semi-circular and Circular Punches)
  1. When the coating has greater shear modulus than the substrate, the content of ceramic in the coating increases the magnitude of normalized contact stress S_{XX}.
  2. Material gradation decreases the lateral stress S_{YY} near the wake of the punch.
  3. Ceramic content in the coating may increase the punch force more than three times and SIF more than two times as shown in Table 5.17.
  4. Punch speed reduces the magnitude of S_{XX}, punch force and SIF, yet enhances the magnitude of S_{YY} in most of the interval of s.
  5. Thicker coatings generate greater S_{XX}, S_{YY} when $s \to -1^-$, punch force and SIF.

6. Frictionless contact makes S_{YY} fully negative. As frictional effects and shear stress are involved, the sign of the lateral stress behind the trailing end changes and the lateral stress shoots to positive peaks at $s = -1$.

- Elastic Periodic Coating (Circular Punch)

1. Normalized punch speed weakens the normal stress and punch force.
2. As $\eta \uparrow$, the lateral stress S_{YY} at the trailing end boosts but normalized punch force $P/(\mu(0)(b+a))$ and eccentricity parameter $(b-a)/R$ slightly decrease.

- Multi-layer Coating (Flat and Triangular Punches)

1. For both punch profiles, the magnitude of the normal contact stress S_{XX} is seen to decrease as the dimensionless velocity as $\lambda_{(1)}\uparrow$. Although reverse variation is observed for S_{YY} for flat punch indentation when $s > -1$, we detect that noticable differences exist for triangular punch indentation only if $s < -1$.
2. $K_I(-1)$ and $K_I(1)$ generated by loading the structure by flat punch go up as $\lambda_{(1)}\uparrow$, whereas both $K_I(-1)$ and $P/(\mu(0)\tan(\theta)b)$ occurred due to applying pressure by the triangular punch go down.

- Multiferroic Less Stiff Coating (Flat and Triangular Punches)

1. The smallest magnitude of normal stress S_{ZZ} is calculated for H coating.
2. While a rise in MEE content in the coating augments S_{XX} in the region behind the contact of flat punch, noticeable decrements are observed in S_{XX} for $s > -1$.
3. Although electric displacement for H coating is substantially greater than FGM coatings for the results of both punches, the augmentation of magnetic induction is valid in only flat punch results. Table 5.8 shows that the lowest $K_I(-1)$ and $K_I(1)$ values are obtained for FGM1 (linear) coating which possesses the lowest MEE content.
4. Though an increment in punch speed $\lambda_{(1)}$ results in the rise in both of the magnitudes of S_{ZZ} and S_{XX} inside the contact region in flat punch results, we observe the opposite trend in the results of triangular punch.
5. $\lambda_{(1)}$ acts like a neutral parameter in electromagnetic response. Both SIFs and punch force tend to diminish as $\lambda_{(1)}$ increases.

6. The general tendency in the effects of thicker coatings is that the energy generated due to contact is transferred to electromagnetic functions more. Although greater stress intensifications occur for thicker coatings at the sharp ends of the flat punch, the increase in coating thickness leads SIF and punch force to fall off for triangular punch results.

- Multiferroic Less Stiff Coating (Semi-circular and Circular Punches)
  1. In general, it is found that MEE rich coatings lower the magnitude of contact stress S_{ZZ}.
  2. The lateral stress S_{XX} behaves like S_{ZZ} for $s > 0$.
  3. The curves of electromagnetic functions plotted for different coatings are usually close. The magnitude of electric displacement in general is larger for H coating.
  4. The coating types differ particularly the punch force. Linear coating possesses the greatest punch force.
  5. Normal stress S_{ZZ} tends to drop as $\lambda_{(1)}\uparrow$, however, $\lambda_{(1)}$ has no critical impact on S_{XX}, Ω_X and Γ_X in general.
  6. Thin coatings result in the generation of larger S_{ZZ} and S_{XX} magnitudes in the contact region. Thicker coatings show stronger electromagnetism.
  7. Though the variation of η has limited effects on S_{ZZ}, tremendous rises can be noticed for S_{XX}. Friction coefficient is also strongly coupled with electromagnetism.

To sum up, material gradation lowers the possibility of failure due to lateral stress concentration for both stiffer and less stiff coatings. The dynamic effects of the punch cannot be ignored in the analyses. Lastly, the friction coefficient and the coating thickness are crucial in the models.

6.2 Future Studies

Smart structures developed to respond in a reversible way when exposed to external stimuli such as mechanical stress, electric and magnetic fields, solar radiation and temperature will shape the future of many technological applications. Piezoelectric (mechanic-electric coupling), photochromic (solar radiation triggered), thermoelectric (thermal-electric coupling), magneto-electro-elastic materials and shape memory alloys (heat induced) constitute the main types of smart materials. Piezoelectric materials possess the ability of converting mechanical energy into electric energy (polarization) and vice versa. The direct piezoelectric effect is the generation of electric polarization in response to an applied stress. The discussed contact mechanics analyses can be extended for piezoelectric structures.

A crucial concept in multi-layer coating design is the utilization of thinner and higher number of sublayers. Despite examining a single type of multi-layer elastic coating in the present study, Penkov et al. (2015) suggest many periodic coating specimens. By keeping the total thickness of Co/C layers same, decreasing the sublayer thicknesses of Co/C and increasing the number of sublayers, the contact analyses may be repeated and the variations in these results may be tracked.

In contacting bodies, subsurface stresses reach peak levels in a region beneath the surface. This region is prone to failure due to high stress levels. At the first stages of loading, micro cracks originate in this region. Then, these cracks unite and form larger kinked cracks and lead to deterioration of the body. The prediction of the region exposed to high subsurface stresses can be made by determining the distribution of stresses in the thickness direction of the coating. For HMLM, plotting these stresses is a difficult and time consuming job since N is a large number. For each sublayer in the coating, these stress distributions must be calculated considering different $G_{(i)j}$ functions and connected with each other in order to illustrate the total stress distributions. A fast algorithm can be developed to prepare such figures analysing subsurface stress distributions.

In multiferroic structures, electro-magnetic insulation is implemented by Eqs. (3.249) and (3.250). Such an insulated multiferroic structure is proposed by Zhang et al. (2017). However, insulation conditions may not be valid in some applications if a punch made of conducting material is prefered as the loading agent. For such a case, $D_{(N+M+1)Z}(X,0)$ and $B_{(N+M+1)Z}(X,0)$ become nonzero and possess unknown distributions in the contact region. Therefore, a conducting punch problem of heterogeneous multiferroic structures emerges. The solution of this problem is possible only if three singular integral equations are solved simultaneously for normal stress, electric displacement and magnetic induction in Z direction inside the contact zone. Thus, a conducting punch problem can be studied as a future work.

The author is also planning to prepare a project proposal for TÜBİTAK 2218 or 2219 Post-Doctarate Research Scholarship Programs on fracture mechanics of piezoelectric hetero-structures. The scope of the project involves the examination of quasi-static and elastodynamic surface, embedded, oblique and interface fracture models of graded piezoelectric systems. The main goal of the project will be determining quasi-static and dynamic stress and electric intensity factors which identify the fracture characteristics.

REFERENCES

Abdullaev et al. (2015) 'Density and Thermal Expansion of High Purity Nickel over the Temperature Range from 150 K to 2030 K', *Int J Thermophys*, 36, pp. 603–619. Available at: https://doi.org/10.1007/s10765-015-1839-x.

Abramowitz, M. and Stegun, I. A. (1964) Handbook of Mathematical Functions with Formulas, Garphs and Mathematical Tables, National Bureu of Standards, Applied Mathematics Series.

Afonin, S. M. (2019) 'Electro Magneto Elastic Actuator for Nanomedical Research', *Global Journal of Anesthesia & Pain Medicine*, 2(1), pp. 118–120. Available at: https://doi.org/10.32474/gjapm.2019.02.000128.

Aguesse, F. et al. (2012) 'Enhanced magnetic performance of $CoFe_2O_4/BaTiO_3$ multilayer nanostructures with a $SrTiO_3$ ultra-thin barrier layer', *Scripta Materialia*, 67, pp. 249–252. Available at: https://doi.org/10.1016/j.scriptamat.2012.04.030.

Ajdour, M. et al. (2016) 'Modeling and analysis of loaded multilayered magneto-electro-elastic structures composite materials: Applications', *Advanced Electromagnetics*, 5(3), pp. 91–97.

Alinia, Y. and Espo, M. (2020) 'Sliding contact problem of an FGM coating/substrate system with two-dimensional material property grading', *Acta Mechanica*, 231, pp. 649–659. Available at: https://doi.org/10.1007/s00707-019-02563-z.

Annamalai, A. R. et al. (2018) 'Effect of heating mode on sinterability of YSZ+CeO_2 ceramics', *Metals*, 8(3), p:189.

Apu, E. H. et al. (2022) 'Biomedical applications of multifunctional magnetoelectric nanoparticles', *Materials Chemistry Frontiers*, 6, pp. 1368–1390. Available at: https://doi.org/10.1039/d2qm00093h.

Arslan, O. (2016) 'Contact Mechanics of Graded Orthotropic Coatings', Ph.D. dissertation, Middle East Technical University.

AZO Materials, Cobalt (Co) – Properties, Applications. (2023) https://www.azom.com/article.aspx?ArticleID=9077.

Bai, X. M. et al. (2013) 'A dynamic piecewise-exponential model for transient crack problems of functionally graded materials with arbitrary mechanical properties', *Theoretical and Applied Fracture Mechanics*, 66, pp. 41–51. Available at: https://doi.org/10.1016/j.tafmec.2013.09.001.

Balci, M. N. (2018) 'Dynamic Frictional Contact Problems Involving Functionally Graded Materials', Ph.D. dissertation, Middle East Technical University.

Balci, M. N. (2020) ‘The effect of punch speed on frictional contact mechanics of finite-thickness graded layer resting on the rigid foundation’, *Journal of the Brazilian Society of Mechanical Sciences and Engineering*, 42, p. 343. Available at: https://doi.org/10.1007/s40430-020-02406-2.

Balci, M. N. and Dag, S. (2018a) ‘Dynamic frictional contact problems involving elastic coatings’, *Tribology International*, 124, pp. 70–92. Available at: https://doi.org/10.1016/j.triboint.2018.03.033.

Balci, M. N. and Dag, S. (2018b) ‘Dynamic behavior of a functionally graded coating subjected to moving contact with a semi-circular punch’, *15th International Symposium on Functionally Graded Materials*.

Balci, M. N. and Dag, S. (2019a) ‘Solution of the dynamic frictional contact problem between a functionally graded coating and a moving cylindrical punch’, *International Journal of Solids and Structures*, 161, pp. 267–281. Available at: https://doi.org/10.1016/j.ijsolstr.2018.11.020.

Balci, M. N. and Dag, S. (2019b) ‘Mechanics of dynamic contact of coated substrate and rigid cylindrical ended punch’, *Journal of Mechanical Science and Technology*, 33(5), pp. 2225–2240. Available at: https://doi.org/10.1007/s12206-019-0425-8.

Balci, M. N. and Dag, S. (2020) ‘Moving contact problems involving a rigid punch and a functionally graded coating’, *Applied Mathematical Modelling*, 81, pp. 855–886. Available at: https://doi.org/10.1016/j.apm.2020.01.004.

Bayat, M. et al. (2019) ‘Thermo-mechanical contact problems and elastic behaviour of single and double sides functionally graded brake disks with temperature-dependent material properties’, *Scientific Reports*, 9, p. 15317. Available at: https://doi.org/10.1038/s41598-019-51450-z.

Behera, B., Sutar, B. C. and Pradhan, N. R. (2021) ‘Recent progress on 2D ferroelectric and multiferroic materials, challenges, and opportunity’, *Emergent Materials*, 4, pp. 847–863. Available at: https://doi.org/10.1007/s42247-021-00223-4.

Bhattarai, B., Pandey, A. and Drabold, D. A. (2018) ‘Evolution of amorphous carbon across densities: An inferential study’, *Carbon*, 131, pp. 168–174. Available at: https://doi.org/10.1016/j.carbon.2018.01.103.

Bhavar et al. (2017) ‘A Review on Functionally Gradient Materials (FGMs) and Their Applications’, *IOP Conference Series: Materials Science and Engineering*, 229, p. 012021. Available at: https://doi.org/10.1088/1757899X/229/1/012021.

Bhoi, K. et al. (2021) ‘Unravelling the nature of magneto-electric coupling in room temperature multiferroic particulate ($PbFe_{0.5}Nb_{0.5}O_3$)–

($Co_{0.6}Zn_{0.4}Fe_{1.7}Mn_{0.3}O_4$) composites', *Scientific Reports*, 11, p. 3149. Available at: https://doi.org/10.1038/s41598-021-82399-7.

Bhushan, B. and Peng, W. (2002) 'Contact mechanics of multilayered rough surfaces', *Applied Mechanics Reviews*, 55(5), pp. 435–479. Available at: https://doi.org/10.1115/1.1488931.

Bishay, P. L. et al. (2012) 'Analysis of functionally graded magneto-electro-elastic composites using hybrid/mixed finite elements and node-wise material properties', *Computers, Materials and Continua*, 29(3), pp. 213–261.

Chang, S. J. et al. (2019) '$GdFe_{0.8}Ni_{0.2}O_3$: A Multiferroic material for low-power spintronic devices with high storage capacity', *ACS Applied Materials and Interfaces*, 11(34), pp. 31562–31572. Available at: https://doi.org/10.1021/acsami.9b11767.

Chaudhuri, A. and Mandal, K. (2015) 'Large magnetoelectric properties in $CoFe_2O_4$:$BaTiO_3$ core-shell nanocomposites', *Journal of Magnetism and Magnetic Materials*, 377, pp. 441–445. Available at: https://doi.org/10.1016/j.jmmm.2014.10.142.

Chen, W. et al. (2010) 'Theory of indentation on multiferroic composite materials', *Journal of the Mechanics and Physics of Solids*, 58, pp. 1524–1551. Available at: https://doi.org/10.1016/j.jmps.2010.07.012.

Chen, X. Z. et al. (2016) 'Magnetoelectric micromachines with wirelessly controlled navigation and functionality', *Materials Horizons*, 3, pp. 113–118. Available at: https://doi.org/10.1039/c5mh00259a.

Chudzikiewicz, A. and Myśliński, A. (2011) 'On Wheel - Rail Elastic Contact Problems for Multi-Layer Structure', *Computer Methods in Mechanics*.

Comez, I. (2015) 'Contact problem for a functionally graded layer indented by a moving punch', *International Journal of Mechanical Sciences*, 100, pp. 339–344. Available at: https://doi.org/10.1016/j.ijmecsci.2015.07.006.

Comez, I. (2021a) 'Thermoelastic contact problem of a magneto-electro-elastic layer indented by a rigid insulating punch', *Mechanics of Advanced Materials and Structures*, 29, pp. 7231–7245. Available at: https://doi.org/10.1080/15376494.2021.1995087.

Comez, I. (2021b) 'Frictional moving contact problem between a conducting rigid cylindrical punch and a functionally graded piezoelectric layered half plane', *Meccanica*, 56, pp. 3039–3058. Available at: https://doi.org/10.1007/s11012-021-01407-2.

Comez, I. (2021c) 'Frictional moving contact problem of a magneto-electro- lastic half plane', *Mechanics of Materials*, 154, p. 103704. Available at: https://doi.org/10.1016/j.mechmat.2020.103704.

Dag, S. (2001) ‘Crack and Contact Problems in Graded Materials’, Ph.D. dissertation, Lehigh University.

Dag, S. (2007) ‘Mixed-mode fracture analysis of functionally graded materials under thermal stresses: A new approach using Jk-integral’, *Journal of Thermal Stresses*, 30, pp. 269–296. Available at: https://doi.org/10.1080/01495730601130943.

Dag, S. et al. (2013) ‘Frictional Hertzian contact between a laterally graded elastic medium and a rigid circular stamp’, *Acta Mechanica*, 224, pp. 1773–1789. Available at: https://doi.org/10.1007/s00707-013-0844-z.

Daga, A., Ganesan, N. and Shankar, K. (2009) ‘Behaviour of magneto-electro-elastic sensors under transient mechanical loading’, *Sensors and Actuators, A: Physical*, 150, pp. 46–55. Available at: https://doi.org/10.1016/j.sna.2008.11.035.

Dai, Y. Q. et al. (2014) ‘Thickness effect on the properties of $BaTiO_3$-$CoFe_2O_4$ multilayer thin films prepared by chemical solution deposition’, *Journal of Alloys and Compounds*, 587, pp. 681–687. Available at: https://doi.org/10.1016/j.jallcom.2013.11.026.

De, J. and Patra, B. (1994). Dynamic punch problems in an orthotropic elastic half-plane. *International J. Pure and Applied Math*., 25(7), pp. 767-776.

Du, L., Shi, G. and Zhao, J. (2013) ‘Static characteristics of micro disc magneto electric generator--simulation and experiment’, *Applied Mechanics and Materials*, 365–366, pp. 356–359. Available at: https://doi.org/10.4028/www.scientific.net/AMM.365-366.356.

Elloumi, R. et al. (2013) ‘Closed-form solutions of the frictional sliding contact problem for a magneto-electro-elastic half-plane indented by a rigid conducting punch’, *International Journal of Solids and Structures*, 50, pp. 3778–3792.

Elloumi, R. et al. (2014) ‘On the frictional sliding contact problem between a rigid circular conducting punch and a magneto-electro-elastic half-plane’, *International Journal of Mechanical Sciences*, 87, pp. 1–17. Available at: https://doi.org/10.1016/j.ijmecsci.2014.04.024.

Elloumi, R. et al. (2016) ‘The contact problem of a rigid stamp with friction on a functionally graded magneto-electro-elastic half-plane’, *Acta Mechanica*, 227, 1123–1156. Available at: https://doi.org/10.1007/s00707-015-1504-2.

El-Wazery, M. S. and El-Desouky, A. R. (2015) ‘A review on Functionally Graded Ceramic-Metal Materials A review on Functionally Graded Ceramic-Metal Materials’, *Journal of Materials and Environmental Science*, 6(5), pp. 1369-1376.

Erdem, D. et al. (2016) ‘Nanoparticle-Based Magnetoelectric $BaTiO_3$-$CoFe_2O_4$ Thin Film Heterostructures for Voltage Control of Magnetism’, *ACS Nano*, 10(11), pp. 9840–9851. Available at: https://doi.org/10.1021/acsnano.6b05469.

Erdogan, F. (1978) ‘Mixed boundary value problems in mechanics’, In: Nemat-Nasser S, editor. Mechanics today, Pergamon Press, 4, 1–86.

Eringen, A. C. and Suhubi, E. S. (1975) *Elastodynamics: Linear Theory*, Academic Press Inc, Fifth Avenue, NewYork, 10003.

Erum, N. and Iqbal, M. A. (2020) ‘Elastomechanical and magneto-optoelectronic investigation of $RbCoF_3$: An ab initio DFT Study’, *Acta Physica Polonica A*, 138(3), pp. 509–517. Available at: https://doi.org/10.12693/APhysPolA.138.509.

Eshraghi, I. and Dag, S. (2018) ‘Domain-boundary element method for elastodynamics of functionally graded Timoshenko beams’, *Computers and Structures*, 195, pp. 113–125. Available at: https://doi.org/10.1016/j.compstruc.2017.10.007.

Fujii, S. et al. (2022) ‘Giant converse magnetoelectric effect in a multiferroic heterostructure with polycrystalline Co_2FeSi’, *NPG Asia Materials*, 14, p. 43. Available at: https://doi.org/10.1038/s41427-022-00389-1.

Gao, W. et al. (2018) ‘Energy transduction ferroic materials’, *Materials Today*, 21(7), pp. 771–784. Available at: https://doi.org/10.1016/j.mattod.2018.01.032.

Gao, J. et al. (2021) ‘Review of magnetoelectric sensors’, *Actuators*, 10, p. 109. Available at: https://doi.org/10.3390/act10060109.

Giannakopoulos, A.E. and Parmaklis, A.Z. (2007) ‘The contact problem of a circular rigid punch on piezomagnetic materials’, *International Journal of Solids and Structures*, 44, pp. 4593–4612. Available at: https://doi.org/10.1016/j.ijsolstr.2006.11.040.

Giraud, S. and Canel, J. (2008) ‘Young’s modulus of some SOFCs materials as a function of temperature’, *Journal of the European Ceramic Society*, 28, pp. 77–83.

Golalikhani, M. et al. (2018) ‘Nature of the metal-insulator transition in few-unit-cell-thick $LaNiO_3$ films’, *Nature Communications*, 9, p. 2206.

Gradauskaite, E. et al. (2021) ‘Multiferroic heterostructures for spintronics’, *Physical Sciences Reviews*, 6(2), p. 20190072.

Guler, M. A. (2001) ‘Contact Mechanics of FGM coatings’, Ph.D. dissertation, Lehigh University.

Guler, M. A. and Erdogan, F. (2004) ‘Contact mechanics of graded coatings’, *International Journal of Solids and Structures*, 41, pp. 3865–3889. Available at: https://doi.org/10.1016/j.ijsolstr.2004.02.025.

Guler, M. A. and Erdogan, F. (2007) ‘The frictional sliding contact problems of rigid parabolic and cylindrical stamps on graded coatings’, *International Journal of Mechanical Sciences*, 49, pp. 161–182. Available at: https://doi.org/10.1016/j.ijmecsci.2006.08.006.

Gulver, Y. F. (2009) ‘İşlevsel Derecelendirilmiş Kaplamalara Bağlı İnce Filmlerin Mekanik Modellenmesi’, M.S. Thesis, TOBB University.

Guo, L. et al. (2018) ‘The interface crack problem for a functionally graded coating-substrate structure with general coating properties’, *International Journal of Solids and Structures*, 146, pp. 136–153. Available at: https://doi.org/10.1016/j.ijsolstr.2018.03.025.

Guo, L. C. and Noda, N. (2007) ‘Modeling method for a crack problem of functionally graded materials with arbitrary properties-piecewise-exponential model’, *International Journal of Solids and Structures*, 44, pp. 6768–6790. Available at: https://doi.org/10.1016/j.ijsolstr.2007.03.012.

Hadouchi, M. et al. (2020) ‘Enhanced magnetization in multiferroic nanocomposite $Bi_{0.9}Gd_{0.1}Fe_{0.9}Mn_{0.05}X_{0.05}O_3$ (X= Cr, Co) thin films’, *Thin Solid Films*, 709, p. 138025. Available at: https://doi.org/10.1016/j.tsf.2020.138025.

Hasanyan, D. et al. (2012) ‘Theoretical and experimental investigation of magnetoelectric effect for bending-tension coupled modes in magnetostrictive-piezoelectric layered composites’, *Journal of Applied Physics*, 112, p. 013908. Available at: https://doi.org/10.1063/1.4732130.

Hayward, S. A. et al. (2005) ‘Phase transitions in $BaTiO_3$: A high-pressure neutron diffraction study’, *Zeitschrift fur Kristallographie*, 220, pp. 735–739. Available at: https://doi.org/10.1524/zkri.220.8.735.67077.

Hao, L. et al. (2013) ‘Multiferroic properties of multilayered $BaTiO_3$-$CoFe_2O_4$ composites via tape casting method’, *Journal of Materials Science*, 48, pp. 178–185. Available at: https://doi.org/10.1007/s10853-012-6726-2.

He, W. and Liu, S. (2022) ‘A magnetoelectric energy harvester for low-frequency vibrations and human walking’, *Journal of Magnetism and Magnetic Materials*, 542, p. 168609. Available at: https://doi.org/10.1016/j.jmmm.2021.168609.

Hosseini, M. et al. (2018) ‘Nanoscale mass nanosensor based on the vibration analysis of embedded magneto-electro-elastic nanoplate made of FGMs via nonlocal Mindlin plate theory’, *Microsystem Technologies*, 24, pp. 2295–2316. Available at: https://doi.org/10.1007/s00542-017-3654-8.

Hong, J. et al. (2021) ‘On the bending and vibration analysis of functionally graded magneto-electro-elastic timoshenko microbeams’, *Crystals*, 11, p. 1206. Available at: https://doi.org/10.3390/cryst11101206.

Hu, J. (2020) ‘High Frequency Multiferroic Devices’, Ph.D. dissertation, University of California Los Angeles.

Huang, W. and Liu, T. (2019) ‘The Investigation on Adhesive Contact Problem of Gradient Piezoelectric Coating under Insulating Punch’, *IOP Conference Series: Materials Science and Engineering*, 472, p. 012053. Available at: https://doi.org/10.1088/1757-899X/472/1/012053.

Jahedi, R. and Adibnazari, S. (2015) ‘Multi layered finite element analysis of graded coatings in frictional rolling contact’, *International Journal of Advanced Design and Manufacturing Technology*, 8(1), pp. 1–12. Available at: http://admt.iaumajlesi.ac.ir/index/index.php/me/article/view/883.

Jian, G. and Wong, C. P. (2017) ‘Orientation dependence of magnetoelectric coefficient in $BaTiO_3/CoFe_2O_4$’, *AIP Advances*, 7, p. 075307. Available at: https://doi.org/10.1063/1.4994042.

Jobin, K. J., Abhilash, M. N. and Murthy, H. (2017) ‘A simplified analysis of 2D sliding frictional contact between rigid indenters and FGM coated substrates’, *Tribology International*, 108, pp. 174–185. Available at: https://doi.org/10.1016/j.triboint.2016.09.021.

Katta, R. R. et al. (2009) ‘Plane strain sliding contact of multilayer magnetic storage thin-films using the finite element method’, *Microsystem Technologies*, 15(7), pp. 1097–1110. Available at: https://doi.org/10.1007/s00542-009-0859-5.

Ke, L. L. and Wang, Y. S. (2006) ‘Two-dimensional contact mechanics of functionally graded materials with arbitrary spatial variations of material properties’, *International Journal of Solids and Structures*, 43, pp. 5779–5798. Available at: https://doi.org/10.1016/j.ijsolstr.2005.06.081.

Ke, L. L. and Wang, Y. S. (2007) ‘Two-dimensional sliding frictional contact of functionally graded materials’, *European Journal of Mechanics, A/Solids*, 26, pp. 171–188. Available at: https://doi.org/10.1016/j.euromechsol.2006.05.007.

Ke, L. L. et al. (2008a) ‘Frictionless contact analysis of a functionally graded piezoelectric layered half-plane’, *Smart Materials and Structures*, 17, p. 025003. Available at: https://doi.org/10.1088/0964-1726/17/2/025003.

Ke, L. L. et al. (2008b) ‘Electro-mechanical frictionless contact behavior of a functionally graded piezoelectric layered half-plane under a rigid punch’, *International Journal of Solids and Structures*, 45, pp. 3313–3333. Available at: https://doi.org/10.1016/j.ijsolstr.2008.01.028.

Ke, L. L. et al. (2010) ‘Sliding frictional contact analysis of functionally graded piezoelectric layered half-plane’, *Acta Mechanica*, 209, pp. 249–268. Available at: https://doi.org/10.1007/s00707-009-0181-4.

Kieback, B., Neubrand, A. and Riedel, H. (2003) ‘Processing techniques for functionally graded materials’, *Materials Science and Engineering: A*, 362, pp. 81–106. Available at: https://doi.org/10.1016/S0921-5093(03)00578-1.

Kopyl, S. et al. (2021) ‘Magnetoelectric effect: principles and applications in biology and medicine– a review’, *Materials Today Bio*, 12, p. 100149. Available at: https://doi.org/10.1016/j.mtbio.2021.100149.

Kot, M. (2012) ‘Contact mechanics of coating-susbtrate systems: Monolayer and multilayer coatings’, *Archives of Civil and Mechanical Engineering*, 12, pp. 464-470.

Kravchuk, A., Rymuza, Z. and Jarzabek, D. (2009). Penetration of a pyramid indenter into a multilayer coating. *Int. J. Mat. Res. (formerly Z. Metal.lkd.)* 100, p. 7.

Kumar, D. and Sarangi, S. (2018) ‘Instability analysis of an electro-magneto-elastic actuator: A continuum mechanics approach’, *AIP Advances*, 8(11), p. 115314. Available at: https://doi.org/10.1063/1.5055793.

Kumar, M. et al. (2020) ‘Progress in multiferroic and magnetoelectric materials: applications, opportunities and challenges’, *Journal of Materials Science: Materials in Electronics*, 31, pp. 19487–19510. Available at: https://doi.org/10.1007/s10854-020-04574-2.

Li, M., Liu, M. and Zhou, L. (2020) ‘The static behaviors study of magneto-electro-elastic materials under hygrothermal environment with multi-physical cell-based smoothed finite element method’, *Composites Science and Technology*, 193, p. 108130. Available at: https://doi.org/10.1016/j.compscitech.2020.108130.

Li, W. and Han, B. (2018) ‘Research and Application of Functionally Gradient Materials’, *IOP Conference Series: Materials Science and Engineering*, 394, p. 022065. Available at: https://doi.org/10.1088/1757-899X/394/2/022065.

Liang, X., Chen, H. and Sun, N. X. (2021) ‘Magnetoelectric materials and devices’, *APL Materials*, 9, p. 041114. Available at: https://doi.org/10.1063/5.0044532.

Liu, G., Ci, P. and Dong, S. (2014) ‘Energy harvesting from ambient low-frequency magnetic field using magneto-mechano-electric composite cantilever’, *Applied Physics Letters*, 104, p. 032908. Available at: https://doi.org/10.1063/1.4862876.

Liu, H. and Lyu, Z. (2020) ‘Modeling of novel nanoscale mass sensor made of smart FG magneto-electro-elastic nanofilm integrated with graphene layers’, *Thin-*

Walled Structures, 151, p. 106749. Available at: https://doi.org/10.1016/j.tws.2020.106749.

Liu, J., Ke, L. L. and Wang, Y. S. (2011) 'Two-dimensional thermoelastic contact problem of functionally graded materials involving frictional heating', *International Journal of Solids and Structures*, 48, pp. 2536–2548. Available at: https://doi.org/10.1016/j.ijsolstr.2011.05.003.

Liu, J. et al. (2012) 'Thermoelastic frictional contact of functionally graded materials with arbitrarily varying properties', *International Journal of Mechanical Sciences*, 63, pp. 86–98. Available at: https://doi.org/10.1016/j.ijmecsci.2012.06.016.

Liu, T. J. and Wang, Y. S. (2008) 'Axisymmetric frictionless contact problem of a functionally graded coating with exponentially varying modulus', *Acta Mechanica*, 199, pp. 151–165. Available at: https://doi.org/10.1007/s00707-007-0556-3.

Liu, T. J. et al. (2016) 'The axisymmetric stress analysis of double contact problem for functionally graded materials layer with arbitrary graded materials properties', *International Journal of Solids and Structures*, 96, pp. 229–239. Available at: https://doi.org/10.1016/j.ijsolstr.2016.06.006.

Ma, J. et al. (2011) 'Recent progress in multiferroic magnetoelectric composites: From bulk to thin films', *Advanced Materials*, 23, pp. 1062–1087. Available at: https://doi.org/10.1002/adma.201003636.

Ma, J., Ke, L. L. and Wang, Y. S. (2014) 'Frictionless contact of a functionally graded magneto-electro-elastic layered half-plane under a conducting punch', *International Journal of Solids and Structures*, 51, pp. 2791–2806. Available at: https://doi.org/10.1016/j.ijsolstr.2014.03.028.

Ma, J., Ke, L. L. and Wang, Y. S. (2015) 'Sliding Frictional Contact of Functionally Graded Magneto-Electro-Elastic Materials under a Conducting Flat Punch', *Journal of Applied Mechanics, Transactions ASME*, 82, p. 011009-1. Available at: https://doi.org/10.1115/1.4029090.

Ma, J. et al. (2016) 'Frictional contact problem between a functionally graded magnetoelectroelastic layer and a rigid conducting flat punch with frictional heat generation', *Journal of Thermal Stresses*, 39(3), pp. 245–277. Available at: https://doi.org/10.1080/01495739.2015.1124648.

Malleron, K. et al. (2019) 'Experimental study of magnetoelectric transducers for power supply of small biomedical devices', *Microelectronics Journal*, 88, pp. 184–189. Available at: https://doi.org/10.1016/j.mejo.2018.01.013.

Masys, S. and Jonauskas, V. (2015) 'Elastic properties of rhombohedral, cubic, and monoclinic phases of $LaNiO_3$ by first principles calculations', *Computational Materials Science*, 108, pp. 153–159.

Matavž, A. et al. (2021) ‘Nanostructured multiferroic $Pb(Zr,Ti)O_3$–$NiFe_2O_4$ thin-film composites’, *Thin Solid Films,* 732, p. 138740. Available at: https://doi.org/10.1016/j.tsf.2021.138740.

McGuiggan, P. M. et al. (2007) ‘Contact mechanics of layered elastic materials: Experiment and theory’, *Journal of Physics D: Applied Physics*, 40, pp. 5984–5994. Available at: https://doi.org/10.1088/0022-3727/40/19/031.

MEMSnet. (2023) ‘Material: Silicon (Si) bulk’, https://www.memsnet.org/material/siliconsibulk/, reached on: September 22, 2023.

Merle, B. (2013) ‘Mechanical Properties of Thin Films Studied by Bulge Testing’, Ph.D. dissertation, University of Erlangen-Nuremberg.

Miteva, A. M. (2014) ‘An Overview of the Functionally Graded Materials’, *Scientific Proceedings II International Scientific-Technical Conference Technics, Technologies, Education, Safety,* pp. 71-74.

Miura, K., Sakamoto, M. and Tanabe, Y. (2020) ‘Analytical solution of axisymmetric indentation of multi-layer coating on elastic substrate body’, *Acta Mechanica*, 231, pp. 4077–4093. Available at: https://doi.org/10.1007/s00707-020-02752-1.

Opalinska, A. et al. (2015) ‘Size-dependent density of zirconia nanoparticles’, *Beilstein Journal of Nanotechnology*, 6, pp. 27–35. Available at: https://doi.org/10.3762/bjnano.6.4.

Palneedi, H. et al. (2016) ‘Status and perspectives of multiferroic magnetoelectric composite materials and applications’, *Actuators*, 5, p. 9. Available at: https://doi.org/10.3390/act5010009.

Penkov, O. V. et al. (2015) ‘Toward Zero Micro/Macro-Scale Wear Using Periodic Nano-Layered Coatings’, *ACS Applied Materials and Interfaces,* 7, pp. 18136–18144. Available at: https://doi.org/10.1021/acsami.5b05599.

Popoola, P. et al. (2016) ‘Laser Engineering Net Shaping Method in the Area of Development of Functionally Graded Materials (FGMs) for Aero Engine Applications - A Review’, *Fiber Laser,* pp. 383-400. Available at: https://doi.org/10.5772/61711.

Pradhan, D. K., Kumari, S. and Rack, P. D. (2020) ‘Magnetoelectric composites: Applications, coupling mechanisms, and future directions’, *Nanomaterials*, 10, p. 2072. Available at: https://doi.org/10.3390/nano10102072.

Ramesh, R. (2022) ‘Materials for a Sustainable Microelectronics Future: Electric Field Control of Magnetism with Multiferroics’, *Journal of the Indian Institute of Science,* 102(1), pp. 489–511. Available at: https://doi.org/10.1007/s41745-021-00277-7.

Riccardi, B. and Montanari, R. (2004) 'Indentation of metals by a flat-ended cylindrical punch', *Materials Science and Engineering: A*, 381, pp. 281–291. Available at: https://doi.org/10.1016/j.msea.2004.04.041.

Popov, V. L., Heß, M. and Willert, E. (2019) *Handbook of contact mechanics: Exact solutions of axisymmetric contact problems*, Springer-Verlag GmbH, Heidelberger Platz 3, 14197 Berlin, Germany.

Roy, A., Gupta, R. and Garg, A. (2012) 'Multiferroic memories', *Advances in Condensed Matter Physics*, 2012, p. 926290. Available at: https://doi.org/10.1155/2012/926290.

Rupp, T. et al. (2019) 'Magnetoelectric transducer designs for use as wireless power receivers in wearable and implantable applications', *Materials*, 12, p. 512. Available at: https://doi.org/10.3390/ma12030512.

Saiyathibrahim, A. et al. (2015) 'Processing Techniques of Functionally Graded Materials – A Review', *International Conference on Systems, Science, Control, Communication, Engineering and Technology*, pp. 98–105. Available at: https://www.semanticscholar.org/paper/Processing-Techniques-of-Functionally-Graded-A-Saiyathibrahim-Nazirudeen/ b53d758b3ceb544ea53ee414f8f62000a10b92a0.

Saleh, B. et al. (2020) '30 Years of functionally graded materials: An overview of manufacturing methods, Applications and Future Challenges', *Composites Part B: Engineering*, 201, p. 108376. Available at: https://doi.org/10.1016/j.compositesb.2020.108376.

Sayed, F. et al. (2021) 'Synthesis of $BaTiO_3$-$CoFe_2O_4$ nanocomposites using a one-pot technique', *Inorganica Chimica Acta*, 520, p. 120313. Available at: https://doi.org/10.1016/j.ica.2021.120313.

Schmitz-Antoniak, C. et al. (2013) 'Electric in-plane polarization in multiferroic $CoFe_2O_4$/$BaTiO_3$ nanocomposite tuned by magnetic fields', *Nature Communications*, 4, p. 2051. Available at: https://doi.org/10.1038/ncomms3051.

Scigaj, M. et al. (2016) 'Monolithic integration of room-temperature multifunctional $BaTiO_3$-$CoFe_2O_4$ epitaxial heterostructures on Si(001)', *Scientific Reports*, 6, p. 31870. Available at: https://doi.org/10.1038/srep31870.

Spaldin, N. A. (2020) 'Multiferroics beyond electric-field control of magnetism', *Proceedings of the Royal Society A: Mathematical, Physical and Engineering Sciences*, 476, p. 20190542. Available at: https://doi.org/10.1098/rspa.2019.0542.

Su, J., Ke, L. L. and Wang, Y. S. (2015) 'Two-dimensional fretting contact analysis of piezoelectric materials', *International Journal of Solids and Structures*, 73–74, pp. 41–54. Available at: https://doi.org/10.1016/j.ijsolstr.2015.07.026.

Su, J. et al. (2018) ‘An effective method for the sliding frictional contact of a conducting cylindrical punch on FGPMs’, *International Journal of Solids and Structures*, 141–142, pp. 127–136. Available at: https://doi.org/10.1016/j.ijsolstr.2018.02.017.

Suk, J. W. et al. (2012) ‘Mechanical measurements of ultra-thin amorphous carbon membranes using scanning atomic force microscopy’, *Carbon*, 50, pp. 2220–2225. Available at: https://doi.org/10.1016/j.carbon.2012.01.037.

Surowiak, Z. and Bochenek, D. (2008). “Multiferroic materials for sensors, transducers and memory devices”, 33, pp. 243-260.

Suzuki, K. et al. (2019) ‘Thermal and mechanical properties of CeO_2’, *Journal of the American Ceramic Society*, 102, pp. 1994–2008.

Tabakh, A. et al. (2019) ‘Magnetoelectric experiments and modelling in bi-layer composites consisting of polyurethane loaded with magnetic particles/piezoelectric ceramic’, *Applied Physics A: Materials Science and Processing*, 125, p. 667. Available at: https://doi.org/10.1007/s00339-019-2962-5.

Toktas, S. E. and Dag, S. (2022a) ‘Multi-layer model for moving contact problems of functionally graded coatings with general variations in physical properties’, *Proceedings of the Institution of Mechanical Engineers, Part L: Journal of Materials: Design and Applications*, 236(10), pp. 1967–1980. Available at: https://doi.org/10.1177/14644207221092119.

Toktas S. E. and Dag, S. (2022b) ‘On the moving contact problem between an arbitrarily graded coating and a semi-circular punch’, *Contact Mechanics International Symposium*, Chexbres, Lausanne, Switzerland.

Toktas, S. E. and Dag, S. (2022c) ‘Stresses in multi-layer coatings in Hertzian contact with a moving circular punch’, *Tribology International*, 171. Available at: https://doi.org/10.1016/j.triboint.2022.107565.

Toktas, S. E. and Dag, S. (2023a) ‘Mechanics of moving contacts involving functionally graded multiferroics’, *Archives of Mechanics*, 75(4), pp. 431–468. Available at: https://doi.org/10.24423/aom.4292.

Toktas S. E. and Dag, S. (2023b) ‘Fonksiyonel derecelendirilmiş multiferroik kaplama ile yarı-dairesel Zımba Arasında Hareketli Temas Problemi’, *23rd National Mechanics Congress*, KTUN, Konya, Türkiye.

Toktas S. E. and Dag, S. (2024) ‘Magneto-electro-elastic response of functionally graded multiferroic coatings under moving hertzian contact’, *Journal of Mechanics of Materials and Structures*, Manuscript is accepted.

Tricomi, F. G. (1957) *Integral Equations*, Interscience, New York, 1957.

Uetsuji, Y. and Wada, T. (2020) 'Computational study on microstructural optimization of multiferroic magnetoelectric composites', *Computational Materials Science*, 172, p. 109365. Available at: https://doi.org/10.1016/j.commatsci.2019.109365.

Vinyas, M. (2021) 'Computational Analysis of Smart Magneto-Electro-Elastic Materials and Structures: Review and Classification', *Archives of Computational Methods in Engineering*, 28, 1205–1248. Available at: https://doi.org/10.1007/s11831-020-09406-4.

Vopson, M. M. (2015) 'Fundamentals of multiferroic materials and their possible applications', *Critical Reviews in Solid State and Materials Sciences*, 40, pp. 223–250. Available at: https://doi.org/10.1080/10408436.2014.992584.

Wadhawan, V.K. (2002) 'Ferroic materials: A primer', *Resonance*, 7, pp. 15–24. Available at: https://doi.org/10.1007/bf02836749.

Wang, W., Li, P. and Jin, F. (2016) 'Two-dimensional linear elasticity theory of magneto-electro-elastic plates considering surface and nonlocal effects for nanoscale device applications', *Smart Materials and Structures*, 25 p. 095026. Available at: https://doi.org/10.1088/0964-1726/25/9/095026.

Wang, Z., Guo, L. and Zhang, L. (2014) 'A general modelling method for functionally graded materials with an arbitrarily oriented crack', *Philosophical Magazine*, 94, pp. 764–791. Available at: https://doi.org/10.1080/14786435.2013.863437.

Xu, X. et al. (2015) 'Zero-Biased Magnetoelectric Effects in Five-Phase Laminate Composites With FeCoV Soft Magnetic Alloy', *IEEE Transactions on Magnetics*, 51(11), p. 2006204.

Yan, J. and Mi, C. (2017) 'Double contact analysis of multilayered elastic structures involving functionally graded materials', *Archives of Mechanics*, 69(3), pp. 199–221.

Yastrebov, V. A. et al. (2011) 'Rough surface contact analysis by means of the Finite Element Method and of a new reduced model', *Comptes Rendus - Mecanique*, 339, pp. 473–490. Available at: https://doi.org/10.1016/j.crme.2011.05.006.

Zhang, C. et al. (2019) 'Additive manufacturing of functionally graded materials: A review', *Materials Science and Engineering: A*, 764, p. 138209. Available at: https://doi.org/10.1016/j.msea.2019.138209.

Zhang, H. et al. (2019) 'Semi-analytic modelling of transversely isotropic magneto-electro-elastic materials under frictional sliding contact', *Applied Mathematical Modelling*, 75, pp. 116–140. Available at: https://doi.org/10.1016/j.apm.2019.05.018.

Zhang, X. et al. (2017) ‘Frictional contact involving a multiferroic thin film subjected to surface magnetoelectroelastic effects’, *International Journal of Mechanical Sciences*, 131–132, pp. 633–648. Available at: https://doi.org/10.1016/j.ijmecsci.2017.07.039.

Zhang, X. et al. (2018) ‘Contact involving a functionally graded elastic thin film and considering surface effects’, *International Journal of Solids and Structures*, 150, pp. 184–196. Available at: https://doi.org/10.1016/j.ijsolstr.2018.06.016.

Zhao, Z. Y. et al. (2014) ‘Experimental observation of ferrielectricity in multiferroic $DyMn_2O_5$’, *Scientific Reports*, 4, p. 3984. Available at: https://doi.org/10.1038/srep03984.

Zhou, H. et al. (2013) ‘Theoretical and experimental study of multilayer piezo-magnetic structure based surface acoustic wave devices for high sensitivity magnetic sensor’, *IEEE International Ultrasonics Symposium, IUS*, pp. 212–215. Available at: https://doi.org/10.1109/ULTSYM.2013.0055.

Zhou, L. et al. (2021) ‘Evaluation of performance of magneto-electro-elastic sensor subjected to thermal-moisture coupled load via CS-FEM’, *Thin-Walled Structures*, 169, p. 108370. Available at: https://doi.org/10.1016/j.tws.2021.108370.

Zhou, Y. T. and Kim, T. W. (2013) ‘Frictional moving contact over the surface between a rigid punch and piezomagnetic materials - Terfenol-D as example’, *International Journal of Solids and Structures*, 50, pp. 4030–4042. Available at: https://doi.org/10.1016/j.ijsolstr.2013.08.015.

Zhou, Y. T. and Kim, T. W. (2014) ‘An exact analysis of sliding frictional contact of a rigid punch over the surface of magneto-electro-elastic materials’, *Acta Mechanica*, 225, pp. 625–645. Available at: https://doi.org/10.1007/s00707-013-0992-1.

Zhou, Y. T. and Lee, K. Y. (2012a) ‘Contact problem for magneto-electro-elastic half-plane materials indented by a moving punch. Part I: Closed-form solutions’, *International Journal of Solids and Structures*, 49, pp. 3853–3865. Available at: https://doi.org/10.1016/j.ijsolstr.2012.08.017.

Zhou, Y. T. and Lee, K. Y. (2012b) ‘Contact problem for magneto-electro-elastic half-plane materials indented by a moving punch. Part II: Numerical results’, *International Journal of Solids and Structures*, 49, pp. 3866–3882. Available at: https://doi.org/10.1016/j.ijsolstr.2012.08.018.

Zhou, Y. T. and Lee, K. Y. (2013) ‘Theory of sliding contact for multiferroic materials indented by a rigid punch’, *International Journal of Mechanical Sciences*, 66, pp. 156–167. Available at: https://doi.org/10.1016/j.ijmecsci.2012.11.004.

Zhou, Y. T. and Lee, K. Y. (2014) ‘Dynamic behavior of a moving frictional punch over the surface of anisotropic materials’, *Applied Mathematical Modelling*, 38, pp. 2311–2327. Available at: https://doi.org/10.1016/j.apm.2013.10.038.

Zhou, Y. T., Lee, K. Y. and Jang, Y. H. (2014) ‘Indentation theory on orthotropic materials subjected to a frictional moving punch’, *Archives of Mechanics*, 66(2), pp. 71–94.

APPENDICES

A. The Details of Asymptotic Analyses

For sample calculation of $\omega_{11}^{\infty}(X,\zeta)$, the following simplification is done considering Eqs. (3.65) and (3.69).

$$\omega_{11}(X,\zeta) = \text{coeff}\left(I\zeta \sum_{i=1}^{4} G_{(N+1)i} e^{s_{(N+1)i}X}, \frac{P}{\mu_{(N+1)}} \right), \tag{A.1}$$

$$\omega_{11}^{\infty}(X,\zeta) = I\frac{\zeta}{|\zeta|} p_{11} \exp\left(s_{(N+1)2}X\right) + I\frac{\zeta}{|\zeta|} p_{12} \exp\left(s_{(N+1)4}X\right), \tag{A.2}$$

Observe that there is no term in Eq. (A.2) for roots with positive real parts $s_{(N+1)1}$ and $s_{(N+1)3}$. Guler (2001) states that the terms for $s_{(N+1)1}$ and $s_{(N+1)3}$ in Eq. (A.1) vanish as $\zeta \to \infty$. This simplification is proved in the following way. Recall Eqs. (3.50) and (3.51) for i=N.

$$\begin{bmatrix} z_{(N+1)1} & z_{(N+1)2} \\ z_{(N+1)3} & z_{(N+1)4} \end{bmatrix} = \begin{bmatrix} e^{-s_{(N+1)1}d_{(N)}} & 0 \\ 0 & e^{-s_{(N+1)3}d_{(N)}} \end{bmatrix} \begin{bmatrix} w_{(N)1} & w_{(N)2} \\ w_{(N)3} & w_{(N)4} \end{bmatrix} \begin{bmatrix} e^{s_{(N+1)2}d_{(N)}} & 0 \\ 0 & e^{s_{(N+1)4}d_{(N)}} \end{bmatrix}, \tag{A.3}$$

$$\begin{bmatrix} z_{(N+1)1} & z_{(N+1)2} \\ z_{(N+1)3} & z_{(N+1)4} \end{bmatrix} = \begin{bmatrix} w_{(N)1} e^{\left(s_{(N+1)2}-s_{(N+1)1}\right)d_{(N)}} & w_{(N)2} e^{\left(s_{(N+1)4}-s_{(N+1)1}\right)d_{(N)}} \\ w_{(N)3} e^{\left(s_{(N+1)2}-s_{(N+1)3}\right)d_{(N)}} & w_{(N)4} e^{\left(s_{(N+1)4}-s_{(N+1)3}\right)d_{(N)}} \end{bmatrix}, \tag{A.4}$$

$$\begin{Bmatrix} G_{(N+1)1} \\ G_{(N+1)3} \end{Bmatrix} = \begin{bmatrix} w_{(N)1} e^{\left(s_{(N+1)2}-s_{(N+1)1}\right)d_{(N)}} & w_{(N)2} e^{\left(s_{(N+1)4}-s_{(N+1)1}\right)d_{(N)}} \\ w_{(N)3} e^{\left(s_{(N+1)2}-s_{(N+1)3}\right)d_{(N)}} & w_{(N)4} e^{\left(s_{(N+1)4}-s_{(N+1)3}\right)d_{(N)}} \end{bmatrix} \begin{Bmatrix} G_{(N+1)2} \\ G_{(N+1)4} \end{Bmatrix}. \tag{A.5}$$

Now, we expand

$$\sum_{i=1}^{4} G_{(N+1)i} e^{s_{(N+1)i}X} = G_{(N+1)1} e^{s_{(N+1)1}X} + G_{(N+1)2} e^{s_{(N+1)2}X} + G_{(N+1)3} e^{s_{(N+1)3}X} + G_{(N+1)4} e^{s_{(N+1)4}X}. \tag{A.6}$$

Using Eq. (A.5), $G_{(N+1)1}$ and $G_{(N+1)3}$ are substituted into Eq. (A.6).

$$G_{(N+1)1}^{\infty}e^{s_{(N+1)1}X}=w_{(N)1}G_{(N+1)2}^{\infty}e^{\left(s_{(N+1)2}-s_{(N+1)1}\right)d_{(N)}+s_{(N+1)1}X}+w_{(N)2}G_{(N+1)4}^{\infty}e^{\left(s_{(N+1)4}-s_{(N+1)1}\right)d_{(N)}+s_{(N+1)1}X},\quad 0\leq X\leq d_N. \tag{A.7}$$

$$G_{(N+1)3}^{\infty}e^{s_{(N+1)3}X}=w_{(N)1}G_{(N+1)2}^{\infty}e^{\left(s_{(N+1)2}-s_{(N+1)3}\right)d_{(N)}+s_{(N+1)3}X}+w_{(N)2}G_{(N+1)4}^{\infty}e^{\left(s_{(N+1)4}-s_{(N+1)3}\right)d_{(N)}+s_{(N+1)3}X},\quad 0\leq X\leq d_N. \tag{A.8}$$

Considering the interval of X, the exponential functions in Eqs. (A.7) and (A.8) approach to zero as $\zeta\to\infty$.

$$e^{\left(s_{(N+1)2}-s_{(N+1)1}\right)d_{(N)}+s_{(N+1)1}X}=e^{\left(s_{(N+1)4}-s_{(N+1)1}\right)d_{(N)}+s_{(N+1)1}X}=0,\quad G_{(N+1)1}^{\infty}e^{s_{(N+1)1}X}=0 \tag{A.9}$$

$$e^{\left(s_{(N+1)2}-s_{(N+1)3}\right)d_{(N)}+s_{(N+1)3}X}=e^{\left(s_{(N+1)4}-s_{(N+1)3}\right)d_{(N)}+s_{(N+1)3}X}=0,\quad G_{(N+1)3}^{\infty}e^{s_{(N+1)3}X}=0. \tag{A.10}$$

Remember that $s_{(N+1)i}$, i=1,…,4 are given by Eq. (3.24). Then, $G_{(N+1)2}^{\infty}$ and $G_{(N+1)4}^{\infty}$ are calculated and using (3.55) and (3.56) as $\zeta\to\infty$.

$$\begin{Bmatrix} G_{(N+1)2} \\ G_{(N+1)4} \end{Bmatrix}=\left[\Theta\right]\frac{1}{\mu_{(N+1)}}\begin{Bmatrix} \left(\kappa_{(N+1)}-1\right)P(\zeta) \\ Q(\zeta) \end{Bmatrix}, \tag{A.11}$$

$$\left[\Theta\right]=\left[\begin{bmatrix} r_{(N+1)2} & r_{(N+1)4} \\ r_{(N+1)6} & r_{(N+1)8} \end{bmatrix}+\begin{bmatrix} r_{(N+1)1} & r_{(N+1)3} \\ r_{(N+1)5} & r_{(N+1)7} \end{bmatrix}\begin{bmatrix} z_{(N+1)1} & z_{(N+1)2} \\ z_{(N+1)3} & z_{(N+1)4} \end{bmatrix}\right]^{-1}. \tag{A.12}$$

As $\zeta\to\infty$, one can modify Eqs. (A.11) and (A.12) as

$$\begin{Bmatrix} G_{(N+1)2}^{\infty} \\ G_{(N+1)4}^{\infty} \end{Bmatrix}=\left[\Theta\right]^{\infty}\frac{1}{\mu_{(N+1)}}\begin{Bmatrix} \left(\kappa_{(N+1)}-1\right)P(\zeta) \\ Q(\zeta) \end{Bmatrix}, \tag{A.13}$$

$$\left[\Theta\right]^{\infty}=\begin{bmatrix} r_{(N+1)2} & r_{(N+1)4} \\ r_{(N+1)6} & r_{(N+1)8} \end{bmatrix}^{-1}. \tag{A.14}$$

When $G^{\infty}_{(N+1)2}$ and $G^{\infty}_{(N+1)4}$ are inserted in Eq. (A.1), only constant terms p_{11} and p_{12} in Eq. (A.2) appear. Lastly, p_{11} and p_{12} are summed up and form the asymptotic coefficient p_1 in Eq. (3.87). Note that similar calculations are done for each $\omega_{ij}(X,\zeta)$.

B. The Coefficients Found by Asymptotic Analyses

The coefficients of the asymptotic analyses of the kernels for elastic structures are provided below.

$$p_1 = \frac{\sqrt{1-\lambda_{(N+1)}^2}\sqrt{1-\lambda_{(N+1)}^2\frac{\left(\kappa_{(N+1)}-1\right)}{\left(\kappa_{(N+1)}+1\right)}\lambda_{(N+1)}^2}}{\sqrt{1-\lambda_{(N+1)}^2}\left(\lambda_{(N+1)}^4-4\lambda_{(N+1)}^2+4\right)+\sqrt{1-\lambda_{(N+1)}^2\frac{\left(\kappa_{(N+1)}-1\right)}{\left(\kappa_{(N+1)}+1\right)}}\left(4\lambda_{(N+1)}^2-4\right)}, \tag{B.1}$$

$$p_2 = \frac{\sqrt{1-\lambda_{(N+1)}^2}\left(2-\lambda_{(N+1)}^2\right)+\sqrt{1-\lambda_{(N+1)}^2\frac{\left(\kappa_{(N+1)}-1\right)}{\left(\kappa_{(N+1)}+1\right)}}\left(2\lambda_{(N+1)}^2-2\right)}{\sqrt{1-\lambda_{(N+1)}^2}\left(\lambda_{(N+1)}^4-4\lambda_{(N+1)}^2+4\right)+\sqrt{1-\lambda_{(N+1)}^2\frac{\left(\kappa_{(N+1)}-1\right)}{\left(\kappa_{(N+1)}+1\right)}}\left(4\lambda_{(N+1)}^2-4\right)}, \tag{B.2}$$

$$p_3 = \frac{\lambda_{(N+1)}^2\left(1-\lambda_{(N+1)}^2\right)}{\sqrt{1-\lambda_{(N+1)}^2}\left(\lambda_{(N+1)}^4-4\lambda_{(N+1)}^2+4\right)+\sqrt{1-\lambda_{(N+1)}^2\frac{\left(\kappa_{(N+1)}-1\right)}{\left(\kappa_{(N+1)}+1\right)}}\left(4\lambda_{(N+1)}^2-4\right)}, \tag{B.3}$$

$$p_4 = -\frac{\sqrt{1-\lambda_{(N+1)}^2}\left(2-\lambda_{(N+1)}^2\right)+\sqrt{1-\lambda_{(N+1)}^2\frac{\left(\kappa_{(N+1)}-1\right)}{\left(\kappa_{(N+1)}+1\right)}}\left(2\lambda_{(N+1)}^2-2\right)}{\sqrt{1-\lambda_{(N+1)}^2}\left(\lambda_{(N+1)}^4-4\lambda_{(N+1)}^2+4\right)+\sqrt{1-\lambda_{(N+1)}^2\frac{\left(\kappa_{(N+1)}-1\right)}{\left(\kappa_{(N+1)}+1\right)}}\left(4\lambda_{(N+1)}^2-4\right)}. \tag{B.4}$$

The coefficients for multiferroic structures, p_i, i=1,…,8, are calculated by numerical asymptotic analyses of the integrands.

C. Properties of Jacobi Polynomials

Integrals related to Cauchy kernels are calculated utilizing the equations below provided by Tricomi (1957).

$$\begin{aligned}\frac{1}{\pi}\int_{-1}^{1}(1-r)^{\alpha_1}(1+r)^{\alpha_2}P_n^{(\alpha_1,\alpha_2)}(r)\frac{dr}{s-r} &= -\cot(\pi\alpha_1)(1-s)^{\alpha_1}(1+s)^{\alpha_2}P_n^{(\alpha_1,\alpha_2)}(s)\\ &+\frac{2^{(\alpha_1+\alpha_2)}\Gamma(\alpha_1)\Gamma(n+\alpha_2+1)}{\pi\,\Gamma(n+\alpha_1+\alpha_2+1)}F\left(n+1;-n-\alpha_1-\alpha_2;1-\alpha_1;\frac{1-s}{2}\right),\quad -1<s<1\end{aligned} \tag{C.1}$$

where $\alpha_1 > -1$, $\alpha_2 > -1$, $\alpha_1 \neq 0,1,2,\ldots$, and $\Gamma(\ )$ is the Gamma Function. Note that, $F(\ )$ designates Hypergeometric Function in this relation. Providing that $\varpi = -(\alpha_1+\alpha_2) = -1,0,1$, Eq. (C.1) reduces to

$$\begin{aligned}\frac{1}{\pi}\int_{-1}^{1}(1-r)^{\alpha_1}(1+r)^{\alpha_2}P_n^{(\alpha_1,\alpha_2)}(r)\frac{dr}{s-r} &= -\cot(\pi\alpha_1)(1-s)^{\alpha_1}(1+s)^{\alpha_2}P_n^{(\alpha_1,\alpha_2)}(s)\\ &+\frac{2^{-\varpi}}{\sin(\pi\alpha_1)}P_{n-\varpi}^{(-\alpha_1,-\alpha_2)}(s),\quad -1<s<1\end{aligned} \tag{C.2}$$

In the calculation of lateral stress, electric displacement and magnetic induction, the following recurrence type closed form solutions of Cauchy principal value integrals are calculated referring Arslan (2016).

$$L_n(s)=\int_{-1}^{1}\frac{(1-r)^{\alpha_1}(1+r)^{\alpha_2}}{r-s}P_n^{(\alpha_1,\alpha_2)}(r)\,dr,\quad -\infty<s<\infty. \tag{C.3}$$

The recurrence relation is written as follows:

$$L_n(s)=\frac{1}{P_{n-1}^{(\alpha_1,\alpha_2)}(s)}\left(P_n^{(\alpha_1,\alpha_2)}(s)L_{n-1}(s)+\frac{h_{n-1}}{G_{n-1}}\right),\quad -\infty<s<\infty,\quad n=1,2,\ldots, \tag{C.4}$$

$$h_0=\frac{2^{\alpha_1+\alpha_2+1}\Gamma(\alpha_1+1)\Gamma(\alpha_2+1)}{\Gamma(\alpha_1+\alpha_2+2)}, \tag{C.5}$$

$$h_n = \frac{2^{\alpha_1+\alpha_2+1}\Gamma(n+\alpha_1+1)\Gamma(n+\alpha_2+1)}{(2n+\alpha_1+\alpha_2+1)n!\Gamma(n+\alpha_1+\alpha_2+1)}, \quad n=1,2,..., \tag{C.6}$$

$$G_n = \frac{2(n+1)(\alpha_1+\alpha_2+n+1)}{(\alpha_1+\alpha_2+2n+1)(\alpha_1+\alpha_2+2n+2)}, \quad n=0,1,2,.... \tag{C.7}$$

Depending on the strength of singularities of the end points of the contact, the initial function $L_0(s)$ of the recurrence varies. Three possibilities of $L_0(s)$ are explicitly given below.

Case 1. $\alpha_1 < 0, \quad \alpha_2 < 0, \quad \alpha_1+\alpha_2 = -1.$

$$L_0(s) = \frac{\pi}{\sin(\pi\alpha_1)}\begin{cases} -(1-s)^{\alpha_1}(-1-s)^{\alpha_2}, & -\infty < s < -1 \\ (1-s)^{\alpha_1}(1+s)^{\alpha_2}\cos(\pi\alpha_1), & -1 < s < 1 \\ (s-1)^{\alpha_1}(s+1)^{\alpha_2}, & 1 < s < \infty \end{cases} \tag{C.8}$$

Case 2. $\alpha_1 > 0, \quad \alpha_2 < 0, \quad \alpha_1+\alpha_2 = 0.$

$$L_0(s) = \frac{\pi}{\sin(\pi\alpha_1)}\begin{cases} (1-s)^{\alpha_1}(-1-s)^{\alpha_2}-1, & -\infty < s < -1 \\ (1-s)^{\alpha_1}(1+s)^{\alpha_2}\cos(\pi\alpha_1)-1, & -1 < s < 1 \\ (s-1)^{\alpha_1}(s+1)^{\alpha_2}-1, & 1 < s < \infty \end{cases} \tag{C.9}$$

Case 3. $\alpha_1 > 0, \quad \alpha_2 > 0, \quad \alpha_1+\alpha_2 = 1.$

$$L_0(s) = \frac{\pi}{\sin(\pi\alpha_1)}\begin{cases} -(1-s)^{\alpha_1}(-1-s)^{\alpha_2}-s+\alpha_1-\alpha_2, & -\infty < s < -1 \\ (1-s)^{\alpha_1}(1+s)^{\alpha_2}\cos(\pi\alpha_1)-s+\alpha_1-\alpha_2, & -1 < s < 1 \\ (s-1)^{\alpha_1}(s+1)^{\alpha_2}-s+\alpha_1-\alpha_2, & 1 < s < \infty \end{cases} \tag{C.10}$$

D. The Method of Evaluation of Fredholm Kernels

Numerical methods applied in the calculation of Fredholm Kernels play a critical role in the accuracy of the results. A sample calculation for kernel $k_{11}(t,X)$ is explained below. Note that similar calculations are done for all Fredholm Kernels.

$$k_{11}(t,X)=\int_{0}^{\infty}\left(h_{11}(\zeta)-p_1\right)\sin\left(\zeta(t-X)\right)d\zeta, \tag{D.1}$$

At this point, Fredholm kernel is normalized and updated.

$$X=\frac{b}{2}s+\frac{b}{2},\ \ t=\frac{b}{2}r+\frac{b}{2},\ \ h_{11}(\zeta)=\frac{b}{2}h_{11}^{*}\left(\zeta^{*}\right), \tag{D.2}$$

$$\zeta=\frac{2}{b}\zeta^{*},\ \ p_1=\frac{b}{2}p_1^{*},\ \ k_{11}(r,s)=\frac{2}{b}K_{11}^{*}(r,s), \tag{D.3}$$

$$K_{11}(r,s)=\int_{0}^{\infty}\left(h_{11}^{*}\left(\zeta^{*}\right)-p_1^{*}\right)\sin\left(\zeta^{*}(r-s)\right)d\zeta^{*}. \tag{D.4}$$

Now, a suitable integration cut-off point $\left(A^{*}\right)$ is selected. Note that this cut-off point must be great enough in order to make the second term in the right-hand side of Eq. (D.5) zero.

$$K_{11}(r,s)=\int_{0}^{A^{*}}\left(h_{11}^{*}\left(\zeta^{*}\right)-p_1^{*}\right)\sin\left(\zeta^{*}(r-s)\right)d\zeta^{*}+\int_{A^{*}}^{\infty}\left(h_{11}^{*}\left(\zeta^{*}\right)-p_1^{*}\right)\sin\left(\zeta^{*}(r-s)\right)d\zeta^{*}, \tag{D.5}$$

Then, the interval with the cut-off point is normalized and Gauss-Legendre Quadrature method is performed.

$$\zeta^{*}=\frac{A^{*}}{2}\xi+\frac{A^{*}}{2}, \tag{D.6}$$

$$K_{11}(r,s)=\frac{A^*}{2}\int_{-1}^{1}\left(h_{11}^*(\xi)-p_1^*\right)\sin\left(\left(\frac{A^*}{2}\xi+\frac{A^*}{2}\right)(r-s)\right)d\xi\cong\sum_{k=1}^{T}w_k n_{11}(\xi_k), \tag{D.7}$$

$$n_{11}(\xi_k)=\frac{A^*}{2}\left(h_{11}^*(\xi)-p_1^*\right)\sin\left(\left(\frac{A^*}{2}\xi+\frac{A^*}{2}\right)(r-s)\right). \tag{D.8}$$

where w_k, $k=1,\ldots,T$, are the weights of quadrature method and ξ_k, $k=1,\ldots,T$, are the roots of Legendre functions. In order to avoid excessive computation time, the integration interval $0\le\xi\le A^*$ is divided into many parts. For each part, 20-point Gauss-Legendre Quadrature method is carried out and the results are summed up. Note that the weight function of Gauss-Legendre Quadrature method is 1 and it can be applied to any Fredholm kernel.

E. Closed Form Solution of Contact Mechanics of Homogenous MEE Half-Plane Indented by Circular Punch

In this appendix, the problem of homogeneous MEE half-plane in Hertzian contact with a rigid circular punch is briefly discussed. Referring to Eqs. (3.137)-(3.140), the field quantities are written in the simplified form as

$$U\left(X,Z\right)=\frac{1}{2\pi}\int_{-\infty}^{\infty}\sum_{j=1}^{4}G_{j}e^{\left(s_{j}Z+I\zeta X\right)}d\zeta,\ -\infty<X<\infty, \tag{E.1}$$

$$W\left(X,Z\right)=\frac{1}{2\pi}\int_{-\infty}^{\infty}\sum_{j=1}^{4}G_{j}F_{j}e^{\left(s_{j}Z+I\zeta X\right)}d\zeta,\ -\infty<X<\infty, \tag{E.2}$$

$$\Phi\left(X,Z\right)=\frac{1}{2\pi}\int_{-\infty}^{\infty}\sum_{j=1}^{4}G_{j}R_{j}e^{\left(s_{j}Z+I\zeta X\right)}d\zeta,\ -\infty<X<\infty, \tag{E.3}$$

$$\Psi\left(X,Z\right)=\frac{1}{2\pi}\int_{-\infty}^{\infty}\sum_{j=1}^{4}G_{j}Y_{j}e^{\left(s_{j}Z+I\zeta X\right)}d\zeta,\ -\infty<X<\infty. \tag{E.4}$$

where s_j are the roots with negative real parts given by Eqs. (3.150) and (3.151) and F_j, R_j and Y_j are provided by Eq. (3.155). Similar to Eq. (4.93), the singular integral equation of the homogenous MEE half-plane

$$\eta p_{2}S_{ZZ}\left(s\right)+\frac{p_{1}}{\pi}\int_{-1}^{1}\frac{S_{ZZ}\left(r\right)}{r-s}dr=-\frac{\left(b+a\right)s}{2Rc_{44}\left(0\right)}-\frac{\left(b-a\right)}{2Rc_{44}\left(0\right)},\ -1<s<1, \tag{E.5}$$

is written and the dimensionless coordinates, s, r and contact stress, S_{ZZ} are previously specified in Section 4.4.2. Next, the punch eccentricity parameter is derived as below.

$$\frac{b-a}{R}=\frac{b+a}{R}\left(1-2\alpha_{1}\right). \tag{E.6}$$

Substitution of Eq. (E.6) into Eq. (E.5) leads to

$$\eta p_2 S_{ZZ}(s)+\frac{p_1}{\pi}\int_{-1}^{1}\frac{S_{ZZ}(r)}{r-s}dr=-\frac{(b+a)P_1^{(-\alpha_1,-\alpha_2)}(s)}{Rc_{44}(0)},\ -1<s<1. \tag{E.7}$$

From Eq. (E.7), the normal stress is found as

$$S_{ZZ}(s)=A_0(1-s)^{\alpha_1}(1+s)^{\alpha_2},\quad -1<s<1. \tag{E.8}$$

where the first and the only nonzero coefficient A_0 is determined as follows:

$$A_0=\frac{\sin(\pi\alpha_1)(b+a)}{2p_1c_{44}R}. \tag{E.9}$$

Dimensionless lateral stress S_{XX}, electric displacement Ω_X and magnetic induction Γ_X are defined below.

$$S_{XX}(s)=\frac{\sigma_{XX}(X,0)}{c_{44}},\quad \Omega_X(s)=\frac{D_X(X,0)}{c_{44}/p_{16}},\quad \Gamma_X(s)=\frac{B_X(X,0)}{c_{44}/p_{17}}. \tag{E.10}$$

and they are explicitly stated as follows:

$$\frac{S_{XX}(s)}{A_0}=\begin{cases}\dfrac{p_3p_{10}\eta}{\sin(\pi\alpha_1)}\Big(-(1-s)^{\alpha_1}(-1-s)^{\alpha_2}-s+\alpha_1-\alpha_2\Big)\\ \qquad +(p_9+p_4p_{10})(1-s)^{\alpha_1}(1+s)^{\alpha_2}, \quad -\infty<s<-1,\\ \dfrac{p_3p_{10}\eta}{\sin(\pi\alpha_1)}\Big((1-s)^{\alpha_1}(1+s)^{\alpha_2}\cos(\pi\alpha_1)-s+\alpha_1-\alpha_2\Big)\\ \qquad +(p_9+p_4p_{10})(1-s)^{\alpha_1}(1+s)^{\alpha_2}, \quad -1<s<1,\\ \dfrac{p_3p_{10}\eta}{\sin(\pi\alpha_1)}\Big((s-1)^{\alpha_1}(1+s)^{\alpha_2}-s+\alpha_1-\alpha_2\Big)\\ \qquad +(p_9+p_4p_{10})(1-s)^{\alpha_1}(1+s)^{\alpha_2}, \quad 1<s<\infty,\end{cases} \tag{E.11}$$

$$\frac{\Omega_X(s)}{A_0}=\begin{cases}-\dfrac{(p_{12}p_5+p_{13}p_7)\,p_{16}}{\sin(\pi\alpha_1)}\left(-(1-s)^{\alpha_1}(-1-s)^{\alpha_2}-s+\alpha_1-\alpha_2\right)\\ +\eta\,p_{16}\left(p_{11}-p_{12}p_6-p_{13}p_8\right)(1-s)^{\alpha_1}(1+s)^{\alpha_2}, \quad -\infty<s<-1,\\ -\dfrac{(p_{12}p_5+p_{13}p_7)\,p_{16}}{\sin(\pi\alpha_1)}\left((1-s)^{\alpha_1}(1+s)^{\alpha_2}\cos(\pi\alpha_1)-s+\alpha_1-\alpha_2\right)\\ +\eta\,p_{16}\left(p_{11}-p_{12}p_6-p_{13}p_8\right)(1-s)^{\alpha_1}(1+s)^{\alpha_2}, \quad -1<s<1,\\ -\dfrac{(p_{12}p_5+p_{13}p_7)\,p_{16}}{\sin(\pi\alpha_1)}\left((s-1)^{\alpha_1}(1+s)^{\alpha_2}-s+\alpha_1-\alpha_2\right)\\ +\eta\,p_{16}\left(p_{11}-p_{12}p_6-p_{13}p_8\right)(1-s)^{\alpha_1}(1+s)^{\alpha_2}, \quad 1<s<\infty,\end{cases} \tag{E.12}$$

$$\frac{\Gamma_X(s)}{A_0}=\begin{cases}-\dfrac{(p_{13}p_5+p_{15}p_7)\,p_{17}}{\sin(\pi\alpha_1)}\left(-(1-s)^{\alpha_1}(-1-s)^{\alpha_2}-s+\alpha_1-\alpha_2\right)\\ +\eta\,p_{17}\left(p_{14}-p_{13}p_6-p_{15}p_8\right)(1-s)^{\alpha_1}(1+s)^{\alpha_2}, \quad -\infty<s<-1,\\ -\dfrac{(p_{13}p_5+p_{15}p_7)\,p_{17}}{\sin(\pi\alpha_1)}\left((1-s)^{\alpha_1}(1+s)^{\alpha_2}\cos(\pi\alpha_1)-s+\alpha_1-\alpha_2\right)\\ +\eta\,p_{17}\left(p_{14}-p_{13}p_6-p_{15}p_8\right)(1-s)^{\alpha_1}(1+s)^{\alpha_2}, \quad -1<s<1,\\ -\dfrac{(p_{13}p_5+p_{15}p_7)\,p_{17}}{\sin(\pi\alpha_1)}\left((s-1)^{\alpha_1}(1+s)^{\alpha_2}-s+\alpha_1-\alpha_2\right)\\ +\eta\,p_{17}\left(p_{14}-p_{13}p_6-p_{15}p_8\right)(1-s)^{\alpha_1}(1+s)^{\alpha_2}, \quad 1<s<\infty,\end{cases} \tag{E.13}$$

The constants, p_i, i=1,…,17, are same as the constants derived in Sections 3.2 and 4.1.2. The force required for moving contact is computed by Eq. (4.99).

CURRICULUM VITAE

Surname, Name: Toktaş, Selim Ercihan

EDUCATION

Degree	Institution	Year of Graduation
MS	METU Mechanical Engineering	2018
BS	METU Mechanical Engineering	2013
High School	Turhan Tayan Anatolian High School, Bursa	2008

WORK EXPERIENCE

Enrollment	Place	Year
Teaching Assistant	METU Mech. Eng. Dept.	2019-Present
Teaching Assistant	Baskent University Mech. Eng. Dept.	2015-2017
Second Lieutenant	Turkish Armed Forces	2013-2014

SCHOLARSHIPS & REWARDS

Program Name	Institution	Year of
2250	TÜBİTAK	2023
1002A	TÜBİTAK	2023
2224A	TÜBİTAK	2022
2211A	TÜBİTAK	2021

FOREIGN LANGUAGES

Advanced English

PUBLICATIONS

1. Toktas S. E., Dag, S. "Magneto-electro-elastic response of functionally graded multiferroic coatings under moving hertzian contact", Journal of Mechanics of Materials and Structures, Manuscript is accepted, (2024).

2. Toktas S. E., Dag S. "Mechanics of moving contacts involving functionally graded multiferroics", Archives of Mechanics, 75(4), 431–468, (2023).

3. Toktas S. E., Dag S. "Stresses in multi-layer coatings in Hertzian contact with a moving circular punch", Tribology International, 171, 107565 (2022).

4. Toktas S. E., Dag S. "Multi-layer model for moving contact problems of functionally graded coatings with general variations in physical properties", Proceedings of the Institution of Mechanical Engineers, Part L: Journal of Materials: Design and Applications, 236(10), 1967–1980, (2022).

5. Toktas S. E., Dag S. "Oblique surface cracking and crack closure in an orthotropic medium under contact loading", Theoretical and Applied Fracture Mechanics, 109, 102729 (2020).

HOBBIES

Games of Strategy, Table Tennis, Trading, Watching Movies, Fishing.